ISSN 0911-5730
UVSOR-48
August 2021

UVSOR ACTIVITY REPORT 2020

UVSOR Synchrotron Facility
Institute for Molecular Science
National Institutes of Natural Sciences

UVSOR III since 2012





Preface

This Activity Report covers scientific and technological activities carried out using the UVSOR-III Synchrotron in FY2019 (April 2019 - March 2020). We present scientific examples of how the users study at the UVSOR Synchrotron Facility.

The present UVSOR-III Synchrotron is one of the most advanced low-energy SR facilities of the 3rd generation SR in the world and is now one of the critical resources in doing molecular science. The UVSOR-III Synchrotron has a small electron storage ring but has powerful 6-undulator beamlines (3 VUV and 3 in-vacuum soft X-ray undulators) with 8-dipole beamlines. We never stop improving and upgrading our micro- and nano-scale photoabsorption and photoemission approaches and in situ/operando measurements in the VUV and soft X-ray regions, based on our strategic international collaboration program in molecular science. We are grateful to all the people who use our facility and support our efforts.

UVSOR operates for 40 weeks/year (ca. 2,200 h user time), accepts ~220 proposals, about 1,300 researchers meaning ca. 100 people/beamline and ca. 30 people/week. Most users stay for one or two weeks for doing the experiment. To continue high-level achievements in science and technology at the UVSOR-III Synchrotron, our in-house staff is constantly committed to maintaining and improving high-performance accelerators and beamlines. The FY2020 would be a challenging year for all researchers, and COVID-19 issues will have a major impact on synchrotron users around the world. We decided to operate the UVSOR as planned after completing



the scheduled maintenance weeks, however the most of users may not come to the experiments at UVSOR because of limitation of the working activity by COVID-19. Considering the situation, it was decided to allocate a beamtime to the second half period by transferring the same project approved in the first half period with or without beamtime cancellation.

In terms of personnel, an associate professor, Yoshitaka Taira, joined to UVSOR from April 2020. We hope he will spice up some of the uniqueness of our facility, that is, a development and utilization of novel quantum beam sources as like gamma-ray related experiments dedicated at the beamline BL1U.

On the experimental side, technology development will not stop, hence we will make a progress on the imaging-related techniques to inspire the advanced molecular science. We have started to construct the new endstation at the undulator-based soft X-ray beamline BL6U. The new apparatus is based on the momentum-resolved photoelectron emission microscopy and spectro-microscopy, we call it “photoelectron momentum microscope”. The project will be developed by three steps, and in the end the novel function will be uniquely added to our apparatus to keep future developments ranging for 10-15 years in the UVSOR Synchrotron Facility. The advanced SR-related instrument will offer opportunities in characterizing the electronic structure of surface atomic sites, thin films, molecular adsorbates, bulk crystals, and so on.

We look forward to receiving your feedback and suggestions on the continuing evolution of the UVSOR Synchrotron Facility. And we hope many users will perform excellent work by fully utilizing the UVSOR-III Synchrotron as a unique international hub for the SR research in advanced molecular science.

April 2020

Satoshi Kera

Director of the UVSOR Synchrotron Facility

The 7th JSSRR Achievement Award Given to Mr. Toshio HORIGOME

Mr. Toshio HORIGOME, Senior Engineer in UVSOR, has been awarded "the 7th Achievement Award" from the Japanese Society for Synchrotron Radiation Research (JSSRR). The award is given by JSSRR to persons who made a significant contribution to support for synchrotron radiation research and technology for many years. The award was presented in the award ceremony in the 33rd Annual Meeting of JSSRR in January, 2020.



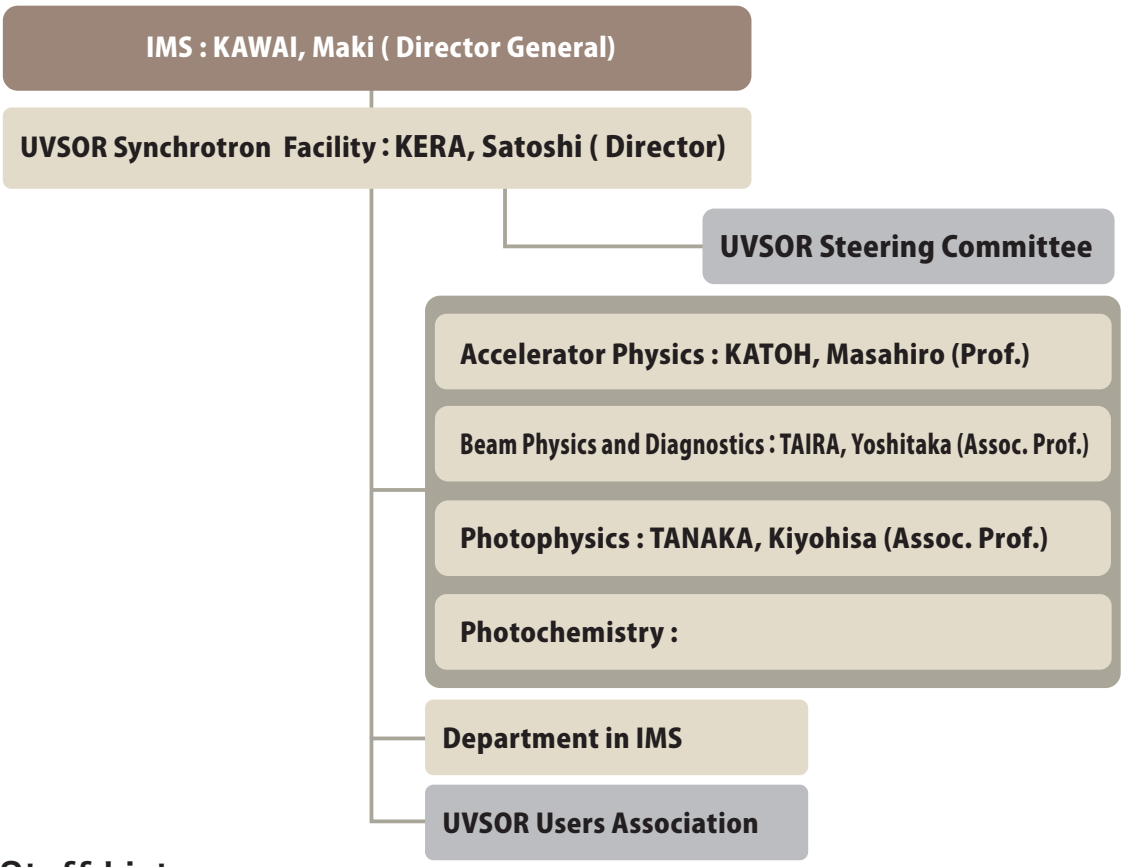
I

Organization and Staff List



UVSOR Synchrotron Facility Organization

May 2020



Staff List

UVSOR Staff

Director

KERA, Satoshi	Professor	kera@ims.ac.jp	

Light Source Division (Accelerator Physics)

KATOH, Masahiro	Project Professor	mkatoh@ims.ac.jp	
KANEYASU, Tatsuo	Visiting Associate Professor		
FUJIMOTO, Masaki	Assistant Professor	mfmoto@ims.ac.jp	
SALEHI, Elham	Project Research Staff	elham@ims.ac.jp	(since Sep. 2019)
YAMAZAKI, Jun-ichiro	Unit Chief Engineer	yamazaki@ims.ac.jp	
HAYASHI, Kenji	Unit Chief Engineer	h-kenji@ims.ac.jp	
TESHIMA, Fumitsuna	Assistant Unit Chief Engineer	tetsu@ims.ac.jp	
OTA, Hiroshi	Engineer	ota@ims.ac.jp	(since Nov. 2019)
MINAKUCHI, Aki	Supporting Engineer	minakuchi@ims.ac.jp	

Light Source Division (X-ray Imaging Optics)

TAIRA, Yoshitaka	Associate Professor	yostaira@ims.ac.jp	(since Apr. 2020)

MATSUI, Fumihiko	Senior Researcher	matui@ims.ac.jp
OHIGASHI, Takuji	Assistant Professor	ohigashi@ims.ac.jp
MATSUDA, Hiroyuki	Project Research Staff	hmatsuda@ims.ac.jp
YUZAWA Hayato	Engineer	hayato@ims.ac.jp

Beamline Division (Photophysics)

TANAKA, Kiyohisa	Associate Professor	k-tanaka@ims.ac.jp
IDETA, Shin-ichiro	Assistant Professor	idetas@ims.ac.jp
SAKAI, Masahiro	Unit Chief Engineer	sakai@ims.ac.jp

Beamline Division (Photochemistry)

IWAYAMA, Hiroshi	Assistant Professor	iwayama@ims.ac.jp
NAKAMURA, Eiken	Facility Chief Engineer	eiken@ims.ac.jp
KONDO, Naonori	Assistant Unit Chief Engineer	nkondo@ims.ac.jp
YANO, Takayuki	Assistant Unit Chief Engineer	yano@ims.ac.jp
MAKITA, Seiji	Assistant Unit Chief Engineer	makita@ims.ac.jp
HORIGOME, Toshio	Senior Engineer	horigome@ims.ac.jp

Secretary

HAGIWARA, Hisayo	hagiwara@ims.ac.jp	(until Aug. 2019)
INAGAKI, Itsuko	itsuko@ims.ac.jp	
ISHIHARA, Mayumi	mayu@ims.ac.jp	(since Oct. 2019)

UVSOR Steering Committee (* Chair)

KERA, Satoshi *	UVSOR, IMS	
KATOH, Masahiro	UVSOR, IMS	
TANAKA, Kiyohisa	UVSOR, IMS	
TAIRA, Yoshitaka	UVSOR, IMS	(since Apr. 2020)
SHIMADA Kenya	UVSOR, IMS(Hiroshima Univ.)	(since Apr. 2020)
KANEYASU, Tatsuo	UVSOR, IMS (Kyushu Synchrotron Light Research Center)	(until Mar. 2020)
MATSUI, Fumihiko	UVSOR, IMS	
YOKOYAMA, Toshihiko	IMS	
AKIYAMA, Shuji	IMS	
KUSAMOTO, Tetsuro	IMS	(since Apr. 2019)
YAMAMOTO, Hiroshi	IMS	
KITAURA, Mamoru	Yamagata Univ.	(until Mar. 2020)
KOMORI, Fumio	Univ. of Tokyo	(until Mar. 2020)
OKABAYASHI, Jun	Univ. of Tokyo	(until Mar. 2020)
HATSUI, Takaki	JASRI	
OKUDA, Taichi	Hiroshima Univ.	
KUMIGASHIRA, Hiroshi	KEK-PF	

TAKAKUWA, Yuji	Tohoku Univ.	(until Mar. 2020)
KANEMITSU, Yoshihiko	Kyoto Univ,	(since Apr. 2020)
KIMURA, Shin-ichi	Osaka Univ.	(since Apr. 2020)
HARADA, Yoshihisa	Univ. of Tokyo	(since Apr. 2020)
FUKUSHIMA, Takanori	Tokyo Insititute of Technology	(since Apr. 2020)

UVSOR Users Association (* Chair)

KIMURA, Shin-ichi *	Osaka Univ.	
KITAURA, Mamoru	Yamagata Univ.	(since Apr. 2020)
OKABAYASHI, Jun	Univ. of Tokyo	
KONDO, Hiroshi	Keio Univ.	(until Mar. 2020)
ITO, Takahiro	Nagoya Univ.	(until Mar. 2020)
YAMANE, Hiroyuki	RIKEN	
HIKOSAKA, Yasumasa	Toyama Univ.	(since Apr. 2020)

Graduate Students

KIMURA, Keigo	Nagoya Univ.	(until Sep. 2019)
KIMURA, Shinnosuke	Nagoya Univ.	(until Sep. 2019)
NABEHIRA, Naoki	Nagoya Univ.	(until Sep. 2019)
HAYASHI, Naoki	Nagoya Univ.	(until Sep. 2019)
MATSUNAGA, Yukihiro	Nagoya Univ.	(until Sep. 2019)

Visiting Scientists

PEI, Xiangyu	Univ. of Gothenburg	Jun. 2019
KONG, Xiangrui	Univ. of Gothenburg	Jun. 2019, Oct. 2019
KHODABANDEH, Aminreza	Univ. of South Australia	Jul. 2019
CHANG, Han-Wei	Tamkang Univ.	Jul. 2019
HUANG, Tzu-His	Tamkang Univ.	Jul. 2019
HUANG, Yu-Cheng	Tamkang Univ.	Jul. 2019, Aug. 2019, Jan. 2020
HSU, Wei-Hao	Tamkang Univ.	Aug. 2019
BOUILLAUD, Thomas	Univ. of Pierre Marie Curie	Jul. 2019
CEOLIN, Denis	Synchrotron SOLEIL	Aug. 2019
SAISOPA, Thanit	Suranaree Univ. of Technology	Aug. 2019
Borsup, Jongrak	Suranaree Univ. of Technology	Aug. 2019
Klaiphet, Kanchanasuda	Suranaree Univ. of Technology	Aug. 2019
LAI, Yu-Ling	National Synchrotron Radiation Research Center	Aug. 2019
SHIU, Hung-Wei	National Synchrotron Radiation Research Center	Aug. 2019
YU, Li-Chung	National Synchrotron Radiation Research Center	Aug. 2019
HSU, Wei-Hao	Academia Sinica	Aug. 2019
PARK, Heonjoon	Seoul National Univ.	Sep. 2019, Nov. 2019, Feb. 2020
LEE, Suyoung	Seoul National Univ.	Sep. 2019, Nov. 2019, Feb. 2020

OH, Dong Jin	Seoul National Univ.	Sep.2019, Nov. 2019, Feb. 2020
RÜEHL, Eckart	Free Univ. of Berlin	Sep. 2019, Mar. 2020
GERMER, Gregor	Free Univ. of Berlin	Sep. 2019
FLESCH, Roman	Free Univ. of Berlin	Sep. 2019
PRIESTLEY, Michael	Univ. of Gothenburg	Oct. 2019
HE, Ruihua	Westlake Univ.	Oct. 2019
ZHAO, Geng	Westlake Univ.	Oct. 2019
WEN, Wei	Westlake Univ.	Oct. 2019
HONG, Caiyun	Westlake Univ.	Oct. 2019
SONG, Zhen	Westlake Univ.	Oct. 2019
MAHATNIRUNKUL, Thanisorn	NANOTEC	Nov. 2019
ZHANG, Chao	Tsinghua Univ.	Nov. 2019
ZHAO, Yufei	Tsinghua Univ.	Nov. 2019
JIANG. Xuefeng	Tsinghua Univ.	Nov. 2019
XU. Pengfei	Tsinghua Univ.	Nov. 2019
CHUANG, Cheng-Hao	Tamkang Univ.	Jan. 2020
VELASCO Velez Jesus Juan	Max Planck Institute for Chemical Energy Conversion	Jan. 2020
YOO, Han Young	Seoul National Univ.	Feb. 2020
PATANEN, Minna	Univ. of Oulu	Feb. 2020
MANSIKKALA, Leo	Univ. of Oulu	Feb. 2020
MICHAILOUDI, Georgia	Univ. of Oulu	Mar. 2020
LIN, Jack	Univ. of Oulu	Mar. 2020
KAMAL, Raj R	Univ. of Oulu	Mar. 2020

II

Current Status of Light Sources and Beamlines

Light Source in 2019

1. Status of UVSOR Accelerators

In the fiscal year 2019, we had scheduled to operate UVSOR-III from May to March, for 36 weeks for users. We had several machine troubles as described later. In June we had a trouble in the vacuum chamber of the booster synchrotron. Since we had another trouble on the beam-line vacuum in the same week, we canceled users operation for one week, which was compensated with a machine study week which had been scheduled in the latter half of the year. In cases of other minor troubles, we extended the operation time for compensation. We had a scheduled shutdown period in April for 4 weeks. This was mainly for the scheduled maintenance works. We had one week shut down period in August and October, two week one around the New Years day and one week one at the end of March. We had 2 weeks for machine and beamline conditioning in May after the spring shut down. We had 4 weeks for machine conditionings and studies, in the latter half of the year, although one week was replaced with users run as described above. The machine study week in November was mainly for the machine conditioning after the annual planned power outage.

We operated the machine for 34 weeks in the multi-bunch top-up mode at 300 mA, and 2 weeks in the single-bunch top-up mode at approximately 40 mA. The monthly statistics of the operation time and the integrated beam current are shown in Fig. 1.

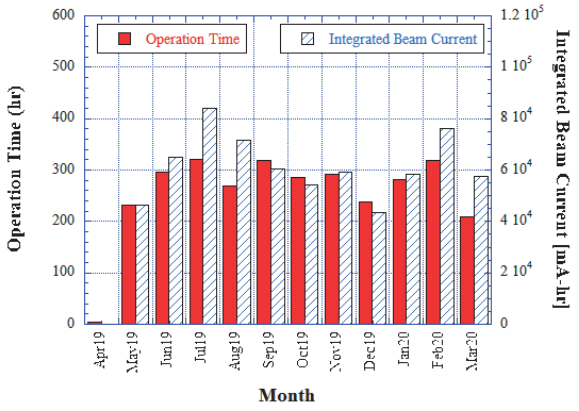


Fig. 1. Monthly statistics in FY2018.

The weekly operation schedule is as follows. On Monday, from 9 am to 9 pm, the machine is operated for machine conditionings and studies. On Tuesday and Wednesday, from 9 am to 9 pm, the machine is operated for users. From Thursday 9 am to Friday 9 pm, the machine is operated for 36 hours continuously for users. Therefore, the beam time for users in a week is 60 hours. In the single bunch operation weeks, the machine is operated for 12 hours per day from Tuesday to Friday.

We had a vacuum leakage trouble at the booster synchrotron. We quickly localized the leaking position, which was on the vacuum chamber at a bending magnet. Fortunately, we could stop the leakage by using a liquid vacuum seal.



Fig. 2. Sextupole coil for multipole magnets.

The cooling water leakage from the sextupole coils wound on the pole faces of the multipole (quadrupole/sextupole) magnets have been getting more serious. As cutting the hollow conductor which was removed, from the magnet, it was confirmed that the walls of the hollow conductor have been eroded by the water flow during the fifteen year operation. In the spring shutdown 2019, we applied liquid sealant for all the coils for life prolonging. However, even after this, some coils started leaking. In parallel with repairing the leaking coils, we have constructed new coils for a half of the 32 multipole magnets in FY2019. We have started the replacement in March, 2020. The coils for the half of the magnets will be replaced by the end of April 2020. Those of another half will be replaced by the end of April 2021.

2. Improvements and Developments

The pulse magnet power supplies for the injection kickers of the booster-synchrotron malfunction a few times in a year. It has been recognized that the IGBT in the power supply caused the trouble. We have started replacing them one after another with more robust ones for high voltage.

The vacuum data acquisition system was replaced after nearly 15 year operation, which has been collecting the vacuum pressure for all part of the accelerator system and beam-line front ends. The PLCs were replaced and the data display ability was improved.

The timing system of the linear accelerator was improved. Now the trigger of the electron gun and that of the klystron can be adjusted independently from the control room.

The access bridge to the inside of the storage ring was replaced to create a space for a new beam-line. The pulse motor of an undulator U6, which was constructed in 2002, has been replaced to be compatible with the new control system.

Light Source Developments and Beam Physics Studies

We continue the efforts to develop novel light sources technologies and their applications such as free electron lasers, coherent harmonic generation, coherent synchrotron radiation, laser Compton scattering gamma-rays, intense polarized and vortex UV radiation at the source development station BL1U, which was constructed under the support of Quantum Beam Technology Program by MEXT/JST.

In these years, we continued studying the generations of structured light beams, such as optical vortex beams and optical vector beams, from undulators in collaboration with Hiroshima U., Nagoya U. and other institutes. Moreover, we have demonstrated a novel method to utilize temporal structure of undulator radiation for coherent control of atoms. BL1U is a unique beam-line, which enables us to use the direct beam from a tandem undulator system for coherent control experiments, which are described in these reports.

The laser Compton scattering gamma-rays are powerful tools for nuclear science and technologies. By using various external lasers, we have demonstrated generating quasi-monochromatic gamma-rays in the energy range from 1MeV to around 10MeV. We continue the experiments in collaboration with Kyoto U., AIST and QST towards imaging applications. At BL1U, we have a special port for the laser injection for 90 degree Thomson scattering, which enable us to generate short gamma-ray pulses of sub-picosecond order. With this novel light source, we have started new experiments on positron lifetime spectroscopy in collaboration with Yamagata U., Nagoya U. and AIST.

Masahiro KATOH
(UVSOR Synchrotron)

UVSOR Accelerator Complex

Injection Linear Accelerator

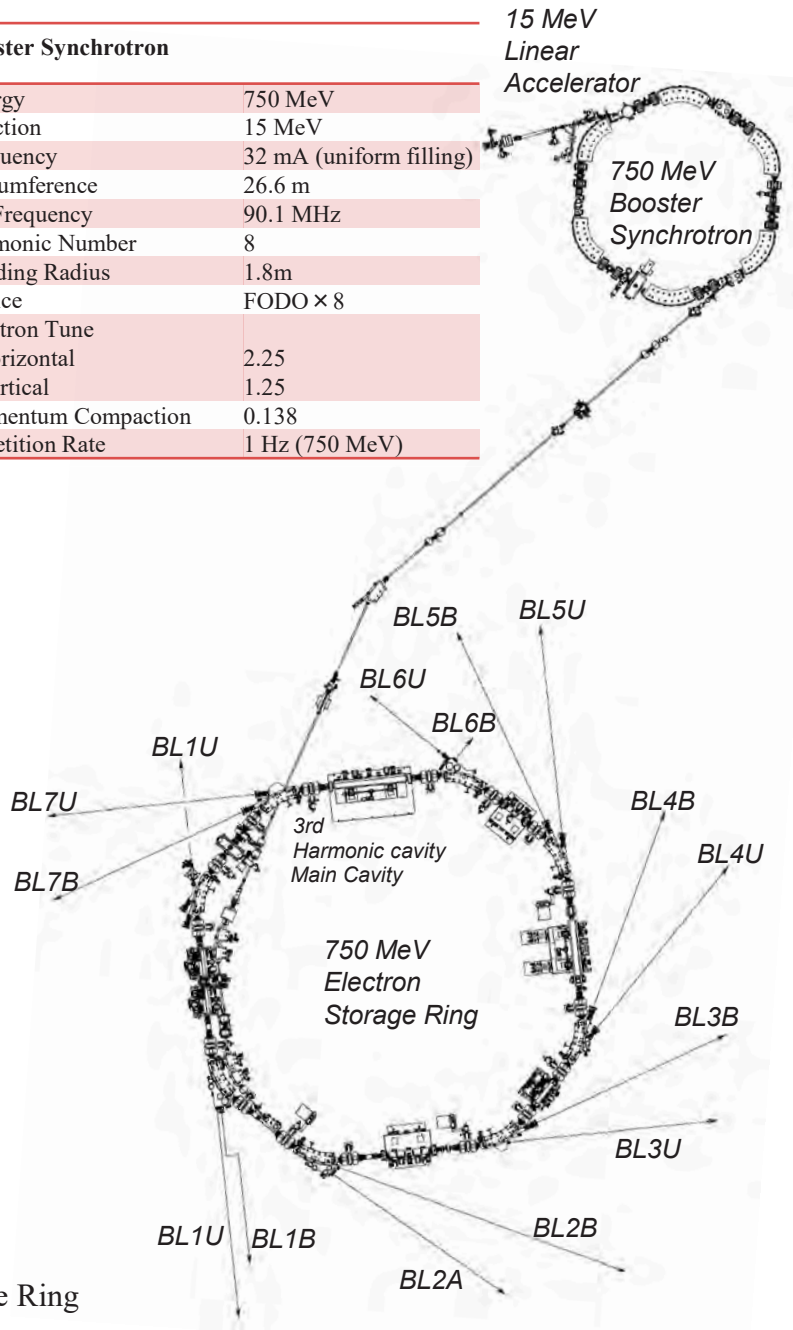
Energy	15 MeV
Length	2.5 m
Frequency	2856 MHz
Accelerating RF Field	2π/3 Traveling Wave
Klystron Power	1.8 MW
Energy Spread	~1.6 MeV
Repetition Rate	2.6 Hz

UVSOR-III Storage-Ring

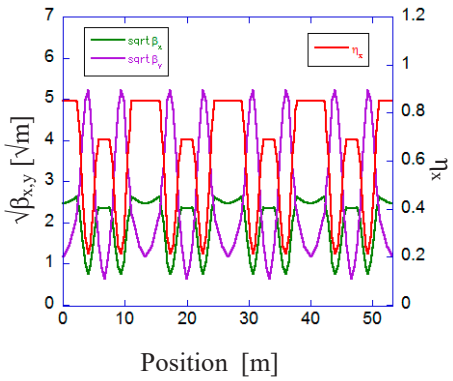
Energy	750 MeV
Injection Energy	750 MeV
Maximum Storage Current	500 mA (multi bunch) 100 mA (single bunch)
Normal operation current (Top-up mode)	300 mA (multi bunch) 50 mA (single bunch)
Natural Emittance	17.5 nm-rad
Circumference	53.2 m
RF Frequency	90.1 MHz
Harmonic Number	16
Bending Radius	2.2 m
Lattice	Extended DBA × 4
Straight Section	(4 m × 4)+(1.5 m × 4)
RF Voltage	120 kV
Betatron Tune	
Horizontal	3.75
Vertical	3.20
Momentum Compaction	0.030
Natural Chromaticity	
Horizontal	-8.1
Vertical	-7.3
Energy Spread	5.26×10^{-4}
Coupling Ratio	1%
Natural Bunch Length	128 ps

Booster Synchrotron

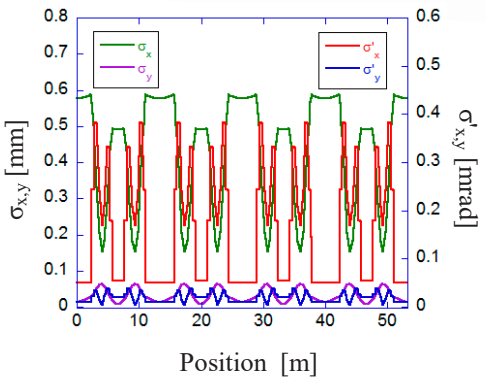
Energy	750 MeV
Injection	15 MeV
Frequency	32 mA (uniform filling)
Circumference	26.6 m
RF Frequency	90.1 MHz
Harmonic Number	8
Bending Radius	1.8m
Lattice	FODO × 8
Betatron Tune	
Horizontal	2.25
Vertical	1.25
Momentum Compaction	0.138
Repetition Rate	1 Hz (750 MeV)



Electron Beam Optics of UVSOR-III Storage Ring

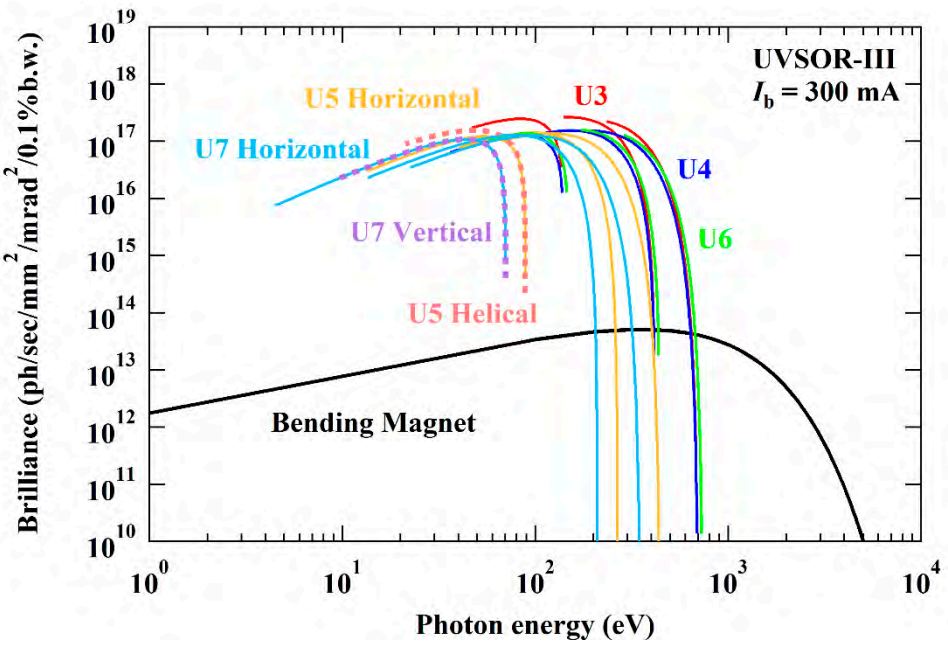


Horizontal/vertical betatron functions and dispersion function



Horizontal/vertical electron beam size and beam divergences

Insertion Device



Brilliance of radiation from the insertion devices (U3, U4, U5, U6 and U7) and a bending magnet of UVSOR-III

U1 Apple-II Undulator /

Optical Klystron

Number of Periods	10+10
Period length	88 mm
Pole Length	0.968 m + 0.968 m
Pole Gap	24-200 mm
Deflection Parameter	7.36 (Max. Horizontal) 4.93 (Max. Vertical) 4.06 (Max. Herical)

U3 In-vacuum Undulator

Number of Periods	50
Period length	38 mm
Pole Length	1.9 m
Pole Gap	16.5-40 mm
Deflection Parameter	1.8-0.24

U4 In-vacuum Undulator

Number of Periods	26
Period length	38 mm
Pole Length	0.99 m
Pole Gap	13-40 mm
Deflection Parameter	2.4-0.19

U5 Apple-II

Variable Polarization Undulator

Number of Periods	38
Period length	60 mm
Pole Length	2.28 m
Pole Gap	24-190 mm
Deflection Parameter	3.4 (Max. Horizontal) 2.1 (Max. Vertical) 1.8 (Max. Helical)

U6 In-vacuum Undulator

Number of Periods	26
Period length	36 mm
Pole Length	0.94 m
Pole Gap	13-40 mm
Deflection Parameter	1.78 - 0.19

U7 Apple-II

Variable Polarization Undulator

Number of Periods	40
Period length	76 mm
Pole Length	3.04 m
Pole Gap	24-200 mm
Deflection Parameter	5.4 (Max. Horizontal) 3.6 (Max. Vertical) 3.0 (Max. Helical)

Bending Magnets

Bending Radius	2.2 m
Critical Energy	425 eV

Beamlines in 2019

Kiyohisa TANAKA
UVSOR synchrotron Facility, Institute for Molecular Science

UVSOR is one of the highest-brilliance light sources in the extreme-ultraviolet region among the synchrotron radiation facilities with electron energies of less than 1 GeV. The natural emittance of the UVSOR-III storage ring is as low as 17.5 nm-rad after the successful completion of the storage ring upgrade project (the UVSOR-III project) in 2012.

Eight bending magnets and six insertion devices are available as synchrotron light sources at UVSOR. As of 2018 there are a total of fourteen operational beamlines, which are classified into two categories. Twelve of them are the so-called "Open beamlines", which are open to scientists from universities and research institutes belonging to the government, public organizations, private enterprises and also those from foreign countries. The remaining two beamlines are the "In-house beamlines", and are dedicated to the use of research groups within Institute for Molecular Science (IMS).

There is one soft X-ray station equipped with a double-crystal monochromator, seven extreme ultraviolet and soft X-ray stations with grazing incidence monochromators, three vacuum ultraviolet (VUV) stations with normal incidence monochromators, two infrared (IR) stations equipped with Fourier-Transform interferometers, and one direct radiation station located after two undulators installed in tandem, as shown in the appended table (next page) for all available beamlines at UVSOR in 2019. The details of the updates for several beamlines are the followings.

BL4U, equipped with a scanning transmission soft X-ray microscope (STXM), is popular not only for academic users but also many industrial users. In FY2019, a new Fresnel zone plate, whose focal length is different from the previous one, was prepared to perform measurements with energy of photons from 55 eV. This zone plate makes users possible to perform Li K-edge measurements, which is important to study all solid state Li batteries.

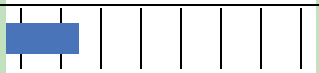
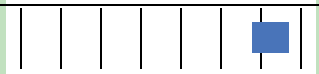
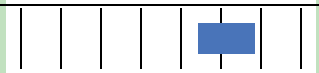
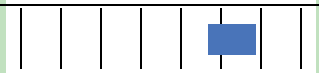
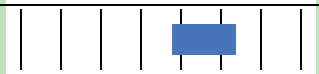
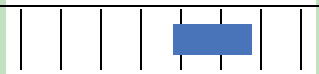
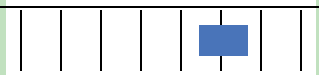
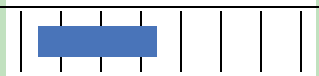
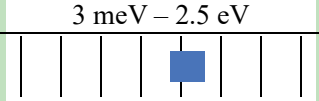
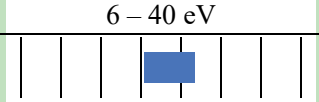
BL5U has been officially opened for users from 2016 as high energy resolution angle-resolved photoemission spectroscopy (ARPES) beamline. In FY2019, the latest version of ARPES analyzer has been installed (MB Scientific AB, A-1 analyzer Lens#5). Users can now use so-called "deflector mapping" for all kinetic energies and lens modes. By combining with the micro-focused beam (23 x 40 μm), users can perform measurements on small samples or inhomogeneous samples without changing sample position.

In BL6U, which is one of the in-house beamlines, so-called "Momentum microscope (MM)", which is an electronic spectroscopy with both the real space and momentum space resolution, has been installed in February 2020 (SPECS Surface Nano Analysis GmbH, KREIOS 150 MM). It will be upgraded to double hemispherical analyzer in FY2020 and will also be upgraded for spin-resolved measurements in the future.

In June 2019, a serious vacuum leakage accident occurred from water cooling line at M0 mirror located at upstream of BL7B. It was installed 20 years ago, and cooling water made a hole through 1 mm thick copper pipe. Although the accident occurred during user operation, fortunately, the upper most valves of beamline was closed because of the vacuum interlock system and the effect was very limited to the storage ring. Since it was hard to repair the copper pipe quickly because of the limited space during the user operation, we decided to shut down BL7B during FY2019. In the meantime, we pumped the water cooling line with vacuum to stop the water leakage and investigated the stability of the beam spot position at endstation without water cooling of M0 mirror. According to the investigation, we concluded that the manual adjustment of M0 mirror angle for every 3 hours can make users perform experiments. BL7B will start to accept users from FY2020.

All users are required to refer to the beamline manuals and the UVSOR guidebook (the latest revision in PDF format uploaded on the UVSOR web site in June 2018), on the occasion of conducting the actual experimental procedures. Those wishing to use the open and in-house beamlines are recommended to contact the appropriate beamline master (see next page). For updated information on UVSOR, please see http://www.uvsor.ims.ac.jp.

Beamlines at UVSOR

Beamline	Monochromator / Spectrometer	Energy Range	Targets	Techniques	Contact
BL1U	Free electron laser, Tandem undulator, LSC Gamma-rays	 1.6 – 13.9 eV, 1-10MeV		(Irradiation)	Y. Taira yostaira@ims.ac.jp
BL1B	Martin-Puplett FT-FIR	 0.5 – 30 meV	Solid	Reflection Absorption	K. Tanaka k-tanaka@ims.ac.jp
BL2A	Double crystal	 585 – 4 keV	Solid	Reflection Absorption	K. Tanaka k-tanaka@ims.ac.jp
BL2B	18-m spherical grating (Dragon)	 24 – 205 eV	Solid	Photoemission	S. Kera kera@ims.ac.jp
BL3U	Varied-line-spacing plane grating (Monk-Gillieson)	 60 – 800 eV	Gas Liquid Solid	Absorption Photoemission Photon-emission	M. Nagasaka nagasaka@ims.ac.jp
BL3B	2.5-m off-plane Eagle	 1.7 – 30 eV	Solid	Reflection Absorption Photon-emission	K. Tanaka k-tanaka@ims.ac.jp
BL4U	Varied-line-spacing plane grating (Monk-Gillieson)	 50 – 770 eV	Gas Liquid Solid	Absorption (Microscopy)	T. Ohigashi ohigashi@ims.ac.jp
BL4B	Varied-line-spacing plane grating (Monk-Gillieson)	 25 eV – 1 keV	Gas Solid	Photoionization Photodissociation Photoemission	H. Iwayama iwayama@ims.ac.jp
BL5U	Spherical grating (SGM-TRAIN†)	 5 – 250 eV	Solid	Photoemission	K. Tanaka k-tanaka@ims.ac.jp
BL5B	Plane grating	 6 – 600 eV	Solid	Calibration Absorption	K. Tanaka k-tanaka@ims.ac.jp
BL6U*	Variable-included-angle varied-line-spacing plane grating	 30 – 500 eV	Gas Solid	Photoionization Photodissociation Photoemission	F. Matsui matui@ims.ac.jp
BL6B	Michelson FT-IR	 3 meV – 2.5 eV	Solid	Reflection Absorption IR microscope	K. Tanaka k-tanaka@ims.ac.jp
BL7U	10-m normal incidence (modified Wadsworth)	 6 – 40 eV	Solid	Photoemission	S. Ideta idetas@ims.ac.jp
BL7B	3-m normal incidence	 1.2 – 25 eV	Solid	Reflection Absorption Photon-emission	K. Tanaka k-tanaka@ims.ac.jp

Yellow columns represent undulator beamlines.
* In-house beamline.

BL1U

Light Source Development Station

▼Description

BL1U is dedicated for developments and applications of various novel photon sources including free electron laser in the range from visible to deep UV, coherent harmonic generation in the deep UV and VUV, laser Compton scattering gamma-rays and undulator radiation with various polarization properties including optical vortex beam and optical vector beam.

The beam-line is equipped with a dedicated twin polarization variable undulator system with a buncher section, which can be used for a FEL oscillator and a VUV CHG. It is also equipped with a femto-second laser system synchronized with the accelerator, which is used for CHG, slicing, LCS and coherent THz radiation generation.

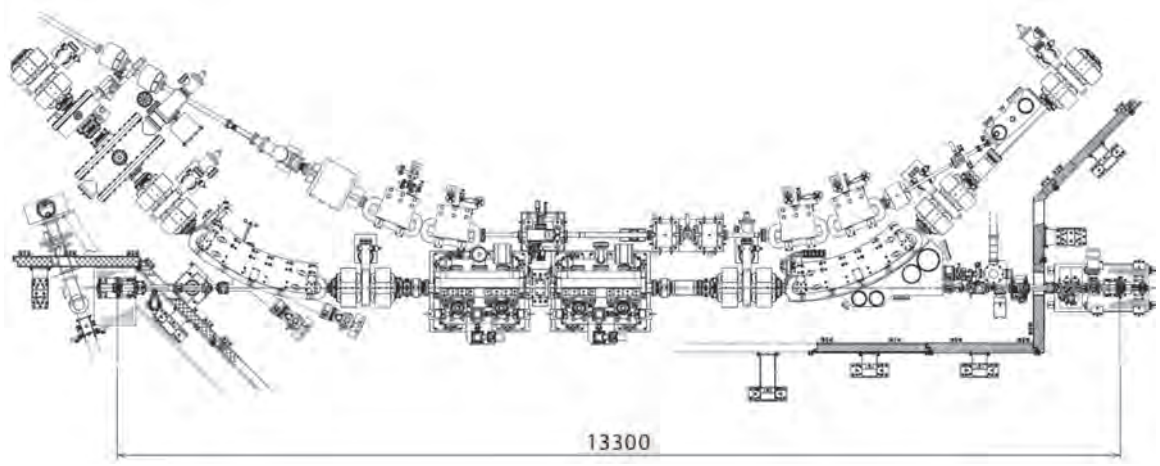


Fig. 1. Configuration of the free electron laser (under reconstruction)



Fig. 2. Twin Apple-II Undulator

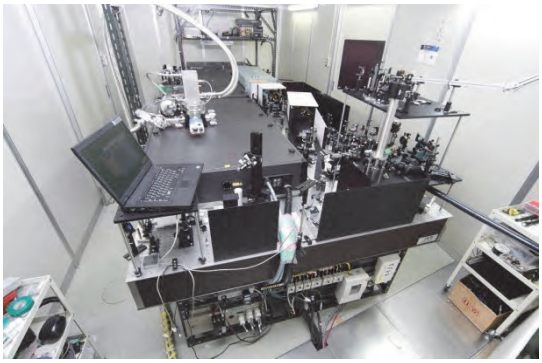


Fig. 3. Accelerator synchronized Laser System

▼Technical Data of FEL

Wave Length	199-800 nm
Spectral Band Width	~10^{-4}
Polarization	Circular/Linear
Pulse Rate	11.26 MHz
Max. Ave. Power	~1W

▼Technical Data of Ti:Sa Laser

Wave Length	800 nm		
Pulse Length	130 fsec		
Oscillator	90.1 MHz		
Pulse Energy	2.5mJ	10mJ	50mJ
Repetition Rate	1kHz	1kHz	10Hz

BL1B

Terahertz Spectroscopy Using Coherent Synchrotron Radiation

▼Description

Coherent synchrotron radiation (CSR) is a powerful light source in the terahertz (THz) region. This beamline has been constructed for basic studies on the properties of THz-CSR. However, it can be also used for measurements of reflectivity and transmission spectra of solids using conventional synchrotron radiation.

The emitted THz light is collected by a three-dimensional magic mirror (3D-MM, M0) of the same type as those already successfully installed at BL43IR in SPring-8 and BL6B in UVSOR-II. The 3D-MM was installed in bending-magnet chamber #1 and is controlled by a 5-axis pulse motor stage (x, z translation; θ_x, θ_y, θ_z rotation). The acceptance angle was set at 17.5-34 degrees (total 288 mrad) in the horizontal direction. The vertical angle was set at ±40 mrad to collect the widely expanded THz-CSR.

The beamline is equipped with a Martin-Puplett type interferometer (JASCO FARIS-1) to cover the THz spectral region from 4 to 240 cm^{-1} ($h\nu$ = 500 μeV-30 meV). There is a reflection/absorption spectroscopy (RAS) end-station for large samples (~ several mm). At the RAS end-station, a liquid-helium-flow type cryostat with a minimum temperature of 4 K is installed.

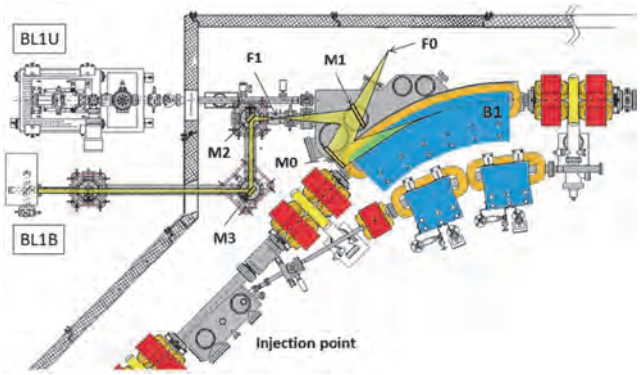


Fig. 1. Schematic top view of the beam extraction part of the THz-CSR beamline, BL1B. The three-dimensional magic mirror (3D-MM, M0) and a plane mirror (M1) are located in the bending-magnet chamber. A parabolic mirror (M2) is installed to form a parallel beam. The straight section (BL1U) is used for coherent harmonic generation (CHG) in the VUV region.

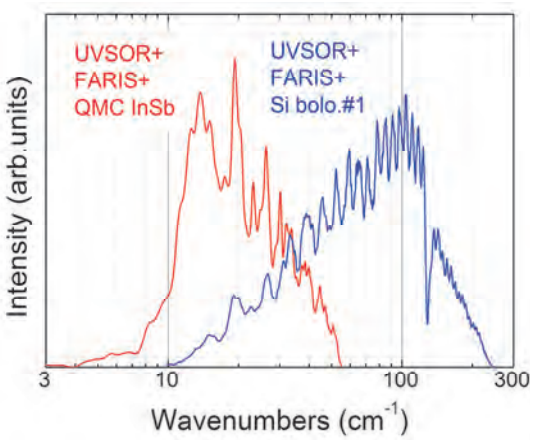


Fig. 2. Obtained intensity spectra with the combination of a light source (UVSOR), interferometer (FARIS-1), and detectors (Si bolometer and InSb hot-electron bolometer).

▼Technical Data

Interferometer	Martin-Puplett (JASCO FARIS-1)
Wavenumber range (Energy range)	4-240 cm^{-1} (500 μeV-30 meV)
Resolution in cm^{-1}	0.25 cm^{-1}
Experiments	Reflection/transmission spectroscopy
Miscellaneous	Users can use their experimental system in this beamline.

BL2A

Soft X-Ray Beamline for Photoabsorption Spectroscopy

▼Description

BL2A is a soft X-ray beamline for photoabsorption spectroscopy. The beamline is equipped with a focusing premirror and a double-crystal monochromator [1]. The monochromator serves soft X-rays in the energy region from 585 to 4000 eV using several types of single crystals, such as beryl, KTP ($KTiOPO_4$), InSb, and Ge. The throughput spectra measured using a Si photodiode (AXUV-100, IRD Inc.) are shown in Fig. 1. The typical energy resolution (E / ΔE) of the monochromator is approximately 1500 for beryl and InSb.

There is a small vacuum chamber equipped with an electron multiplier (EM) detector. Photoabsorption spectra for powdery samples are usually measured in total electron yield mode, with the use of the EM detector. In addition, a hemispherical electron analyzer for photoelectron spectroscopy is equipped.

Recently, a new omnidirectional photoelectron acceptance lens (OPAL) has been developed aiming to realize 2π-steradian photoelectron spectroscopy and photoelectron holography [2]. As shown in Fig. 2, by combining OPAL and the existing hemispherical electron analyzer, a photoelectron spectrometer with high energy resolution can be realized, and a full range (±90°) 1D angular distribution can be measured at once. This upgrade is currently in the commissioning phase.

[1] Hiraya *et al.*, Rev. Sci. Instrum. **63** (1992) 1264.
[2] H. Matsuda and F. Matsui, Jpn. J. Appl. Phys. **59** (2020) 046503.

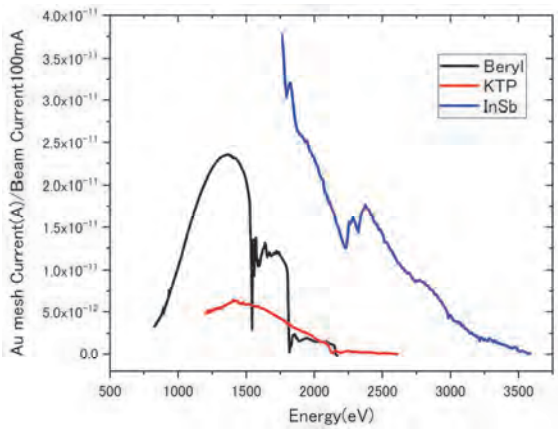


Fig. 1. Throughput spectra of the double-crystal monochromator at BL2A.

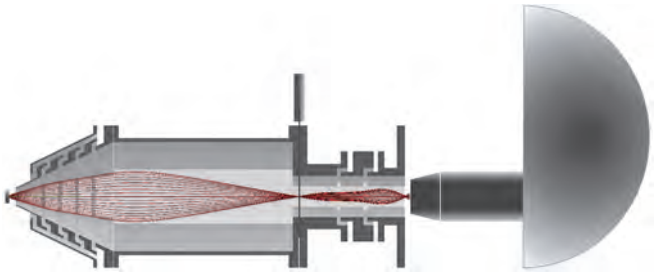


Fig. 2. Schematic diagram of Omnidirectional photoelectron acceptance lens (OPAL) and projection-type analyzer.

▼Technical Data

Monochromator	Double crystal monochromator
Monochromator crystals: (2d value, energy range)	beryl (15.965 Å, 826–2271 eV), KTP (10.95 Å, 1205–3310 eV), InSb (7.481 Å, 1764–4000 eV), Ge (6.532 Å, 2094–4000 eV)
Resolution	E/ΔE = 1500 for beryl and InSb
Experiments	Photoabsorption spectroscopy (total electron yield using EM and partial fluorescence yield using SDD)

BL2B

Photoelectron spectroscopy of molecular solids

▼Description

This beamline previously dedicated for experiments in the field of gas phase photoionization and reaction dynamics. Then, the beamline has been reconstructed for photoelectron spectroscopy of molecular solids with a new end station, and experiments can be performed from May 2014. The monochromator is a spherical grating Dragon type with 18-m focal length. High throughput (1×10^{10} photons s^{-1}) and high resolution ($E/\Delta E$ = 2000 - 8000) are achieved simultaneously under the condition of the ring current of 100 mA [1]. The optical system consists of two pre-focusing mirrors, an entrance slit, three spherical gratings (G1 - G3), two folding mirrors, a movable exit slit, and a refocusing mirror [2]. The monochromator is designed to cover the energy range of 23–205 eV with the three gratings: G1 (2400 lines mm^{-1}, R = 18 m) at 80–205 eV; G2 (1200 lines mm^{-1}, R = 18 m) at 40–100 eV; G3 (2400 lines mm^{-1}, R = 9.25 m) at 23–50 eV. The percentage of the second-order light contamination at $h\nu$ = 45.6 eV is 23% for G2 or 7% for G3.

A UHV chamber is placed downstream of the refocusing mirror chamber and equipped silicon photodiode, sapphire plate Au mesh and filters for absolute photon flux measurement, monitor the photon-beam position, relative photon flux measurements and attenuate higher order light, respectively.

The new end station consists of a main chamber with a hemispherical analyzer (SCIENTA R3000) and a liquid-He-cooled cryostat (temperature range of 15-400 K) with 5-axis stage, a sample preparation chamber with a fast-entry load-lock chamber and a cleaning chamber with LEED, ion gun for sputtering and IR heating unit.

[1] M. Ono, H. Yoshida, H. Hattori and K. Mitsuke, Nucl. Instrum. Meth. Phys. Res. A **467-468** (2001) 577.
[2] H. Yoshida and K. Mitsuke, J. Synchrotron Radiation **5** (1998) 774.

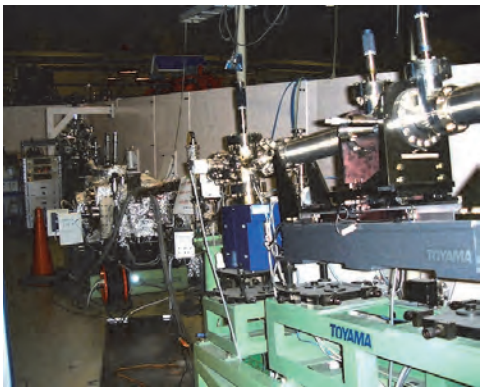


Fig. 1. 18 m spherical grating monochromator at BL2B.

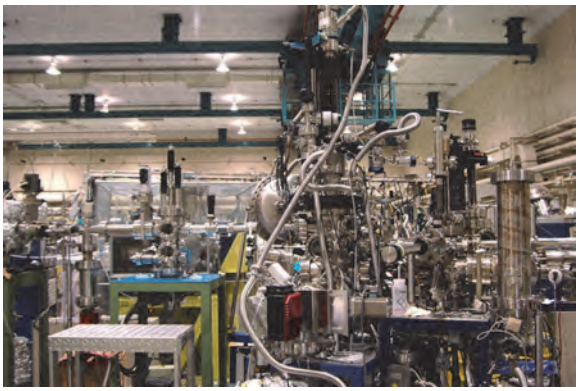


Fig. 2. End station of BL2B for photoelectron spectroscopy of molecular solids.

▼Technical Data

Monochromator	18 m spherical grating Dragon-type
Wavelength Range	23-205 eV
Resolution	2000–8000 depending on the gratings
Experiments	Angle-resolved ultraviolet photoelectron spectroscopy

BL3U

Varied-Line-Spacing Plane Grating Monochromator for Molecular Soft X-Ray Spectroscopy

▼Description

The beamline BL3U is equipped with an in-vacuum undulator composed of 50 periods of 3.8 cm period length. The emitted photons are monochromatized by the varied-line-spacing plane grating monochromator (VLS-PGM) designed for various spectroscopic investigations in the soft X-ray range. Three holographically ruled laminar profile plane gratings are designed to cover the photon energy range from 40 to 800 eV. The beamline has liquid cells for soft X-ray absorption spectroscopy (XAS) in transmission mode as shown in Fig. 1. The liquid cell is in the atmospheric helium condition, which is separated by a 100 nm thick Si_3N_4 membrane with the window size of 0.2×0.2 mm^2 from the beamline in an ultrahigh vacuum condition. The thin liquid layer is assembled by using two 100 nm thick Si_3N_4 membranes. The thickness of the liquid layer is controllable from 20 to 2000 nm by adjusting the helium pressures around the liquid cell in order to transmit soft X-rays. Liquid samples are exchangeable *in situ* by using a tubing pump. The liquid cell has two types of windows: one is the liquid part to obtain the soft X-ray transmission of liquid (I), and the other is the blank part to obtain the transmission without liquid (I_0). We can obtain the reliable XAS spectra based on the Lambert-Beer law $\ln(I_0/I)$. Since the liquid cell is in the atmospheric condition, we can measure XAS of liquid samples in the real environment. *Operando* XAS observation of several chemical reactions such as catalytic, electrochemical reactions are also possible by using our liquid cells developed for these purposes.

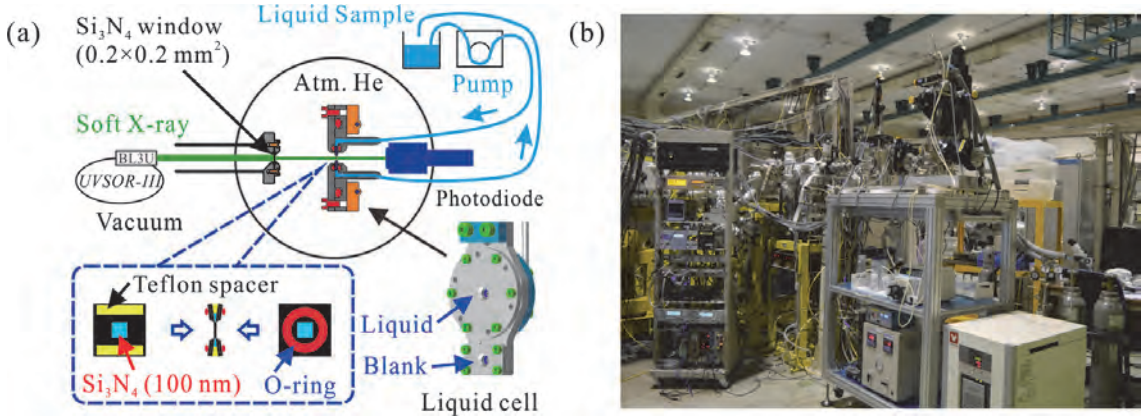


Fig. 1. (a) Schematics of a liquid cell for XAS in transmission mode settled in BL3U. The blowup shows a thin liquid layer assembled by two Si_3N_4 membranes with the thickness of 100 nm. (b) Photograph of a XAS measurement system for liquid samples at the end station of BL3U.

▼Technical Data

Monochromator	Varied-line-spacing plane grating monochromator
Energy Range	40-800 eV
Resolution	$E / \Delta E > 10\,000$
Experiments	Soft X-ray absorption spectroscopy of liquid in transmission mode

BL3B (HOTRLU)

VIS-VUV Photoluminescence and Reflection/Absorption Spectroscopy

▼Description

BL3B has been constructed to study photoluminescence (PL) in the visible (VIS) to vacuum ultraviolet (VUV) region. This beamline consists of a 2.5 m off-plane Eagle type normal-incidence monochromator, which covers the VUV, UV, and VIS regions, i.e., the energy (wavelength) region of 1.7-31 eV (40-730 nm), with three spherical gratings having constant grooving densities of 1200, 600, and 300 l/mm optimized at the photon energies of ~20, ~16, and ~6 eV, respectively. The schematic side view and top view layouts are shown in Figs. 1(a) and 1(b), respectively. The FWHM of the beam spot at the sample position is 0.25 mm (V) × 0.75 mm (H). Low energy pass filters (LiF, quartz, WG32, OG53) can be inserted automatically to maintain the optical purity in the G3 (300 l/mm) grating region (1.7~11.8 eV). Figure 2 shows the throughput spectra (photon numbers at a beam current of 300 mA) for each grating with entrance and exit slit openings of 0.1 mm (resolving power E / ΔE of ~2000 (G3, ~6.8 eV)). Since both slits can be opened up to 0.5 mm, a monochromatized photon flux of 10^{10} photons/s or higher is available for PL measurements in the whole energy region.

The end station is equipped with a liquid-helium-flow type cryostat for sample cooling and two detectors; one of which is a photomultiplier with sodium salicylate and the other a Si photodiode for reflection/absorption measurement. For the PL measurements in the wide energy region from VIS to VUV, two PL monochromators, comprising not only a conventional VIS monochromator but also a VUV monochromator with a CCD detector, are installed at the end station.

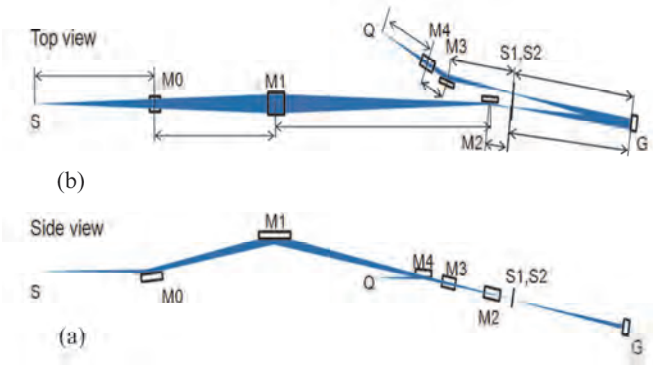


Fig. 1. Schematic layout of the BL3B (a) side view and (b) top view.

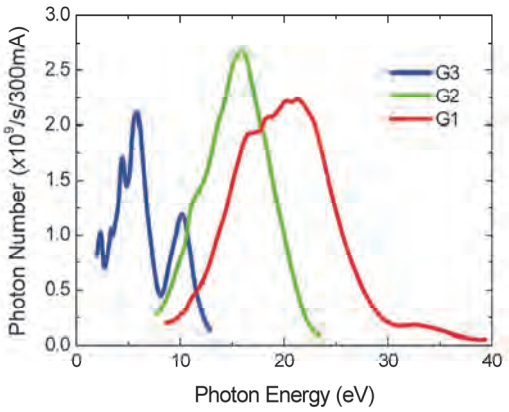


Fig. 2. Throughput spectra for each grating (G1:1200 l/mm, G2:600 l/mm and G3:300 l/mm) with S1 = S2 = 0.1 mm.

▼Technical Data

Monochromator	-2.5 m normal-incidence monochromator
Energy range	1.7-31 eV (40~730 nm)
Resolution (Δhν/ hν)	≥ 12000 (at ~ 6.9 eV, 0.02 mm slits, G1 (1200 l/mm)
Experiments	Photoluminescence, reflection, and absorption spectroscopy, mainly for solids

BL4U

Scanning Transmission X-ray Microscopy in the Soft X-ray Region

▼Description

In the soft x-ray region, there are several absorption edges of light elements and transition metals. The near edge X-ray absorption fine structure (NEXAFS) brings detailed information about the chemical state of target elements. A scanning transmission X-ray microscope (STXM) in the soft X-ray region is a kind of extended technique of the NEXAFS with high spatial resolution. The STXM has a capability of several additional options, for example, in-situ observations, 3-dimensional observation by computed tomography and ptychography, by utilizing the characteristics of the X-rays. The STXM can be applied to several sciences, such as polymer science, material science, cell biology, environmental science, and so on.

This beamline equips an in-vacuum undulator, a varied-line-spacing plane grating monochromator and a fixed exit slit. The soft X-ray energy range from 50 to 770 eV with the resolving power (E/ΔE) of 6,000 is available. The aperture size of the fixed exit slit determines not only the resolving power but also the size of a microprobe. A Fresnel zone plate is used as a focusing optical device through an order select aperture and its focal spot size of ~30 nm is available at minimum. An image is acquired by detecting intensities of the transmitted X-rays by a photomultiplier tube with scintillator with scanning a sample 2-dimensionally. By changing the energy of the incident beam, each 2-dimensional NEXAFS image is stacked. A main chamber of STXM is separated from the beamline optics by a silicon nitride membrane of 50-nm thickness; therefore, sample folders can be handled in vacuum or in helium.

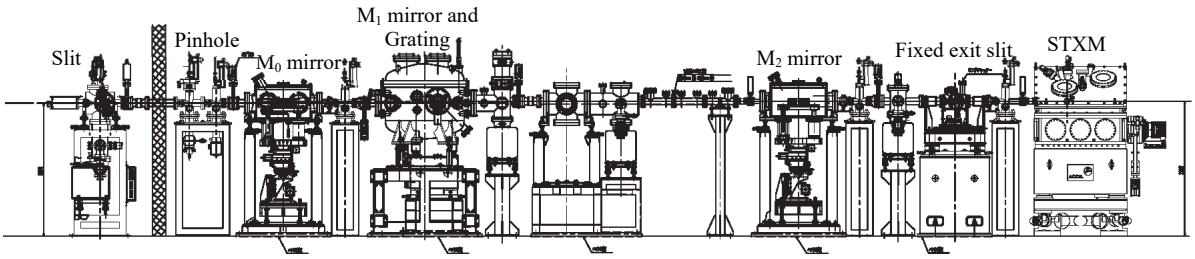


Fig. 1. Schematic image of BL4U

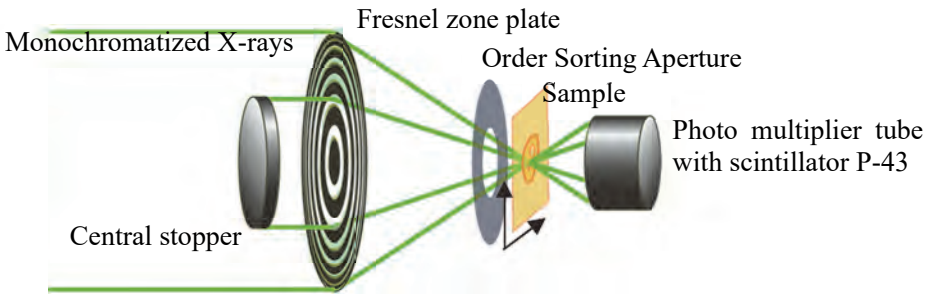


Fig. 2. Schematic image of STXM

▼Technical Data

Energy range (E)	50 -770 eV
Resolving power (E/ΔE)	~6,000
Focusing optical element	Fresnel zone plate
Spatial resolution	~30 nm
Experiments	2-dimensional absorption spectroscopy
Measurement environment	standard sample folder in vacuum or in helium, specially designed sample cell in ambient condition

BL4B

Varied-Line-Spacing Plane Grating Monochromator for Molecular Soft X-Ray Spectroscopy

▼Description

The beamline BL4B equipped with a varied-line-spacing plane grating monochromator (VLS-PGM) was constructed for various spectroscopic investigations in a gas phase and/or on solids in the soft X-ray range. Three holographically ruled laminar profile plane gratings with SiO_2 substrates are designed to cover the photon energy range from 25 to 800 eV. The gratings with groove densities of 100, 267, and 800 l/mm cover the spectral ranges of 25–100, 60–300, and 200-1000 eV, respectively, and are interchangeable without breaking the vacuum. Figure 1 shows the absolute photon flux for each grating measured using a Si photodiode (IRD Inc.), with the entrance- and exit-slit openings set at 50 and 50 μm, respectively. The maximum resolving power ($E/\Delta E$) achieved for each grating exceeds 5000.

There is no fixed endstation on this beamline. A small vacuum chamber equipped with an electron multiplier (EM) detector is available. Soft X-ray absorption spectra of solid samples are usually measured by means of the total electron yield method using EM, and the partial fluorescence yield method using a silicon drift detector (SDD).

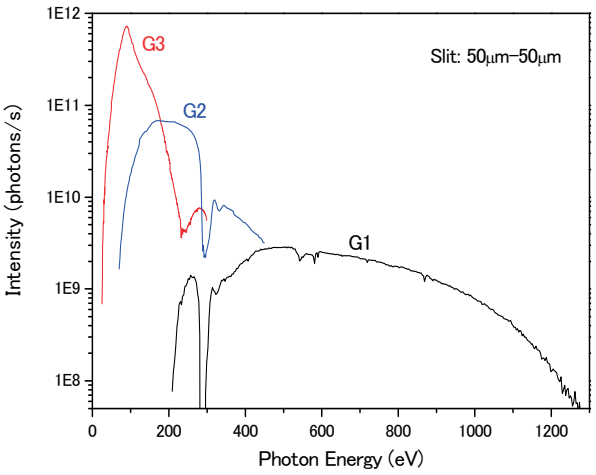


Fig. 1. Throughput from the VLS-PGM monochromator on BL4B.



Fig. 2. Photo of BL4B.

▼Technical Data

Monochromator	Varied-line-spacing Plane Grating Monochromator
Energy range	25-1000 eV
Resolution	$E / \Delta E > 5000$ (at maximum)
Experiments	Soft X-ray spectroscopy (mainly, photoabsorption spectroscopy for solid targets by means of total electron yield method using EM and partial fluorescence yield method using SDD)

BL5U

Photoemission Spectroscopy of Solids and Surfaces

▼Description

Since the monochromator of BL5U was an old-style spherical grating type SGMTRAIN constructed in 1990s and the throughput intensity and energy resolution were poor, the whole beamline has been replaced to state-of-the-art monochromator and end station. The new beamline has been opened to users from FY2016 as high-energy resolution ARPES beamline. Samples can be cooled down to 3.8 K with newly developed 5-axis manipulator to perform high energy resolution measurements. Users can also obtain spatial-dependence of the electronic structure of solids using micro-focused beam (~ 50 μm). The new electron lens system makes it possible to obtain ARPES spectra without moving samples. This beamline will also have new capability to perform high-efficient spin-resolved ARPES in the future.

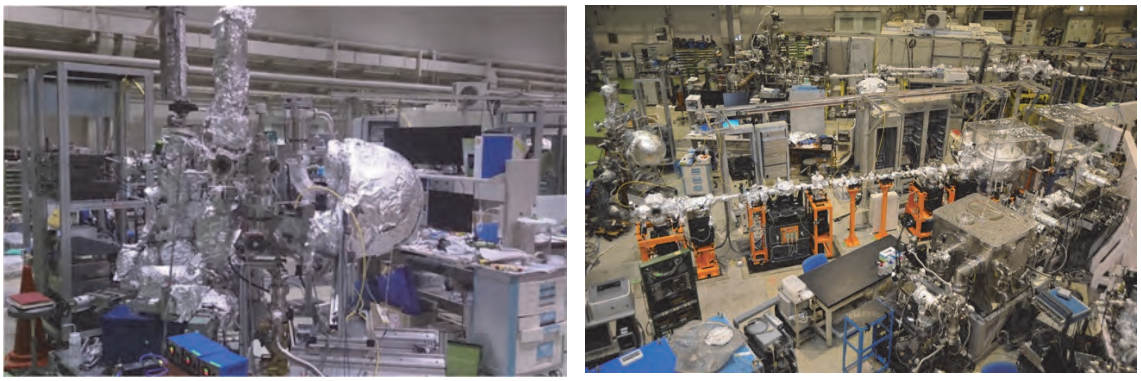


Fig. 1. Pictures of BL5U.

▼Technical Data (Expected Performance)

Light source	APPLE-II type undulator (λ_u = 60 mm, N = 38) vertical/horizontal, right/left circular (depending on *hv*)
Monochromator	Monk-Gillieson VLS-PGM
Energy Range	20-200 eV
Resolution	$h\nu/\Delta E$ > 10,000 for < 10 μm slits
Experiment	ARPES, Space-resolved ARPES, Spin-resolved ARPES
Flux	$<10^{12}$ photons/s for <10 μm slits (at the sample position)
Beam spot size	23 (H) x 40 (V) μm
Main Instruments	Hemispherical photoelectron analyzer with deflector scan (MBS A-1 Lens#4), Liq-He flow cryostat with 5-axis manipulator (3.8 K-350 K)

BL5B

Calibration Apparatus for Optical Elements and Detectors

▼Description

BL5B has been constructed to perform calibration measurements for optical elements and detectors. This beamline is composed of a plane grating monochromator (PGM) and three endstations in tandem. The most upstream station is used for the calibration measurements of optical elements, the middle one for optical measurements for solids, and the last for photo-stimulated desorption experiments. The experimental chamber at the most downstream station is sometimes changed to a chamber for photoemission spectroscopy. The calibration chamber shown in Fig. 2 is equipped with a goniometer for the characterization of optical elements, which has six degrees of freedom, X-Y translation of a sample, and interchanging of samples and filters. These are driven by pulse motors in vacuum. Because the polarization of synchrotron radiation is essential for such measurements, the rotation axis can be made in either the horizontal or vertical direction (s- or p-polarization).

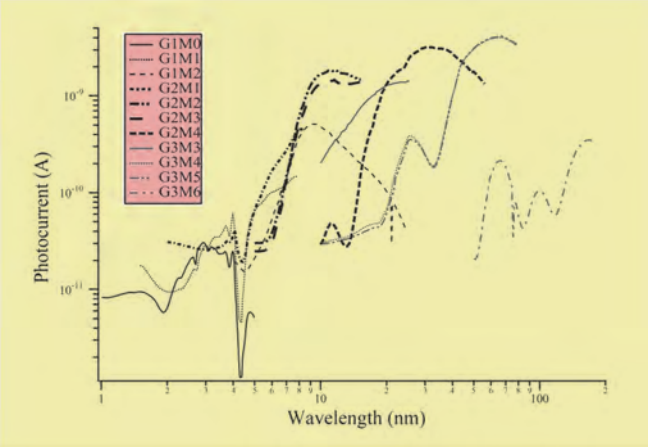


Fig. 1. Throughput spectra for possible combinations of gratings and mirrors at BL5B measured by a gold mesh.

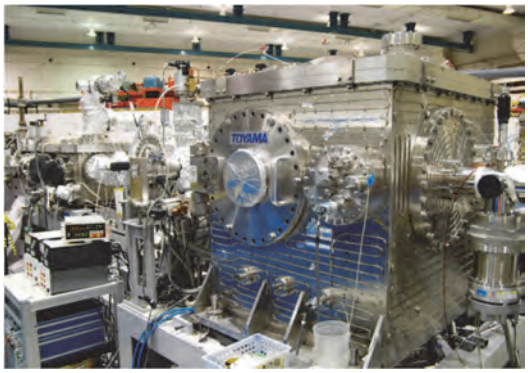


Fig. 2. A side view of the experimental chamber for calibration measurements.

▼Technical Data

Monochromator	Plane Grating Monochromator
Energy range	6-600 eV (2-200 nm)
Resolution	$E / \Delta E$ ~500
Experiments	Calibration of optical elements, reflection and absorption spectroscopy mainly for solids

BL6U

Variable-Included-Angle / Variable-Line-Spacing Plane Grating Monochromator for Soft X-Ray photoelectron Spectroscopy

▼Description

The beamline BL6U equipped with a variable-included-angle Monk-Gillieson mounting monochromator with a varied-line-spacing plane grating was constructed for various spectroscopic investigations requiring high-brilliance soft X-rays on solid surfaces. Through a combination of undulator radiation and sophisticated monochromator design (entrance slit-less configuration and variable-included-angle mechanism), using a single grating, the monochromator can cover the photon energy ranging from 40 to 500 eV, with resolving power of greater than 10000 and photon flux of more than 10^{10} photons/s. Figure 1 shows an example of the monochromator throughput spectra measured using a Si photodiode, with the exit-slit opening set at 30 μm, which corresponds to the theoretical resolving power of 10000 at 80 eV.

A new Momentum Microscope experimental station for photoelectron spectroscopy resolved in 3D momentum space with a microscopic field of view has been built at BL6U (SPECS KREIOS 150 MM). A momentum resolution of 0.01 $Å^{-1}$ in $\boldsymbol{k}_x/\boldsymbol{k}_y$ as well as $\boldsymbol{k}_z$ is achieved. A spatial resolution of 50 nm, an energy resolution of 20 meV at 9 K, and a field of view of 2 μm for ARPES are successfully demonstrated. This experimental station specializes in characterizing the electronic structure of surface atomic sites, thin films, molecular adsorbates, and bulk crystals. This method opens the door to direct observation of the Fermi surface of μm-sized crystals, which was difficult with conventional ARPES-type hemispherical analyzers.

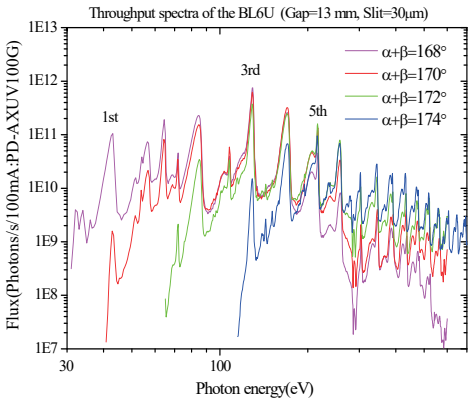


Fig. 1. Throughput spectra of the BL6U monochromator at various included angles.

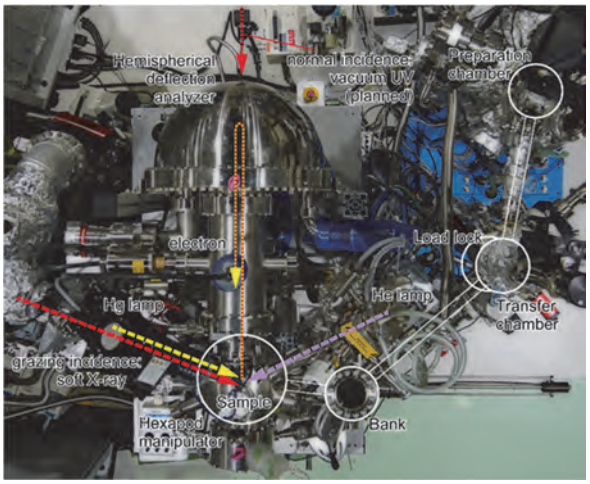


Fig. 2. Photograph of BL6U end station

▼Technical Data

Monochromator	Variable-included-angle Varied-line-spacing Plane Grating Monochromator
Energy range	45-600 eV(practical)
Resolution	E / ΔE > 10000 (at maximum)
Experiments	High-resolution soft X-ray spectroscopy (photoelectron spectroscopy for solid surfaces)

BL6B
Infrared and Terahertz Spectroscopy of Solids

▼Description

Synchrotron radiation (SR) has good performance (high brilliance and high flux) not only in the VUV and soft X-ray (SX) regions but also in the infrared (IR) and THz regions. BL6B covers the IR and THz regions. The previous beamline, BL6A1, which was constructed in 1985, was the pioneer in IRSR research. The beamline was deactivated at the end of FY2003 and a new IR/THz beamline, BL6B (IR), was constructed in FY2004. The front-end part including bending duct #6 was replaced with a new part having a higher acceptance angle (215 (H) × 80 (V) mrad^2) using a magic mirror, as shown in Fig. 1.

There are two Michelson type interferometers in this endstation; with first one (Bruker Vertex70v), which covers a wide spectral region from 30 to 20,000 cm^{-1} ($h\nu$ = 4 meV-2.5 eV), reflection/absorption spectroscopy measurements of large samples (up to several mm) and IR/THz microscopy measurements of tiny samples (up to several tens of μm) can be performed. For reflection/absorption spectroscopy measurements, a liquid-helium- flow type cryostat with a minimum temperature of 4 K is installed. The other interferometer (Jasco FT/IR-6100), which covers 350 to 15,000 cm^{-1} ($h\nu$ = 45 meV-1.8 eV), has been available for IR microscopy imaging measurements from FY2014. One can also perform ATR measurements using diamond ATR prism.

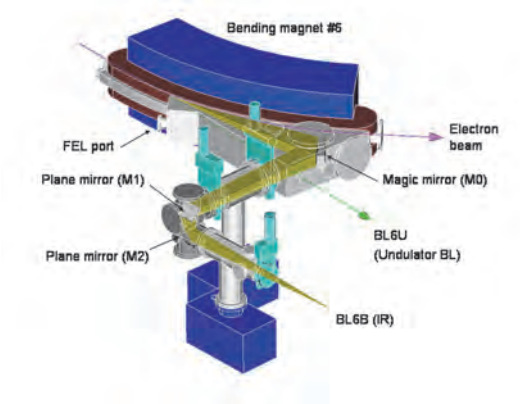


Fig. 1. Design of the optics and front end of BL6B.

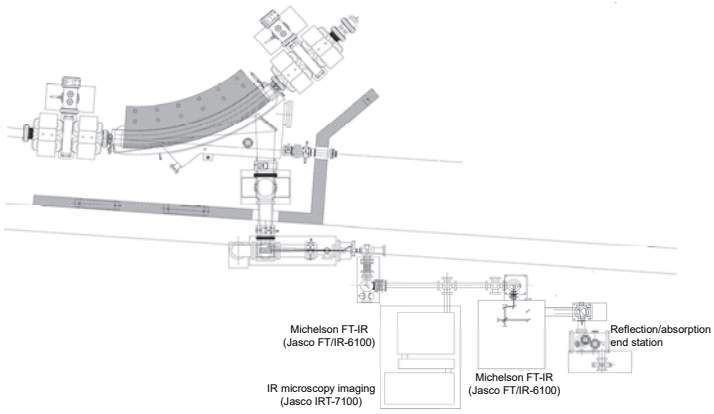


Fig. 2. Schematic top view of BL6B.

▼Technical Data

Interferometer	Michelson (Bruker Vertex70v)	Michelson (Jasco FT/IR-6100)
Wavenumber Range (Energy range)	30-20,000 cm^{-1} (4 meV-2.5 eV)	350-15,000 cm^{-1} (45 meV-1.8 eV)
Resolution in cm^{-1}	0.1 cm^{-1}	0.5 cm^{-1}
Experiments	Reflectivity and transmission spectroscopy THz Microspectroscopy	IR microscopy imaging (JASCO IRT-7000) ATR spectroscopy

BL7U (SAMRAI)

Angle-Resolved Photoemission of Solids in the VUV Region

▼Description

Beamline 7U, named the Symmetry- And Momentum-Resolved electronic structure Analysis Instrument (SAMRAI) for functional materials, was constructed to provide a photon flux with high energy resolution and high flux mainly for high-resolution angle-resolved photoemission spectroscopy, so-called "ARPES", of solids [1]. An APPLE-II-type variable-polarization undulator is installed as the light source. The undulator can produce intense VUV light with horizontal/vertical linear and right/left circular polarization. The undulator light is monochromatized by a modified Wadsworth type monochromator with three gratings (10 m radius; 1200, 2400, and 3600 lines/mm optimized at $h\nu$ = 10, 20, and 33 eV). The energy resolution of the light ($h\nu/\Delta h\nu$) is more than 10^4 with a photon flux of 10^{11}-10^{12} ph/s or higher on samples in the entire energy region. The beamline has a photoemission end-station equipped with a 200 mm-radius hemispherical photoelectron analyzer (MB Scientific AB, A-l analyzer) with a wide-angle electron lens and a liquid-helium-cooled cryostat with 6-axis pulse motor control. The main function of the beamline is to determine the electronic structure of solids and its temperature dependence in order to reveal the origin of their physical properties.

[1] S. Kimura, T. Ito, M. Sakai, E. Nakamura, N. Kondo, K. Hayashi, T. Horigome, M. Hosaka, M. Katoh, T. Goto, T. Ejima and K. Soda, Rev. Sci. Instrum. **81** (2010) 053104.

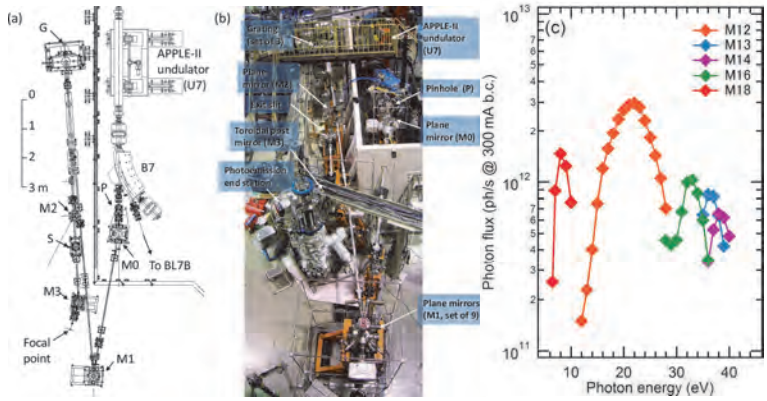


Fig. 1. SAMRAI beamline [(a), (b)] consisting of an APPLE-II type undulator (U7), a modified Wadsworth type monochromator (M0-S), and a high-resolution photoemission analyzer at the focal point. The monochromator has five major optical components: two plane mirrors (M0 and M1) with water cooling, one set of three spherical gratings (G), an exit slit (S), and one toroidal refocusing mirror (M3). (c) Example of flux intensity *versus* photon energy [1]

▼Technical Data

Light source	APPLE-II type undulator (λ_u = 76 mm, N = 36) vertical/horizontal, right/left circular (depending on $h\nu$)
Monochromator	10 m normal-incidence monochromator (modified Wadsworth type)
Photon energy range	6 – 40 eV (λ = 30 – 200 nm)
Resolution ($h\nu/\Delta h\nu$)	E / ΔE > 10000-50000
Photon flux on sample	≥ 10^{11}-10^{12} ph/s (depending on $h\nu$)
Beam size on sample	200 (H) × 50 (V) μm^2
Experiments	Angle-resolved photoemission of solids (MV Scientific A-1 analyzer, acceptance angle: ± 18 deg)

BL7B

3 m Normal-Incidence Monochromator for Solid-State Spectroscopy

▼Description

BL7B has been constructed to provide sufficiently high resolution for conventional solid-state spectroscopy, sufficient intensity for luminescence measurements, wide wavelength coverage for Kramers–Kronig analyses, and minimum deformation to the polarization characteristic of incident synchrotron radiation. This beamline consists of a 3-m normal incidence monochromator, which covers the vacuum ultraviolet, ultraviolet, visible, and infrared, i.e., the wavelength region of 50–1000 nm, with three gratings (1200, 600, and 300 l/mm). Two interchangeable refocusing mirrors provide two different focusing positions. For the mirror with the longer focal length, an LiF or a MgF_2 window valve can be installed between the end valve of the beamline and the focusing position. Figure 1 shows the absolute photon intensity for each grating with the entrance and exit slit openings of 0.5 mm. A silicon photodiode (AXUV-100, IRD Inc.) was utilized to measure the photon intensity and the absolute photon flux was estimated, taking the quantum efficiency of the photodiode into account.

The cooling system for the pre-focusing mirror has been removed, resulting in longer beam settling times. Currently, BL7B is opened during single bunch mode, but limited use is possible during multi bunch mode.

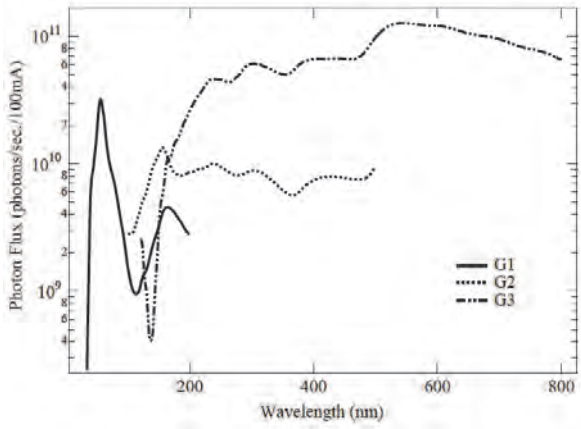


Fig. 1. Throughput spectra of BL7B measured using a silicon photodiode.

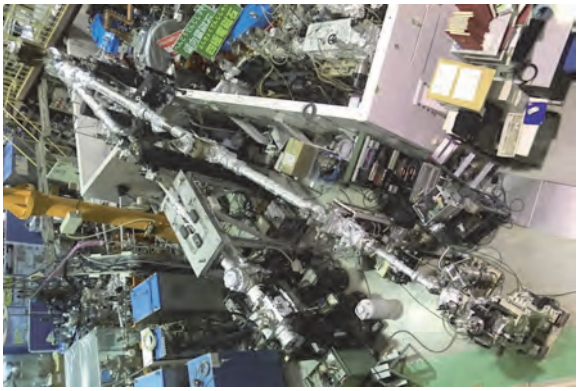


Fig. 2. Photo of BL7B.

▼Technical Data

Monochromator	3 m Normal-Incidence Monochromator
Wavelength Range	50-1000 nm (1.2-25 eV)
Resolution	$E / \Delta E$ = 4000-8000 for 0.01 mm slits
Experiments	Absorption, reflection, and fluorescence spectroscopy, mainly for solids

III-1

Accelerators and Instruments

Highlight

BL3U

Soft X-ray Absorption Spectroscopy in the Low Energy Region Explored by the Argon Gas Window

M. Nagasaka[1,2]

[1]*Institute for Molecular Science, Okazaki 444-8585, Japan*

[2]*The Graduate University for Advanced Studies, SOKENDAI, Okazaki 444-8585, Japan*

Soft X-ray absorption spectroscopy (XAS) is an element specific method to investigate local electronic structures of materials. Since soft X-rays are strongly absorbed by air and liquids [1], XAS spectra of gas and solid samples under an ultrahigh vacuum condition have been extensively studied. Recently, several groups measured XAS spectra in an atmospheric condition by using the high soft X-ray transmission of helium gas. A differential pumping system is used between a soft X-ray beamline under an ultrahigh vacuum condition and a measurement chamber in an atmospheric helium condition [2]. However, the helium gas window is not able to apply XAS in the low energy region below 200 eV since transmitted soft X-rays mostly consist of high order X-rays due to the low transmission of first order X-rays. In this study, we propose the argon gas window for the newly soft X-ray transmission window in the low energy region covering K-edges of Li and B and L-edges of Si, P, S, and Cl [3].

The experiments were performed at soft X-ray beamline BL3U. The measurement chamber in the atmospheric helium or argon condition is separated by a Si_3N_4 membrane with the thickness of 100 nm from the soft X-ray beamline under an ultrahigh vacuum condition. Soft X-rays under vacuum pass through the Si_3N_4 membrane window, the atmospheric helium or argon environment, and finally reach a photodiode detector. The distance between the Si_3N_4 membrane and the photodiode detector is estimated to be 41 mm.

Figure 1 shows the soft X-ray transmission spectra of argon gas in the low energy region. Argon gas has a role to remove high order X-rays above 240 eV due to the absorption of the Ar L-edge. The absorption peak of the Si_3N_4 membrane around 104 eV is observed in the Si L-edge. When the small amount of dimethyl sulfoxide (DMSO) gas is mixed with the argon gas, we have successfully observed the absorption peaks of DMSO gas at the S L-edge (170 eV), which clearly observes the spectral difference between DMSO/Ar mixed gas and argon gas. These peaks are not able to be observed in the atmospheric helium condition since the ratio of the high order X-rays is extremely high in the helium environment.

Figure 2 shows the XAS spectrum of helium gas, where the small amount of helium gas is mixed in the atmospheric argon condition. The XAS spectrum is derived using the Lambert-Beer law, $\ln(I_0/I)$, where I_0 and I are the transmission signals of argon gas and Ar/He mixed gas, respectively. The spectrum shows the helium resonance energy E_2 of the n = 2 double excitation Rydberg series at 60.147 eV [4]. It means that soft X-rays at the Li K-edge (60 eV) are transmittable in the atmospheric argon condition. As a result, the argon gas window enables us to measure XAS in the atmospheric condition in the low energy region from 60 to 240 eV.

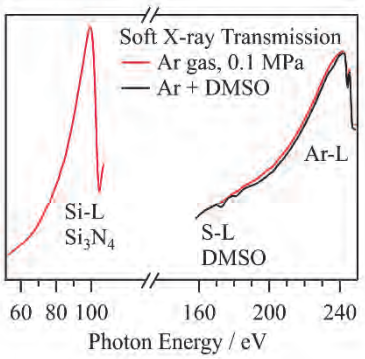


Fig. 1. The soft X-ray transmission spectra of argon gas in the atmospheric condition in the low energy region. The transmission spectrum of argon gas mixed with DMSO gas is also shown.

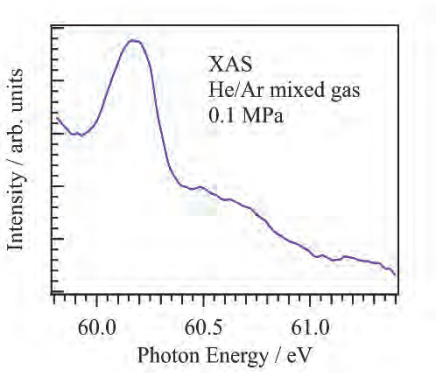


Fig. 2. The XAS spectrum of helium gas mixed with argon gas in the atmospheric condition.

[1] C. T. Chantler, J. Phys. Chem. Ref. Data **29** (2000) 597.
[2] Y. Tamenori, J. Synchrotron Rad. **17** (2010) 243.
[3] M. Nagasaka, submitted.
[4] M. Domke *et al*., Phys. Rev. A **53** (1996) 1424.

Highlight

BL4U

Microscopic Study of Li K-edge

T. Ohigashi[1,2] and H. Yuzawa[1]

[1]*UVSOR Synchrotron Facility, Institute for Molecular Science, Okazaki 444-8585, Japan*

[2]*School of Physical Sciences, The Graduate University for Advanced Studies, SOKENDAI, Okazaki 444-8585, Japan*

Lithium is the lightest solid element and is a main element for a lithium ion battery (LIB). Currently, the LIBs are widely used and are essentials in our lives as energy storage devices. Demand of the LIBs is still increasing and higher performance is expected. However, behavior of lithium in the LIB, such as distribution and chemical state during charge/discharge process, is still unclear. To elucidate this process, it is necessary to develop an analytical tool which can analyze lithium with high spatial resolution. So far, analyses of lithium by using an Auger electron microscope [1], a transmission electron microscope with electron energy loss spectroscopy [2] and a secondary ion mass spectroscopy were reported [3]. In addition to these instruments, a scanning transmission X-ray microscope (STXM) also can be a powerful technique. STXM performs X-ray absorption spectroscopy with high spatial resolution in transmission mode. This technique is bulk sensitive and lower damage to a sample [4]. To analyze lithium by STXM, it is necessary to have an access around 55 eV, Li K-edge. This low energy region makes the Li K-edge analyses difficult because tremendous higher order harmonics from a monochromator should be suppressed to obtain X-ray absorption spectra of high quality. Furthermore, focal length of a Fresnel zone plate (FZP) depends on energy of an incoming X-ray so that focal length of the FZP around Li K-edge is typically too short (e.g. 266 μm by the FZP with 25 nm outermost zone width) to construct microbeam optics. Additionally, efficiency of the FZP is low. In this study, we overcame these issues by designing a FZP with a new concept [5].

The optics of STXM at BL4U, a combination of the FZP with chromatic aberration and a pinhole (OSA, order select aperture) is not only to produce a microbeam but also to work as a linear monochromator. This optics theoretically suppresses the higher order harmonics at odd diffractive orders larger than 3rd and cut off even diffractive orders. We designed the new FZP for analysis below 100 eV. The concept of the new FZP is a combination of a phase FZP and a substrate as a low pass filter. Then, the silicon substrate was chosen because of high transmittance of main harmonics, from 50 to 100 eV, and cut-off by Si L_2 and L_3 edge above 100 eV. The parameters of the new FZP are as follows; diameter of 240 μm, outermost zone width of 60 nm, 1,000 zones and gold pattern on silicon substrate of thickness of 200 nm. The focal length of the new FZP is 639 μm at 55 eV. Intensities of the higher order harmonics was evaluated by changing the focal position of the FZP, *f*, along an optical axis, such as 2*f*, 3*f*, 4*f*, and 5*f* which are corresponded with focal length of +1st diffractions of 2nd, 3rd, 4th and 5th higher harmonics respectively. Then intensity of the 3rd order harmonics, which is the strongest diffractive order, was suppressed less than 0.1 %.

As a test measurement, Li K-edge of a droplet of LiCl solution on a TEM grid was measured by using a conventional FZP and the new one. Figure 1 (a) show an STXM image of the droplet at 60 eV. In Fig. 1 (b), the spectrum analyzed by the new FZP obviously shows some peaks compared to the conventional one. From comparison with Fig. 1 (b) and spectra in reference [6], the droplet of LiCl reacted with CO_2 in the air and became mixture of LiCl and Li_2CO_3. As an evaluation of spatial resolution, another FZP with the outermost zone width of 36 nm was measured and line and its space pattern of 72 nm pitch was resolved. This resolution implies diffraction limit of the STXM optics with the new FZP.

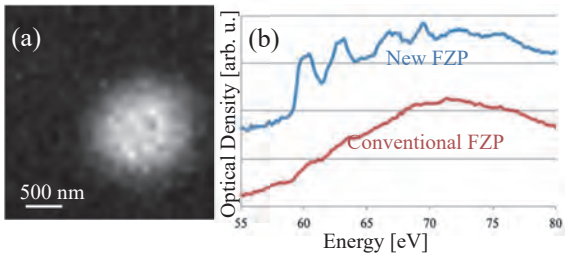


Fig. 1. STXM measurement at Li K-edge of a droplet of LiCl solution, (a) an STXM image at 60 eV and (b) its spectra by using the new and the conventional FZPs.

[1] N. Ishida, H. Fukumitsu, H. Kimura and D. Fujita, J. Power Sources **248** (2014) 1118.
[2] J. Kikkawa, T. Akita, M. Tabuchi, M. Shikano, K. Tatsumi and M. Kohyama, Electrochem. Solid-State Lett. **11** (2008) 399.
[3] H. Masuda, N. Ishida, Y. Ogata, D. Ito and D. Fujita, J. Power Sources **400** (2018) 527.
[4] R. Qiao, Y-D. Chuang, S. Yan and W. Yang, PLOS ONE **7** (2012) e49182.
[5] T. Ohigashi, in preparation
[6] J. Tsuji, H. Nakamatsu, T. Mukoyama, K. Kojima, S. Ikeda and K. Taniguchi, X-Ray Spectrom. **31** (2002) 319.

Accelerators

Development of Long-term Stable Nuclear Emulsion for Cosmic-ray Imaging

A. Nishio, K. Morishima, K. Kuwabara, T. Yoshida and M. Nakamura
Graduate School of Science, Nagoya University, Nagoya 464-8602, Japan

Cosmic ray imaging is the a new non-destructive inspection technique of large-scale constructions with cosmic ray muon. Cosmic ray muon has high penetrating power and it always comes from the whole sky. In the same way of taking a X-ray photograph, we can obtain integrated density of constructions which thickness are several tens cm to several km. We had ever applied this technique to the pyramid of khufu at Egypt, and discovered a large void [1].

In cosmic-ray imaging observations, we used nuclear emulsion as a detector. Nuclear emulsion is a kind of photographic film and has sensitivity for ionizing radiation. The film record tracks of charged particle with angular accuracy under several mrad. In Nagoya University, started a emulsion gel production machine in 2010. It was enable us to develop new-type emulsion gel by ourselves.

We have succeeded to develop the Long-term Stable Nuclear Emulsion for the purpose of long-term observation of cosmic ray imaging. The problem was Latent image fading which is phenomenon decreasing Grain density (GD, indicator of sensitivity) with time. To enable long-term observation and outdoor use throughout the year, we investigated factors that affect the latent image fading of nuclear emulsion. We found that gelatin, additive chemicals, and packing material affected. The developmental version of newly nuclear emulsion are shown in Table 1.

The latent image fading characteristics of Versions 1 to 5 were investigated. The test was conducted at a temperature of 30 °C and a humidity of 40 % RH. Version 5 was also tested at a humidity of 20 % RH. The results are shown in Fig. 1. Figure 2 shows optical micrographs of tracks on days 0, 30, and 180.

The new stable nuclear emulsion achieved its goal of a GD that remained at 25 or more for half a year at 30 °C. The developed stable nuclear emulsion is being used for cosmic-ray imaging observations in the pyramid of Khufu and is expected to be used for future cosmic-ray imaging observations and other elementary particle research.

Table 1. Developmental version history and the components of each version of the nuclear emulsion. Version 1 is a conventional nuclear emulsion. Versions 2 to 4 are the stages of development, and Version 5 is the stable nuclear emulsion developed.

Version	Gelatin (Volume occupancy of crystals)	Additive chemicals (mol/molAg) BTS	Chemical A	Chemical B	Chemical E	Packing material
1	55 %	1.0×10^{-4}	-	-	-	Meiwa C
2	35 %	1.0×10^{-4}	-	-	-	Meiwa C
3	35 %	-	-	-	-	Meiwa C
4	35 %	-	1.2×10^{-4}	1.2×10^{-4}	1.7×10^{-3}	Meiwa C
5	35 %	-	1.2×10^{-4}	1.2×10^{-4}	1.7×10^{-3}	ASO

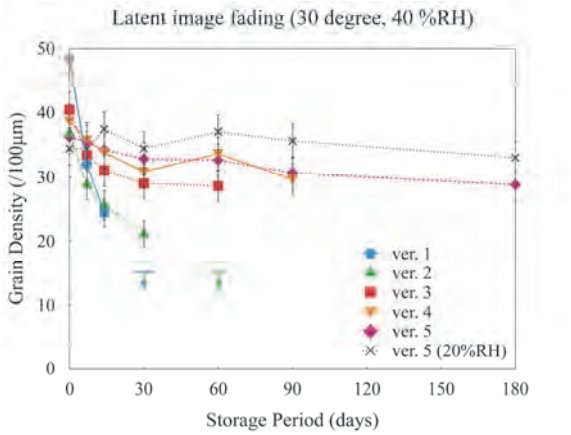


Fig. 1. Latent image fading of Versions 1 to 5 at 30 °C, 40 % RH. The Version 3 samples after day 90 and Version 4 samples on day 180 were impossible to evaluate for the GD due to the large amount of noise.

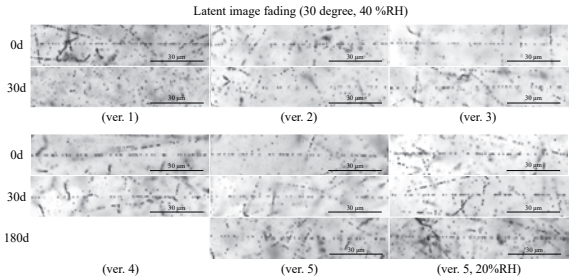


Fig. 2. Optical micrographs of electron beam (several tens of MeV) tracks exposed to Versions 1 to 5 nuclear emulsion on days 0, 30, and 180. Latent image fading at 30 °C, 40 % RH. The length of the black bar is 30 μm. The electron beam was exposed at UVSOR. In the Versions 1, 2, 3, and 4 samples on day 180, there was no track that could be recognized due to the low GD or large amount of noise.

[1] K. Morishima *et al*., Nature **552** (2017) 386.

BL1U

Construction of Laser Transport System for CHG Experiment at BL1U

M. Hosaka[1], Y. Matsunaga[1], A. Mano[1], Y. Takashima[1], M. Fujimoto[2] and M. Katoh[2,3]
[1]*Nagoya University, Nagoya 464-8603, Japan*
[2]*UVSOR Synchrotron Facility, Institute for Molecular Science, Okazaki 444-8585, Japan*
[3]*Hiroshima University, Higashi-hiroshima 739-0046, Japan*

Coherent harmonic generation (CHG) is a method to imprint external laser information to an electron beam and produce coherent radiation from it with various properties such as polarization [1], temporal and spectral structures [2]. We are planning to conduct the CHG study using an optical klystron and a short pulse Ti:Sa mode lock laser at BL1U. The optical klystron consists of two Apple-II variable polarization undulators and a buncher inserted between them [3]. The laser is injected into the first part of the undulators and energy exchange between it and an electron beam circulating in the storage ring occurs. This leads energy modulation inside the electron beam, that is further converted to density modulation with laser wavelength (micro-bunch) in the buncher section. Coherent radiation is emitted from the micro-bunched beam in the second part of the undulators. Polarization of the emitted radiation can be controlled by tuning the undulator.

In order to perform the CHG experiment, we constructed a laser transport system from the laser room to a laser injection window, whose path length is about 10 m. For simplification, vacuum chamber of the optical klystron is used for laser transportation as seen in Fig.1. The laser is returned to the injection window using a waveplate and a polarization beam splitter. The coherent radiation and the returned laser after the interaction with the electron beam separated using a dichroic mirror. We also prepared a monitoring system to make precise alignment between the laser beam and the electron beam, temporally and spatially.

The CHG experiment was made with an electron energy of 600 MeV. Radiation wavelength of Apple-II undulators was adjusted by changing a magnetic gap length. Fundamental radiation of the first undulator tuned to the wavelength of Ti:Sa laser (800 nm) for the resonant interaction and that of the second undulator is tuned to a wavelength of 267 nm, which corresponds to the 3rd harmonics of the micro-bunching. Spatial alignment between the electron beam and the laser was made looking at radiation from the first undulator. Observed image at the position using a CMOS camera coupled with a telescope is shown in Fig. 2. Laser position in the figure was shifted on purpose and the power was kept low (~10 μW). The laser beam could be well focused on the electron beam using the monitoring system. We also carried out temporal alignment using a streak camera. Figure 3 shows the measured streak camera images. The laser pulse of 1psec could be well overlapped on the synchrotron radiation (the electron beam) of 100 psec. After the alignment, we increased the laser power to 1W (1 mJ per pulse) to generate the CHG. We used the streak camera and a narrow band pass filter (2 nm-FWHM) for the observation but no signal arising from the CHG could be seen. We noticed that focusing position of the laser moved considerably with increased laser power. This weaken the laser electric field at the interaction point and suppressed the CHG. We think that the degradation of focusing comes from non-linear effects in transmission type optical elements such as polarization beam splitters. We are planning to remodel the laser transport system for the experiment.

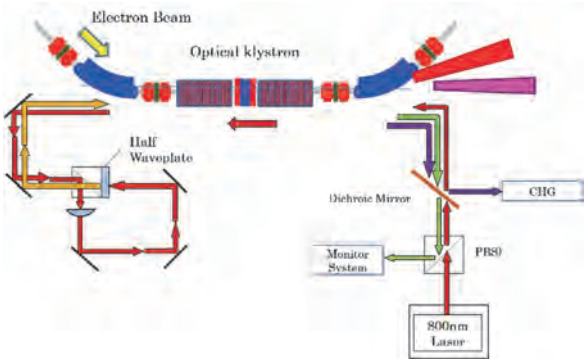


Fig. 1. Schematic of the laser transport system.

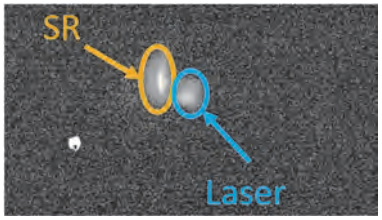


Fig. 2. SR and laser image at interaction point. Electron beam size is around 0.5 mm.

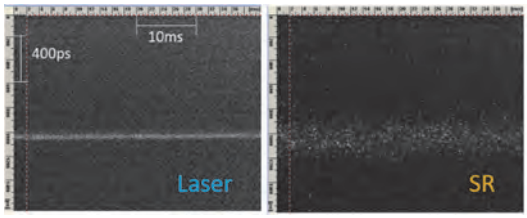


Fig. 3. Streak camera images of SR and laser. The vertical axis is synchronized with accelerator RF signal.

[1] M. Labat *et al.*, Phys. Rev. Lett. **102** (2009) 014801.
[2] S. Bielawski *et al.*, Nat. Phys. **4** (2008) 390.
[3] M. Adachi *et al.*, Proc. IPAC' **10** (2010) 2573.

BL1U

Feasibility Study of Measurement of Polarized Pulsed Gamma-ray by Laser Compton Scattering at 90°

Y. Takashima[1], M. Hosaka[1], U. Shikano[1], A. Mano[1], M. Fujimoto[2] and M. Katoh[2,3]
[1]*Synchrotron Radiation Research Center, Nagoya University, Nagoya 464-8603, Japan*
[2]*UVSOR Synchrotron Facility, Institute for Molecular Science, Okazaki 444-8585, Japan*
[3]*HiSOR, Hiroshima University, Higashi-hiroshima, 739-0046, Japan*

Ultra-short pulse gamma-rays of the pulse width of several picoseconds are generated in UVSOR by 90° scattering of short pulse laser with the electron beam circulating in the storage ring [1]. When the laser is circularly polarized, it is expected that gamma rays generated by Compton scattering are also circularly polarized. There have been some experiments conducted to confirm the polarization of gamma rays generated by the head-on collision of the electron beam and the laser [2]. However, there are no experiments performed to measure the polarization of gamma rays generated in the condition of which the laser and the electron beam collided at a 90° in a laboratory system.

We performed measurements of the spatial distribution of gamma-rays by laser Compton scattering at 90° as a feasibility study to measure the polarization of gamma-rays. In the experiment, we stored 750 MeV electron beam of 30 mA as a single bunch. We used a mode-locked Ti:Sa laser synchronized to the RF frequency of the storage ring. The wavelength and the pulse power of the laser were 800 nm and 1.5 mJ/pulse, respectively. In order to change the direction of the polarization of the laser, we installed a λ/2 waveplate in front of the injection window on the beam duct of the storage ring. The maximum energy of the gamma-ray is about 6.6 MeV. Figure 1 shows the spectrum of the scattered gamma-rays detected by a NaI scintillator.

We installed photostimulable phosphor plates after the extraction window of BL1U in order to measure the spatial distribution of the gamma-rays. The size of the plate was 11.5 cm x 11.5 cm, and the resolution is 100 μm. Figure 2 show the images of spatial distributions of the gamma-rays generated by 90° scattering of the laser and the electron beam. Fig. 2(a) is the image obtained by the Compton scattering of the laser with linear polarization perpendicular to the direction of the electron beam in the horizontal plane. Fig. 2(b) shows the image by using the laser with linear polarization parallel to the direction of the electron beam. There are some differences in those spatial distributions. The figures indicate that the spatial distribution varies according to the polarization of the incident laser, as suggested by theoretical consideration.

In farther studies, we plan to measure the polarization of the scattered gamma-rays quantitatively by the method of magnetic Compton scattering [2].

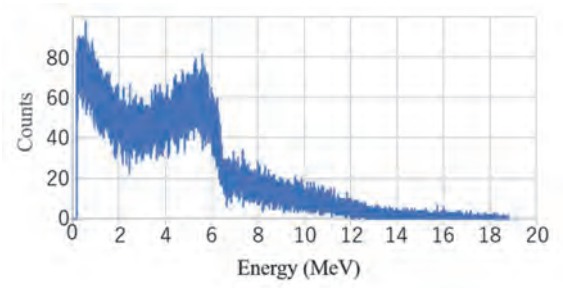


Fig. 1. Energy spectrum of gamma-ray detected by NaI scintillator.

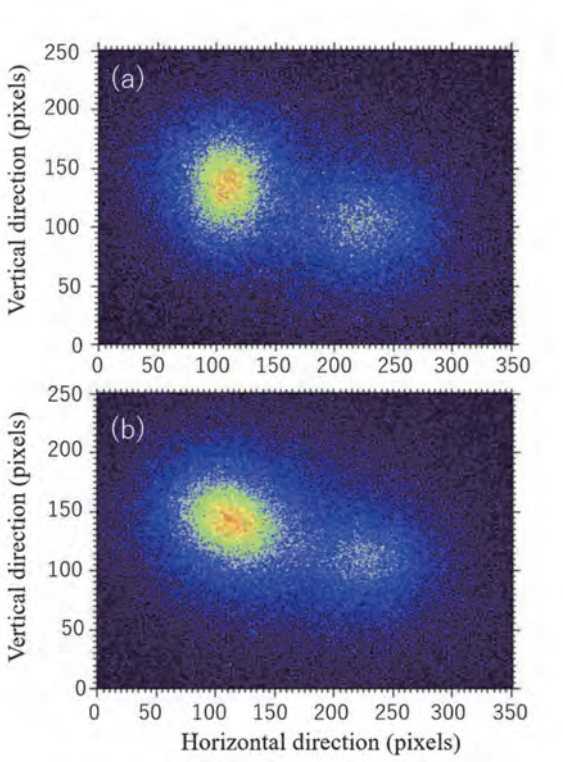


Fig. 2. Spatial distribution of gamma-rays detected by photostimulable phosphor plates. (a) is the image using the horizontally linear polarized laser, and (b) is the image using the laser with linear polarization parallel to the direction of the electron beam.

[1] Y. Taira *et al*., Nucl. Instrum. and Meth. A **637** (2011) S116.
[2] M. Fukuda *et al*., Phys. Rev. Lett. **91** (2003) 164801.

BL1U

Study on Isotope 3D Imaging Using NRF Absorption Method in UVSOR-BL1U

H. Ohgaki[1], H. Zen[1], T. Kii[1], K. Ali[1], T. Hayakawa[2], T. Shizuma[2], H. Toyokawa[3], Y. Taira[3], V. Iancu[4], V. G. Turturica[4], M. Fujimoto[5] and M. Katoh[5]

[1]*Institute of Advanced Energy, Kyoto University, Kyoto 611-0011, Japan*
[2]*Tokai Quantum Beam Science Center, National Institutes for Quantum and Radiologicl Science and Techonology, Tokai 319-1106, Japan*
[3]*National Institute of Advanced Industrial Science and Technology (AIST) Tsukuba Central 2-4, Tsukuba 305-8568, Japan*
[4]*Extreme Light Infrastructure - Nuclear Physics, s/ Horia Hulubei National Institute for R&D in Physics and Nuclear Engineering, Bucharest-Magurele, Judet Ilfov, RO-077125, Romania*
[5]*UVSOR Synchrotron Facility, Institute for Molecular Science, Okazaki 444-8585, Japan*

A Nuclear Resonance Fluorescence (NRF) method is a powerful tool for investigation not only of the nuclear physics but also of isotope imaging inside the spent nuclear fuel canisters and nuclear wastes. We have been developing an isotope imaging technique by using NRF [1] as well as by Nuclear Resonance Absorption (NRA) [2].

A demonstration experiment of the NRF-CT imaging by using a LCS gamma-ray beam with a natural lead target has been carried out at the LCS gamma-ray beamline BL1U at UVSOR-III [3]. In 2019, two enriched isotope targets ^{206}Pb (>93.3 %) and ^{208}Pb (>97.8 %) were prepared as the CT target which is made of an aluminum holder as shown in Fig.1.

The LCS gamma-ray beam with a maximum energy of 5.528 MeV was generated by using a fiber laser (wavelength of 1,896 nm, 50 W). The gamma-ray beam with a flux of approximately 1×10^8 photons/s was used for the experiment with a 1-mm lead collimator and the excited $J^\pi = 1^-$ state at 5.512 MeV of ^{208}Pb was populated through NRA. By using the NRF absorption method a NRF-CT image has been taken by 2-mm step in the horizontal direction (x=-14 to 14 mm) and 30-deg. step in the rotation angle (θ=0 to 150°). The NRF signals from the witness target (^{208}Pb enriched) were measured by two Ge detectors with 120 % and 130 % relative efficiencies. At the same time, the transmission gamma-rays have been measured by a 3.5" × 4" $LaBr_3$(Ce) detector, which gives a density distribution of the sample target. We have developed the segmented CT reconstruction method [3] and we obtained clear a ^{208}Pb distribution as shown in Fig. 2. On the other hand, by using the γ-ray transmission CT, we cannot distinguish between ^{206}Pb and ^{208}Pb as shown in Fig. 3. We demonstrated the isotope selectivity of the NRF-CT technique at the UVSOR-BL1U beamline.

[1] N. Kikuzawa *et al.*, Appl. Phys. Express **2** (2009) 036502.
[2] H. Zen *et al.*, Energy Procedia **89** (2016) 335.
[3] H. Zen *et al.*, AIP Advanced **9** (2019) 35101.

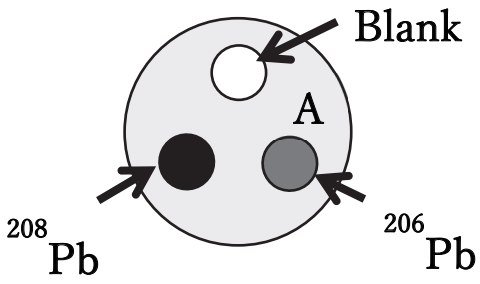


Fig. 1. NRF-CT target.

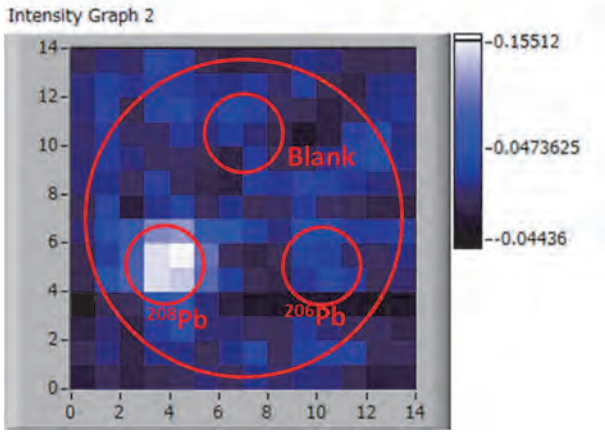


Fig. 2. NRF-CT image.

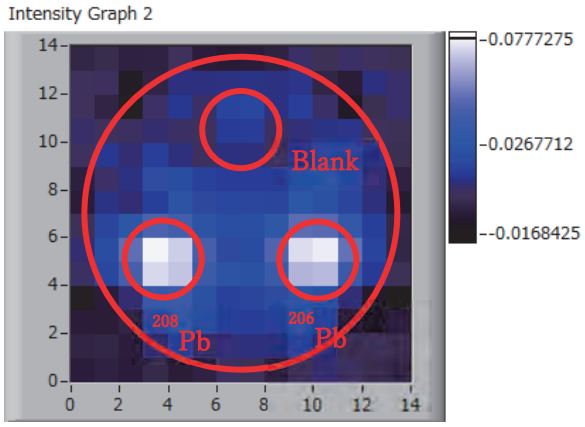


Fig. 3. γ-ray transmission CT image.

BL1U

Study on Temporal Structure of Synchrotron Radiation by Using Interferometer

S. Notsu[1], S. Matsuba[2], K. Kawase[3] and M. Katoh[1,4]
[1]*Hiroshima University, Higashi-Hiroshima, 739-0046, Japan*
[2]*JASRI, Sayo-cho 679-5198 Japan*
[3]*QST, Tokai-mura 319-1106, Japan*
[4]*UVSOR Synchrotron Facility, Institute for Molecular Science, Okazaki 444-8585, Japan*

Temporal structure of synchrotron radiation may be separated into two categories. The first one is the that of a photon wave packet emitted from a single electron. Another temporal structure is the width of the light pulse emitted from a bunch of electrons, which comprises of many wave packets randomly distributing over the length of the electron bunch.

Usually the pulse length of synchrotron radiation, which is typically 10 to 100 psec, is measured with a streak camera. However, there is no report on the direct measurement of the wave packet length. In the laser field, it was demonstrated to measure both the light pulse width and the wave packet length (coherence length) by using an interferometer based on the photon correlation [1]. By using same method, it was demonstrated to measure the pulse width of the bending radiation [2].

We constructed an interferometer as shown in Figs. 1 and 2, which is a modification of Michelson-type interferometer. Two experiments can be conducted on this interferometer. The first one is two-photon correlation and another is autocorrelation. We conducted these experiments by using an undulator beamline BL1U (Fig. 3). We extracted the undulator radiation at a wavelength of 355 nm and introduced it to the interferometer.

The details of the results will be presented in a future paper. Here, we only give a short summary. Concerning two-photon correlation, so far, we could not get a significant result, which gives the information on the pulse length. The reason is presumably on the alignment of two light beams at the detector. We shall improve the alignment method and try this experiment in near future. On the other hand, in the autocorrelation experiment, we can get a promising result on the coherence length. Also, we note that the mechanical vibration produces a significant effect on the results. We shall improve the mechanical stability of the interferometer and try the next experiment in the nearest future.

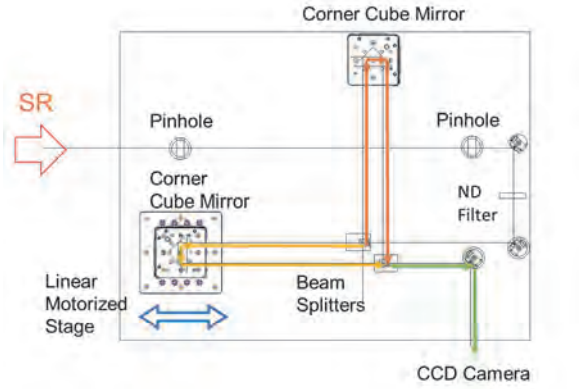


Fig. 1. Interferometer (Autocorrelation setup is shown).

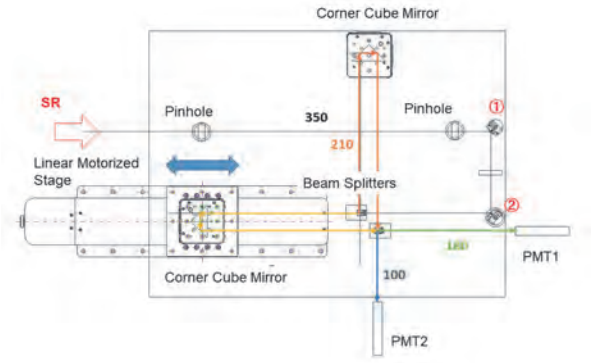


Fig. 2. Interferometer (Two photon correlation setup is shown).

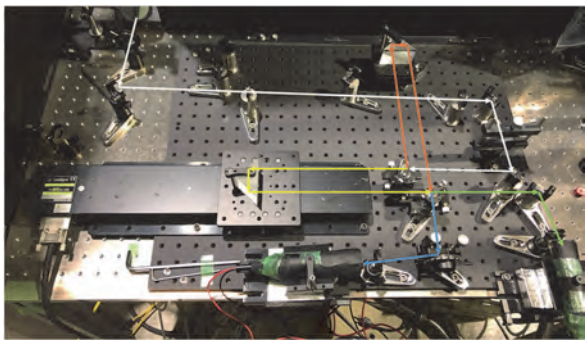


Fig. 3. Interferometer set at BL1U.

[1] Y. Miyamoto *et al*., Opt. Lett. **18** (1993) 900.
[2] T. Mitsuhashi and M. Tadano, Proc. EPAC2002 (Paris, 2002), 1936.

BL2A

X-ray Transmission Measurements for Optical Blocking Filters on Board the Third Focusing Optics X-ray Solar Imager (FOXSI-3) Sounding Rocket

I. Mitsuishi[1], S. Shimizu[1], T. Yamaguchi[1] and N. Narukage[2]
[1]*Nagoya University, Nagoya 464-8601, Japan*
[2]*National Astronomical Observatory of Japan, Mitaka 181-8588, Japan*

The solar corona is full of dynamic phenomena. They are accompanied by interesting physical processes, namely, magnetic reconnection, particle acceleration, shocks, waves, flows, evaporation, heating, cooling, and so on. The understan dings of these phenomena and processes have been progressing step-by-step with the evolution of the observation technology in EUV and X-rays from the space. But, there are fundamental questions remain unanswered, or haven't even addressed so far. Our scientific objective is to understand underlying physics of dynamic phenomena in the solar corona, covering some of the long-standing questions in solar physics such as particle acceleration in flares and coronal heating, and so on. In order to achieve these science objectives, we identify the imaging spectroscopy (the observations with spatial, temporal and energy resolutions) in the soft X-ray range (from ~0.5 keV to ~10 keV) is a powerful approach for the detection and analysis of energetic events [1]. This energy range contains many lines emitted from below 1 MK to beyond 10 MK plasmas plus continuum component that reflects the electron temperature.

For the first imaging spectroscopic observation of the solar corona in soft X-ray range, we launched a NASA's sounding rocket (FOXSI-3) on September 7th, 2018 [2] and successfully obtained the unprecedented data [3] using a combination of X-ray mirror and high speed X-ray camera with a back-illuminated CMOS sensor [4-6].

In this instrument, filters made of thin polyimide films with aluminum coating were deployed to reject the intense visible light from the sun and to adjust the incident X-ray flux into the camera. These optical blocking filters (hereafter OBFs) are located in front of both X-ray optics and the CMOS detector. Actually, we confirmed our OBFs worked successfully during the observation. To achieve our scientific goals, X-ray transmission through OBFs should be taken into account accurately and thus, X-ray transmission measurements were conducted in BL2A as shown in Fig. 1. We took X-ray transmission data at 830, 1000, 1200, 1400, 1600, 1800, and, 2000 eV to obtain a proper model representing the observed transmission. Consequently, the observed thicknesses of polyimide and aluminum coating films are 2.8 μm / 180 nm and 5.0 μm / 320 nm and we extracted the expected models with accuracies of typically <10 % and <5 % for OBFs of X-ray optics and the CMOS detector, respectively as shown in Fig. 2.

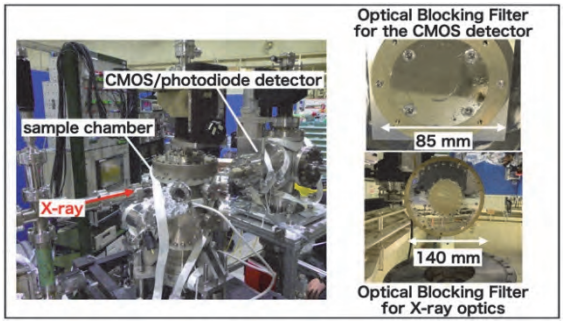


Fig. 1. Overview of our experimental setup (left) and OBFs for X-ray optics (top right) and the CMOS detector (bottom right) on board FOXSI-3.

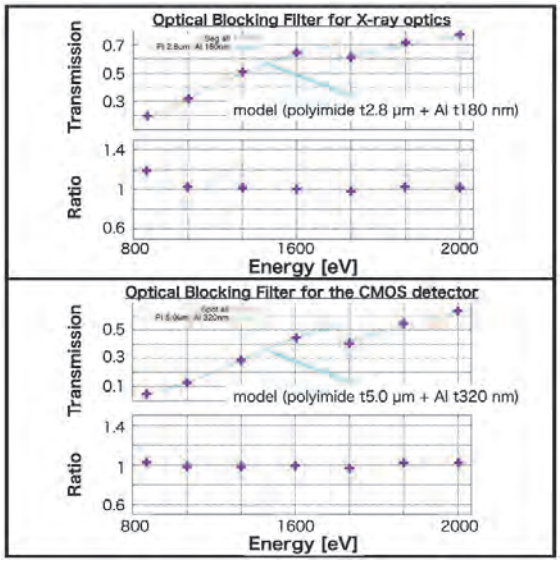


Fig. 2. Observed transmission of OBFs for X-ray optics (top) and CMOS detector (bottom) and the ratio of the observed to the expected value.

[1] N. Narukage *et al.*, White paper of the "soft X-ray imaging spectroscopy", arXiv:1706.04536 (2017).
[2] Web Release: https://hinode.nao.ac.jp/en/news/topics/foxsi-3-180907/
[3] Web Release: https://hinode.nao.ac.jp/en/news/topics/foxsi-3-data-release-en-20190115/
[4] N. Narukage *et al.*, Nuclear Instruments and Methods in Physics Research Section A **950** (2020) 162974.
[5] S. Ishikawa *et al.*, Nuclear Instruments and Methods in Physics Research Section A **912** (2018) 191.
[6] N. Narukage and S. Ishikawa, UVSOR Activity Report 2018 **46** (2019) 36.

BL3B

Study on the Electronic State of Fine-grained AgBr:I Crystals by Luminescence under Low Temperatures

T. Naka[1], T. Shiraishi[1], S. Kurosawa[2] and H. Sone[3]

[1] *Department of Physics, Toho University, Funabashi 274-8510, Japan*

[2] *New Industry Creation Hatchery Center (NICHe), Tohoku University, Sendai 980-8577, Japan*

[3] *Industrial Technology Institute, Miyagi Prefectural Government, Sendai 981-3206, Japan*

This is a study on the electronic state of AgBr:I nano-crystals in the nuclear emulsion by their luminescence response. The nuclear emulsion in which AgBr:I crystals are dispersed in gelatin is a particle tracking detector with sub-micrometric accuracy. Each crystal behaves a charged particle sensor of the indirect-transition semiconductor. Among electrons and holes excited in the crystal by the ionizing loss of charged particles, a few electrons are contributed to the track (latent image) formation. On the other hand, we found in previous studies that luminescence occurs with high efficiency at below the liquid nitrogen temperature by recombination of electrons and holes through iodine center [1].

For the AgBr:I crystal of the nuclear emulsion, the typical crystals are sub-micro sizes; in particular, a Nano Imaging Tracker (NIT) [2,3] in which super fine-grained crystals of approximately 40 nm are dispersed with a high density of 10,000 crystal/μm^3 was implemented as a track detector with the world's highest spatial resolution. It is used for the directional dark matter search, neutrons or heavy ions detector. However, their response for charged particles is still under studying. Because the behavior of electrons in nanoscale AgBr:I crystals leads to the greater understanding of the latent image formation mechanism, we study their electronic states, such as electron traps or the band structure, through the luminescence response by photoexcitation. In this year, we compared them with the previous knowledge by using a 200 nm crystal size, which is well understood in photographic science.

In thermo-luminescence measurement, after exciting with 240 nm light at 10 K for 10 min, the luminescence spectrum was measured at a constant temperature increase rate up to 300 K. A result at the rate of 4.9 K/min is shown in Fig. 1. The depth of the electron trap calculated from this measurement was estimated to be several tens meV. This is consistent with the trap due to interstitial silver ions [4], however such a very shallow trap is not considered to be contributed to the latent image formation. It is expected the existence of deeper electron traps by measuring up to more high temperature.

In addition, we measured the excitation spectrum dependency of the luminescence intensity (Fig. 2), and showed that this result was consistent with the predicted band structure by the calculation in bulk crystals [5].

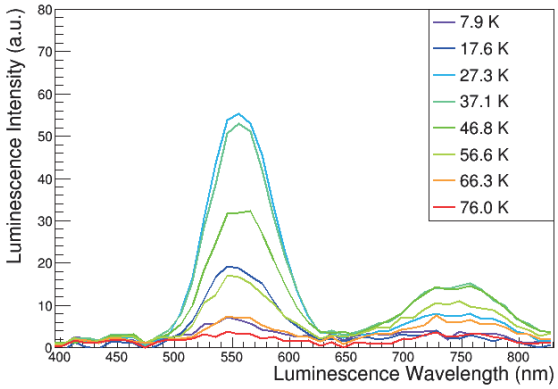


Fig. 1. Thermo-luminescence spectrum of AgBr:I crystal of 200 nm size at temperature increase rate of 4.9 K/min.

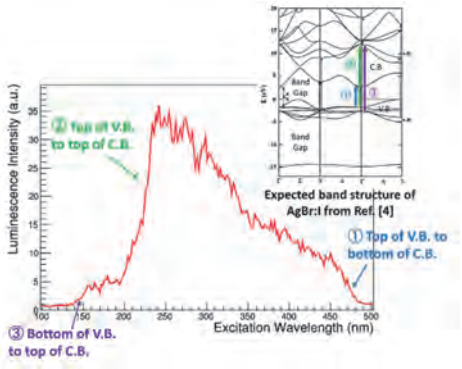


Fig. 2. Excitation spectrum of AgBr:I crystal of 200 nm size at 10 K.

[1] T. Shiraishi, H. Ichiki and T. Naka, Nucl. Inst. Meth. A **927** (2019) 202.
[2] T. Naka *et al.*, Nucl. Inst. Meth. A **718** (2013) 519.
[3] T. Asada, T. Naka, K. Kuwabara and M. Yoshimoto, Prog. Theor. Exp. Phys. **063H01** (2017).
[4] S. Sakuragi and H. Kanzaki, Phys. Rev. Lett. **38** (1977) 1302.
[5] V. Oleshko, M. Amkreutz and H. Overhof, Phys. Rev. B **67** (2003) 115409.

BL4B

Photoelectron Based Soft X-ray Detector for Removing High Order X-rays

M. Nagasaka[1,2] and H. Iwayama[1,2]
[1]*Institute for Molecular Science, Okazaki 444-8585, Japan*
[2]*The Graduate University for Advanced Studies, SOKENDAI, Okazaki 444-8585, Japan*

Soft X-ray absorption spectroscopy (XAS) in the low energy region below 200 eV is important to investigate chemical and biological phenomena since this energy region includes K-edges of Li and B and L-edges of Si, S, P, and Cl. However, it is difficult to measure XAS in the low energy region because transmitted soft X-rays mainly consist of high order X-rays due to the low transmission of first order X-rays. There are several techniques for removing high order X-rays, such as metal filters, energy analysis by the silicon drift detector [1], controlling the incident angle of a focused mirror in the beamline [2]. However, these methods are not able to apply the selection of the first order X-rays below 200 eV from those of the high order X-rays. In this study, we have developed a photoelectron based soft X-ray (PBSX) detector that removes contributions of high order X-rays for XAS below 200 eV [3].

The experiments were performed at soft X-ray beamline BL4B. Figure 1 shows schematics of our PBSX detector system, which consists of an Au plate, an Einzel lens, and an MCP detector. Transmitted soft X-rays from a sample film are irradiated to the Au plate, and the emitted Au 4f photoelectrons are collected into the MCP detector with the Einzel lens. The Einzel lens have three electrodes (P1, P2, and P3). V_1 is a constant voltage, whereas V_2 is a pulsed gate voltage. The Au 4f photoelectrons excited by both the first order X-rays and the high order X-rays detects with the gate-off voltage, whereas those excited by the high order X-rays only detect with the gate-on voltage. The photon flux of the first order X-rays is obtained by subtracting the intensities of the photoelectrons with the gate-on voltage from those with the gate-off voltage.

Figure 2 shows Si L-edge XAS spectra of the polymer/SiC film, where the thickness of the polymer (MOXTEK ProLINE) and SiC membrane (NTT AT) is 150 and 100 nm, respectively. Both photodiode (IRD AXUV100) and PBSX detectors are settled behind the sample films. XAS spectra in transmission mode are based on the Lambert-Beer law, $\ln(I_0/I)$, where I_0 and I are the transmission signals of blank and sample, respectively.

As observed in the Si L-edge XAS of SiC wafers [4], the XAS spectra show the large peak around 103.63 eV and small peaks around 112.5, 115.5, 120, and 142 eV. The broad peak is also observed around 158 eV. Since the contributions of the high order X-rays around 97 eV are removed by the PBSX detector, the intensity of the first SiC peak (103.63 eV) becomes higher than that obtained by the photodiode detector. In addition, due to removing the contributions from the fifth order X-rays at the O K-edge, the peak width also becomes narrower and is nearly same as that in the SiC film. The contribution from the second order X-rays at the C K-edge is also removed in the XAS spectra. As a result, we have successfully measured Si L-edge XAS spectra of the polymer/SiC film with avoiding the contribution of the high order X-rays by using the PBSX detector.

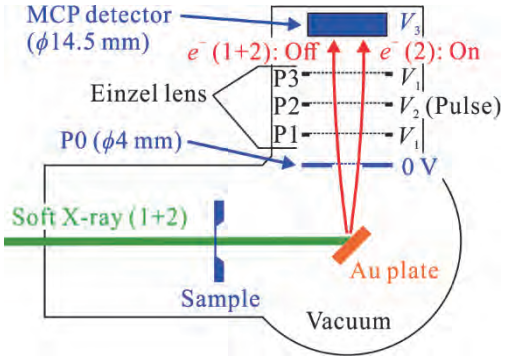


Fig. 1. Schematics of the PBSX detector. Photon flux of the first order X-rays is separately collected from those of the high order X-rays by using the energy difference of the Au 4f photoelectrons.

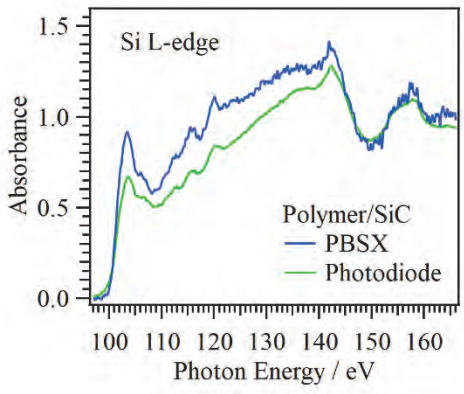


Fig. 2. Si L-edge XAS spectra of the polymer/SiC film by using the photodiode and PBSX detectors.

[1] P. Lechner *et al.*, Nucl. Instrum. Methods Phys. Res. A **377** (1996) 346.
[2] Y. Kitajima *et al.*, J. Electron Spectrosc. Relat. Phenom. **101-103** (1999) 927.
[3] M. Nagasaka and H. Iwayama, in preparation.
[4] S. Muto and T. Tanabe, J. Appl. Phys. **93** (2003) 3765.

BL5B

Multilayer Reflectometry for Evaluation of Second Harmonic Spectral Impurity in 100 nm Wavelength Output of BL5B UVSOR

T. Hatano[1], Y. Matsuda[2] and T. Ejima[1]
[1]*IMRAM, Tohoku University, Sendai 980-8577, Japan*
[2]*Department of Chemistry, Graduate School of Science, Tohoku Universuty, Sendai 980-8578, Japan*

VUV generation of rare gas excited by intense laser pulse can be used for ionization experiments when it is focused using a suitable condenser optics. VUV of a 118 nm wavelength from Xe is used [1], and VUV of a 100 nm wavelength from Ar is proposed as a new source. Al even with an oxide film on the surface is a high reflectance material in VUV region above 160 nm, and LiF overcoat extends the high reflectance region down to 101 nm [2]. Around 100 nm, however, no normal incidence mirror has been developed so far. Therefore, a condenser mirror having a high normal reflectance at 100 nm is demanded for 100 nm wavelength VUV sources. For that purpose, authors are planning to test thick large-*k* material or Al overcoated with thin small-*n* material. In any case, characterization accuracy is crucial. The spectral purity of the output of grating monochromators, especially, is important rather than the geometrical alignment in normal incidence reflectance measurements. In the present study, the second harmonic spectral impurity has been investigated at BL5B UVSOR, which is one of most useful beamlines for calibration of optical elements around a wavelength of 100 nm.

A 20 period Al (17 nm)/Si (16 nm) multilayer reflecting 50 nm (24.8 eV) VUV at an angle of incidence of 18.1° was fabricated for the second harmonic detection at 100 nm (12.4 eV). When the monochromator setting is for 100 nm, the multilayer reflection has an additional signal due to the 50 nm second order diffraction of the grating. The detailed analysis of the measured spectral reflectance gives the ratio of the power of the second order light to that of the total output [3]. The measured spectral reflectance at an angle of incidence of 18.1° is shown in Fig. 1 by blue line. The grating and mirror choice of the monochromator was G3M5. The major peak where the grating diffraction order m_G and the multilayer Bragg reflection order m_M are both 1, was found at 24.8 eV. It gives the reflectance at 24.8 eV as 5.4 %.

The second peak was found at 12.4 eV. Orders of the grating diffraction and the multilayer reflection of this peak were assigned as $m_G = 2$ and $m_M = 1$. The evidence can be seen in the spectral reflectance of another multilayer, 15 period Al (50 nm)/Si (17 nm) which is shown in Fig. 1 by green line. This multilayer is similar to the first one if the Si layers were alternatively replaced with Al layer. Therefore it reflects 24.8 eV VUV at a similar angle of incidence of the first one with $m_M = 2$. Two other peaks appeared at lower energy side. There might be a question; which is of the fundamental Bragg reflection ($m_G = 1$ and $m_M = 1$)? The answer is easy when the dispersion of refractive index n is considered. Since n of Al rapidly decrease from 24.8 eV to 12.4 eV, the $m_M = 1$ peak is expected to appear at much higher energy than 12.4 eV by the refraction effect. Thus, the second peak around 18.6 eV can be attributed to $m_G = 1$ and $m_M = 1$. The third peak located at exactly the half energy of $m_G = 1$ and $m_M = 2$ must be $m_G = 2$ and $m_M = 2$.

Back to the 12.4 eV peak of the first multilayer, the peak height on the baseline of the $m_G = 1$ background reflectance was 2.2 %. It corresponds to the product of the second harmonic ratio and the 24.8 eV reflectance [3]. The conclusion is that 41 % of the monochromator output power is the second harmonic, which means that the experimental result around 100 nm (12.4 eV) must be analyzed with the spectral purity of 59 % at highest taken into account.

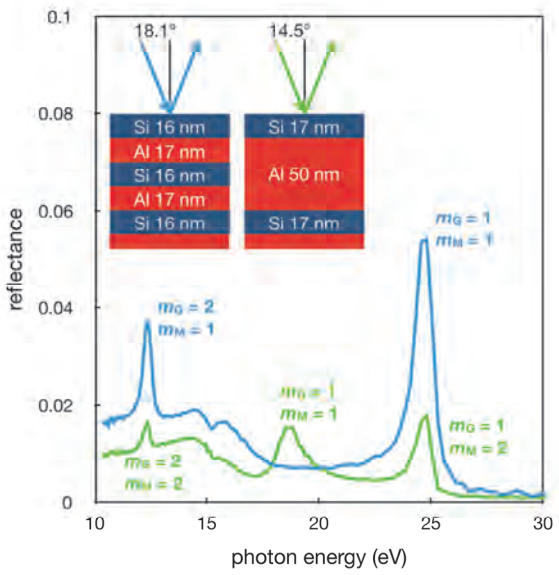


Fig. 1. Measured spectral reflectances of Al/Si multilayers.

[1] Y. Matsuda, A. Yamada, K. Hanaue, N. Mikami and A. Fujii, Angew. Chem. Int. Ed. **49** (2010) 4898.
[2] W. R. Hunter, J. F. Osantowski and G. Hass, Appl. Opt. **10** (1971) 540.
[3] T. Hatano and T. Harada, J. Electron Spectrosc. Relat. Phenom. **196** (2014) 156.

BL5B

Investigation of the Source of the Photon-Energy Drift of BL5B

H. Zen[1], E. Nakamura[2], K. Hayashi[2] and K. Tanaka[2,3]

[1]*Institute of Advanced Energy, Kyoto University, Uji 611-0011, Japan*

[2]*UVSOR Synchrotron Facility, Institute for Molecular Science, Okazaki 444-8585, Japan*

[3]*School of Physical Sciences, The Graduate University for Advanced Studies, SOKENDAI, Okazaki 444-8585, Japan*

The variation of the photon beam properties, such as beam position, photon energy, and so on, during user operation in the beamline is a big issue in synchrotron radiation (SR) facilities. After introducing the top-up operation in 2010, the average photon flux of the UVSOR has been doubled. Then the heat load on to the mirrors have been doubled and heat induced mirror deformation could induce the variation of the photon beam properties in some beamlines. A photon-energy drift at BL5B has been observed during user experiments [1]. We have started a detailed investigation of the source of the photon-energy drift. Results of our investigation and efforts to reduce the drift are reported.

The first candidate of the source of the photon-energy drift was the M0 mirror, which is water cooled but directly illuminated with SR. At first, a system to monitor the angle of the M0 mirror using a laser diode and a CCD camera was developed to investigate the deformation of M0 mirror and its influence to the photon energy. As the result of the continuous measurement of the photon energy and the M0 mirror angle (Fig. 1), we found that the angle of M0 mirror is not the main source of the photon-energy drift.

The M1 mirror, which is not water cooled, was the second candidate of the source. Several thermocouples were installed to measure the temperature of the M1 mirror and its holder. The measured results of the temperature rise are shown in Fig. 2. After opening the front end valve at 10 o'clock, temperature of M1 mirror and its holder gradually increased. The temperature of the center of the M1 mirror (CH2) was significantly higher than those of the upstream (CH3) and downstream (CH1). This large temperature gradient may cause the deformation of the M1 mirror. Moreover, the temperature of the mirror holder (CH4) has higher temperature than that of M1 mirror. Even after 10 hours from the start of SR injection, the holder temperature continuously increased. This continuous temperature rise could be the source of the continuous photon-energy drift shown in Fig. 1 which lasted for 20 hours.

We found that some stray light of SR directly hit the holder of M1 mirror. This could be the reason why the temperature of the holder (CH4) was higher than that of the M1 mirror (CH2). A horizontal slit after the M0 mirror was adjusted to reduce the amount of the stray light hitting on the M1 mirror holder without significant reduction of SR intensity. This treatment worked well and the amount of temperature rise of the M1 mirror holder could be significantly suppressed from 73 to 57 ºC (Fig. 3).

Moreover, a heater was installed to compensate the SR induced temperature rise of M1 mirror. The temperature of M1 mirror was stabilized by a feedback control. Then the amount of photon-energy drift was decreased from -0.19 to -0.08 eV@73.1 eV. In the present condition, some stray light still hitting on the holder. Further improvement can be achieved by installing a metalic mask in front of the M1 mirror. This will enable us complete cutting out of the stray light and more reduction of the photon-energy drift.

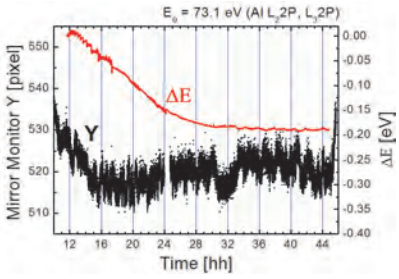


Fig. 1. Result of continuous measurement of the M0 mirror angle and the relative photon-energy of the SR after the monochrometer of BL5B.

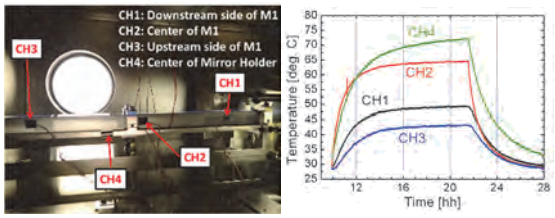


Fig. 2. (Left) Photograph of thermocouples attached to the M1 mirror. (Right) Measured temperature rise.

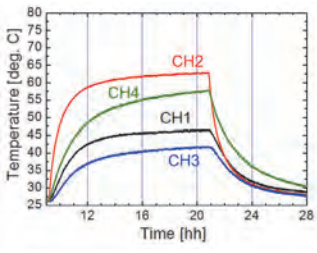


Fig. 3. Measured temperature rise with insertion of slit to reduce the stray light hitting on the holder.

[1] K. Hayashi, UVSOR Activity Report 2011 **39** (2012) 121.

BL7B

Interference Analysis by Composite Type VIS-VUV Complex Refractive Index Measurement Device

J. Omae[1], K. Fukui[1], K. Yamamoto[2] and T. Saito[3]

[1]*Department of Electrical and Electronics Engineering, University of Fukui, Fukui 910-8507, Japan*
[2]*Far-infrared region Development Research Center, University of Fukui, Fukui 910-8507, Japan*
[3]*Department of Environment and Energy, Tohoku Institute of Technology, Sendai 982-8577, Japan*

There is spectroscopic ellipsometry (SE) as a measurement method for obtain accurate complex refractive index spectrum of solid material. However, a commercially available SE device has measurement upper limit of about 5.5 eV. Therefore, based on the instrument designed by the AIST group, we had developed a SE that can measure from visible (VIS) to vacuum ultraviolet (VUV) using BL7B [1].

The VIS-VUV SE can obtain the accurate complex refractive index, but it cannot obtain a wavelength continuous spectrum due to the measurement principle of this SE. On the other hand, there is Kramars-Kronig analysis (KKA) as a method to obtain a wavelength continuous spectrum of complex refractive index. KKA obtains a complex refractive index spectrum through the Kramars-Kronig relation to the reflection spectrum measured in a sufficiently wide wavelength range. However, considering that the quantitative measurement of the reflection spectrum is extremely difficult, the absolute value of the complex refractive index obtained by KKA is uncertain. However, the VIS-VUV SE and KKA have complementary features. Therefore, with the aim of obtaining complex refractive indeies spectra from these two analysis methods, we have been incorporating reflectometer into this VIS-VUV SE. However, this combined system cannot take advantage of both features when the measurement target is thin film and the optical interference occurs. Then, in this report, we tried to establish an analytical method in wavelength region where optical interference occurs.

In our combined system, the absolute value of the reflection spectrum obtain by the reflection measurement can be corrected by calculating the reflectance from VIS-VUV SE. The optical interference can be expressed using an appropriate optical model by complex refractive indices ***n*** and ***k***. Therefore, applying the fitting calculation with the appropriate optical model to the corrected reflectance spectrum in optical interference energy region allows the complex refractive indices spectra to be obtained directly from the reflection spectrum. Figure 1 shows the corrected reflection spectrum of AlN thin film evaporated on SiO2 substrate by RF sputtering method. Optical interference was observed at 2 to 5.5 eV, and this analysis was performed in this wavelength region. Figure 2 shows the complex refractive index obtained by this analysis. To evaluate the analysis results, the absorption coefficient was calculated from the extinction coefficient ***k***, and the shape was compared with the absorption spectrum of this AlN thin film.

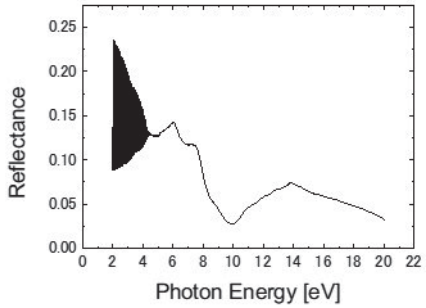


Fig. 1. Reflection spectrum of AlN thin film

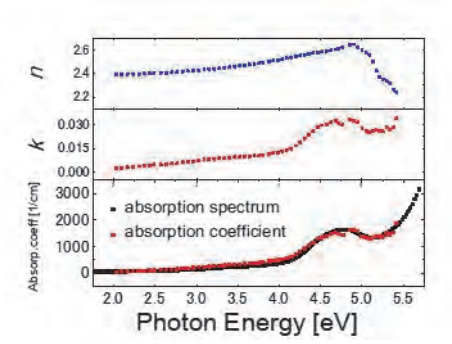


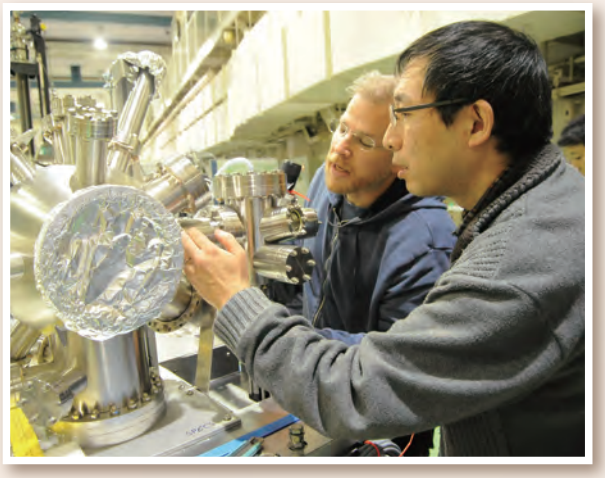
Fig. 2. Complex refractive indices, absorption coefficient and absorption spectrum of AlN thin film

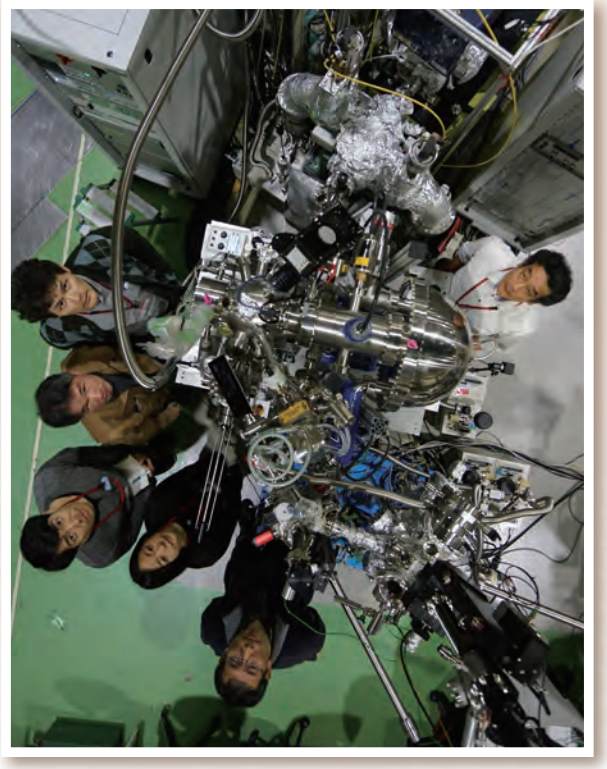
[1] T. Saito, M. Yuri and H. Onuki, Rev. Sci. Instrum. **66** (1995) 1570.

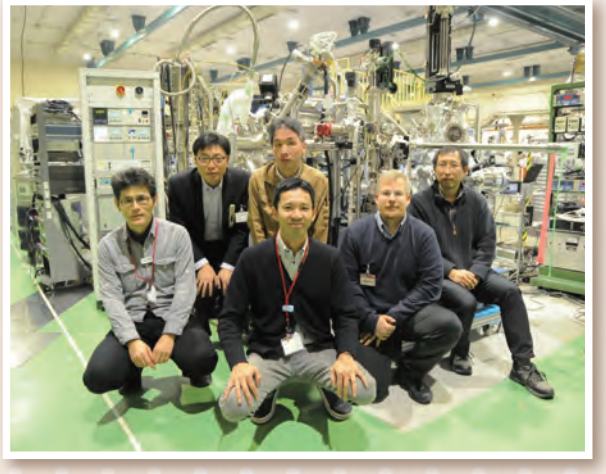
Installation of Momentum Microscope at BL6U





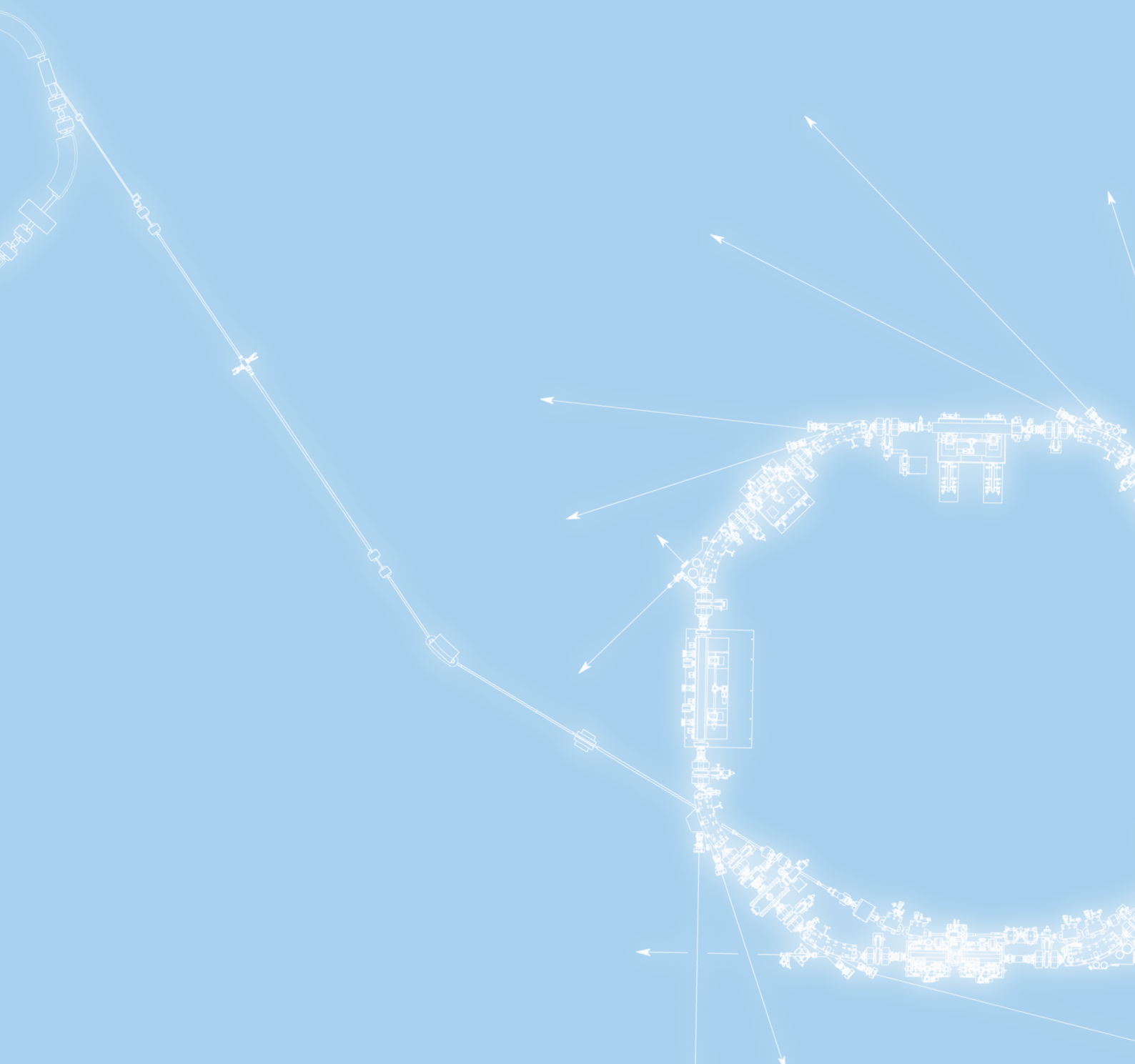






Ⅲ-2

Materials Sciences



Highlight

BL1U

Evidence for Suppression of Cation Vacancies in Ce:$Gd_3Al_2Ga_3O_{12}$ Scintillator by Mg Codoping

K. Fujimori[1], M. Kitaura[1], Y. Taira[2], M. Fujimoto[3], Y. Okano[4], H. Zen[5], M. Katoh[3,8], M. Hosaka[6], J. Yamazaki[3], K. Kamada[7] and A. Ohnishi[1]

[1]*Faculty of Science, Yamagata University, Yamagata 990-8560, Japan*
[2]*National Institute of Advanced Industrial Science and Technology, Tsukuba 305-8568, Japan*
[3]*UVSOR Synchrotron Facility, Institute for Molecular Science, Okazaki 444-8585, Japan*
[4]*Center for Mesoscopic Sciences, Institute for Molecular Science, Okazaki 444-8585, Japan*
[5]*Institute of Advanced Energy, Kyoto University, Uji 611-0011, Japan*
[6]*Synchrotron Radiation Research Center, Nagoya University, Nagoya 464-8603, Japan*
[7]*New Industry Creation Hatchery Center, Tohoku University, Sendai 980-8579, Japan*
[8]*Hiroshima Synchrotron Radiation Center, Hiroshima University, Higashi-Hiroshima, 739-0046*

Recently, it was clarified that Mg codoping is an effective manner to suppress the trapped electron centers responsible for phosphorescence of Ce doped $Gd_3Al_2Ga_3O_{12}$ (Ce:GAGG) scintillator [1]. The trapped electron centers are formed due to charge compensation of Ga/Al vacancies at the octahedral site. It is thus expected that such Ga/Al vacancies are decreased by Mg codoping. The Gamma-ray induced positron annihilation lifetime spectroscopy (GiPALS) is known to be the unique experimental method that can obtain the information on negatively charged defects such as cation vacancy of bulk crystal [2]. This method makes it clear whether Mg codoping is effective for the suppression of cation vacancies in Ce:GAGG scintillators. In the present study, GiPALS spectra of GAGG, Ce:GAGG, and Ce,Mg:GAGG crystals were measured using ultrashort γ-ray pulses available in BL1U, UVSOR [2]. The preliminary result of the GiPALS has been reported in Ref. [3].

Figures 1(a)-1(c) show PALS spectra of GAGG, Ce:GAGG, and Ce,Mg:GAGG crystals, respectively. These data were obtained at 300 K. The relative intensities and lifetimes were analyzed using the program LT10 [4]. The analyzed results are listed in Table 1. As shown by broken lines in Fig.1, PALS spectra are reproduced by two exponential decay functions with different lifetimes. This fact suggests that there are at least two annihilation sites for positrons. Such two annihilation sites are of intrinsic origins in GAGG, because the relative intensities and lifetimes are almost the same within uncertainties between GAGG and Ce:GAGG. The first and second components are assigned to positron annihilation at bulk and defect states respectively. The lifetimes of the second component are almost the same as those for positron annihilation at the sites of Al monovacancy and Al-O divacancy, which were obtained from the theoretical calculation [5]. On this basis, the second component is assigned to the positron annihilation at the defect sites of Ga/Al monovacancy and Ga/Al-O divacancy.

It was pointed out that Mg codoping has the ability to reduce cation vacancies. Figures 1(a)-1(c) revealed that the relative intensities of the second component are clearly decreased by Mg codoping. From this result, it is evident that Mg codoping is effective for the suppression of cation vacancies in Ce:GAGG scintillator.

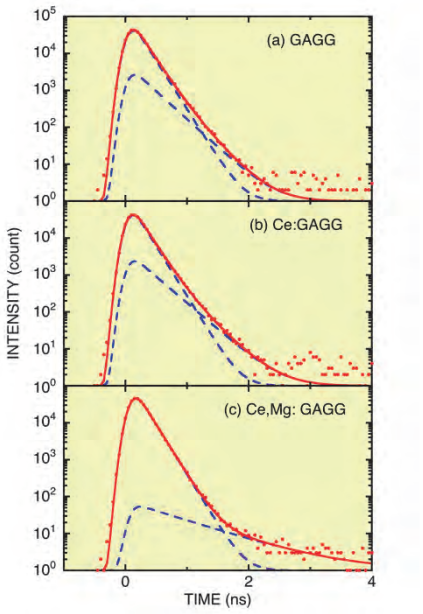


Fig. 1 :PALS spectra of (a) GAGG, (b) Ce:GAGG, (c) Ce,Mg:GAGG crystals, measured at 300 K under ultrashort γ-ray pulses.

Table 1. Lifetimes τ_i and relative intensities I_i of the first and second components for GAGG, Ce:GAGG, Ce,Mg:GAGG crystals.

	τ_1 (ps)	I_1 (%)	τ_2 (ns)	I_2 (%)
GAGG	165±1	92±3	286±17	8±3
Ce:GAGG	161±2	92±4	304±17	8±4
Ce,Mg:GAGG	161±1	99±1	812±30	1±1

[1]M. Kitaura *et al.*, Appl. Phys. Lett. **113** (2018) 041906.
[2] Y. Taira *et al.*, Rev. Sci. Instrum. **84** (2013) 053305.
[3] K. Fujimori *et al.*, UVSOR Activity Report 2018 **46** (2019) 44.
[4] D. Giebal and J. Kansy, Phys. Procedia **35** (2012) 122.
[5] A. G. Marinopoulos, Eur. Phys. J. B **92** (2019) 242.

BL1B

Effect of Electron-Irradiation on Acceptor State of Germanium

A. Hara and T. Awano
Faculity of Engineering, Tohoku Gakuin University, Tagajo 985-8537, Japan

Germanium (Ge) has better mobility for both electrons and holes than those of silicon (Si). Moreover, as the melting point of Ge is lower than that of Si by approximately 450 °C, crystallization occurs at a lower temperature than Si. Thus, Ge is attracting attention as a semiconductor material for plastic substrates and three-dimensional integrated circuits. However, a large number of holes are generated in polycrystalline Ge due to crystal defects; hence, defect control is an important issue.

Although it is proposed by theoretical approach that Ge vacancies are related with source of the holes, detailed researches have not been disclosed. As Ge has a high dielectric constant, the energy level of the acceptor is expected to be very shallow as group-III impurities; hence, the BL1B line of UVSOR was selected to detect such defects.

Electron irradiation (e-irradiation) is convenient method to introduce vacancies and self-interstitials. Bulk p-type [Indium (In)-doped] Ge samples with 2.0 mm thickness and 12 ohm-cm resistivity were used in this experiment. The samples were irradiated with an electron beam at 4.5 MeV with 3×10^{15} cm^{-2} at room temperature to introduce lattice defects related to Ge vacancies, and the transmission spectra was measured at liquid He temperature. Samples were annealed at 200, 300, and 400 °C for 30 min in a conventional furnace system to evaluate variations of the spectra.

Figure 1 shows the optical transmission spectra of the In-acceptor [1,2]. Sharp lines correspond to electronic transition between ground and excited states. Owing to the complex structure of the Ge valence band, many lines exist. Figure 1 shows the spectra of as-grown and as-e-irradiated samples; in addition, samples annealed at 200, 300, and 400 °C.

Intensity of the In-acceptor decreased after e-irradiation, but increased and returned to that of as-grown sample with increasing annealing temperature at 400 °C. This indicates that e-irradiation introduced donors that were eliminated at 400 °C. Thus, simple structural defects, such as vacancies, self-interstitials and their aggregates, are not the origin of holes because the holes survive in polycrystalline Ge annealed at 500 °C.

In addition, it was clarified that the new sharp lines related to effective-mass states did not form between 20 and 100 cm^{-1}. The thermal stability of e-irradiation defects and hole-related defects generated in poly-Ge are different. Thus, more complex defects including impurities may be related to the generation center of holes.

In summary, optical transmission spectra of e-irradiated Ge were measured at liquid He temperature. It was found that e-irradiation generated donors that were eliminated at temperatures at 400 °C. This indicates that simple structure, such as vacancies, self-interstitials and their aggregates, are not the origin of holes. In addition, new lines related to effective-mass states were not found.

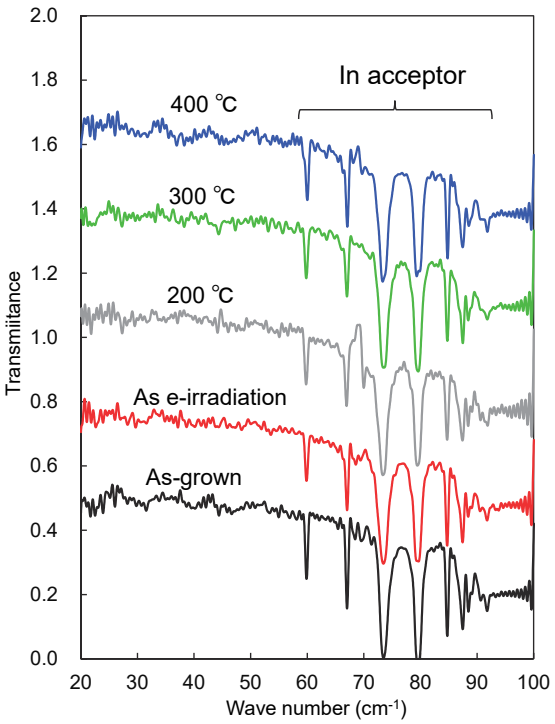


Fig. 1. Transmittance of Ge.

[1] R. L. Jones and P. Fisher, J. Phys. Chem. Solids **26** (1965) 1125.
[2] W. Kohn, in Solid State Physics, ed. F. Seitz and D. Turnbull (Academic Press, New York, 1957) Vol. **5**, p. 257.

BL1B

Change of Phase Transition Temperature of KDP Single Crystal by Alanine Doping

Z. Mita[1], A. Goto[1], H. Watanabe[1,2] and S. Kimura[1,2]
[1]*Graduate School of Frontier Biosciences, Osaka University, Suita, 565-0871, Japan*
[2]*Department of Physics, Graduate School of Science, Osaka University, Toyonaka 560-0043, Japan*

Second harmonic generation (SHG) is used in laser pointers and other compact laser devices. Among many SHG materials, potassium dihydrogen phosphate (KH_2PO_4, KDP) is well known and used in applications. Recently, it has been reported that the doping of 0.5-wt% alanine in KDP improves the SHG efficiency by a factor of about two [2].

However, many basic physical properties about the origin of the increase of the SHG efficiency due to the alanine doping has never been reported so far. To clarify the origin of the SHG efficiency change by the doping, we have measured polarization and temperature dependences of optical conductivity spectra of single-crystalline samples of pristine KDP and L-alanine-doped KDP.

We have grown KDP single crystals with and without the doping of 0.5-wt% L-alanine using the solvent evaporation method and confirmed to be orthorhombic structure at room temperature by taking X-ray Laue diffraction patterns. Anisotropic optical reflectivity spectra in the terahertz (THz) region around the phase transition temperature from 117 K to 124 K has been measured by using BL1B of UVSOR-III and laboratorial equipments. The obtained spectra were converted to optical conductivity [$\sigma(\omega)$] spectra by the Kramers-Kronig analysis. Temperature dependence of the $\sigma(\omega)$ spectrum with the electric vector perpendicular to the c axis ($E \perp c$) in the THz region is shown in Fig. 1.

As shown in Fig. 1, we found a unique peak appearing only at the low-temperature phase (namely I). By the fitting of a Gaussian function to the peak I after subtracting the high-temperature–phase spectrum, the temperature dependences of the energy, intensity, and width of the peak were obtained as shown in Fig. 2. The peak energy shifts to the higher energy side and the intensity and width increases as the temperature decreases. The peak energy shift suggests the contraction of the lattice constant at lower temperature, so the spectra in Fig. 1 are considered to be the spectra with the electric vector parallel to the a axis because only the axis monotonically shrinks of the three independent axes [1]. Figure 3 shows the temperature dependence of the peak area of I. For pristine KDP, the phase transition temperature can be evaluated as 122 K, which is the same as that reported in the previous work [1]. For 0.5-wt% doping, the transition temperature slightly increased. To clarify the doping effect systematically, further experiments with more doping amounts or detailed temperature steps are needed.

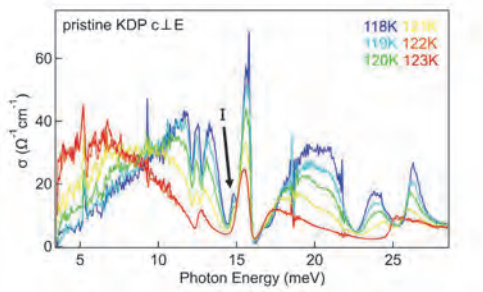


Fig. 1. Anisotropic optical conductivity [$\sigma(\omega)$] spectra at temperatures from 118 to 123 K in the THz region perpendicular to the c-axis ($E \perp c$). A peak at 14.8 meV (namely I) appears below the phase transition temperature of 122 K.

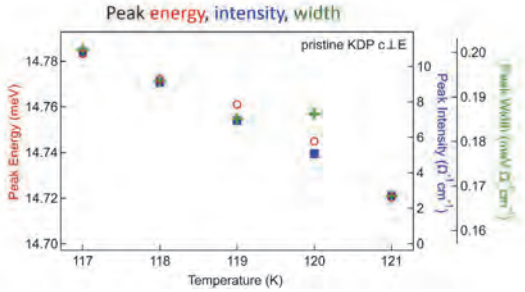


Fig. 2. Peak energy (red), intensity (blue), and width (green) of the 14.8-meV peak as a function of temperature.

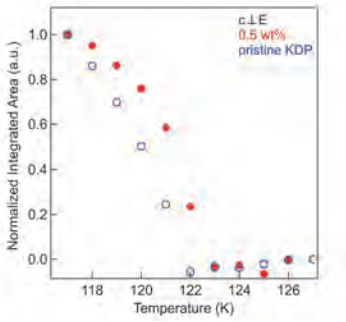


Fig. 3. Temperature dependence of the area of the 14.8-meV peak of pristine KDP (blue) and 0.5-wt% L-alanine-doped KDP (red). The area is normalized by the intensity at 117 K.

[1] G. Busch and P. Scherrer, Naturwiss. **23** (1935) 737.
[2] K. D. Parikh *et al.*, Cryst. Res. Technol. **45** (2010) 603.

BL2A

Mo L_{III}-edge XANES Study of Catalytically Active Mo Species on H-MFI for Methane Dehydroaromatization with Hydrogen

H. Aritani[1], K. Kuramochi[2], R. Yamazaki[2], S. Sato[1], Y. Nozawa[1], A. Kato[1] and A. Nakahira[3]
[1]*Graduate School of Engineering, Saitama Institute of Technology, Fukaya 369-0293, Japan* [2]*Advanced Science Research Laboratory, Saitama Institute of Technology, Fukaya 369-0293, Japan*
[3]*Graduate School of Engineering, Osaka Prefecture University, Sakai 599-8531, Japan*

Molybdenum-modified H-MFI zeolite is a typical GTL (Gas To Liquid) catalyst for methane dehydroaromatization (Methane To Benzene: MTB). On the Mo/H-MFI catalysts, it is a serious problem for development of MTB reaction, and thus, clarification of the deactivation process over the catalysts is one of the important points. Not only carbon deposition on acid sites of H-MFI but also excess carbonization of active Mo species causes the deactivation of MTB. Hydrogen addition to methane reactant is effective for inhibiting the deactivation [1]. However, reductive effect for active Mo species (well dispersed Mo_2C, in major) cannot be avoided. In the present study, Mo L_3-edge XANES study is introduced to characterize the active Mo-carbide species on H-MFI after the methane dehydroaromatization with H_2. For inhibiting excess Mo carburization, V co- modification effect on Mo/H-MFI has also been studied.

Mo(5wt%)/H-MFI and Mo-V/H-MFI catalysts were prepared by impregnation of H-MFI (Si/Al_2=30-72) support with $MoO_2(acac)_2$–$CHCl_3$ or $MoO_2(acac)_2$–$VO(acac)_2$–$CHCl_3$ solution (Mo/V=10-40), and followed by drying overnight and calcination at 773 K. The reaction condition for methane dehydroaromatization was described in a previous report [2,3]. Mo L_{III}-edge XANES spectra were obtained in BL2A of UVSOR-IMS in a total-electron yield mode using InSb double-crystal monochromator. Photon energy was calibrated by using Mo metal-foil at Mo L_{III}-edge, and normalized XANES spectra were presented by using REX-2000 (Rigaku) software.

As shown in Fig. 1 (top), edge energy of L_{III}-edge strongly relate to the valence of Mo ions. Using the references of Mo metal and α-Mo_2C, the reduction degree of active Mo species on H-MFI after the MTB reaction with H_2 are evaluated. For the XANES spectra of Mo-H-MFI catalysts in Fig. 1 (middle), the active Mo species are likely due to deeply reduced carbide species which is more carbonized than Mo_2C. The reduction degree almost independent on H_2 co-feed in the MTB reaction, and therefore, The MoC_x (x>0.5) species are formed through the deep reduction by methane. On these catalysts, H_2 co-feed (1-2 %) affect the inhibition of coke deposition. To suppress excess reduction, V co-modification on Mo/H-MFI (in Mo/V=10) has been found to be effective towards the enhancement of reactivity. In Fig. 1 (bottom), XANES spectra of these catalysts are shown. By V co-modification, the reduction degree of Mo species slightly suppressed in MTB reaction. The study about optimal Mo/V ratio is now in progress.

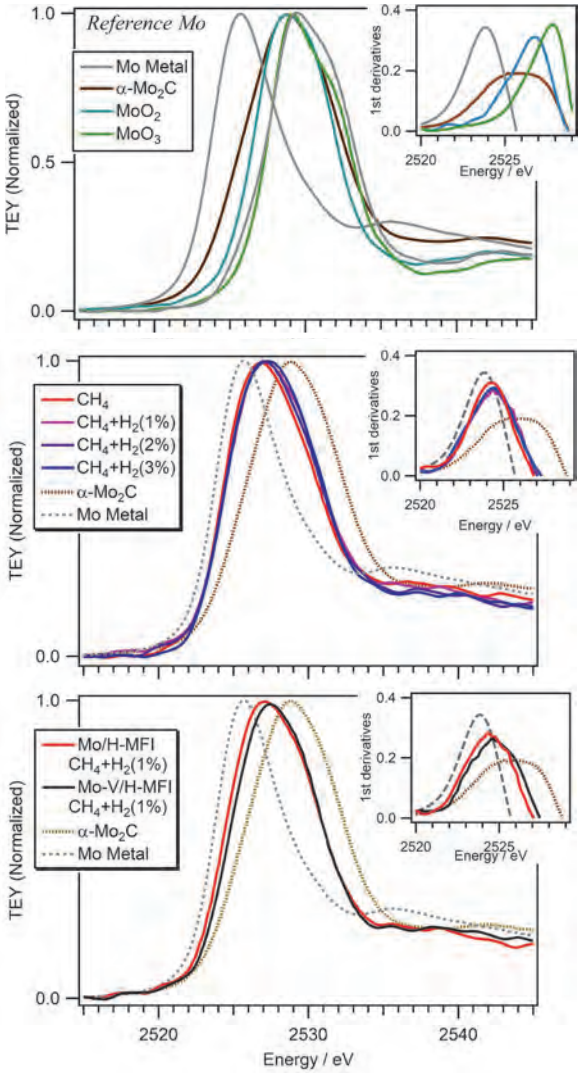


Fig. 1. Mo L_{III}-edge XANES of reference Mo samples [top], Mo/H-MFI catalysts reacted with CH_4-H_2(0-3 %) [middle], and V co-modified catalysts reacted with CH_4-H_2(1 %). First derivatives of XANES are shown in upper right of each figure.

[1] H. Aritani *et al.*, J. Environm. Sci. **21** (2009) 736.
[2] H. Aritani *et al.*, UVSOR Activity Report 2018 **46** (2019) 49.
[3] H. Aritani *et al.*, UVSOR Activity Report 2017 **45** (2018) 44.

BL2A

Local Environment of Mg^{2+} on Hydroxyapatite Surface

T. Nakamura, R. Kawanabe, H. Murata and A. Nakahira
Department of Materials Science, Osaka Prefecture University, Sakai 599-8531, Japan

Hydroxyapatite ($Ca_5(PO_4)_3OH$, HAp) is a main inorganic component of human bones and teeth. It has both of cation- and anion-exchange abilities. In human bodies, it is exposed to various ions of body fluids. Indeed, biological HAp is not pure but contains various kinds of defects and impurity ions, which affect properties of HAp [1,2]. Therefore, it is important to investigate reactions of these ions with the surface of HAp.

Mg^{2+} is one of the main impurities of human bones, which plays an important role of bone-remodeling. In the present study, we investigated local environments of Mg^{2+} reacted on the surface of HAp using X-ray absorption near edge structure (XANES).

HAp samples were synthesized by the solution-precipitation method [3]. Starting materials were 0.1 mol/L $Ca(NO_3)_2$ and 0.1 mol/L $(NH_4)_2HPO_4$ aqueous solutions. They were mixed and matured at 80 °C for 5 h. The pH was kept at 10 by adding 0.1 mol/L KOH aqueous solution. In order to prevent formation of Ca^{2+} vacancies, the initial Ca/P was set to 2, which is larger than stoichiometric composition of HAp, 1.67. Then, they were filtrated, washed by ion-exchanged water and dried at 50 °C. Mg^{2+}-doped HAp samples as a reference material were also synthesized by same procedures with addition of 0.1 mol/L $Mg(NO_3)_2$ aqueous solution to starting materials.

Obtained HAp powders were pressed into pellets of 10 mm in diameter. Parts of them were calcined at 1100 °C. The pellets were soaked in 50 mL of 0.01 mol/L $Mg(NO_3)_2$ aqueous solution for 10 min. Then, they were well washed by ion-exchanged water.

Mg-*K* XANES spectra were collected by the partial fluorescent (PFY) mode using a silicon-drift detector (SDD) at BL2A in UVSOR. Fluorescence X-ray spectra were de-convoluted using gauss functions, which was reported elsewhere [4]. X-ray beams were monochromated using beryl double crystals. Samples were mounted using carbon tapes on an Ti plate.

X-ray diffraction measurements indicated that samples consists of HAp and no secondary phases were observed even after calcination at 1100°C. This result indicates that our HAp samples have stoichiometric composition [1,3].

Figure 1 shows Mg-*K* XANES of Mg^{2+}-adsorbed samples. They have the same features to those of Mg^{2+}-doped HAp. This results indicated that Mg^{2+} was incorporatied into HAp crystals. As-dried HAp gave smooth spectra but ones calcined at 1100 °C gave rather noisy spectra. In this case, we observed only 1 cps of fluorescence X-ray of Mg even at the peak, 1312 eV. Such weak fluorescence X-ray of Mg indicated that HAp calcined at 1100 °C catched only small amounts of Mg^{2+}. Since the as-dried HAp samples have higher solubility in water than ones calcined at 1100 °C [3], there results implies that the reaction of Mg^{2+} with surface of HAp proceeds via a dissolution-reprecipitation process.

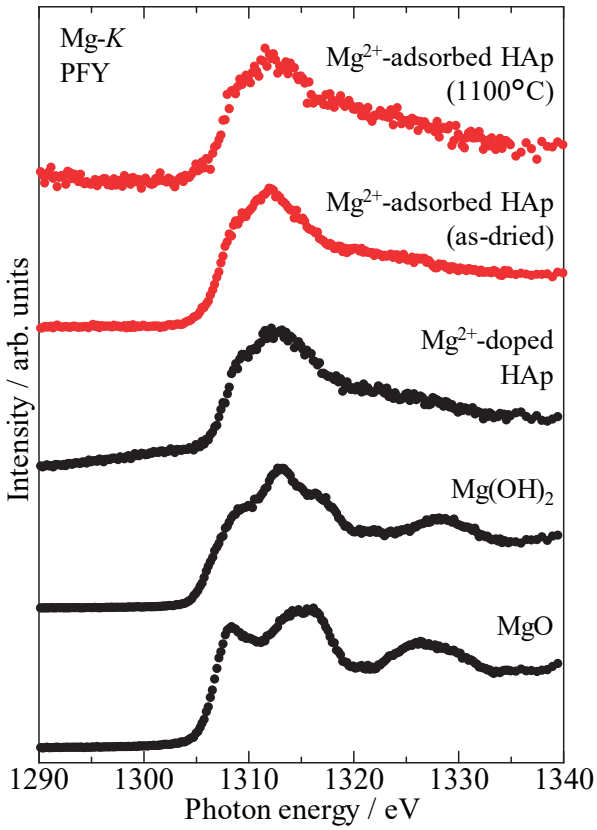


Fig. 1. Mg-*K* XANES of Mg^{2+}-adsorbed HAp samples (red lines) and reference materials (black lines).

[1] J. C. Elliott, Structure and Chemistry of the Apatites and Other Calcium Orthophosphates (Elsevier, Amsterdam, 1994).
[2] E. Boanini *et al.*, Acta Mater. **6** (2010) 1882.
[3] K. Shitara *et al.*, J. Asian Ceram. Soc. **2** (2014) 64.
[4] H. Murata, UVSOR Activity Report 2018 **46** (2019) 53.

BL2A

XAFS Analysis of Ga_2O_3 Loaded Al_2O_3 Photocatalysts for Carbon Dioxide Reduction

T.Yoshida[1], M. Akatsuka[2], R. Ito[2], A. Ozawa[2], M. Yamamoto[1] and T. Tanabe[1]
[1]*Advanced Research Institute for Natural Science, Osaka City University, Osaka 558-8585, Japan*
[2]*Graduate School of Engineering, Osaka City University, Osaka 558-8585, Japan*

Gallium oxide (Ga_2O_3) photocatalysts can reduce CO_2 to CO with H_2O, although the efficiency of CO production is very low [1]. Generally, photocatalytic activity depends on the local structure of the surface active site. However, there are few works investigating the influence of Ga_2O_3 local structure on the CO_2 photoreduction activity. In the present study, we have focused to geometrical or morphological effects of Ga_2O_3 particles supported on Al_2O_3 (referred as Ga_2O_3/Al_2O_3, hereafter) for CO_2 reduction under UV light irradiation. The reasons of utilization of Al_2O_3 as the support are twofold, (1) to increase surface area of Ga_2O_3, as evidenced by the observation that Ga_2O_3/Al_2O_3 was used for the removal of NOx, and (2) that Al_2O_3 hardly show the photocatalytic activity for both water splitting and CO_2 reduction.

Ga_2O_3/Al_2O_3 samples were prepared by impregnation of γ-Al_2O_3 with aqueous solution of gallium nitrate followed by dry and calcination in the air at 773 K for 4 h, as described elsewhere [2]. The loading amounts of Ga_2O_3 were 1, 5, 10 and 20 wt%. Unsupported Ga_2O_3 and Ga_2O_3/SiO_2 samples were also prepared in the similar way to Ga_2O_3/Al_2O_3. The Ga_2O_3 sample was employed for XRD measurement to identify the crystal phase of Ga_2O_3. Surface areas of all the prepared samples were measured by BET method. Ga L_3-edge XANES were measured with the beam line of BL2A at UVSOR, Institute for Molecular Science in Japan, in a total electron yield mode.

Photocatalytic CO_2 reduction with H_2O was carried out over the Ga_2O_3/Al_2O_3 sample. CO production rates over 5, 10 and 20 wt% Ga_2O_3/Al_2O_3 samples were higher than those over β-Ga_2O_3 and Al_2O_3 samples, while over 1 wt% Ga_2O_3/Al_2O_3, it was almost the same as that over Al_2O_3 sample.

Unsupported Ga_2O_3 was identified as γ-Ga_2O_3 by the XRD pattern. On the other hand, very weak and broad lines due to Ga oxide phase were observed for Ga_2O_3/Al_2O_3 samples but could not be identified clearly. Based on the BET measurements for a bare Al_2O_3 and Ga_2O_3/Al_2O_3 samples, we roughly estimated the surface area of Ga oxide phase in each Ga_2O_3/Al_2O_3 sample by subtracting the component of Al_2O_3 support. We regarded that the surface areas of Ga oxide phase are almost the same each other.

Figure 1 shows Ga L_3-edge XANES spectra. Two peaks around 1121 and 1123 eV are observed for Ga_2O_3/Al_2O_3 samples. A peak appeared near 1123 eV is caused by a Ga-O-Al bond [3], indicating that some interaction between Ga_2O_3 and Al_2O_3 occurred in all the samples. On the other hand, Ga_2O_3/SiO_2 samples showed no prominent peaks in XANES, suggesting that Ga species are highly dispersed on SiO_2 surface.

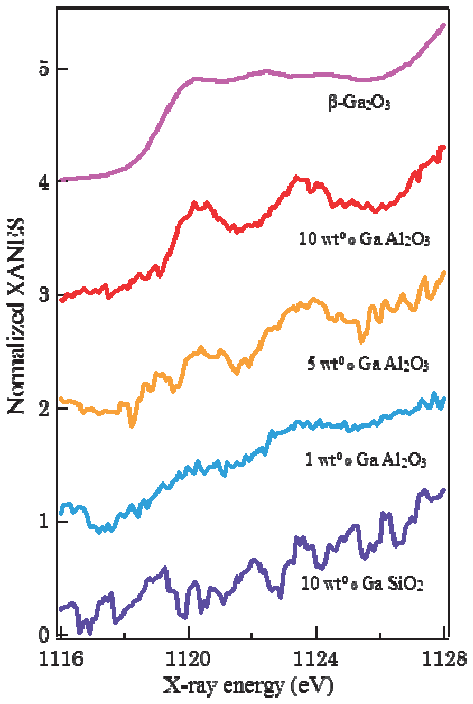


Fig. 1. Ga L_3-edge XANES spectra of all prepared samples. The spectrum of β-Ga_2O_3 is also given for comparison.

[1] H. Yoshida, L. Zhang L, M. Sato, T. Morikawa, T. Kajino, T. Sekito, S. Matsumoto and H. Hirata, Catal. Today, **251** (2015) 132.
[2] K. Nishi, K. Shimizu, M. Takamatsu, H. Yoshida, A. Satsuma, T. Tanaka, S. Yoshida and T. Hattori, J. Phys. Chem. B **102** (1998) 10190.
[3] K. Shimizu, M. Takamatsu, K. Nishi, H. Yoshida, A. Satsuma, T. Tanaka, S. Yoshida and T. Hattori, J. Phys. Chem. B **103** (1999) 1542.

BL2A

Local Structure Investigations of Al in Spinel Compounds Induced on Swift Heavy Ion Irradiations

S. Yoshioka[1], K. Yasuda[1], S. Matsumura[1], E. Kobayashi[2] and K. Okudaira[3]
[1]*Department of Applied Quantum Physics and Nuclear Engineering Kyushu University, Fukuoka 819-0395, Japan*
[2]*Kyushu Synchrotron Light Research Center (SAGA-LS), Tosu 841-0005, Japan*
[3]*Graduate School of Advanced Integration Science, Chiba University, Chiba 263-8522, Japan*

Magnesium aluminate oxide ($MgAl_2O_4$) is one of the common spinel compounds. Since it shows a variety of interesting physical and chemical properties, its microstructure has been extensively investigated. A cationic disordered $MgAl_2O_4$ spinel is represented by the formula of $[Mg_{1-x}Al_x](Mg_xAl_{2-x})O_4$, where the square brackets and the parentheses denote the tetrahedral and octahedral sites, respectively. The variable x is called the inversion parameter, which quantifies the cation disorder. Radiation with swift heavy ions (SHIs) interacts with materials and causes the structural change. It is therefore applied to material processing, modifications, etc. SHI irradiation provides high energy deposition through electronic stopping to the materials. SHIs in insulating solid materials are known to leave trails of damage along the ion path with a diameter of several nanometers. Structural change related to the cationic disorder has been also observed in $MgAl_2O_4$ with SHI irradiation using transmission electron microscopy observation. In this study, we clarify local coordination of each cation element, on which we conducted synchrotron radiation-based X-ray analysis.

Plates of poly-crystal $MgAl_2O_4$ with the shape of 10×4×0.5 mm were used in this study. These specimens were irradiated with 200 MeV Xe ions to fluences of 1×10^{13} cm^{-2} at the H1 beamline of the tandem ion accelerator facility in the Japan Atomic Energy Agency (JAEA)-Tokai. At the beginning of each paragraph, two space characters should be inserted as an indent. Mg *K*-edge and Al *K*-edge XANES measurements were performed at the BL2A beamline of UVSOR Okazaki, Japan, using the partial fluorescence yield method (PFY). A $KTiOPO_4$ (KTP) double crystal monochromator defined Mg *K* and Al *K* absorption edges in the energy region from 1290 to 1340 eV and 1540 to 1610 eV, respectively. The samples were set with their surface perpendicular to the incident X-ray beam. Fluorescence X-rays of Mg *K*α and Al *K*α were collected using an energy dispersible silicon drift detector (SDD). All measurements of XANES spectra were carried out in vacuum of 1×10^{-5} Pa at room temperature.

Figure 1 shows the XANES spectra with the Mg *K*-edge (1300 eV) acquired from the $MgAl_2O_4$ samples before and after irradiation with 200 MeV Xe ions with fluences of 1×10^{13} cm^{-2}. The Mg *K*-edge spectrum features of the irradiated $MgAl_2O_4$ sample were clearly different from those of the pristine sample. Especially, both the peak intensity ratio of *A*/*B* and *C*/*B* decreased after the irradiation. The spectrum shapes on Al *K*-edge also changed by the irradiation. Detailed analyses on the local environment of Mg and Al in the $MgAl_2O_4$ irradiated with SHI are in progress by combined use of the XANES and the first principles band structure calculations.

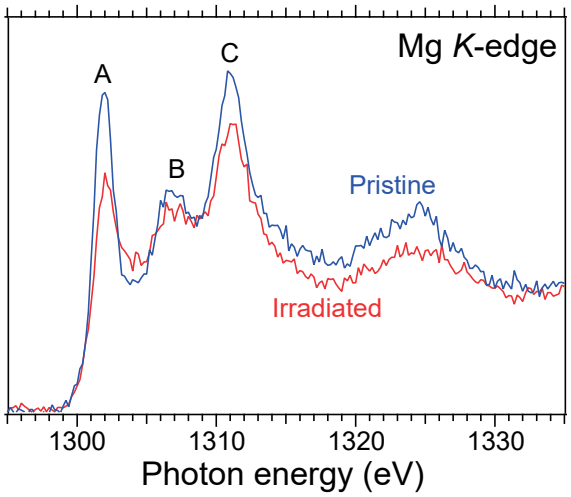


Fig. 1. Mg *K*-edge XANES spectra of pristine and irradiated $MgAl_2O_4$ with 200 MeV Xe ions to fluences of 1×10^{13} cm^{-2}.

[1] T. Yamamoto *et al*., Nucl. Instrum. Meth. B. **245** (2006) 235.
[2] K. Yasuda *et al*., Nucl. Instrum. Meth. B. **250** (2006) 238 .

BL2A

X-ray Absorption Analysis of Rb Ions in $FAPbI_3$

K. Osonoe[1,2], M. Tohyama[1], M. Ishida[1], K. Hirose[1,2] and T. Yamamoto[1,3,4]

[1]*Faculty of Science and Engineering, Waseda University, Tokyo 169-8555, Japan*

[2]*Institute of Space and Astronautical Science, JAXA, Sagamihara 252-5210, Japan*

[3]*Institute of Condensed-Matter Science, Waseda University, Tokyo 169-8555, Japan*

[4]*Kagami Memorial Research Institute for Materials Science and Technology, Waseda University, Tokyo 169-0051, Japan*

Organic-inorganic hybrid perovskite-type solar cells have attracted significant interest owing to their low-cost fabrication and high performance, exhibiting a rapid increase in power conversion efficiency after the discovery of its application for solar-cells [1]. The organic-inorganic hybrid perovskite is used as a light-absorption layer in the stacking structure of the thin films in a perovskite solar cells (PSC). Although methyl-ammmonium lead tri-iodide ($CH_3NH_3PbI_3$; hereafter $MAPbI_3$) was used at early stage, $MAPbI_3$ is not stable at high temperature and under humid condition. Recently, $FAPbI_3$, FA = formamidinium: $CH(NH_2)_2$, based materials have been investigated to get higher stability and efficiency than $MAPbI_3$. In these researches, cations at FA site and anions were often partially replaced by other ions to control the tolerance factor, which is a well-known parameter to estimate a stability of perovskite structure [2]. It was reported among such studies that Rb-doping could enhance the light absorption efficiency. However, the mechanism of such enhancement of efficiency has not yet been understood. Although it is important to know a local environment of such doped ions in the host materials in an atomic scale, such analysis is often skipped due to a difficulty of the analysis for dilute dopants. In the present study, we have synthesized Rb-doped $(CsFAMA)Pb(IBr)_3$ and the local environment of doped Rb ions in the synthesized materials have been investigated by the X-ray absorption near-edge structure (XANES) measurements.

Thin films of Rb-doped $(CsFAMA)Pb(IBr)_3$ were prepared by the spin coating method on the glass substrate. After the coatings, thermal treatment was given changing the temperature. Rb concentration was approx. 3 at% to CsFAMA. Synthesized films were characterized by the conventional powder X-ray diffraction method using Cu Kα X-rays, which showed all the synthesized films crystallized in a singular phased perovskite structure. Sample morphology was also observed by the scanning electron microscope (SEM), which showed the grain size changes according to the temperature of thermal treatment. Rb L_3-edge X-ray absorption near edge structure (XANES) spectra of synthesized films were observed at BL2A in UVSOR by the total electron yield method. Sample films on the glass substrate were put on the carbon adhesive tape, which were attached on the first dinode of the electron multiplier. In order to avoid charge-up of the sample films on the insulating glass substrate, carbon adhesive tape is also attached on the film surface and dinode, which could keep the electrical conductivity between sample film and dinode.

Observed Rb-L_3 XANES spectra are shown in Fig. 1 together with the reference spectrum of RbI. Significant difference between these spectra depending upon the grain size could be clearly seen. From the results, we could confirm that the local environment of Rb ions is sensitive to change in grain size of $(CsFAMA)Pb(IBr)_3$.

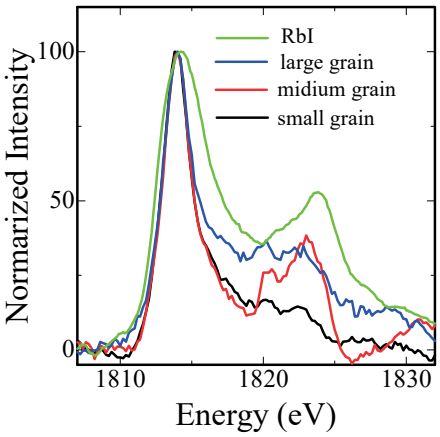


Fig. 1. Observed Rb-L_3 XANES spectra of RbI and $(RbCsFAMA)Pb(IBr)_3$.

[1] A. Kojima *et al*., J. Am. Chem. Soc. **131** (2009) 6050.
[2] S. Burger *et al*., J. Mater. Chem. A **6** (2018) 21785.

BL2A, BL5B

Luminescence Decay Curves of Inorganic Scintillators Excited with Soft X-ray Pulses under Single Bunch Operation Mode

K. Kawai[1], H. Zen[2], E. Nakamura[3], M. Kitaura[1], K. Kamada[4] and A. Ohnishi[1]
[1]*Faculty of Science, Yamagata University, Yamagata 990-8560, Japan*
[2]*Institute of Advanced Energy, Kyoto University, Uji 611-0011, Japan*
[3]*UVSOR Synchrotron Facility, Institute for Molecular Science, Okazaki 444-8585, Japan*
[4]*New Industry Creation Hatchery Center, Tohoku University, Sendai 980-8579, Japan*

The single bunch operation mode in UVSOR synchrotron facility is one of the advantages over other synchrotron facilities. This mode is characterized by the repetitive light pulses of sub-micro second. Users can carry out time-resolved spectroscopy experiment of solids, liquids, and gases. On the other hand, the beamlines used under the single bunch operation mode are not so many, so we have to develop experimental systems to explore unique time-resolved spectroscopy with vacuum ultraviolet (VUV) light and soft X-ray (SX). Actually, there are many proposals for the usage of VUV and SX photons in measurements of luminescence decay curves.

In order to respond such user's request, we tried to measure luminescence decay curves of typical inorganic scintillators at the BL2A and BL5B beamlines. The former and latter allow us to use photons in SX and VUV regions, respectively. The luminescence detection systems with a time correlated single photon counting were installed at the two beamlines. Here, we report the results of luminescence spectra and luminescence decay curves of Ce-doped $Gd_3Al_2Ga_3O_{12}$ (Ce:GAGG) and Mg-codoped Ce:GAGG scintillators, measured at 300 K under excitation with SX photons of 1.05 keV.

Figure 1 shows luminescence spectra of Ce:GAGG and Ce,Mg;GAGG scintillators. The intensities were normalized to unity at the maximum of Ce:GAGG. A prominent band is observed around 550 nm. This band has been assigned to Ce^{3+} 5d-4f transition [1]. The Ce^{3+} band is weakened by Mg codoping. Luminescence decay curves of the 550-nm band were shown in Fig. 2. The luminescence decay curves are composed of short- and long-lived components. The long-lived component appears as a pile-up component. This component is enhanced under host excitation with VUV and SX photons, compared to Ce^{3+} 4f-5d excitation with visible photons [2]. Since the luminescence intensity is given by time-integration of the decay curve, it should be clearly decreased by Mg-codoping. This situation can be seen in Fig. 1. The lifetime of the short-lived component also becomes shorter, and the pile-up component is weakened. These results are in agreement with those in Refs. 3.

Now, the BL2A and BL5B beamlines are ready to use SX and VUV light pulses under the single bunch operation mode. Especially, the research and development of scintillators, requiring high-energy light pulses, may be suitable. Users who want to use VUV and SX pulses are welcome to the use of these beamlines.

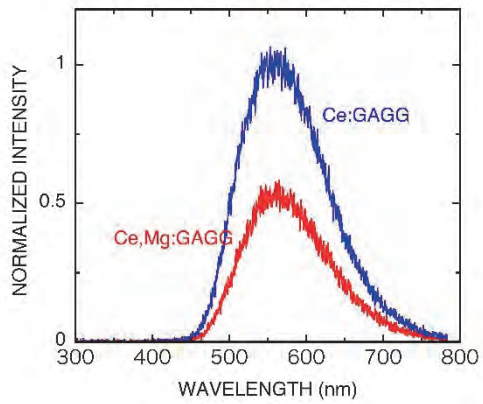


Fig. 1: Luminescence spectra of Ce:GAGG, and Ce,Mg:GAGG scintillators, measured at 300 K under excitation with SX photons of 1.05 keV.

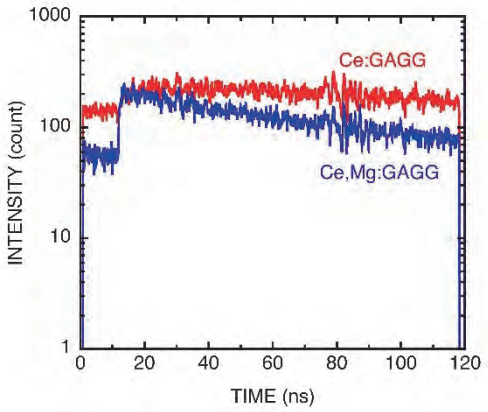


Fig. 2: Luminescence decay curves of Ce:GAGG, and Ce,Mg:GAGG scintillators, measured at 300 K under excitation with SX photons of 1.05 keV.

[1] M. Kitaura *et al.*, J. Appl. Phys. **113** (2014) 041906.
[2] M. Kitaura *et al.*, Opt. Mater. **41** (2015) 45.
[3] K. Kamada *et al.*, Opt. Mater. **41** (2015) 63.
[4] M. Kitaura *et al.*, Appl. Phys. Express **9** (2016) 072602.

BL3B

Intrinsic Luminescence from Self-trapped Excitons in $(Ca_{1-x}Na_x)_2(Mg_{1-2x}Al_{2x})Si_2O_7$ Single Crystals upon Vacuum UV Excitation

N. Kodama, T.Takahashi, T. Inoue and Y. Takahashi
Faculty of Engineering and Resource Science, Akita University, Akita 010-8502, Japan

Na- and Al-substituted melilite $(Ca_{1-x}Sr_x)_2MgSi_2O_7$ crystals are expected to exhibit incommensurate modulations similarly to Sr-substituted $(Ca_{1-x}Sr_x)_2MgSi_2O_7$ [1]. To date, little research has focused on the formation of self-trapped excitons (STEs) in terms of the dimensionality and modulation of the structure. We report intrinsic luminescence from STEs. In addition, we examine the correlation between the intensity and bandwidth of intrinsic luminescence and the two-dimensionality and structure modulation in $(Ca_{1-x}Na_x)_2(Mg_{1-2x}Al_{2x})Si_2O_7$ (x = 0.0, 0.05, 0.10, 0.25) crystals.

Absorption, luminescence, and excitation spectra of STEs in $(Ca_{1-x}Na_x)_2(Mg_{1-2x}Al_{2x})Si_2O_7$ (x = 0, 0.05, 0.10, 0.25) single crystals were measured in the temperature range of 5-293 K using the undulator beamline BL3B at the UVSOR facility. Under VUV excitation at 160 and 70 nm, intrinsic luminescence from STEs was observed in these crystals.

Figures 1(a)-1(d) show the luminescence spectra for $(Ca_{1-x}Na_x)_2(Mg_{1-2x}Al_{2x})Si_2O_7$ (x = 0.0, 0.05, 0.10, 0.25) excited at 160 nm in the 5-293 K range. The luminescence spectra of $(Ca_{1-x}Na_x)_2(Mg_{1-2x}Al_{2x})Si_2O_7$ with x = 0.0, 0.05, 0.10, and 0.25 consisted of two broad bands with peaks at 246-255 nm and 311-332 nm, associated with STE(I) and STE(II) in the 5-293 K range. The STE(I) and STE(II) luminescence intensities decreased rapidly with increasing temperature. With increasing x, the intensity of STE(I) passed through a maximum at the intermediate fraction x = 0.10. On the other hand, the intensity of STE(II) increased with increasing x. There are two plausible explanations for the dependence of luminescence intensities on the Na/Al fraction, x, involving (i) a two-dimensional effect or (ii) an incommensurate structural modulation effect.

The magnitude of two-dimensionality for $(Ca_{1-x}Na_x)_2(Mg_{1-2x}Al_{2x})Si_2O_7$ increased with increasing x due to the larger ionic radius involved in substituting Na^{2+}. Thus, the dependence of the STE(II) intensity on x can be explained in terms of a two-dimensional effect. On the other hand, the dependence of the STE(I) luminescence cannot be accounted for by two-dimensionality, because the maximum of the intensity varies with x. The other possible explanation is that the structural modulation effect of an incommensurate phase increases the number of local sites with larger distortion potentials. The formation of STEs and the luminescence intensity may be strongly affected by whether or not the crystals form a modulated structure (commensurate or incommensurate phase) and by the modulation amplitude. We found that the $(Ca_{1-x}Na_x)_2(Mg_{1-2x}Al_{2x})Si_2O_7$ crystal with x = 0.10 showed the most intense luminescence among the four compositions examined (x = 0.0, 0.05, 0.10, and 0.25). The Na- and Al-substituted $(Ca_{1-x}Sr_x)_2MgSi_2O_7$ crystals with Na fractions, x, ranging from 0.0 to 0.25 are expected to exhibit two-dimensional incommensurate modulations with a modulation vector along [110] and [$1\bar{1}0$], depending on the composition, similarly to Sr-substituted $(Ca_{1-x}Sr_x)_2MgSi_2O_7$ [1]. These structural changes with varying Na composition suggest that the intense luminescence at x = 0.10 is mainly due to a structural modulation effect. The Na composition dependence of the bandwidths of STE(I) and (II) suggests inhomogeneous broadening of the STE luminescence due to the random distributions of the Ca^{2+}/Na^{+} and Al^{3+}/Mg^{2+} sites; this distribution creates different environments for SiO_4 and AlO_4 tetrahedra than STE sites followed by incommensurate modulation.

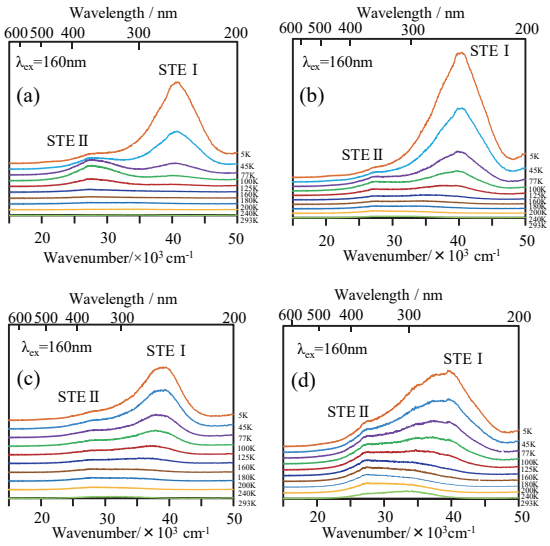


Fig. 1. Dependence of intrinsic luminescence on Na fraction, x, in $(Ca_{1-x}Na_x)_2(Mg_{1-2x}Al_{2x})Si_2O_7$: (a) x=0.0, (b) x=0.05, (c) x=0.10, and (d) x=0.25 under excitation at 160 nm in the temperature range 5-293 K.

[1] J.C. Jiand, M. Schosnig, A.K. Schapaer, K. Ganster, H. Ragaer and L. Toth, Phys. Chem. Minerals **26** (1998) 128.

BL3B, BL5B

Evaluation of Fluorescence Lifetimes of Scintillators for High-energy Particle Experiments

H. Ikeda, H. Oikawa, Y. Hiruma, M. Kitaura, A. Ohnishi, Y. Tajima and H.Y. Yoshida
Department of Physics, Yamagata University, Yamagata 990-8560, Japan

Recently, the operation of particle detectors at higher counting rates is required in a high-energy physics experiment. To satisfy this requirement, the scintillators used in a particle detector need to have a short fluorescence lifetime, which enables fast time response. For this purpose, we have measured fluorescence spectra and decay curves for plastic scintillators used in the J-PARC E14 KOTO experiment [1], commercially available recycled resin plates, and inorganic crystals. The fluorescence decay curves were measured by using light pulses from visible to vacuum ultraviolet under single bunch operation, which ensures a time-correlated single-photon counting method.

The top of Fig. 1 shows the decay curve of a plastic scintillator EJ-200 for the 430 nm band under excitation at 400 nm, and the bottom of Fig. 1 shows for the 420 nm band under excitation at 20 nm. They were measured at room temperature. The blue lines indicate experimental data. Lifetimes were analyzed by using the data analysis framework ROOT [2].

We assumed that the obtained decay curves are fitted with the formula

$$I(t) = \int_{-\infty}^{\infty} P(t')\theta(t'-T_0)G(t-t')\,dt' + B,$$

where

$$P(t) = \sum_{i=1}^{n} A_i \exp\left(-\frac{t}{\tau_i}\right), \qquad (n = 1, 2, 3 \text{ and } A_1 = 1)$$

and

$$G(t-t') = \sum_{i=1}^{m} C_i \exp\left(-\frac{(t-t'-\mu_i)^2}{2\sigma_i^2}\right). \qquad (m = 1, 2)$$

$I(t)$ represents the observed decay curve, and $P(t)$ represents the true fluorescence decay curve. If the true decay curve is composed of multiple components, it is described as the linear combination of exponential decay functions with the parameters of lifetime τ_i and initial intensity A_i. $\theta(t'-T_0)$ is a step function to decide the time origin T_0. $G(t-t')$ represents the resolution of the measurement system, the time structure of the beam, and so on, and is given by a single gaussian or a sum of two gaussians. B is a background constant that has a role in increasing a baseline. Red lines are the fitting curves which reproduce the experimental data.

We carried out the lifetime analysis for a plastic scintillator Scintilex [3] in the same method. The top of Fig. 2 shows the decay curve of Scintirex for the 436 nm band under excitation at 265 nm, and the bottom of Fig. 2 shows for the 430 nm band under excitation at 20 nm. The fitting curves reproduce the experimental data. The fluorescence lifetimes of EJ-200 and Scintirex, determined from our analysis, are summarized in Table 1.

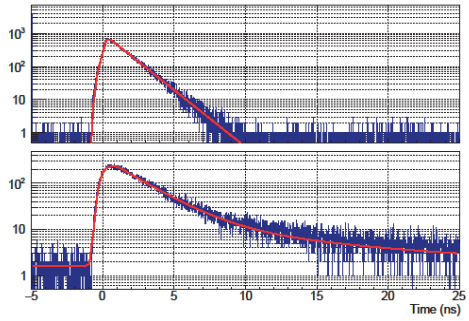


Fig. 1. Decay curve of EJ-200 measured at room temperature under excitation at 400 nm (top) and 20 nm (bottom). The former and latter are obtained for the 430 and 420 nm photoluminescence band.

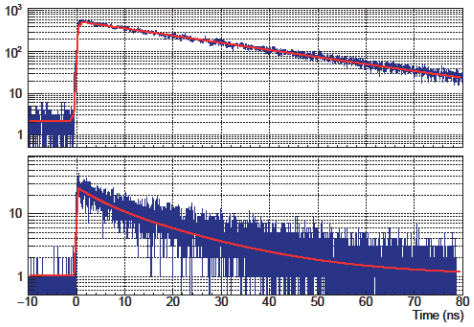


Fig. 2. Decay curve of Scintirex measured at room temperature under excitation at 265 nm (top) and 20 nm (bottom). The former and latter are obtained for the 436 and 430 nm photoluminescence band.

Table 1. Fluorescence lifetimes of EJ-200 and Scintirex, determined from our data analysis.

Sample	λ_{EX} [nm]	λ_{EM} [nm]	τ_1[ns] (Ratio)	τ_2[ns] (Ratio)
EJ-200	400	430	1.27±0.00	-
	20	420	2.25±0.00 (82.5 %)	10.56±0.22 (17.5 %)
Scintirex	265	436	24.79±0.08	-
	20	430	16.89±0.38 (83.3 %)	4.92±0.03 (16.7 %)

[1] J. Comfort *et al.*, Proposal for $K_L \to \pi^0\nu\bar{\nu}$ Experiment at J-PARC (2006).
[2] R. Brun and F. Rademakers, Nucl. Instrum. Methods Phys. Res. A **389** (1997) 81.
[3] H. Nakamura *et al.*, Europhys. Lett. **95** (2011) 22001.

BL3B

Thermoluminescence of Yttrium Aluminum Garnet (YAG) Crystals Grown by Core Heating Method and Micro-pulling Down Method

Y. Kurashima[1], S. Kurosawa[2], R. Murakami[3], A. Yamaji[1], K. Kamada[2,3], M. Yoshino[1], S. Tomida[2], H. Sato[2], Y. Yokota[2], Y. Ohashi[2] and A. Yoshikawa[1,2,3]

[1]*Institute for Materials Research, Tohoku University, Sendai 980-8577, Japan*
[2]*New Industry Creation Hatchery Center, Tohoku University, Sendai 980-8579, Japan*
[3]*C&A Corporation, Sendaii 980-0811, Japan*

Scintillators are used in medical imaging such as Positron Emission Tomography (PET). Gamma-ray stopping power is one of the important scintillation properties for the PET camera and other gamma-ray detectors. Gamma-ray stopping power is proportional to $(Z_{eff})^a$, where Z_{eff} denotes effective atomic number and a=4-5. Hf-based materials like Ce-doped $SrHfO_3$[1] are attractive scintillation materials with high gamma-ray stopping power due to high density and high effective atomic number.

However, Growth of such materials by the conventional melt-growth methods with crucibles like micro-pulling down (μ-PD) method[2] are hard technique, because the melting points of Hf-based materials are typically higher than softening and melting point of the crucibles. The softening and melting point of Ir, for instance, 2000 °C and 2447 °C, respectively, while the melting temperature of SrHfO3 is 2730 °C.

Thus, we have developed a novel crystal growth method to search novel materials with higher melting point than the melting point of the crucibles, and this method is named “Core Heating (CH) method” using electric arc or other heat source. Since, the scintillation properties of crystals grown by the CH method have not been evaluated yet, and we need to confirm the feasibility of CH method as a material search method.

To compare the growth method, we compared the scintillation properties for $(Y_{0.99}Ce_{0.01})_3Al_5O_{12}$ (Ce:YAG), because the melting point of Ce:YAG is 1940 °C and the conventional melt-growth is available. Ce:YAG crystals were grown by the CH and μ-PD method.. The samples grown by CH method (CH sample) and μ-PD method (μ-PD sample) were cut and polished. If the scintillation and optical properties for CH samples are similar to those for the μ-PD sample, the CH method is judged to be a useful technique as a material search method.

We found some optical and scintillation properties such as emission wavelength, transmittance, light output excited by gamma-ray for the CH sample were the same level as those for μ-PD sample. Here, the detail of the results is reported in other papers. However, only scintillation decay time of the CH sample was different from that of the μ-PD sample. This result indicated that the CH sample has different trap sites, defects from the μ-PD sample. Therefore, we measured thermoluminescence (TL) spectra and TL glow curve to compare the trap sites. Measurement of TL spectra and TL glow curves were performed at the beam line BL3B of UVSOR facility. The sample was irradiated with 165-nm photons for 10 min at 7 K. After we check no after-glow emission with a charge-coupled device (CCD, Roper Scientific, SPEC-10) attached to a polychromator (Acton Research Corporation, spectrapro-300i), the sample was heated up to 300 K with a heat rate of approximately 4 K/min. During the heating, the TL emission spectra were observed with the CCD.

Figure 1 shows TL glow curves of CH and μ-PD samples. The results of TL glow curves indicated no differences of number of traps and their depths were observed clearly between the CH and μ-PD samples. Therefore, such we found such trap sites are not the factor to change the decays.

In this time, the TL glow curves up to 300 K was measured, and we observed relatively shallow traps. On the other hand, deep traps observing the glow curves over 300 K might be related to be the decay-time deference, or other defects are also the candidates to make the decay time slower. As future works, we evaluate and discuss such factors.

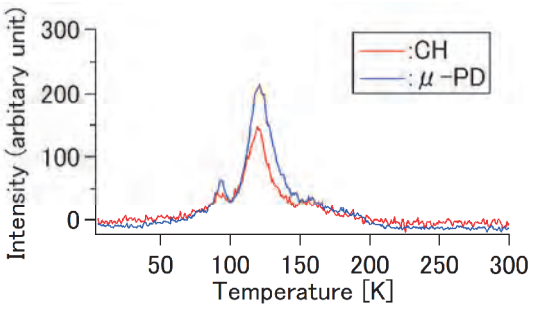


Fig. 1. TL glow curves of CH sample and μ-PD sample.

[1] S. Kurosawa, J. Pejchal, S. Wakahara, Y. Yokota and A. Yoshikawa, Radiat. Meas. **56** (2013) 155.
[2] A. Yoshikawa, M. Nikl, G. Boulon and T. Fukuda, Opt. Mater. (Amst). **30** (2007) 6.

BL3B

Optical Properties of a $Ce_2Si_2O_7$ Single Crystal Using BL3B of the UVSOR Facility

T. Horiai[1], S. Kurosawa[2], A. Yamaji[1], S. Kodama[1], S. Yamato[1], Y. Kurashima[1], M. Yoshino[1], S. Toyoda[2], H. Sato[2], Y. Ohashi[2], K. Kamada[2,3], Y. Yokota[2] and A. Yoshikawa[1,2,3]

[1]*Institute for Materials Research, Tohoku University, Sendai 980-8577, Japan*
[2]*New Industry Creation Hatchery Center, Tohoku University, Sendai 980-8579, Japan*
[3]*C&A Corporation, Sendai 980-0811 Japan*

Scintillators convert energy of ionizing radiation into ultra-violet or visible light. When combined with suitable photodetectors such as a photomultiplier tube (PMT), scintillators are used in radiation detectors. Recently, Ce-doped pyrosilicate type crystals, Ce:$RE_2Si_2O_7$ (RE = rare-earth), have been studied, and Ce-doped $(Gd,La)_2Si_2O_7$ (Ce:La-GPS) has been reported to have a high light yield (~42,000 photons/MeV), relatively short decay time (~63 ns), good energy resolution (~5.0 %, 662 keV, FWHM) and shows a good temperature stability of light output up to 150 ºC [1-3].

$Ce_2Si_2O_7$ nanocrystals and films were found that the emission peaks were located around 358 nm, which well matches the wavelength sensitivity of a typical PMT [4-6]. In addition, the internal quantum efficiency of the $Ce_2Si_2O_7$ was determined to be approximately 37 % at room temperature. Therefore, the $Ce_2Si_2O_7$ is also expected to have good scintillation properties. Thus, in this study, we tried to grow a relatively large mm-scale $Ce_2Si_2O_7$ single crystal, and estimated the optical properties.

We prepared the $Ce_2Si_2O_7$ single crystal using micro-pulling-down method. As starting materials, we used CeO_2 and SiO_2 powders the purities of which were at least 99.99 %. After cutting and mirror polishing the sample to thickness of 1 mm, we measured the photoluminescence spectra with a spectrometer (FLS920, Edinburgh Instruments) consisting of a Xe lamp at room temperature. Moreover, the emission and excitation spectra at 7 K were measured using excitation photons at BL3B of UVSOR, and evaluated the optical properties independent of the lattice vibration. The sample was cooled down to 7 K with liquid helium.

Figure 1 shows the emission and excitation spectra of the $Ce_2Si_2O_7$ at room temperature and 7 K. The emission spectrum of the $Ce_2Si_2O_7$ at room temperature has a single peak around 380 nm, while the emission spectrum at 7 K has double peak of $5d_1$-$^2F_{5/2}$ (358 nm) and $5d_1$-$^2F_{7/2}$ (387 nm). The emission peak around 358 nm consisted with the result measured by Choi in Ref. 4. From the results of emission and excitation spectra of the $Ce_2Si_2O_7$ at room temperature and 7 K, the emission peak of $5d_1$-$^2F_{5/2}$ at room temperature was quenched by the self-absorption. Comparison with the emission spectrum of Ce-doped $La_2Si_2O_7$, which has the same space group as $Ce_2Si_2O_7$ (monoclinic, $P2_1/c$) in the previous study, the emission peak of $Ce_2Si_2O_7$ is shifted to longer wavelength [7]. Here, comparing the ionic radii of Ce^{3+} and La^{3+} in the eight-coordinate sites, the ionic radii are 1.143 and 1.160 Å, respectively [8]. Therefore, it was attributed to the stronger crystal field in $Ce_2Si_2O_7$ than in $La_2Si_2O_7$.

The Ce^{3+} 4f-$5d_x$ (x=1-5) transition peaks were observed in the excitation spectrum of the $Ce_2Si_2O_7$ at 7 K. The excitation peaks from 4f-$5d_1$, -$5d_2$, -$5d_3$, -$5d_4$ and -$5d_5$ were positioned around 327, 292, 273, 254 and 228 nm, respectively. In addition, the excitation peak around 170 nm was observed, and determined to be the host excitation band peaking.

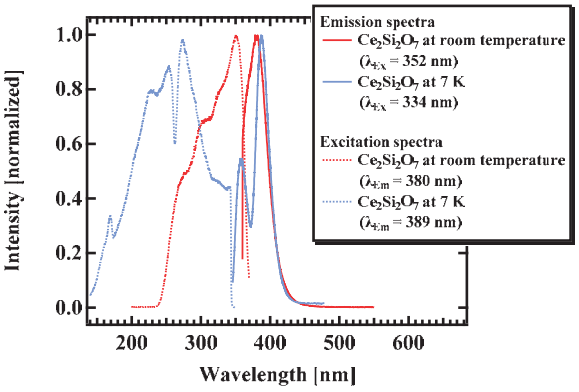


Fig. 1. Emission and excitation spectra of the $Ce_2Si_2O_7$ single crystal at room temperature and 7 K.

[1] A. Suzuki, S. Kurosawa, A. Yoshikawa *et al.*, Appl. Phys. Express **5** (2012) 102601.
[2] A. Yoshikawa, S. Kurosawa *et al.*, Cryst. Growth Des. **15** (2015) 1642.
[3] S. Kurosawa, A. Yoshikawa *et al.*, Nucl. Instruments Methods Phys. Res. Sect. A **772** (2015) 72.
[4] W.C. Choi *et al.*, Appl. Phys. Lett. **75** (1999) 2389.
[5] L. Li *et al.*, Sci. Rep. **5** (2015) 1.
[6] L. Kępiński *et al.*, J. Alloys Compd. **341** (2002) 203.
[7] Q. Wei *et al.*, Materials Letters **126** (2014) 178.
[8] R.D. Shannon, Acta. Cryst. A**32** (1976) 751.

BL3B

Low-temperature Photoluminescence Properties of Rb_2HfI_6

S. Kodama[1], S. Kurosawa[2], A. Yamaji[1], M. Yoshino[1], S. Toyoda[2], H. Sato[2], Y. Ohashi[1], K. Kamada[2,3], Y. Yokota[2] and A. Yoshikawa[1,2,3]

[1]*Institute for Materials Research, Tohoku University, Sendai 980-8577, Japan*
[2]*New Industry Creation Hatchery Center, Tohoku University, Sendai 980-8579, Japan*
[3]*C&A Corporation, Sendai 980-0811 Japan*

Rb_2HfI_6 has been developed as a novel red-emitting scintillator as a K_2PtCl_6-type compound [1]. By substituting Rb into Cs, the scintillation emission peak of Rb_2HfI_6 shifted towards longer wavelength than Cs_2Hf_6, and reached ~725 nm. Rb_2HfI_6 has a scintillation light output of ~40,000 photons/MeV, and such red-emission scintillator with a high light output can be used for a remote scintillation detector coupled with an optical fiber [2]. The mechanism of shift of emission wavelength has been still unclear, thus we evaluated the fundamental photoluminescence properties of Rb_2HfI_6. We measured the low-temperature photoluminescence excitation (PLE) and emission (PL) spectra in order to determine the fundamental luminescence properties of Rb_2HfI_6.

A single-crystalline Rb_2HfI_6 specimen was synthesized by the vertical Bridgman growth method in our laboratory from 99 %-pure HfI_4 and 99.9 %-pure RbI powders. We measured the PLE-PL spectra at 8 K in BL3B. As photo-detectors for PLE measurement, photo-multiplier tubes (PMTs) (Hamamatsu K.K.) of R4220 and R636-10 were used for a blue-green and red region, respectively.

Figures 1 (a) and (b) illustrate the PL and PLE spectra at 8 K, respectively. The excitation and emission wavelengths were indicated as λ_{ex} and λ_{em}, respectively. Rb_2HfI_6 had three PLE-PL bands as follows: the blue band (λ_{ex}: 215 nm and λ_{em}: 440 nm), green band (λ_{ex}: 335 nm and λ_{em}: 590 nm) and red band (λ_{ex}: 455 nm and λ_{em}: 725 nm). The green and red bands were reported also in the case of Cs_2HfI_6 at 8 K [3], and in addition, Rb_2HfI_6 was identified to have the blue band whose λ_{ex} and λ_{em} were similar to the room temperature emission of Rb_2HfCl_6 [4]. The green band had a highest intensity, approximately 3 times higher than the red band, while only red-band emission was observed in the X-ray radioluminescence spectra at room temperature [1]. Although all emission bands had broad and single peaked spectra, PLE spectra of three bands had several excitation peaks, for example, ~180 nm and ~260 nm for blue band, ~335 nm and ~400 nm for green band. For the red band, an intense excitation peak was confirmed at ~455 nm, additionally a small peak at ~520 nm was also observed.

The splitting of the room temperature emission at low temperature was reported in the self-trapped exciton (STE) luminescence of CsI [5]. We confirmed that Rb_2HfI_6 had three photoluminescence bands at 8 K while the room temperature emission was the single band. Thus, the obtained results in this study implies that the emission origin of Rb_2HfI_6 was passively the STE. For future works, the temperature dependence of each PLE-PL band should be studied to determine the emission mechanism.

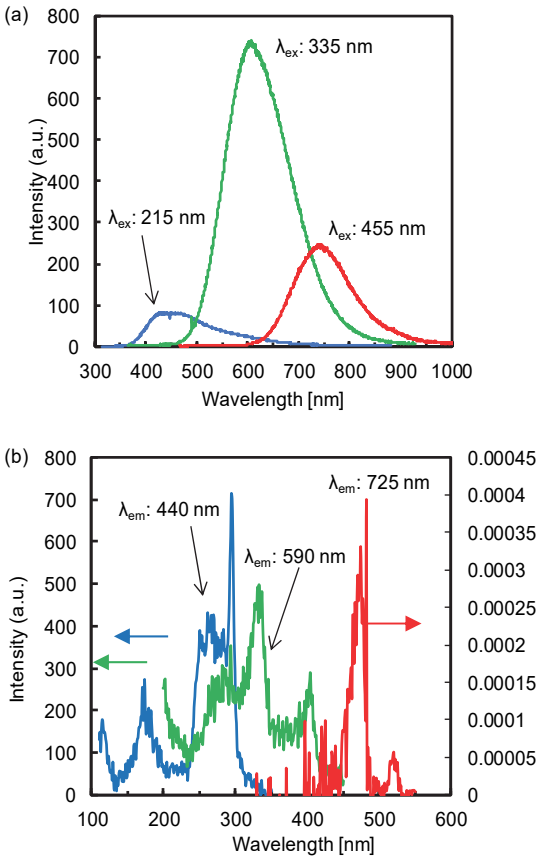


Fig. 1 (a) PL and (b) PLE spectra of Rb_2HfI_6 at 8 K. The PMTs of PLE spectra measurement of the red band (λ_{em} = 725 nm) were R636-10, and others were R4220.

[1] S. Kodama *et al.*, IEEE Trans. Nucl. Sci. (2020) in print.
[2] S. Kodama *et al.*, Appl. Phys. Express **13** (2020) 047002.
[3] S. Kodama *et al.*, UVSOR Activity Report 2018 **46** (2019) 62.
[4] K. Saeki *et al.*, J. J. Appl. Phyis. **55** (2016) 110311.
[5] H. Nishimura *et al.*, Phys. Rev. B **51** (1995) 2167.

BL3B

Temperature Dependence of PL Spectra of *p*-terphenyl at 6-300 K

S. Yamato[1], S. Kurosawa[2], A. Yamaji[1], M. Yoshino[1], H. Sato[2], Y. Ohashi[2], K. Kamada[2,3], Y. Yokota[2] and A. Yoshikawa[1,2,3]

[1]*Institute for Materials Research (IMR), Tohoku University, Sendai 980-8577, Japan*

[2]*New Industry Creation Hatchery Center (NICHe), Tohoku University, Sendai 980-8579, Japan*

[3]*C&A Corporation, Sendai 980-0811, Japan.*

Neutron detectors can be used in several fields such as neutron diffraction for crystal structure, fusion physics [1,2]. Here, nuclear fusion technology is expected as next effective energy generation technology. In fusion reactors, neutrons are emitted from nuclear fusion reactions, and the monitoring these particles is a important technology to control fusion reactors and generate energy effectively.

Among several nuclei, the neutron cross section of hydrogen nucleus is the largest in higher energy range. ^{1}H has relatively higher cross section for the fast neutron than other materials. We focused on organic scintillators which contains many ^{1}H and have low detection efficiency for gamma rays as background noise.

Although the neutron detectors in fusion reactors can be exposed on higher temperature than 373 K, conventional organic scintillators cannot be used at high temperature. Plastic scintillators melt at around 343 K. Liquids evaporate at high temperature and are difficult to handle. Even crystals, only low-melting-point materials were developed. As a first step, we aimed to develop the organic scintillation crystals for such applications at over 373 K.

We grew the pure *p*-terphenyl crystal by the self-seeding vertical Bridgman method using an enclosed chamber [3]. Pulling down rate for growth was ~1 mm/h. The melting point of *p*-terphenyl is 485 K.

We measured the photoluminescence (PL) emission spectra of the samples under 13-300 K at the beamline BL3B of UVSOR Synchrotron Facility. The excitation and emission spectra of *p*-terphenyl are shown in Fig. 1 and Fig. 2, respectively. The excitation spectra were recorded with a cut filter for the shorter wavelength than 370 nm. The emission spectra were recorded for the *p*-terphenyl crystal excited by 280 nm photons.

In Fig. 1, absorption edge around 340 – 360 nm has been monotonically shifted to the lower energy side as the temperature rose, and the emission peaks of 375 and 390 nm were observed for *p*-terphenyl at 300 K (Fig. 2). The shapes of the spectra for *p*-terphenyl changed significantly between 300 K and others (200 K and less than 200 K), and relatively sharp peaks around 350 nm were observed at except 300 K. This is because of structural phase transition at 193.5 K by twisting in a molecule [4,5].

As future works, we study on the relationship between these results and temperature dependence of photo-luminesce decay time.

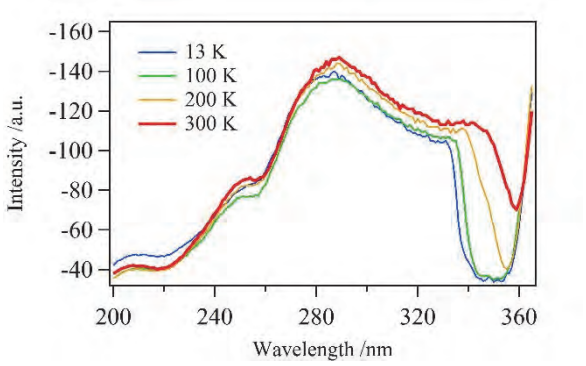


Fig. 1. Excitation spectra of *p*-terphenyl crystal at 13-300 K.

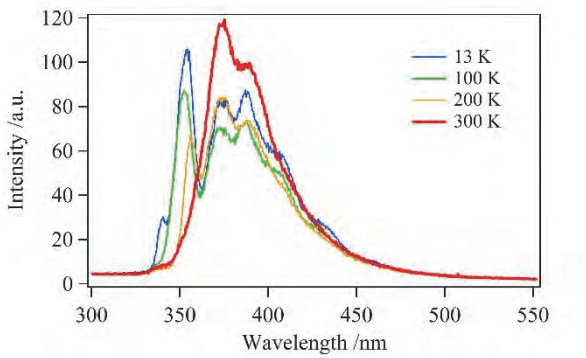


Fig. 2. Emission spectra of *p*-terphenyl crystal excited by 280 nm photons at 13-300 K.

[1] H. K. Lee *et al.*, J. Supercond. Novel Magn. **31** (2018) 1677.
[2] Y. K. Kim *et al.*, J. instrum. **7** (2012) C06013.
[3] A. Arulchakkaravarthi *et al.*, J. Crystal Growth **234** (2002) 159.
[4] Y. Yamamura *et al.*, J. Phys. Condens. Matter **10 15** (1998) 3359.
[5] Hervé Cailleau *et al.*, Faraday Discuss. Chem. Soc. **69** (1980) 7.

BL3B

Composition Dependence of 4*f*-4*f* Emission Spectra in Pr:$SrZr_{1-x}Ti_xO_3$

M. Yoshino, T. Kuyama and J. Sugiyama
Graduate School of Engineering, Nagoya University, Nagoya 464-8603, Japan

In this study, the excitation spectra and emission spectra of Pr^{3+} in $SrZr_{1-x}Ti_xO_3$ crystal have been measured and changes in the spectra with composition and temperature are examined.

The excitation spectra in $x = 0.6$ sample are shown in Fig. 1. The rising energy in excitation spectra is close to the band gap energy estimated from diffuse reflectance spectra. This is also the case in other composition. In order to excite host oxides, higher energies than band gap are selected for excitation. Fig. 2 shows the emission spectrum in $x = 0.6$ sample at 350 nm excitation. The sharp peaks around 500 nm (Greenish-blue) and 600-650 nm (Red) originate from 4*f*-4*f* transitions of Pr^{3+}. The intensity ratios R/(R+G) of Red emission (R) to sum of Red and Greenish-blue emission (G) in Pr:$SrZr_{1-x}Ti_xO_3$ are shown in Fig. 3. It is found that the ratios are large in the intermediate composition. As shown in Fig. 4 and Fig. 5, changes in the intensities of emission in $x = 0.6$ with temperature are different between excitation energy. Thermally activated process is included in 280 nm excitation.

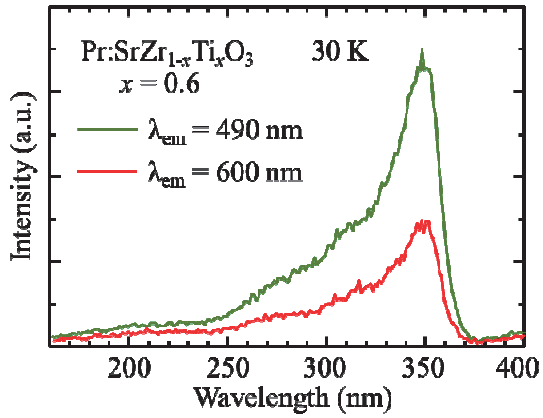


Fig. 1. Excitation spectra of Pr:$SrZr_{0.4}Ti_{0.6}O_3$ (30 K).

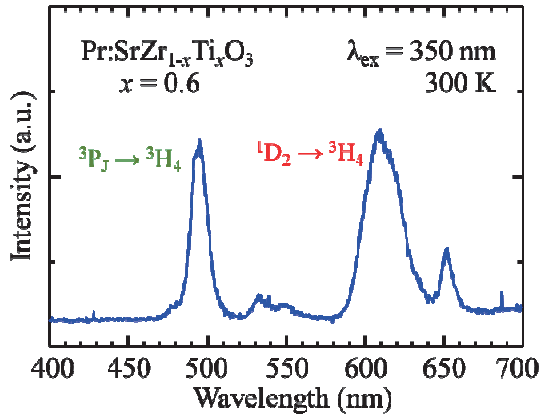


Fig. 2. Emission spectrum of Pr:$SrZr_{0.4}Ti_{0.6}O_3$ (λ_{em} = 350 nm, 300 K).

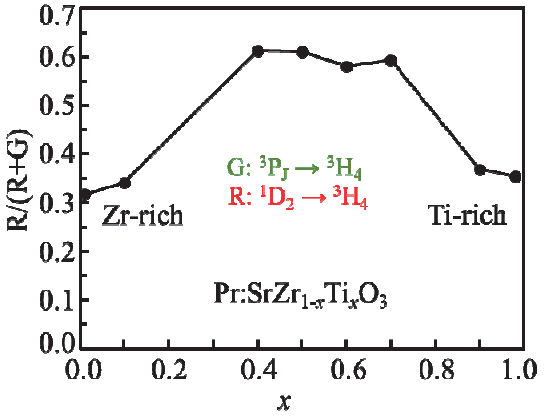


Fig. 3. The intensity ratios R/(R+G) of Red emission (R) to sum of Red and Greenish-blue emission (G) in Pr:$SrZr_{1-x}Ti_xO_3$ (300 K).

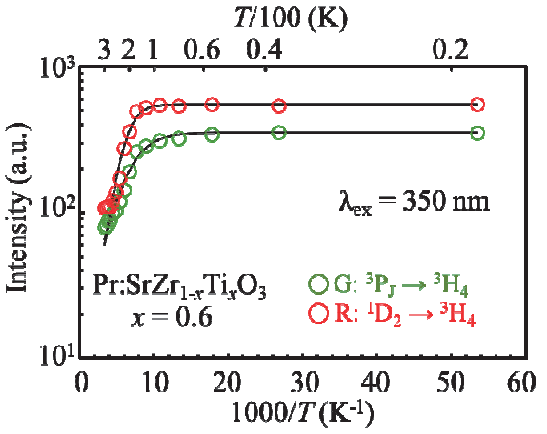


Fig. 4. Change in the intensities of Red emission and Greenish blue emission with temperature in Pr:$SrZr_{0.4}Ti_{0.6}O_3$ (λ_{em} = 350 nm).

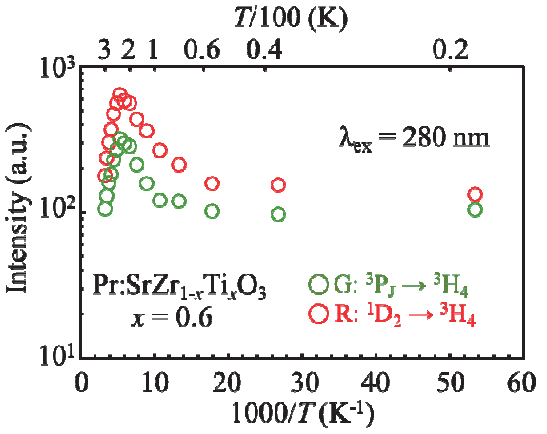


Fig. 5. Change in the intensities of Red emission and Greenish blue emission with temperature in Pr:$SrZr_{0.4}Ti_{0.6}O_3$ (λ_{em} = 280 nm).

BL3B

Excitation Process of Ce^{3+} Ions in La Doped $Gd_2Si_2O_7$ Crystals Caused by VUV Photons

R. Tarukawa[1], M. Kitaura[1], S. Kurosawa[2], T. Makino[3] and A. Ohnishi[1]
[1]*Faculty of Science, Yamagata University, Yamagata 990-8560, Japan*
[2]*New Industry Creation Hatchery Center, Tohoku University, Sendai 980-8579, Japan*
[3]*Department of Electrical and Electronics Engineering, University of Fukui, Fukui 910-8507, Japan*

Multiplication of electronic excitations (MEEs) in wide-gap oxides takes place when the energy of excitation photon exceeds several times of the band-gap energy. The fundamental process of MEEs is based on inelastic scattering of valence electrons with hot photoelectrons. On the other hand, the excitation process of luminescent ions doped in wide-gap oxides by vacuum ultraviolet (VUV) photons is complex, because a number of relaxation processes compete under excitation [1]. Studies on such VUV excitation processes of luminescent ions give us complementary information on impact excitation of luminescent ions by hot carriers, which is important in both sides of fundamental and applied physics.

Ce-doped and La-admixed gadolinium pyrosilicate ($(La,Gd)_2Si_2O_7$:Ce, La-GPS:Ce) is known as an inorganic scintillator. Luminescence properties of La-GPS:Ce crystals have been investigated under excitation with VUV photons [2]. However, the process of MEEs in La-GPS has not yet been cleared. Furthermore, the excitation of Ce^{3+} ions by VUV photons still remains unknown.

In the present study, we have measured emission and excitation spectra of an undoped La-GPS and La-GPS:Ce crystals at 10 K. Experiment was performed at the BL3B beamline of UVSOR in the Institute for Molecular Science (IMS). The emission spectrum of an undoped La-GPS crystal exhibited an emission band peaking at 316 nm. This band is assigned to Gd^{3+} 4f-4f transition. The excitation spectrum for the 316 nm band is shown in Fig. 1 (a). In the region below 7.5 eV, one can see sharp peaks due to Gd^{3+} 4f-4f transitions. The stepwise structures are found around 14 and 20 eV. The bad-gap energy was reported to be 6.6-6.8 eV. The former and latter are close to twice and treble of the band-gap energy, respectively. The fundamental process of MEEs in wide-gap oxides has to satisfy the conservation laws of energy and momentum. When hot photoelectrons and photoholes are created by VUV photons, the threshold energy for MEEs exceeds the twice of the band-gap energy [1]. Especially, it is expected that the threshold energy reaches the treble of the band-gap energy for La-GPS with the wide valence band. It is, therefore, likely that the MEEs in La-GPS occurs in the region above 20 eV.

The excitation spectrum of a La-GPS:Ce crystal showed an emission band at around 393 nm at 10 K. This band is assigned to the Ce^{3+} 5d-4f transition. The excitation spectrum for the 393 nm band is shown in Fig. 1 (b). In the region below 7.5 eV, one can see broad bands due to Ce^{3+} 4f-5d transitions. No sharp peaks are found in Fig. 1(b). This fact suggests the $Gd^{3+}\rightarrow Ce^{3+}$ energy transfer does not occur in La-GPS:Ce, and is contrast with $Gd_3Al_2Ga_3O_{12}$:Ce (GAGG:Ce) [3]. In the region above 7.5 eV, the excitation spectra in Figs. 1(a) and 1(b) are almost the same with each other. This fact explains as follows. Hot photoelectrons and photoholes created by VUV photons relax into the conduction band minimum and valence band maximum, respectively. They are immediately captured by Ce^{3+} ions, and form the excited state of Ce^{3+} ions. Consequently, it is reasonable that the excitation spectrum for the 393 nm band reflects that for the 316 nm band.

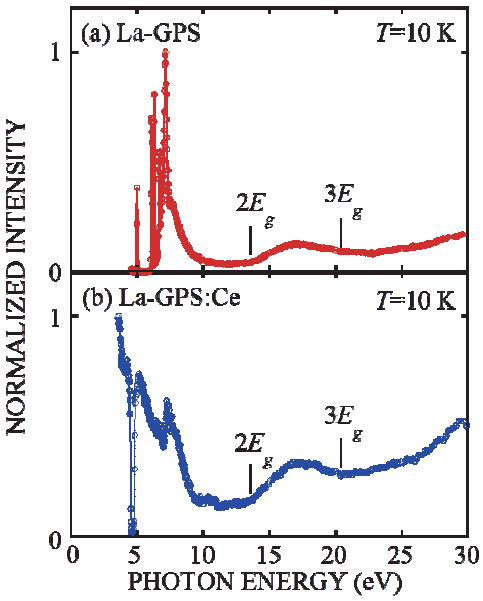


Fig. 1. (a): Excitation spectrum for the 316 nm band of an undoped La-GPS crystal. (b): Excitation spectrum for the 393 nm band of a La-GPS:Ce crystal. These spectra were measured at 10 K.

[1] M. Kitaura *et al.*, J. Lumin. **172** (2016) 243.
[2] M. Koshimizu *et al.*, J. Rare Earths **34** (2016) 782.
[3] M. Kitaura *et al.*, J. Appl. Phys. **115** (2014) 083517.

BL3B

Dynamical Behaviors of the Localized Exciton in NaCl:I⁻ Crystals

T. Kawai

Graduate School of Science, Osaka Prefecture University, Sakai 599-8531, Japan

When alkali chloride crystals are doped with heavier hetero-halogen ions, the absorption bands due to the heavier hetero-halogen ions are observed in the lower energy region than the fundamental absorption edge of the host crystals. The photo-excitation on the absorption bands induces various kinds of relaxed excitons localized to the heavier hetero-halogen ions and the luminescence bands called BG, B, UV, and NE are observed [1-3]. Though the BG, B, UV, and NE luminescence bands are observed in many alkali chloride crystals doped with heavier hetero-halogen ions, NaCl:I⁻ crystals exhibit only the NE luminescence band in the wide temperature range from a low temperature to room temperature. The NE luminescence is attributed to the radiative transition from the relaxed excited states of the one-center-type relaxed exciton, which consists of a hole localized on a hetero-halogen anion and a bound electron. We have investigated the dynamical behaviors of the one-center-type relaxed exciton in the NaCl:I⁻ crystals at the BL3B line of UVSOR.

In the NaCl:I⁻ crystals, the absorption band due to the localized exciton and the NE luminescence are observed around 6.95 and 5.7 eV, respectively, as shown in Fig. 1. Figure 2 shows the temporal profiles of the NE luminescence under various excitation energies around the absorption band. Under the excitation near peak energy of the absorption band, the NE luminescence exhibits the almost single exponential decay profile. On the other hand, it seems that there are two exponential components under the excitation at the off-peak energy of the absorption band. The decay time constants of the fast and slow components are about 2.6 ns and 120 ns, respectively. The decay time constant of 2.6 ns is almost equal to that of the fast component of the intrinsic type I self-trapped exciton (STE) luminescence in pure NaCl crystals [4]. The intrinsic type I STE exhibits the broad luminescence band around 5.2 eV and the luminescence overlaps with the NE luminescence band.

The exciting light with the off-peak energy penetrates deeper into the crystal than that with the peak energy of the absorption band. Thus, the excitation at the off-peak energy of the absorption band would create the one-center-type relaxed exciton inside the crystals. Then, the intrinsic type I STE may be formed from the one-center-type relaxed exciton. Further studies will probably be necessary.

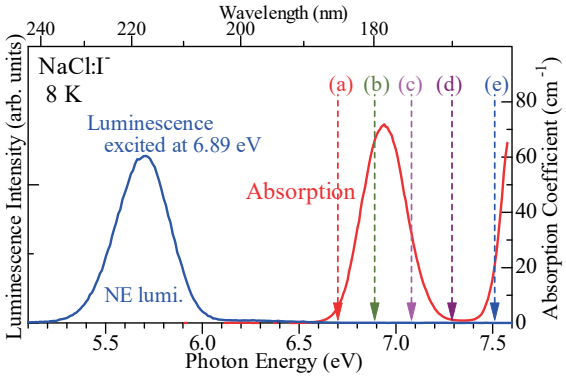


Fig. 1. Luminescence and absorption spectra of NaCl:I⁻ crystals at 8 K.

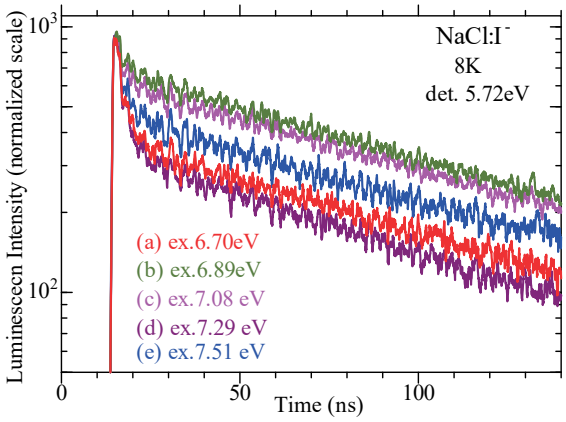


Fig. 2. Temporal profiles of the NE Luminescence under various excitation energies around the absorption band at 8 K. The excitation energies are shown by the down arrows in Fig. 1.

[1] T. Higashimura *et al.*, J. Phys. Soc. Jpn. **53** (1984) 1878.
[2] K. Kan'no *et al.*, J. Phys. Soc. Jpn. **55** (1986) 2443.
[3] I. Akimoto *et al.*, Phys. Status Solidi C **6** (2009) 342.
[4] T. Matsumoto *et al.*, J. Phys. Soc. Jpn. **61** (1992) 4229.

BL3B

VUV Spectroscopy of Magnesium Oxide Treated with Hydrogen Reduction

E. Kobayashi[1], K. K. Okudaira[2], M. Imamura[3], K. K. Bando[3], H. Kakiuchida[3], S. Yoshioka[4] and O. Takahashi[5]

[1]*Kyushu Synchrotron Light Research Center, Tosu 841-0005, Japan*
[2]*Chiba University, Chiba, Chiba 263-8522, Japan*
[3]*National Institute of Advanced Industrial Science and Technology, Tsukuba 305-8565, Japan*
[4]*Graduate School of Engineering, Kyushu University, Fukuoka 819-0395 Japan*
[5] *Graduate School of Science, Hiroshima University, Higashi-Hiroshima 739-8526, Japan*

Magnesium oxide (MgO) is a typical wide electronic band gap insulator and is used in devices such as optical, electrical and catalytic. Characteristics such as light transmission and thermal insulation are greatly affected by defects generated in the production process of crystals and thin films and practical materials. In compounds such as oxide, various types of defects such as point, line and planar defects exist, and the electronic state derived from the defect causes electrical, optical, or magnetic functions. For this reason, many point defects of metal oxides have been studied. MgO defects are generated by methods such as X-ray irradiation [1], UV irradiation [2], neutron scattering [3], electron beam irradiation [4,5], and heat treatment [6,7].

This study focused on magnesium oxide heated in a hydrogen atmosphere and the correlation between the amount of defects and optical properties was investigated using UV absorption spectroscopy. In addition, the plane orientation dependence of the MgO crystal was investigated.

The MgO (100) and MgO (111) were annealed at several temperatures at 473 K ~1173 K in a hydrogen atmosphere for 4 hours. The samples were gradually cooled to room temperature, exposed to the air, then introduced into a vacuum apparatus, and the spectrum was measured. UV spectra of MgO single crystal were measured at the BL3B of UVSOR in the Institute of Molecular Science.

Figure 1 shows UV spectra of MgO(100) and MgO(111). A distinct increase in absorption from 5.6 eV to 7.0 eV in MgO(100) was observed for the treated under hydrogen, compared to an untreated one. This result indicated that a new electronic state was formed in the conduction band due to the oxygen defect produced by the hydrogen reduction treatment, which made the band gap narrower. On the other hand, a decrease in absorption in MgO(111) was observed for the treated under hydrogen. This suggests that the interaction with hydrogen depends on the crystal plane. The spectrum changes because MgO (111) is an unstable polar surface, whereas MgO (100) is electrically neutral. The exact cause has been investigated using other techniques.

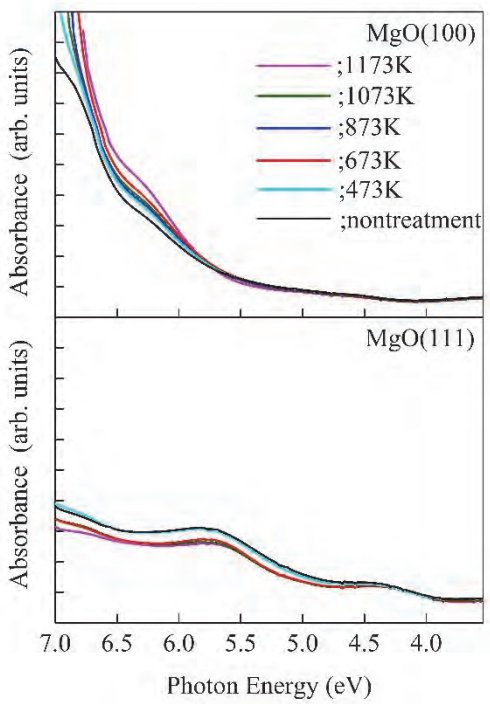


Fig. 1. UV spectra of MgO single crystal.

[1] J. P. Molnar *et al*., Phys. Rev. **79** (1950) 1015.
[2] Y. Chen *et al.*, Phys. Rev. **182** (1968) 960.
[3] H. R. Day, Phys. Rev. **91** (1953) 822.
[4] V. E. Henrich *et al*., Phys. Rev. B **22** (1980) 4764.
[5] P. R. Underhill *et al*., Solid State Commun. **43** (1982) 9.
[6] M. Wu *et al*., Phys. Rev. B **19** (1992) 12688.
[7] L. A. Kappers *et al*., Phys. Rev. B **1** (1970) 4151.

BL3B

Luminescence Characteristics of Cs_2BaCl_4

K. Takahashi[1], M. Koshimizu[1], Y. Fujimoto[1], T. Yanagida[2] and K. Asai[1]

[1]*Department of Applied Chemistry, Graduate School of Engineering, Tohoku University, Sendai 980-8579, Japan*

[2]*Division of Materials Science, Nara Institute of Science and Technology, Ikoma 630-0192, Japan*

Auger-free luminescence (AFL) is caused by the radiative transition of an valence electron to a core hole state. The transition is competitive with the Auger process, which is a much faster process, efficient AFL cannot be observed in many compounds. In other words, efficient AFL has been observed in limited compounds such as alkaline- or alkaline-earth fluorides or CsCl-based compounds.

AFL has been applied to fast scintillators owing to its fast decay. A representative one is BaF_2; however, CsCl-based compounds have an advantage of long emission wavelength appropriate for detection with a photomultiplier tube. Thus far, we have developed fast scintillators based on ternary CsCl-based compounds [1,2]. In this study, we developed fast scintillators based on Cs_2BaCl_4.

Crystal samples of Cs_2BaCl_4 were fabricated using a self-seeding solidification method and the Bridgman method. Powders of CsCl (99.99 %, Mitsuwa Chemical Co. Ltd., Japan) and $BaCl_2$ (99.9 %, Kojundo Chemical Laboratory Co Ltd., Japan) were mixed in a stoichiometric ratio. The mixed powders were poured into quartz ampoules and heated at 350 °C in vacuum for 1 day to remove adsorbed water. For the self-seeding solidification method, the quartz ampoule was set in a tubular furnace, and the furnace was heated to 950 °C for 12 h and subsequently cooled to room temperature over 72 h. For the Bridgman method, the ampoule was set in a Bridgman furnace. The temperatures of the upper and lower heaters in the furnace were set at 950 °C and 750 °C, respectively, during crystal growth, and the ampoules were lowered at a rate of 1.5 mm/h.

The luminescence properties were characterized with vacuum ultraviolet (VUV) light as an excitation source. Measurements were performed at BL7B for the steady state spectra and at BL3B for temporal profiles at the UVSOR Synchrotron Facility at the Institute for Molecular Science, Japan. Synchrotron radiation being monochromatized with a 3-m normal-incidence monochromator was used for the excitation. The luminescence spectra were measured at different excitation wavelengths, and the excitation spectra were obtained from the luminescence spectra. The luminescence temporal profiles were observed using a time-correlated single photon counting method. The single-bunch operation mode was used, and the period between successive pulses was 176 ns.

Figure 1 shows the luminescence spectra with VUV excitation at 150 nm, 180 nm, and 84 nm. For the excitation at 150 nm and 180 nm, the bands at 430 nm and 480 nm were observed, respectively. For the excitation at 84 nm which corresponds to the excitation for the outermost core level of Cs, broad band at 450 nm was observed, but clear bands at 250–320 nm, which corresponds to the expected AFL wavelength, was not observed. Considering that the band gap energy of CsCl is 8.3 eV, that of Cs_2BaCl_4 is possibly located at the energy corresponding to 150–180 nm. Therefore, the bands at 430 nm and 480 nm can be attributed to STEs though it is required to clarify the band structure of Cs_2BaCl_4.

Figure 2 shows the excitation spectrum for the luminescence at 270 nm. A steep rise at approximately 87 nm was observed for the luminescence at 270 nm. This excitation spectrum was quite similar to those of CsCl-based compounds [2,3], and the result clearly indicates that Cs_2BaCl_4 exhibits AFL though clear bands were not observed in the photoluminescence spectrum with the excitation at 84 nm.

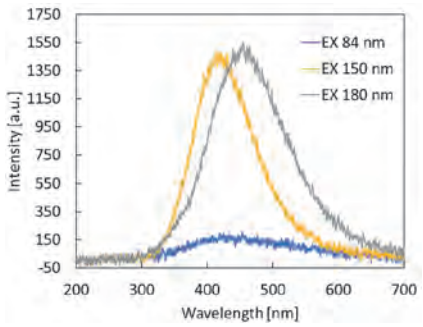


Fig. 1. Luminescence spectra of Cs_2BaCl_4 for the excitation at 84 nm, 150 nm, and 180 nm.

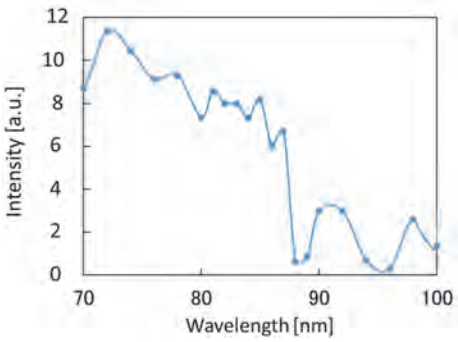


Fig. 2. Excitation spectra of Cs_2BaCl_4 for monitored wavelength of 270 nm.

[1] N. Yahaba *et al.*, Appl. Phys. Express **7** (2014) 062602.
[2] M. Koshimizu *et al.*, Opt. Mater. **36** (2014) 1930.
[3] A. Ohnishi *et al.*, J. Phys. Soc. Jpn. **72** (2003) 2400.

BL3B

Evaluation of Achromatic Vacuum-ultraviolet Lens

T. Shimizu, Y. Minami, K. Kuroda, K. Shinohara, D. Umeno and N. Sarukura
Institute of Laser Engineering, Osaka University, Suita 565-0875, Japan

Vacuum ultraviolet (VUV) has numerous scientific and technological applications including spectroscopy, environmental monitoring, surface micromachining, sterilization and so on. In the study of VUV materials, it has been found that fluoride materials can be applied as new VUV optics including lenses. For VUV lenses, the material must be transparent to the light in the VUV region, have chemical stability, have a high melting point, and be uniform and of good quality. In this study, an achromatic lens made of two materials was fabricated based on a design that minimizes chromatic aberration in the 150-300 nm range using fluoride crystals with high VUV transmittance.

A combination of $LiCaF_6$ and $BaLiF_3$ was used as materials for the convex and concave lenses of the VUV achromatic lens because it has the lowest chromatic aberration in combinations of fluoride crystals with high transmittance in the vacuum ultraviolet region. Chromatic aberration at 150 nm and 300 nm is corrected for in this design. In addition, since there is no lens adhesive that can transmit vacuum ultraviolet light, there is a gap between the convex and concave lenses, which is fixed by sandwiching them with a lens folder. The coating agent used for the anti-reflection coating, which suppresses reflections on the lens surface, is not applied because it cannot penetrate VUV light and may reduce the transmittance and degrade the vacuum due to vaporization.

The performance of VUV achromatic lenses is evaluated in the following three areas: transmittance, chromatic aberration, and focusing performance. In the first half of the year, measurements of transmittance were carried out using BL7B. The evaluation of chromatic aberration was carried out in the second half of the experiment using BL3B. The chromatic aberration is evaluated by measuring the focal length of the light in the range of 150 to 300 nm and comparing them. The results are shown in Fig. 1. The color of the lines indicates the difference in wavelength. Although the complete analysis is not yet complete, there is not much difference in the light-focusing trend for each wavelength.

From the experimental results, it was confirmed that the VUV achromatic lens is practical for the measurement system with a certain beam intensity. In addition, it was confirmed that the design policy of the previous study is useful for the design of achromatic lenses in the VUV region. In order to improve the performance, it is necessary to develop AR coating materials that suppress the reflected light and transmit vacuum ultraviolet light, and to improve the purity and uniformity of the lens materials.

In the future, a rigorous evaluation is required, and it is important to further increase the knowledge of achromatic lenses in the vacuum ultraviolet region. In addition, the development of an imaging spectrometer with a VUV achromatic lens is expected to be carried out in parallel for practical use.

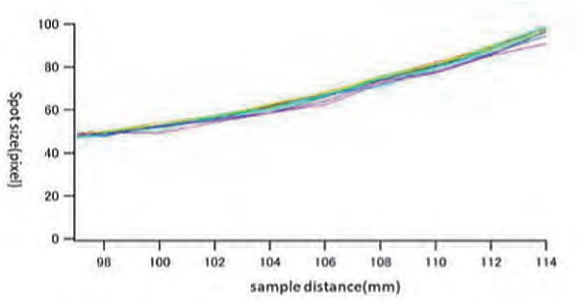


Fig. 1. Chromatic aberration measurement results.

[1] K. Shimamura, H. Sato, A. Bensalah, H. Machida, N. Sarukura and T. Fukuda, J. Alloys Cmpds. **343** (2002) 204.
[2] M. V. Luong, M. J. F. Empizo, M. Cadatal- Raduban, R. Arita, Y. Minami, T. Shimizu, N. Sarukura, H. Azechi, M. H. Pham, H. D. Nguyen, Y. Kawazoe, K. G. Steenbergen and P. Schwerdtferger, Opt. Mater. **65** (2017) 15.
[3] R. Arita, Y. Minami, M. Cadatal-Raduban, M. H. Pham, M. J. F. Empizo, M. V. Luong, T. Hori, M. Takabatake, K. Fukuda, K. Mori, K. Yamanoi, T. Shimizu, N. Sarukura, K. Fukuda, N. Kawaguchi, Y. Yokota and A. Yoshikawa, Opt. Mater. **47** (2015) 462.
[4] T. Shimizu, M. V. Luong, M. Cadatal-Raduban, M. J. F. Empizo, K. Yamanoi, R. Arita, Y. Minami, N. Sarukura, N. Mitsuo, H. Azechi, M. H. Pham, H. D. Nguyen, K. Ichiyanagi, S. Nozawa, R. Fukaya, S. Adachi, K. G. Nakamura, K. Fukuda, Y. Kawazoe, K. G. Steenbergen and P. Schwerdtfeger, Appl. Phys. Lett. **110** (2017) 141902.
[5] M. V. Luong, M. Cadatal-Raduban, M. J. F. Empizo, R. Arita, Y. Minami, T. Shimizu, N. Sarukura, H. Azechi, M. H. Pham, H. D. Nguyen and Y. Kawazoe, Jpn. J. Appl. Phys. **54** (2015) 122602.
[6] K. Yamanoi, T. Murata, Y. Arikawa, T. Nakazato, M. Cadatal-Raduban, T. Shimizu, N. Sarukura, M. Nakai, T. Norimatsu, H. Nishimura, H. Azechi, S. Fujino, H. Yoshida, A. Yoshikawa, N. Satoh and H. Kan, Opt. Mater. **35** (2013) 1962.

BL3B

Electronic States and Charge Dynamics of $Sm_{1-x}Ce_xS$

Y. Yokoyama[1], H. Hasegawa[1], J. Shibutani[1], Y. Kadowaki[1], Y. Okamoto[1], H. S. Suzuki[2], K. Takehana[3], Y. Imanaka[3] and K. Takenaka[1]

[1]*Department of Applied Physics, Nagoya University, Nagoya 464-8603, Japan*
[2]*The Institute of Solid State Physics, The University of Tokyo, Kashiwa 277-8581, Japan*
[3]*National Institute for Materials Science (NIMS), Tsukuba 305-0003, Japan*

Samarium monosulfide (SmS), in which two electronic configurations ($(4f)^6$ and $(4f)^5(5d)^1$) of Sm are energetically competed, is known as a valence fluctuation materials. The electronic state of Sm undergoes transition to $(4f)^5(5d)^1$ by applying pressure and chemical doping, while the $(4f)^6$ state is stable under ordinary pressure and temperature condition [1]. It is promising to be applied to materials for negative thermal expansion (NTE) and actuators by controlling these electronic states [2], because this phenomenon is accompanied with a large volume change up to 10 %. To study changes in the electronic states due to the valence transition, we recently conducted systematic optical reflectivity measurements toward $Sm_{1-x}Y_xS$ single crystalline samples, covering wide energy and compositional region [3]. Consequently, it is clarified that a characteristic structure, which showed the changes in electronic states induced by the valence transition, became appeared in the optical spectra at Y composition of 0.28 [3].

In this study, to investigate the changes in the electronic states by the other dopant, we measured the optical reflectivity $R(\omega)$ spectra of $Sm_{1-x}Ce_xS$ single crystalline samples in the wide (from far-IR to vacuum-UV) energy regions. Normal incident reflectivity spectra were collected at 295 K by using a Fourier-type interferometer (0.005–1.6 eV) and a grating spectrometer (1–3 eV) installed with a microscope. For the measurements from visible to vacuum-UV region (2–30 eV), we used a synchrotron radiation at BL3B of UVSOR, Institute for Molecular Science. Then, optical conductivity $\sigma(\omega)$ was deduced from the $R(\omega)$ using the Kramers-Kronig relation.

Figure 1 shows the $R(\omega)$ spectra of $Sm_{1-x}Ce_xS$ taken at 295 K. The corresponding spectra of $Sm_{1-x}Y_xS$ [3] are shown in the right column for the comparison. As the Ce doping proceeds to $x = 0.20$, reflectivity edge moves to higher energy and the characteristic structure around 1 eV appears, in common with the Y-doped case. However, it seems that the spectral changes occur at lower Ce doping level comparing to the Y-doped case. The $\sigma(\omega)$ spectra (Fig. 2) show that the Ce doping also generates a significant structure in the IR region, which is not characterized by a simple Drude response, at lower dopant composition than the Y-doped case.

The recent works of the NTE function of the $Sm_{1-x}R_xS$ (R: rare-earth elements) reported the steep changes in the lattice parameter induced by the doping; $0.2 < x < 0.3$ for the Y-doping and $0.1 < x < 0.2$ for the Ce-doping [2,4]. Considering these facts together with the present results, it is strongly suggested that the characteristic structure in the IR region of the $\sigma(\omega)$ spectra reflects the valence fluctuating states. The findings in the present study raise a new question: why the valence transition occurred at lower Ce composition level? To answer this question precisely, it is useful that the differences in the electronic states between Y and Ce are elucidated by other methods such as the photoelectron spectroscopy.

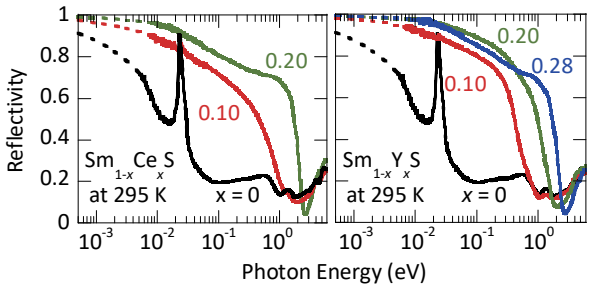


Fig. 1. Reflectivity spectra of $Sm_{1-x}R_xS$ (R=Ce (left), Y (right) [3]) single crystallines at 295 K. Broken lines represents the Hagen-Rubens extrapolation.

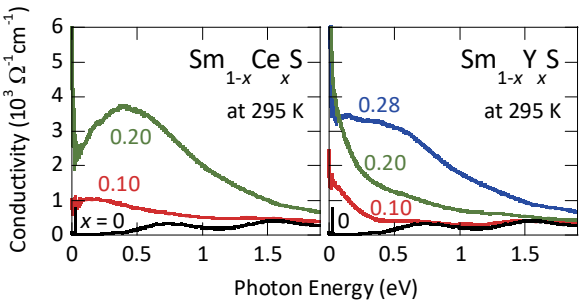


Fig. 2. Optical conductivity spectra of $Sm_{1-x}R_xS$ (R= Ce (left), Y (right) [3]) at 295 K.

[1] A. Jayaraman *et al.*, Phys. Rev. B **11** (1975) 2783.
[2] K. Takenaka *et al.*, Sci. Rep. **9** (2019) 122.
[3] Y. Yokoyama *et al.*, Phys. Rev. B **100** (2019) 245143.
[4] D. Asai *et al.*, Appl. Phys. Lett. **114** (2019) 141902.

BL4U

Analysis of Lithium Insertion/Extraction Process in One-dimensional Single-crystalline Active Materials by Scanning Transmission X-ray Microscopy

E. Hosono[1,2,3], D. Asakura[1,2], H. Yuzawa[4] and T. Ohigashi[4,5]

[1]*Research Institute for Energy Conservation, National Institute of Advanced Industrial Science and Technology, Tsukuba 305-8568, Japan*

[2]*AIST-UTokyo Advanced Operando-Measurement Technology Open Innovation Laboratory (OPERANDO-OIL), National Institute of Advanced Industrial Science and Technology (AIST), Kashiwa 277-8565, Japan.*

[3]*Global Zero Emission Research Center, National Institute of Advanced Industrial Science and Technology, Tsukuba 305-8568, Japan*

[4]*UVSOR Synchrotron Facility, Institute for Molecular Science, Okazaki 444-8585, Japan*

[5]*School of Physical Sciences, The Graduate University for Advanced Studies, SOKENDAI, Okazaki 444-8585, Japan*

Innovative technologies for clean energy devices are desired for the realization of sustainable society by preventing global warming. Development of high-performance Li-ion batteries (LIBs) for electric vehicles and large-scale power storage in renewable energy power plants is attracting much attention.

We have studied the morphology control method of materials, because the properties of materials depend on crystal direction and facet of materials [1]. In addition, we have been studying the charge-discharge mechanism of LIBs. Nevertheless, there are many unsolved mechanisms in the research field of LIBs.

Soft X-ray spectroscopy is a powerful technique to understand the electronic structures of transition-metal oxides used for active materials of LIBs. Moreover, by using scanning transmission X-ray microscope (STXM), we can get the electronic structural information with special information. For the single-crystalline active materials of LIBs, position-dependent Li insertion/extraction reaction is expected to be observed by STXM. Especially, single-crystalline nanowire materials have diffusion paths with limited direction based on the crystal structure. In the case of $LiFe_xMn_{1-x}PO_4$ single-crystalline nanowire materials, the diffusion path is limited to one direction.

Here, we exhibit a result of *ex situ* STXM for $LiFe_xMn_{1-x}PO_4$ single-crystalline nanowire. Figure 1 shows the STXM image measured with an excitation energy of 700 eV. Nanowire image of $LiFe_xMn_{1-x}PO_4$ is obtained by STXM. The Fe $L_{3,2}$-edge absorption spectra of selected regions are shown in Fig. 2. Each spectrum is ascribed to Fe^{3+} state compared with previous X-ray absorption result [2]. Now, we are analyzing the Fe $L_{3,2}$-edge, Mn $L_{3,2}$-edge, and O K-edge results for the $LiFe_xMn_{1-x}PO_4$.

In the near feature, we will establish *operando* STXM measurement system.

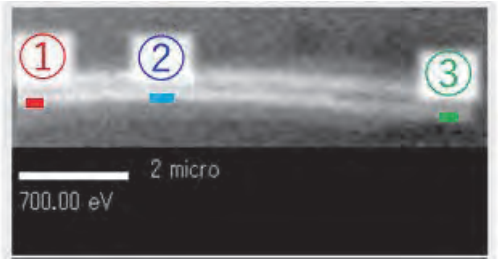


Fig. 1 A STXM image of the $LiFe_xMn_{1-x}PO_4$ single-crystalline nanowire

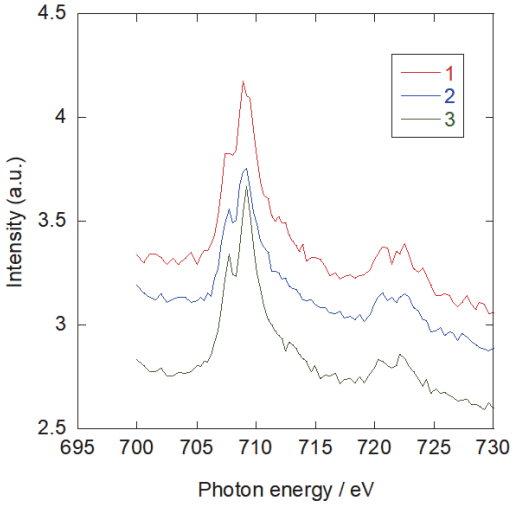


Fig. 2. Fe $L_{3,2}$-edge absorption spectra of selected regions. The numbers correspond to the regions in Fig. 1.

[1] E. Hosono, J. Ceram. Soc. Japan **120** (2012) 47.
[2] D. Asakura, E. Hosono, M. Okubo, Y. Nanba, H. S. Zhou, P. A. Glans and J. H. Guo, ChemPhysChem **17** (2016) 4110.

BL4U

Elucidation of Mechanisms of Nucleation and Crystal Growth for Clean Energy Materials in Aqueous Solutions by Scanning Transmission X-ray Microscope

Y. Miseki [1,2], E. Hosono[1,3,4], D. Asakura[3,4], H. Yuzawa[5] and T. Ohigashi[5,6]

[1]*Global Zero Emission Research Center, National Institute of Advanced Industrial Science and Technology, Tsukuba 305-8568, Japan*

[2]*Research Center for Photovoltaics, National Institute of Advanced Industrial Science and Technology, Tsukuba 305-8565, Japan*

[3]*Research Institute for Energy Conservation, National Institute of Advanced Industrial Science and Technology, Tsukuba, 305-8568, Japan*

[4]*AIST-UTokyo Advanced Operando-Measurement Technology Open Innovation Laboratory (OPERANDO-OIL), National Institute of Advanced Industrial Science and Technology (AIST), Kashiwa 277-8565, Japan.*

[5]*UVSOR Synchrotron Facility, Institute for Molecular Science, Okazaki 444-8585, Japan*

[6]*School of Physical Sciences, The Graduate University for Advanced Studies, SOKENDAI, Okazaki 444-8585, Japan*

We have studied the clean energy devices including lithium ion batteries [1,2] and photocatalytic devices [3] by controlling the morphology and crystal growth. Ceramics materials such metal oxides are main materials to construct many kinds of clean energy devices. The properties of metal oxide materials are depended in large part on crystal direction and facet of materials. Thus, nanostructural control methods have been studied by many researchers to improve each device performance.

For sophistication of nanostructural control techniques, understanding of crystal growth is very important. Especially, the surface and interface between materials and solution is active site for the catalytic reaction in the case of photocatalytic devices. Accurate design of crystal direction and facet and fabrication techniques are needed to create ideal reaction places.

To establish the high-level crystal growth techniques and morphology control methods, we considered that theoretical understanding from electronic structure level by using synchrotron radiation soft X-ray is necessary. A Scanning Transmission X-ray Microscope (STXM) exhibits electronic structure information with spatial information (minimum spatial resolution is ca. 30 nm). We tried the preparation of *operando* measurement system for crystal growth in STXM.

Figure 1 shows the optical microscope image of Fe^{2+} solution sandwiched by Si chips with Si_3N_4 windows.

One of the major features of STXM is that it is possible to obtain a spectrum of the solution by sandwiching it between the Si_3N_4 windows.

Figure 2 shows the spectrum of Fe from other sandwich cell constructed by photocatalytic materials and Fe solution.

In near feature, we will establish in-situ measurement system.

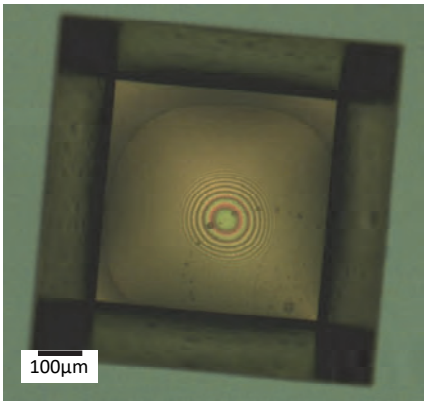


Fig. 1. Optical microscope image of Fe solution

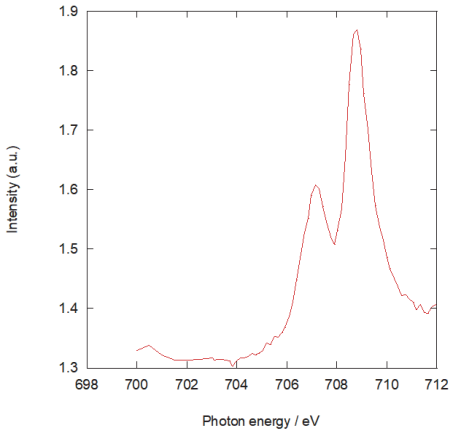


Fig. 2. Absorbance spectrum of Fe.

[1] E. Hosono, J. Ceram. Soc. Jpn. **120** (2012) 47.
[2] D. Asakura, E. Hosono, M. Okubo, Y. Nanba, H. S. Zhou, P. A. Glans and J. H. Guo, ChemPhysChem **17** (2016) 4110.
[3] Y. Miseki and K. Sayama, Chem. Commun. **54** (2018) 2670.

BL4U

Characterization of Network-Domain of Sulfur Cross-linked Isoprene Rubber

K. Miyaji[1], Y. Sakaki[1] and Y. Ikeda[2]
[1]*Graduate School of Science and Technology, Kyoto Institute of Technology, Kyoto 606-8585, Japan*
[2]*Faculty of Molecular Chemistry and Engineering, Kyoto Institute of Technology, Kyoto 606-8585, Japan*

Nowadays, rubber materials have become indispensable to applications such as automobile and airplane tires as well as seismic isolation materials. Many of these products are produced by cross-linking raw rubbers, which forms a three-dimensional network structure with good rubber elasticity. Among conventional cross-linking reactions, sulfur cross-linking reaction, known as "vulcanization" is most widely used all over the world. Despite the progress achieved in this field, controlled formation of rubber networks is generally very difficult and complicated in the rubber industry primarily because of the heterogeneous nature of the cross-linking reactions resulting from various factors such as the influence of cross-linking reagents, fillers, and processing methods. Therefore, the rational design of rubber network structures to produce sturdier and more stable rubber materials is still a challenge. Consequently, a deeper understanding of the rubber network structures is important for the development of rubber science and technology. In 2009, our group revealed the effects of the combination and composition of sulfur cross-linking reagents on the formation of an isoprene rubber network by using small-angle neutron scattering (SANS) [1]. The results showed that the combination of ZnO with other reagents was crucial for controlling the structural network inhomogeneity in the *N*-(1,3-benzothiazol-2-ylsulfanyl)cyclohexanamine (CBS)-accelerated vulcanization system. This specific morphology was found to be controlled by changing the amount of cross-linking reagents. There are several analytical methods to investigate the morphology of rubber vulcanizates. Scanning transmission X-ray microscopy (STXM) is one of methods which provides chemical mapping in nanometer scales. Also, both spatial and compositional chemical information are provided at the same time. In this study, STXM was used to confirm the two network-domain of isoprene rubber vulcanizate in terms of the distribution of sulfur.

The rubber compound was prepared by conventional mixing at room temperature on a two-roll mill with a water cooling system; isoprene rubber was mixed with zinc oxide, CBS and sulfur. Rubber vulcanizate was prepared by conventional pressing method. This rubber vulcanizate was extracted by tetrahydrofuran (THF) to remove the un-reacted sulfur. The vulcanized rubber sheet after THF extraction was cut by an ultra-microtome to prepare a smooth and flat surface with a thickness of approximately 100 nm for STXM measurement.

Figure 1 shows the STXM image of the vulcanized isoprene rubber at 165.4 eV. The intensity of the absorption indicates the concentrations of sulfur. Thus, the green to red regions shown in Figure 1 are the network-domains of the vulcanized isoprene rubber. As predicted by the SANS results, the network domains were formed by the absorption of sulfur and the accelerator, CBS on the ZnO clusters, and followed by sulfur cross-linking on the surface of ZnO clusters [1]. Furthermore, it was also found that the region of strong absorption and the mechanical properties of the vulcanizates increased linearly with the amount of the reagents.

This STXM image successfully confirmed the network-domains in the vulcanized isoprene rubber from the view point of sulfur distribution. The amount of ZnO was clearly suggested to be a key to control the total fraction of network domain phases in the vulcanizates.

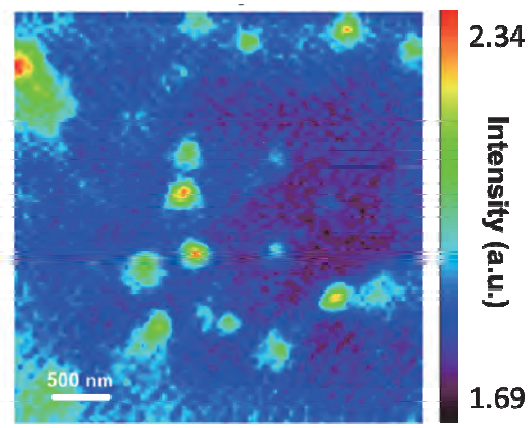


Fig. 1. STXM image of the vulcanized isoprene rubber at 164.5eV.

[1] Y. Ikeda *et. al.*, Macromolecules **42** (2009) 2741.

BL4U

Single-Atom Nickel Decorated Graphitic Carbon Nitride for Efficient Water Splitting

Y. C. Huang[1,2], Y. R. Lu[1,2], C. H. Chuang[1], Y. Li[3], S. Shen[3], W. C. Chou[2], C. L. Dong[1], W. F. Pong[1], T. Ohigashi[4] and N. Kosugi[4]

[1]*Department of Physics, Tamkang University, Tamsui 251, Taiwan*
[2]*Department of Electrophysics, National Chiao Tung University, Hsinchu 30010, Taiwan*
[3]*International Research Center for Renewable Energy, State Key Laboratory of Multiphase Flow in Power Engineering, Xi'an Jiaotong University, Xi'an 710049, China*
[4]*UVSOR Synchrotron Facility, Institute for Molecular Science, Okazaki 444-8585, Japan*

Incorporation of single atomic metals on graphite carbon nitride (g-C_3N_4) has been a promising strategy for designing advanced energy materials over the past decade. The single atom has the ability to separate charge in an aromatic conjugated ring by disrupting the coordination bonds in the microstructure. However, the relative polymerization based on metal ions and its subsequent charge separation are rarely reported. Here, single atomic nickel is used as a polymerization capping agent, which is synthesized by a chemisorption route to control the interface free energy. Scanning transmission X-ray microscope (STXM) and near-edge X-ray absorption fine structure (NEXAFS) were performed to study the chemically imaged K-edge of carbon, nitrogen and oxygen.

In order to hinder the recombination of photogenerated electrons and holes, a novel coordinated structure is proposed to insert an in-gap intermediate state. By adjusting the sp^2 coordination, efficient charge separation and charge transfer can be achieved to enhance photocatalytic ability. These results provide important insights into single-atom Ni/g-C_3N_4 which is of great importance for future overall water decomposition from atomic and electronic perspectives. It is likely that the capping agent Ni can terminate the growing of heptazine chain and build an extra energy state in the gap of the conduction and valence band, which is critical efficient separation of photogenerated electrons and holes.

The optical density images and corresponding stack mapping STXM images for C K-edge and N K-edge of bare ((a) and (b)) and Ni decorated g-C_3N_4 ((c) and (d)) are shown in the Fig. 1. The stack mappings display yellow, red and green areas, corresponding to the different regions that are associated with different regions and chemical properties of the nanorods which is revealed by the NEXAFS spectra. Notably, the incorporation of single atom Ni alters significantly the electronic structure both at C and N sites. Shortly, the increased intensity of N_A resonance suggests the coordination with metal Ni; the decreased intensity of N_B resonance indicates a structure breaking of bridge nitrogen, possibly is caused by the capping agent atomic Ni during the polymerization reaction. This results is consistent with the fact that the atom- distribution Ni could be coordinated with N atom in the heptazine units. Consequently, the strategy to synthesis single-atom Ni incorporated g-C_3N_4 photocatalysis for spontaneous overall water splitting is promising. The single-atom Ni act as the capping agent for polymerization reaction, building novel coordinated structure with a mid-gap state for increasing the photogenrated electrons and holes separation.

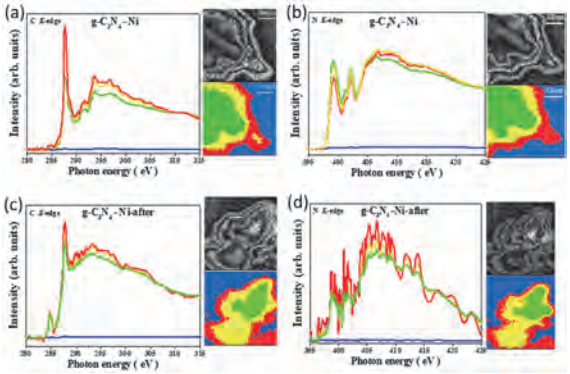


Fig. 1. Optical density images, stack mapped STXM images and corresponding NEXAFS at C and K-edge of pure g-C_3N_4 ((a), (b)) and single atom Ni decorated g-C_3N_4 ((c), (d)).

[1] A. Wang *et al.*, Nat. Rev. Chem. **2** (2018) 65.
[2] L. Cao *et al.*, Nat. Catal. **2** (2019) 134.
[3] H. Yang *et al.*, Nat. Commun. **10** (2019) 4585.

BL4B

Electronic Structure of AlFeN Films Grown on Various Substrates

S. Imada and N. Tatemizo
Faculty of Electrical Engineering and Electronics, Kyoto Institute of Technology, Kyoto 606-8585, Japan

Wurtzite AlN is a wide- and direct-band-gap semiconductor that is a promising material for deep-ultraviolet (DUV) optoelectronic devices, such as light-emitting diodes (LEDs) or laser diodes (LDs). As the energy of deep ultraviolet light is high enough to sterilize and decompose toxic molecules, it is useful in the fields of medicine and healthcare. At present, DUV light sources are mercury lamps and metal halide lamps, which require a measurable amount of power, have a short life-span, and are large in size. To replace the lamps with LED systems that will be energy-saving, long-lasting, and small, the design and development of DUV-LEDs have been sped up around the world.

In the course of the studies, however, it became evident that AlN and related materials have difficult issues in realizing high efficiency devices owing to some electronic properties in the form of thin films, which are traced back to the crystal axis orientation of AlN, *i.e.* the polar-axis orientation. Therefore, non-polar-axis oriented AlN films have generated a lot of interest, because they can avoid these problems.

We have succeeded in growing non-polar-axis oriented wurtzite films by heavy-doping of Fe in AlN films on SiO_2 glass substrates [1] and found that the Fe-doping raised large gap states in the gap of AlFeN *via* Fe-*d* and N-*p* hybridization [2]. To remove the gap states, we conducted annealing of the films and succeeded in desorption of Fe atoms from the AlFeN lattice, resulting in a drastic decrease of the gap states while maintain the non-polar axis orientation [2].

To increasing the crystallinity of the annealed films, Si is more favorable as a substrate because its linear expansion coefficient is similar to that of AlN. Thus, we have grown AlFeN films on Si(100) substrates and investigated the crystallographic orientation and electronic structures. It was found that the AlFeN films with Fe concentrations higher than 10 % have *a*-axis orientation and similar electronic structure to that of the films grown on SiO_2 glass substrates. As representative data, N K-edge XANES spectra grown on Si(100) and SiO_2 glass substrates with 18 % Fe are shown in Fig. 1. The main structure between 400 eV and 409 eV and the pre-edge peak at around 397 eV of the film on a Si(100) substrate are coincident with those of the films on a SiO_2 glass substrate. This result also implies that the *a*-axis oriented growth by heavy Fe doping can proceeds as self-nuclear formation. We are attempting to obtain growth-time dependences of the crystallographic orientation and electronic structures of as-grown AlFeN films. The results from these efforts are expected to be reported in our future publications.

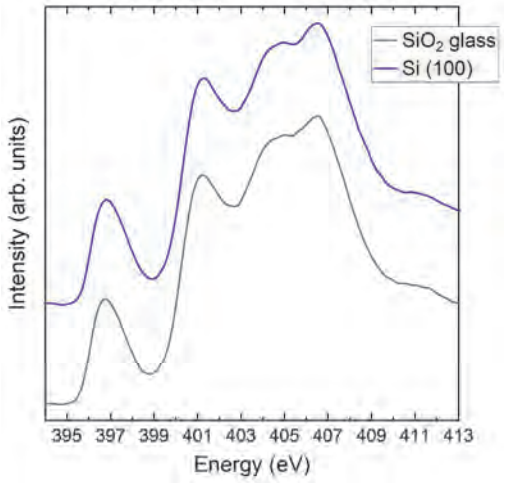


Fig. 1. N K-edge XANES spectra of AlFeN (Fe: 18 %) films deposited on SiO_2 glass and Si(100) substrates. The electric field vectors *E* of the incident X-rays were parallel to the film plane. The measurements were performed in vacuum ~10^{-6} Pa at RT in the fluorescence-detection mode.

[1] N. Tatemizo , S. Imada, K. Nishio and T. Isshiki, AIP advances **8** (2018) 115117.
[2] N. Tatemizo , S. Imada, K. Okahara, H. Nishikawa, K. Tsuruta, T. Ina, Y. Miura, K. Nishio and T. Isshiki, Scientific Reports **10** (2020) 1819.

BL4B

Valence State Analysis of Mn Ions in SnO_2

T. Yamamoto[1,2,3]

[1]*Department of Materials Science, Waseda University, Tokyo 169-8555, Japan*
[2]*Institute of Condensed-Matter Science, Waseda University, Tokyo 169-8555, Japan*
[3]*Kagami Memorial Research Institute for Materials Science and Technology, Waseda University, Tokyo 169-0051, Japan*

Dilute magnetic materials (DMMs) have been extensively studied after a discovery of ferromagnetism in InAs doped with dilute amount of Mn ions [1], since such materials have a potential to be applied in spintronics. At early stage, a Currie temperature, T_C, was low in this type of DMMs. Hence a lot of attempts have been devoted to increase TC for the application in industrial uses. Recently, it was reported that some DMMs show ferromagnetism beyond room temperature, e.g., Mn-doped GaN, Co-doped TiO_2 and Mn, Fe co-doped In_2O_3. However, the mechanism of appearance of ferromagnetism in DMMs have not yet been understood. Although it is essential to know a local environment of doped magnetic ions in host materials, such analysis has not often been done due to a difficulty to analyze it for dilute dopants. It was proposed that two types of local environments of doped magnetic ions exist in DMMs, i.e., substitution and precipitate types. In the former, doped magnetic ions substitute at one of the cation site in the host material, while in the later doped magnetic ions precipitate as small particles. For such analysis, X-ray absorption spectroscopy (XAS) is quite powerful. We have successfully determined the local environment of doped Mn and Fe ions in In_2O_3 by using the XAS analysis [2,3].

In the current study, valence state of Mn ions in SnO_2 was investigated by the Mn-L_3 XAS. Samples were prepared with conventional solid-state reaction method changing a concentration of doped Mn ions. Crystal structures of the synthesized samples were examined by powder X-ray diffraction, which suggest all the samples were in singular phase of rutile structured SnO_2. Mn-L_3 XAS were recorded at BL4B in UVSOR by total electron yield mode using electron multiplier. Sample powders were placed on the carbon adhesive tape, which were attached on the first dinode of the electron multiplier.

Observed Mn-L_3 XAS of Mn(1 %) doped SnO_2 is shown in Fig. 1 together with the representative spectra of Mn^{2+}, Mn^{3+} and Mn^{4+} for comparison. Most intense peak in XAS of Mn-doped SnO_2 coincides with that of Mn^{2+} and the second overlaps that of Mn^{3+}. This result suggests that the major component of Mn ions is 2+ and Mn^{3+} exists as minor one in SnO_2. In the carrier mediated type of the models for DMMs, mixed valence is a key to make the material ferromagnetic as suggested in our earlier work [3]. From our current analysis, it has been suggested that Mn-doped SnO_2 has a possibility to be a ferromagnetic DMM.

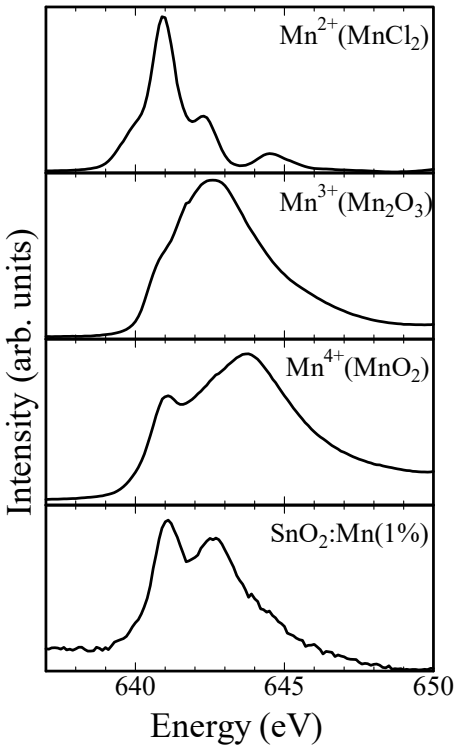


Fig. 1. Mn-L_3 X-ray absorption spectra of $MnCl_2$. Mn_2O_3, MnO_2 and Mn-doped SnO_2.

[1] H. Ohno *et al*., Phys. Rev. Lett. **68** (1992) 2664.
[2] T. Yamamoto *et al*., J. Phys.:Condens. Matter **21** (2009) 104211.
[3] T. Okazaki *et al*., Solid State Comm. **151** (2011) 1749.

BL4B

XAFS Measurements of 1-nanometer Indium-tin Oxide Particles Focusing on O K-edge

T. Tsukamoto[1,2], H. Iwayama[3], M. Nagasaka[3], A. Kuzume[2] and K. Yamamoto[1,2]

[1]*Laboratory for Chemistry and Life Science, Institute of Innovative Research, Tokyo Institute of Technology, Yokohama 226-8503, Japan*

[2]*ERATO, JST, Kawaguchi 332-0012, Japan*

[3]*Institute for Molecular Science, Okazaki 444-8585, Japan*

Sub-nanoparticles (SNPs) with extremely small size reaching 1 nm recently attract attention because they often exhibit unique properties not seen in bulk or general nanoparticles (NPs). One of the interesting behavior in this size range is the change in the chemical states of oxygen atoms in metal oxide SNPs. They don't have crystal structures but amorphous ones with many defects due to their extremely small structures. Additionally, they tend to substitute their lack of oxygen atoms (O^{2-} state) to low-valent hydroxyl groups (OH^- state). Actually, it is reported that tin oxide SNPs and copper oxide SNPs contain many OH^- species in contrast to the bulk and NPs [1,2].

In this study, we newly investigated the effect of the hybridization of different metals in the SNPs for the chemical states of oxygen atoms. We chose indium and tin as two metal elements with different valence electrons in the same period in the periodic table. The oxygen species in indium-tin oxide SNPs were observed and analyzed by XAFS measurements focusing on the O K-edge using BL4B beamline in UVSOR. As a bulk of metal oxides, indium oxide (In_2O_3) and tin oxide (SnO_2) purchased from Sigma-Aldrich Co. LLC. were used. As NPs, indium oxide (100 nm), tin oxide (100 nm), and indium-tin oxide (50 nm, In_2O_3/SnO_2 = 9:1) purchased from Sigma-Aldrich Co. LLC. were used. As SNPs, indium oxide (1 nm, $In_{28}O_x$), tin oxide (1 nm, $Sn_{28}O_x$), and indium-tin oxide (1nm, $In_{12}Sn_{16}O_x$) synthesized by the atom-hybridization method [3] were used. All the samples were cast on the silicon substrate and dried in vacuo in the instrument overnight. The XAFS spectra were recorded according to both the total electron yield and the partial fluorescence yield. The O K-edge XAFS spectra of samples were standardized using the oxide layer on the surface of the reference Si substrate.

In comparison among the bulks, NPs, and SNPs composed of a single metal element, it was suggested that only the SNPs contain OH^- species in contrast to their bulks or NPs, judging from the XAFS spectra in O K-edge region [4,5] (Fig. 1). Moreover, the indium-tin bimetallic oxide SNPs showed remarkably higher peak intensity than the monometallic ones (Fig. 2). This result indicated that the indium-tin oxide SNP has more OH^- species. On the other hand, in the case of the indium-tin oxide NP, the peaks corresponding to OH^- species were not observed. Therefore, the increase in the amount of OH^- species in such binary systems would be a specific phenomenon in the SNPs with 1 nm particle size.

In conclusion, it was suggested that the hybridization of two metal elements in metal oxide SNPs with quantum-sized structure produces more defect structures, leading to the unique chemical states of metal oxides.

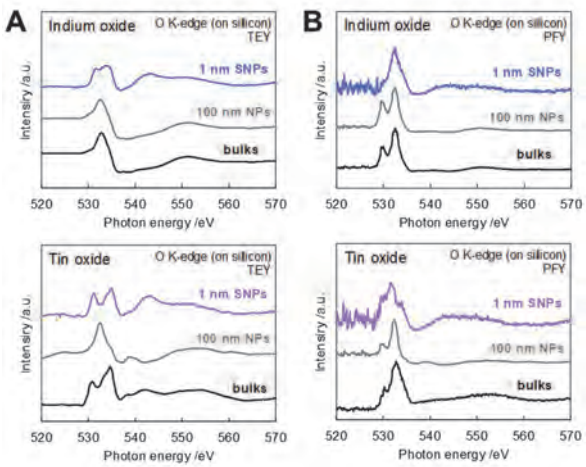


Fig. 1. O K-edge XAFS spectra of bulks, NPs, and SNPs of metal oxides on Si substrate by (A) total electron yield and (B) partial fluorescence yield. Only for the SNPs, signals originating OH^- species at 534 and 542 eV were superimposed on those of O^{2-} one.

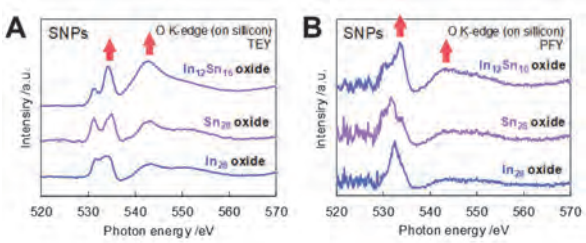


Fig. 2. O K-edge XAFS spectra of indium oxide, tin oxide, and indium-tin oxide SNPs on Si substrate by (A) total electron yield and (B) partial fluorescence yield. For the bimetallic oxide SNPs, signals originating OH^- species at 534 and 542 eV were superimposed on those of O^{2-} one.

[1] A. Kuzume *et al.*, Sci. Adv. **5** (2019) eaax6455.
[2] K. Sonobe *et al.*, ACS Nano **14** (2020) 1804.
[3] T. Tsukamoto *et al.*, Nat. Commun. **9** (2018) 3873.
[4]M. Yoshida *et al.*, J. Phys. Chem. C **119** (2015) 19279.
[5]M. Nagasaka *et al.*, Chem. Phys. Lett. **375** (2003) 419.

BL4B, BL3B

Soft X-ray Excitation Impurity Luminescence of Aluminum Nitride

Y. Maegawa[1], T. Banno[1], K. Fukui[1] and K. Yamamoto[2]

[1]*Department of Electrical and Electronics Engineering, University of Fukui, Fukui 910-8507, Japan*

[2]*Far-infrared region Development Research Center, University of Fukui, Fukui 910-8507, Japan*

AlN is a material having the largest band gap energy ($\boldsymbol{E}_g$ = 6.2 eV) among group III-V nitride semiconductors, and is important as a key material of an ultraviolet (UV) region light emitting device (LED). For LED study, impurity luminescence (IL) that is due to the existence of the state of impurity and/or defect in the band gap gives important information about the impurity atoms. In the case of our bulk AlN sample, visible (VIS) - UV region excitation photoluminescence measurements, three kinds of IL bands (B_L around 2.6 eV, B_H around 2.8 eV, UV around 4.0 eV) were observed [1]. These IL bands were only observed in the excitation region up to $\boldsymbol{E}_g$. Band to band excitation (> $\boldsymbol{E}_g$) is not able to contribute to these IL. Our results are quite similar to those of Alder *et al.* and are considered that B_H and UV bands may be due to carbon (C) defects [2]. Then, we performed soft X-ray excitation IL measurements, because the inner-shell excitation by using soft X-ray shows C, nitrogen (N), and oxygen (O) 1*s* electron contributions to those IL.

A bulk AlN sample is commercially available disk-shaped one and manufactured by physical vapor transport method. Excitation photon energy regions were around C K-edge (270 - 298 eV), N K-edge (400 - 415 eV), O K-edge (538 - 550 eV) and 4.0 – 6.8 eV (BL3B). All measurement were carried out at 10 K.

Figure 1 shows an emission spectrum at an excitation energy of 292 eV (black) and a result of component decomposition. The IL spectrum due to soft X-ray excitation consists of a main peak around 2.7 eV with tail shape on the higher energy side and is different from that due to under $\boldsymbol{E}_g$ energy excitation, which has no tail feature. However, main peak and tail shape of the IL spectrum due to soft X-ray excitation are able to decompose into B_L, B_H, and V_L, V_H emission bands, respectively, where V_L band corresponds to the emission band observed under electron beam excitation [3]. Since the energy region of V_H band matches that of UV emission, V_H band probably includes UV band. Figure 2 shows the excitation spectrum of each band near each absorption edge. The characteristic spectrum shape at C K-edge and the flat-like spectrum shape at O K-edge clearly suggest that C impurity is corresponding to those IL and O impurity is not. The intensity decrease above N K-edge is caused by the decrease of penetration depth of excitation light.

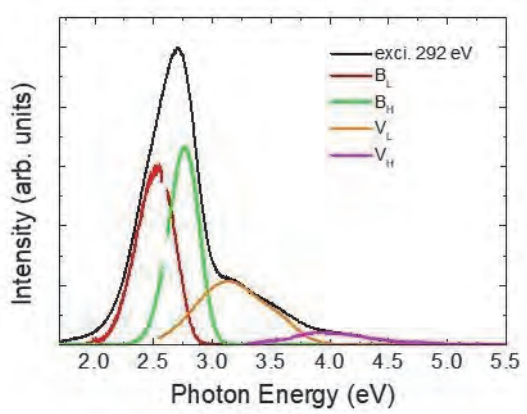


Fig. 1. Emission spectrum (exci. at 292 eV) and component decomposition results

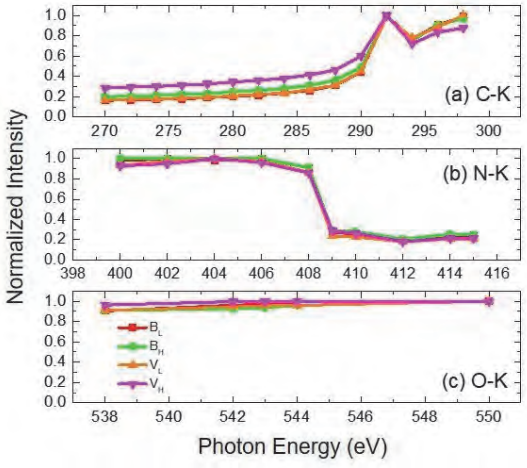


Fig. 2. Excitation spectrum of each emission band around (a) C-, (b) N-, (c) O-K edge, respectively.

[1] W. Kamihigoshi *et al.*, UVSOR Activity Report 2018 **46** (2019) 103.
[2] D. Alden *et al.*, Phys. Rev. Appl. **9** (2018) 054036.
[3] M. Morita *et al.*, Jpn. J. Appl. Phys. **21** (1982) 7.

BL5U

Electronic States of Antiferromagnetic Half-heusler GdPtBi Studied by High-resolution ARPES

D. Takane[1], T. Suzuki[2], S. Souma[3,4], K. Nakayama[1], K. Hori[1], Y. Kubota[1], T. Ren[1], K. Sugawara[1,3,4], T. Takahashi[1,3,4], J. G. Checkelsky[2] and T. Sato[1,3,4]

[1]*Department of Physics, Tohoku University, Sendai 980-8578, Japan*
[2]*Department of Physics, Massachusetts Institute of Technology, Cambridge, MA 02139, USA*
[3]*Center for Spintronics Research Network, Tohoku University, Sendai 980-8577, Japan*
[4]*WPI Research Center, Advanced Institute for Materials Research, Tohoku University, Sendai 980-8577, Japan*

Topological insulators are a novel quantum state of matter in which an inverted nontrivial bulk-band structure leads to gapless edge or surface states protected by the time-reversal symmetry [1-3]. The discovery of topological insulators triggered the search for new types of topological materials, as represented by the experimental discoveries of topological crystalline insulators with gapless surface states protected by the mirror symmetry of the crystal [4] and topological Dirac semimetals with three-dimensional bulk Dirac fermions protected by the rotational symmetry of the crystal [5].

Recent theoretical studies predicted exotic topological phases originating from the interplay between nontrivial band topology and long-range order, e.g. magnetism and superconductivity. A leading platform for exploring such novel topological states is the rare-earth half-Heusler *Re*PtBi (*Re*: rare-earth) which exhibits various ordered phases depending on the rare-earth [see Fig. 1(a) for crystal structure]. Among them, antiferromagnet GdPtBi (Néel temperature T_N = 9K) is attracting particular interests because it exhibits the peculiar physical properties including the large anomalous Hall effect and chiral anomaly [6,7]. It is thus highly desirable to experimentally establish the electronic band structure of GdPtBi and clarify its topological character and relationship with unconventional physical properties.

In this study, by using high-resolution angle-resolved photoemission spectroscopy (ARPES), we determined the fine electronic structure on the GdPtBi (111) surface [see Fig. 1(b) for corresponding bulk and surface Brillouin zones]. High-resolution ARPES measurements have been performed at BL5U. The sample was cleaved *in situ* under an ultrahigh vacuum of 1.0×10^{-10} Torr.

Figure 1(c) displays the valence-band dispersion in the paramagnetic phase measured along a momentum cut crossing the Brillouin-zone center. We observed highly dispersive holelike bands which cross the Fermi level to form Fermi surfaces. The Fermi surfaces are three-fold symmetric, in agreement with the rotational symmetry of the crystal. Also, the observed band dispersions are qualitatively consistent with the first-principles band-structure calculations, confirming their bulk-band nature which was further corroborated by the *hv*-dependent ARPES measurements. Furthermore, we have performed high-resolution ARPES measurements to search for the topological surface sates as well as the electronic reconstruction induced by the antiferromagnetic transition. Our results provide important insights into the origin of exotic physical properties and also into the topological property of GdPtBi.

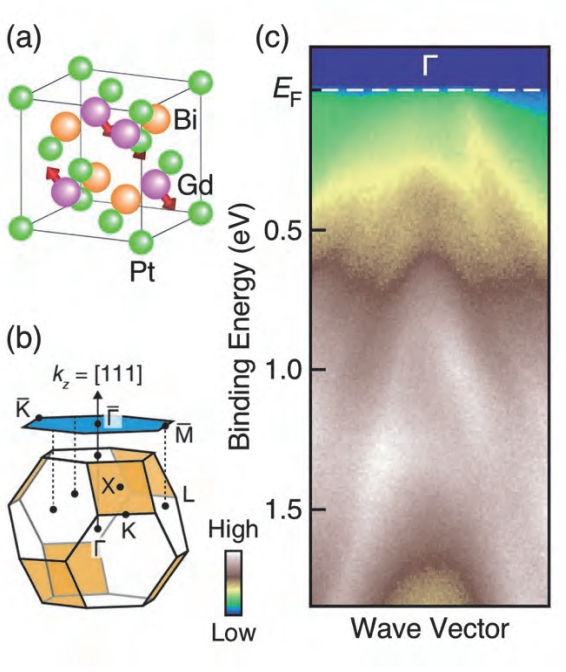


Fig. 1. (a) and (b) Crystal structure and corresponding bulk (bottom) and surface (top) Brillouin zones of GdPtBi, respectively. (c) ARPES intensity plotted as a function of binding energy and wave vector, measured at T = 40 K.

[1] Y. Ando, J. Phys. Soc. Jpn. **82** (2013) 102001.
[2] X.-L. Qi and S.-C. Zhang, Rev. Mod. Phys. **83** (2011) 1057.
[3] M. Z. Hasan and C. L. Kane, Rev. Mod. Phys. **82** (2010) 3045.
[4] Y. Tanaka *et al*., Nature Phys. **8** (2012) 800.
[5] Z. K. Liu *et al*., Science **343** (2014) 864.
[6] T. Suzuki *et al*., Nature Phys. **12** (2016) 1119.
[7] M. Hirschberger *et al*., Nature Mater. **15** (2016) 1161.

BL5U

Electronic Structure Study on WSe_2 / hBN Heterostructure Using Micro-ARPES

D. J. Oh[1,2], S. Lee[1,2], H. Park[1,2], K. Tanaka[3], S. R. Park[4] and C. Kim[1,2]

[1]*Department of Physics and Astronomy, Seoul National University (SNU), Seoul 08826, Republic of Korea*
[2]*Center for Correlated Electron Systems, Institute for Basic Science (IBS), Seoul 08826, Republic of Korea*
[3]*Editorial Board, UVSOR Synchrotron Facility, Institute for Molecular Science, Okazaki 444-8585, Japan*
[4]*Department of physics, Incheon National University, Incheon 406-772, Korea*

Eccentric properties ensue from moiré superlattices formed by constituent layers in van der Waals (vdW) heterostructures. For example, the Hofstadter butterfly pattern stemming from the interplay between the moiré superlattice and an applied magnetic field was measured in monolayer (ML) graphene / h-BN heterostructures [1]. An essential step towards understanding novel properties of these heterostructures is to have electronic structure information. In that respect, direct electronic structure measurement of the ML graphene / h-BN heterostructure by using ARPES was an important development [2]. Recently, mini bands induced by moiré superlattice were observed in graphene / WS_2 heterostructures [3]. These developments open the possibility that a similar scheme may be applied to transition metal dichalcogenide (TMD)-based heterostructures. Since a plethora of intriguing physical properties such as superconductivity, Weyl physics and charge density waves exist in TMDs, even more exciting phenomena may arise in vdW heterostructures constructed from these materials.

Among variety of TMDs, group VI TMDs (MX_2, M= Mo,W, X= S, Se) have been extensively studied due to their valley and spin degrees of freedom induced by large spin-orbit interaction and Berry curvature [4]. In addition, MX_2's are stable in atmosphere, making them suitable for surface-sensitive experiments as well as applications in optoelectronic devices. In order to study electronic structure of TMD-based heterostructures, the samples are fabricated using the following procedures. First, Pt was evaporated into an inverse-T shape on Nb doped TiO_2 or degenerately doped SiO_2 / Si substrates, such that Pt comes into contact with the metal strip and makes a conducting channel for electrons (Fig. 1a). Using the dry-transfer method, mechanically exfoliated h-BN and 1ML WSe_2 are sequentially transferred, so that they make partial contact with a corner of the Pt pattern (Figs. 1b-1d). Thus, we could effectively avoid sample charging at low temperatures (~100 K) even though samples are placed on insulating substrates. In order to efficiently find the precise position of the sample, we mapped out photoemission intensity at the Fermi level (Figs. 1e-1f) and W $4f_{7/2}$ core (Fig. 1g) near the Pt corner by utilizing the micro beam (~30 μm). The so-obtained spatial map was found to be consistent with an optical image of the sample. Then, we moved to the region of interest (1ML WSe_2 region) and obtained the electronic structure of 1ML WSe_2 / h-BN over the Brillouin zone (BZ) (Fig. 2). Here, we did not have to rotate the sample for the BZ mapping because we used a photoelectron analyser equipped with deflectors. By following the procedure, we were able to attain ARPES data with a relatively high success rate.

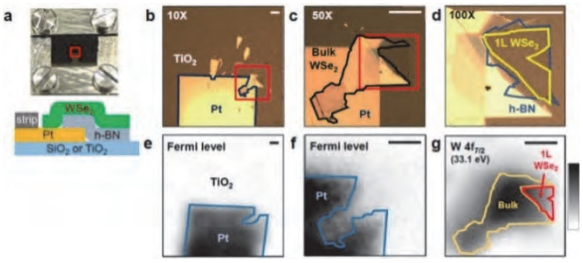


Fig. 1. Optical image (a~d) and spatial map of photemission intensity (e~g) of the monolayer WSe_2 / h-BN heterostructure. Scale bar, 100 μm.

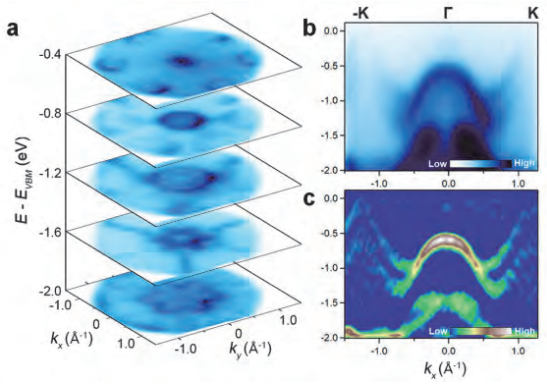


Fig. 2. Electronic structure of monolayer WSe_2 / h-BN heterostructure.

[1] B. Hunt *et al*., Science **340** (6139) (2013) 1427.
[2] E. Wang *et al.*, Nat. Phys. **12** (2016) 1111.
[3] S. Ulstrup *et al*., arXiv : 1904.06681 (2019).
[4] X. Xu *et al*., Nat. Phys. **10** (2014) 343.
[5] Q. Zhu *et al*., Sci. Adv. **5** (1) (2019) eaau6120.

BL5U

Three-dimensional Angle-resolved Photoemission Study of Ullmannite NiSbS with the Cubic Chiral Crystal Structure

T. Ito[1,2], T. Hosoya[2], M. Nakatake[3], S. Ideta[4,5], K. Tanaka[4,5], M. Kakihana[6], D. Aoki[7], A. Nakamura[7], T. Takeuchi[8], H. Harima[9], M. Hedo[10], T. Nakama[10] and Y. Ōnuki[10]

[1]*Nagoya University Synchrotron radiation Research center (NUSR), Nagoya University, Nagoya 464-8603, Japan*
[2]*Graduate School of Engineering, Nagoya University, Nagoya 464-8603, Japan*
[3]*Aichi Synchrotron Research Center, Seto, 489-0965, Japan*
[4]*UVSOR Synchrotron Facility, Institute for Molecular Science, Okazaki 444-8585, Japan*
[5]*The Graduate University for Advanced Studies, SOKENDAI, Okazaki 444-8585, Japan*
[6]*Graduate School of Engineering and Science, University of the Ryukyus, Nishihara-cho 903-0213, Japan*
[7]*Institute for Materials Research, Tohoku University, Sendai 980-8577, Japan*
[8]*Low Temperature Center, Osaka University, Toyonaka 560-0043, Japan*
[9]*Graduate School of Science, Kobe University, Kobe 657-8501, Japan*
[10]*Faculity of Science, University of the Ryukyus, Nishihara-cho 903-0213, Japan*

Non-centrosymmetric compounds have attracted much attention due to their interesting phenomena relating with inversion symmetry breaking. The ullmannite type NiSbS with the non-centrosymmetric cubic chiral structure has recently been suggested to be a possible candidate of Weyl semimetal [1]. Indeed, split Fermi surface topologies reflecting the cubic chiral crystal structure and the spin-orbit interactions have been reported [2]. In this study, we have performed angle-resolved photoemission spectroscopy (ARPES) on NiSbS to directly investigate the electronic band structure of this system.

ARPES measurements were performed at the UVSOR-III BL5U. Data were acquired at T = 25 K with hν= 40 - 96 eV. To directly trace the ΓR high-symmetry line with using photon energy dependent ARPES at the normal emission angle (θ = 0°), clean sample surfaces were obtained by *in situ* cleaving on (111) plane.

Figures 1(a) and (b) show the k_x-k_z constant energy image at the Fermi level E_F (a) and 400 meV (b) on ΓXRM plane of NiSbS. We have clearly found the inclined shape of the obtained images. The observed inclined shape is consistent with the tetragonal shape of ΓXRM plane where k_z axis corresponds to the diagonal ΓR line (Fig.1(c)). From the symmetry of the obtained images, we have estimated the inner potential of V_0 = 33 eV which is relatively larger than one of (001) cleaved surface (V_0 = 24.7eV) [3].

Figure 1(c) shows the band structure along ΓR line obtained from the normal emission ARPES spectra. From the comparison with the band structure calculation (solid lines), we have found slight narrowing of the dispersive features relative to the calculation, while the rough tendency seems to be similar. According to the band calculation, existence of Weyl point (WP) has been expected around k_z = 5.2 Å^{-1}, where we found no band crossing except for the broad distribution between the non dispersive feature around 400 meV and the dispersive feature approaching E_F. To understand the relation between the electronic structure and the chiral crystal structure, we are going to perform linear and circular polarization dependent ARPES on this system in near future.

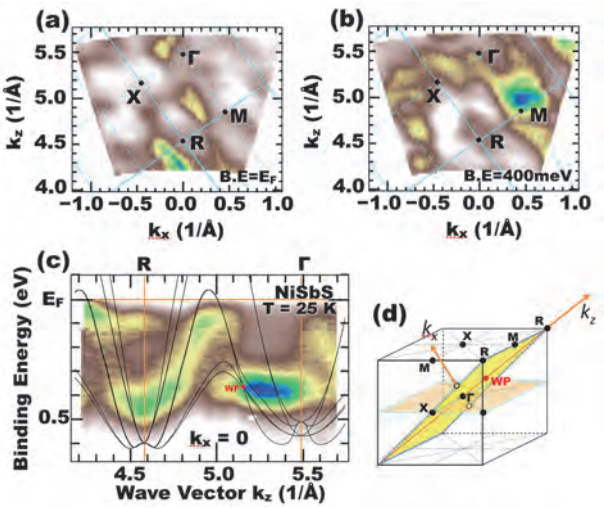


Fig. 1. (a,b) k_x-k_z constant energy image at E_F (a) and 400 meV (b) on ΓXRM plane of NiSbS. (c) Band structure along ΓR line. Solid lines are band calculation [2]. (d) Cubic Brillouin zone shown with k_x and k_z axis defined for the sample surface obtained by cleaving on (111) plane.

[1] A. Furusaki, Sci. Bulletin **62** (2017) 788.
[2] M. Kakihana *et al.*, J. Phys. Soc. Jpn. **84** (2015) 084711.
[3] T. Ito *et al.*, UVSOR Activity Report 2018 **46** (2019) 96.

BL5U

Electronic Band Structure of Sn_4Sb_3

W. Wen[1,2], C. Y. Hong[1,2], G. Zhao[1,2], Z. Song[1,2] and R. -H. He[2]
[1]*Department of Physics, Fudan University, Shanghai 200433, China*
[2]*School of Science, Westlake Institute for Advanced Study, Westlake University, Hangzhou 310064, China*

Recently, alloys consisting of heavy elements have received much attention because of their strong spin-orbit coupling (SOC), which could give rise to a variety of topological phases [1,2], including topological semimetals (TSM), topological (crystalline) insulators and Topological superconductors (TSC). Topological superconductors (TSC) are the superconducting analogues of TI, and have potential applications in fault-tolerant quantum computing [2-4]. The superconducting binary compound Sn_4Sb_3 has been proposed to be a candidate for TSC [5].

To study the electronic band structure of Sn_4Sb_3, we performed systematic ARPES measurements on its cleaved (001) surface, and a series of Fermi surface intensity maps were measured with linearly-horizontally (LH) polarized photons of photon energy (hν) from 60 eV to 140 eV and T=7.0 K. Figures 1(a) and (b) are two Fermi surface maps obtained with hν=70 eV and hν=115 eV. Figures 1 (c) and (d) show the Fermi surface obtained with first-principles calculations in the k_x-k_y plane at k_z=0 and k_z=π. Through comparison, we can see the experimental Fermi surface of hν=70 eV agrees with the calculated one at k_z=0, and that of hν=115 eV agrees with that at k_z=π. A good overall agreement on the Fermi surface between the measured photon energy dependence and the calculated k_z dependence can be obtained by assuming an inner potential V_0 = 12.8 eV (and the c-axis lattice constant 24.85 Å as determined from x-ray diffraction).

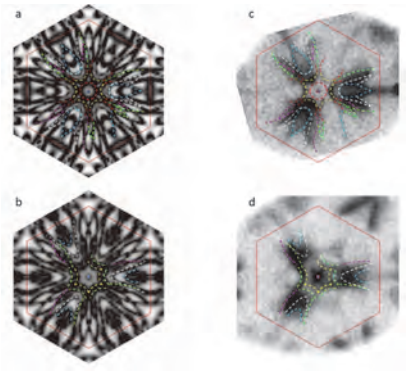


Fig. 1. ARPES measurements of the Fermi surface with LH polarized light with (a) hν = 70 eV and (b) hν= 115 eV. (c) and (d) show the Fermi surfaces in the k_x-k_y plane at k_z = 0 and k_z =π respectively. Dashed curves in different colors identify features observable in both the experiment and calculation.

Nevertheless, there are some states observed in the experiment but absent in the calculations. These states are marked as rounded dashed curves around the K points (corners of the hexagonal Brillouin zone) in Fig. 2 where the k_x-k_y energy contours at binding energy -0.3 eV measured with different photon energies are shown.

These states exhibit linear dispersions extending toward the Fermi level (Fig. 3). This appears to be consistent with the presence of Weyl points in the bulk band structure. Further analyses and comparison with first-principles calculations based on the slab model are necessary in order to establish this plausible connection before one can draw a conclusion on the Weyl nature of Sn_4Sb_3.

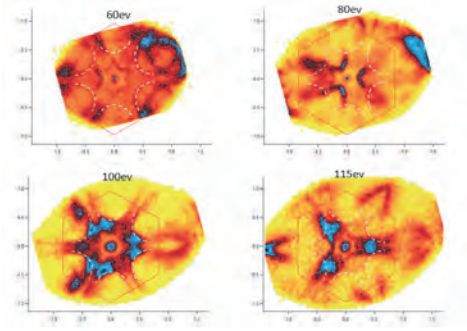


Fig. 2. Observation of surface states with hν=60 eV, 80 eV, 100 eV and 115 eV. k_x-k_y energy contours are shown at binding energy -0.3 eV, with the surface states eyeguided by the white dashed curves.

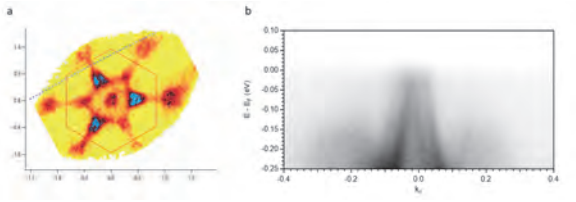


Fig. 3. Bulk-band structure and observation of the Weyl point. (a) Fermi surface maps measured with hν=105 eV. (b) Band dispersion along the blue dashed line in (a).

[1] M. Z. Hasan and C. L. Kane, Rev. Mod. Phys. **82** (2010) 3045.
[2] X. L. Qi and S. C. Zhang, Rev. Mod. Phys. **83** (2011) 1057.
[3] J. Alicea, Rep. Prog. Phys. **75** (2012) 076501.
[4] M. Sato and Y. Ando, Rep. Prog. Phys. **80** (2017) 076501.
[5] B. Liu *et al.*, Phys. Rev. Mater. **3** (2019) 084603.

BL5U

High-resolution ARPES Study of Antiferromagnetic Topological-insulator Candidate CeBi

S. Souma[1,2], K. Nakayama[3], D. Takane[3], Y. Kubota[3], T. Kawakami[3], K. Sugawara[1,2,3], M. Yoshida[4], A. Ochiai[3], T. Takahashi[1,2,3] and T. Sato[1,2,3]

[1]*Center for Spintronics Research Network, Tohoku University, Sendai 980-8577, Japan*
[2]*WPI Research Center, Advanced Institute for Materials Research, Tohoku University, Sendai 980-8577, Japan*
[3]*Department of Physics, Tohoku University, Sendai 980-8578, Japan*
[4]*Max-Planck-Institute for Solid State Research, Heisenbergstrsse 1, 70569 Stuttgart, Germany*

Cerium monopnictides CeX_p (X_p = P, As, Sb, and Bi) are a typical example of heavy-fermion systems showing an exotic and complicated magnetic phase diagram as a function of temperature, pressure, and magnetic field, known as a "devil's staircase" [1-4]. Recently, it was predicted that isostructural material LaX_p becomes a topological insulator due to the band inversion at the X point of bulk Brillouin zone [5]. The proposal of the non-trivial electronic bands has renewed the interest for RX_p (R = La and Ce) systems, and has triggered intensive theoretical and experimental investigations, resulting in the discovery of extremely large magnetoresistance and unusual resistivity plateau in LaSb and LaBi, as well as the observation of Dirac-cone-like energy band in some RX_p compounds. Taking into account such topological aspects of RX_p family, one would naturally expect that CeBi is an excellent candidate to study the interplay between magnetism and topological properties, since it shows interesting magnetic phases characterized by a two-step antiferromagnetic (AF) transition at T = 25 and 14 K under zero-magnetic field [3, 4], in addition to the expected topological nature. In a broader perspective, it is of great importance to experimentally clarify the role of antiferromagnetism to the topological properties, which is currently a target of intensive debates in theories while no concrete experimental data have been hitherto reported.

In this study, we performed high-resolution angle-resolved photoemission spectroscopy (ARPES) of CeBi to determine the bulk and surface electronic states and their evolution across the Néel temperatures. For this sake, we utilized high- energy-resolution and low-accessible-temperature capabilities of BL5U. Single crystalline samples were cleaved *in situ* in an ultrahigh vacuum of 1×10^{-10} Torr along the (100) crystal plane [see Fig. 1(a) for corresponding bulk and surface Brillouin zones].

Figures 1(b) and 1(c) show the ARPES intensity plots along the $\bar{\Gamma}\bar{M}$ cut measured in the paramagnetic (PM) and AF states, respectively. In the PM phase, we observed several bulk bands displaying the holelike and electronlike dispersions centered at the $\bar{\Gamma}$ and $\bar{M}$ points, respectively. In addition, we found the surface states with a Dirac-cone-like dispersion at the $\bar{M}$ point. In the AF phase, the overall bulk band dispersions are similar to those in the PM phase. However, the surface states show a drastic change across T_N; linearly-dispersive Dirac-like band appears at the $\bar{\Gamma}$ point. This finding suggests an intricate interplay between antiferromagnetism and topological surface states in CeBi.

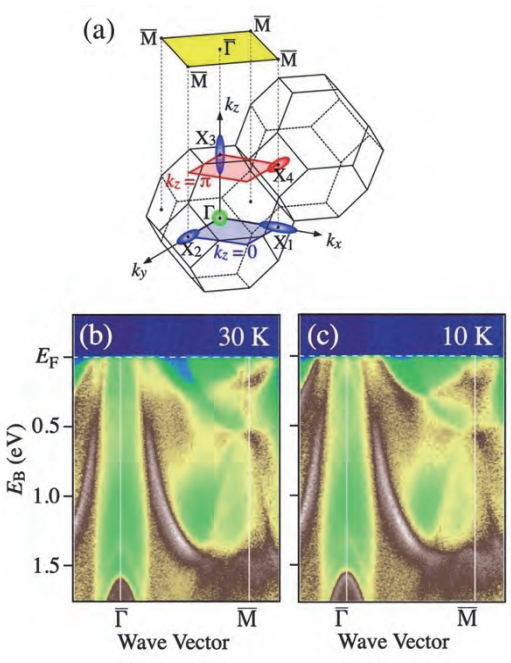


Fig. 1. (a) Bulk and surface Brillouin zones of CeBi(111). (b) and (c) ARPES intensity plots at T = 30 K and 10 K, respectively, measured with $h\nu$ = 53 eV along the $\bar{\Gamma}\bar{M}$ cut.

[1] J. Rossat-Mignod *et al.*, Phys. Rev. B **16** (1977) 440.
[2] J. Rossat-Mignod *et al.*, J. Magn. Magn. Mater. **31-34** (1983) 398.
[3] H. Bartholin *et al.*, Le J. Phys. Colloq. **40** (1979) C5.
[4] M. Kohgi *et al.*, Physica B **281-282** (2000) 417.
[5] M. Zeng *et al.*, arXiv:1504.03492 (2015).

BL5U

ARPES Studies of the Superconductors with Row-carrier-density

Y. Akimoto[1], K. Kuroda[1], K. Kawaguchi[1], S. Sakuragi[1], Y. Arai[1], Y. Wan[1], K. Kurokawa[1], H. Tanaka[1], S. Ideta[2], K. Tanaka[2], D. Hirai[1], Z. Hiroi[1], T. Yamada[3] and T. Kondo[1]

[1]*ISSP, The University of Tokyo, Kashiwa 277-8581, Japan*
[2]*UVSOR Synchrotron Facility, Institute for Molecular Science, Okazaki 444-8585, Japan*
[3]*IMRAM, Tohoku University, Sendai, 980-0812, Japan*

NaAlSi is a three-dimensional superconducting material with T_c ~7 K [1]. Previous first-principles calculations indicate that the electronic structure of NaAlSi shows semimetallic low carrier density states because of occurring of the carrier compensation. In the case of general superconductor with dilute carrier state, T_c~7 K is too high to explain in the standpoint of past reports. Thus, to understand the relationship between electronic states and the superconducting mechanism of NaAlSi will open the new way to develop the high T_c superconductor. In addition, recent theoretical study has shown that the electronic structure of NaAlSi shows Dirac nodal line, and this material is the candidate of topological superconductor [2].

Although the superconductivity of this material has been discovered over 10 years ago [3], the electronic structure has not yet been determined experimentally due to the unstable nature of the material under the atmosphere. In this beamtime, we solved this problem by preparing the sample in a glove box, and directly observed the electronic structure of NaAlSi using angle-resolved photoemission spectroscopy (ARPES) using synchrotron radiation.

As a result of the ARPES measurement, the crossing between valence band originating from the Si-2*p* orbitals and the conduction band originating from the Al-3*sp* orbitals is occurred, and Dirac nodal line, which predicted by theoretical study, is observed. The valence band has a flat shape near the Fermi level. The result of k_z dependent band dispersion measurement indicates that the electronic structure of NaAlSi showing pseudo two dimensionally (Fig. 1). As shown in Fig. 1, the Fermi wave number k_F is observed only at specific k_z.

We tried to evaluate the superconducting gap in this electronic structure from the synchrotron ARPES measurement in BL5U having low temperature / high resolution measurement system. From the comparison between the leading-edge-midpoint measured at 4 K (superconducting state) and that of 8 K (normal state), the leading-edge-midpoint shift, i.e., superconducting gap is observed at 4 K. This result suggests the possivillity of the relationship between unique two-dimensional electronic structure with the dilute carrier state and occurring of the superconductivity in this material.

In future, if the superconducting mechanism and topological states of this material are fixed, we may establish the new standpoint in order to develop the high T_c topological superconductor.

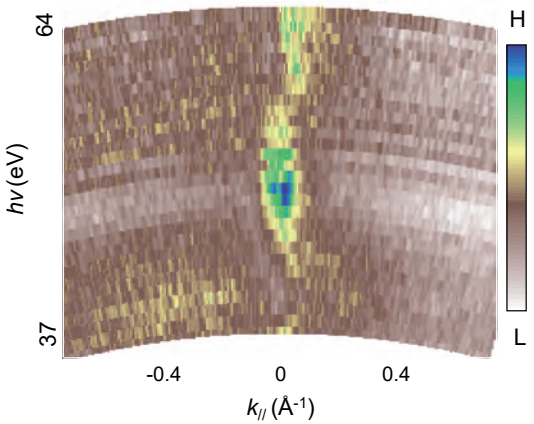


Fig. 1. k_z dispersion around Fermi level of NaAlSi.

[1] H. B. Rhee *et al*., Phys. Rev. B **81** (2010) 245114.
[2] L. Jin *et al*., J. Mater. Chem. **7** (2019) 10694.
[3] S. Kuroiwa *et al*., Physica C **466** (2007) 11.

BL5U

Demonstration of Final State Effect: Deflector Map in Double Layer Cuprate Bi2212

S. Ideta[1,2], S. Ishida[3] and K. Tanaka[1,2]

[1]*National Institutes of Natural Science, Institute for Molecular Science, Okazaki 444-8585, Japan*

[2]*The Graduate University for Advanced Studies, SOKENDAI, Okazaki 444-8585, Japan*

[3]*Electronics and Photonics Research Institute, National Institute of Advanced Industrial Science and Technology, Tsukuba 305-8565, Japan*

To understand the mechanism of high-T_c superconductivity in cuprates is one of the crucial issues. Angle-resolved photoemission spectroscopy (ARPES) is a powerful tool to investigate the electronic structure of solids directly, and has contributed significantly towards an elucidating of the nature of superconductivity of cuprates [1]. However, ARPES spectrum have a strong constraint of the final state effect arising from especially the energy and polarization of the incident photons [2,3]. In addition, in the conventional ARPES experiment, one needs to rotate samples to obtain the information of momentum space. Recently, deflector mode for mapping has been developed and we do not need to rotate samples. We report that the final state effect using a state of the art ARPES system with a new electron lens with deflectors (MB Scientific AB) in Double-layer Bi-based cuprate superconductor, $Bi_2Sr_2Ca_2CuO_{8+\delta}$ (Bi2212).

Bi2212 is the one of the most common samples to study the electronic structure using ARPES. Bi21212 has two equivalent CuO_2 planes and therefore shows the bilayer splitting reflecting bonding and anti-bonding bands. In this study, as a first step to elucidate the final state effect using the deflector mode and sample rotation mode, we have investigated the momentum space mapping using the deflector mode on underdoped Bi2212 along the Cu-O and Cu-Cu directions (*s* polarization).

High-quality single crystals of underdoped $Bi_2Sr_2Ca_2CuO_{8+\delta}$ (UD Bi22212, T_c = 65 K) were grown by the TSFZ method. ARPES experiments were carried out at BL5U of UVSOR-III Synchrotron. Clean sample surfaces were obtained for the ARPES measurements by cleaving single crystals *in-situ* in an ultrahigh vacuum better than 8×10^{-9} Pa. The measurements were performed at 20 K.

In order to estimate the distribution of the spectral weight on momentum space, ARPES experiments have been demonstrated by linearly polarized light and Fermi surfaces (FSs) are observed as displayed in Fig. 1. Figures 1(a) and 1(b) show FSs highlighted by red dotes corresponding to the Fermi momentum, k_F, but the experimental momentum cut is along the Cu-O and Cu-Cu directions, respectively. Due to the photon energy, we could not resolve the bilayer splitting in the present study ($h\nu$ = 60 eV). From this result, we found that the deflector mode mapping shows a similar FS reported in previous ARPES study [4-7]. In addition, integrated spectral intensity plotted as a function of FS angle [Figs. 1(c) and 1(d)], and these two experimental geometries have different momentum dependence for the spectral intensity.

As future work, we need to investigate FS mapping using the conventional sample rotation method to compare the spectral weight on momentum space with the result of Fig.1. In addition, we will demonstrate doping dependence and photon energy dependence. These experimental studies will put additional experimental constraint on various microscopic theories and data analysis.

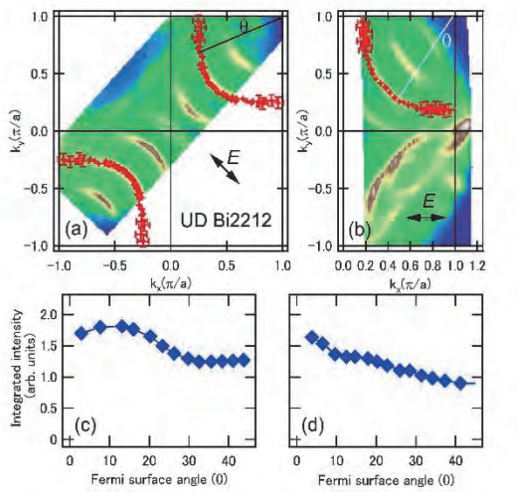


Fig. 1. Momentum-space mappings in underdoped (UD) Bi2212 at energies of -0.01 eV and 0.01 eV ($h\nu$ = 60 eV, T = 20 K). (a) Mapping along Cu-O direction (nodal direction). (b) Mapping along the Cu-Cu direction (antinodal direction). (c), (d) Spectral intensity integrated by ±2 degree around k_F is plotted as a function of Fermi surface angle.

[1] A. Damascell *et al*., Rev. Mod. Phys. **75** (2003) 473.
[2] A. Bansil *et al*, Phys. Rev. Lett **83** (1999) 5154.
[3]D. L. Feng *et al*., Rhys. Rev. B **65** (2002) 220501(R).
[4]T.-G. Zhong *et al*., Phys. Rev. B **98** (2018) 140507(R).
[5]J. D. Rameau *et al*., Phys. Rev. B **90** (2014) 134509.
[6]K. Tanaka *et al*., J. Phys. Soc. Jpn. **88** (2019) 044710.
[7] P. B. Bogdanov *et al*., Phys. Rev. Lett. **89** (2002) 167002.

BL5U

Polarization Dependence of the Photoelectron Intensity Distribution from MoS_2

S. Tanaka[1], K. Ueno[2], S. Ideta[3] and K. Tanaka[3]
[1]*The institute of Scientific and Industrial Research, Osaka Univ., Ibaraki 567-0047, Japan*
[2]*Graduate School of Science and Engineering Saitama University, Saitama 338-8570, Japan*
[3]*UVSOR Synchrotron Facility, Institute for Molecular Science, Okazaki 444-8585, Japan*

The photoelectron intensity in the angle-resolved photoelectron spectroscopy (ARPES) is determined by the Femir's golden rule, where the matrix element $\langle \varphi_f | \mathbf{A} \cdot \mathbf{p} | \varphi_i \rangle$ plays a crucial role. In the matrix element, $< \varphi_f |$ denotes the final state which is approximately the plane wave; $\mathbf{A} \cdot \mathbf{p}$ corresponds to the photoexcitation Hamiltonian and $\mathbf{A}$ and $\mathbf{p}$ respectively denote the vector potential of the photon and the momentum of the electron. We can change $\mathbf{A}$ by controlling the polarization of the photon, and detailed electronic properties of the initial state $|\varphi_i >$ can be investigated by the polarization-dependent photoelectron intensity distribution.

For this purpose, we made an investigation for the band at the top of the valence band in MoS_2, which is mainly constructed from the Mo-4d and S-3p orbitals. Figures 1 show the constant energy maps at the binding energy of 0.77 eV taken at hν=60 eV. The polarizations of the incident photons are linearly horizontal (i.e., p-pol), linearly vertical (i.e., s-pol), circularly right-handed (CW), and circularly left-handed (CCW). The band forms a circular shape around the Γ-point. This means that the operation of rotation for the wavefunction does not change the energy (the eigenvalue of the Hamiltonian), and the angle around the Γ-point is a good quantity for describing the system. The photoelectron intensity distributions are drastically changed with changing the polarization. The intensity distributions as functions of the azimuthal angle are displayed after expanding by repeating the signals as the period of 2π in Figs. 2. The distribution taken with the vertical polarized light shows a complete different one from the other three. The horizontal, CW, and CCW polarizations yield the distribution of nearly the same form $I_0 \cos^2\left(\frac{\theta-\theta_0}{2}\right)$, although the phases are shifted as changing the polarization. The phase-shift in the photoelectron intensity distribution with changing the photon polarization was reported for the Dirac cone of the graphene, where the "Berry's phase" of the wavefunction in the Dirac cone plays a key role [1]. Accordingly, an important information about the wavefuntion of the valence band MoS_2 will be given. Theoretical investigation and more detailed analysis are in progress.

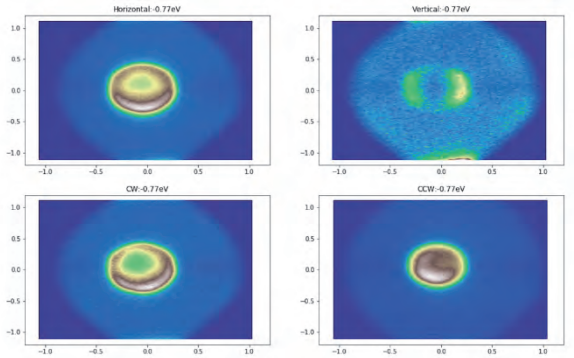


Fig. 1. Polarization-dependent photoelectron intensity map at the binding energy of 0.77 eV near the Γ-point of MoS_2.

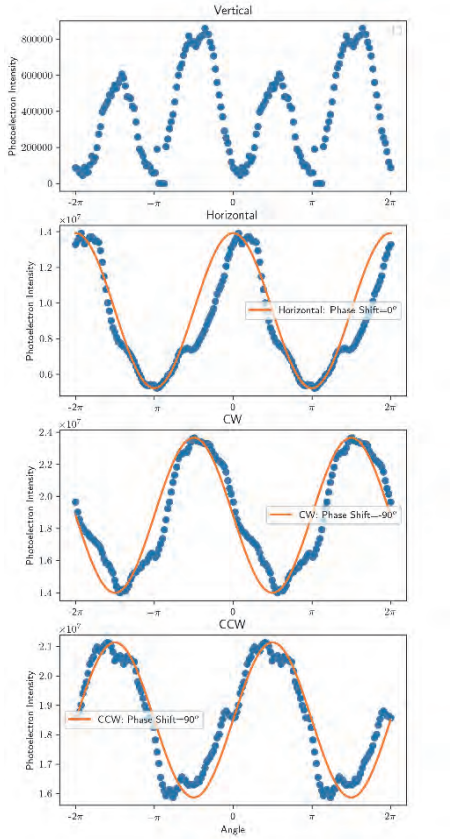


Fig. 2. Photoelectron intensity distribution at the binding energy of 0.8 eV as a function of the angle around the Γ-point of MoS_2. Solid lines show $I_0 \cos^2\left(\frac{\theta-\theta_0}{2}\right)$, where θ_0 is the phase-shift.

[1] Y. Liu *et al.*, Phys. Rev. Lett. **107** (2011) 166803.

BL5B

Study on Optical Properties of Metallic Sodium by Vacuum Ultra Violet in UVSOR (2)

M. Kawaguchi [1,2], J. Saito[1], H. Daido[3] and T. Suemoto[4]

[1]*Sodium Technology Development Group, Japan Atomic Energy Agency, Tsuruga 919-1279, Japan*
[2]*Research Institute of Nuclear Engineering, University of Fukui, Tsuruga 914-0055, Japan*
[3]*Institute for Laser Technology, Suita 565-0871, Japan*
[4]*Toyota Physical and Chemical Research Institute, Nagakute 480-1192, Japan*

Metallic sodium is well-known as a typical alkali metal, but the optical properties in vacuum ultraviolet (VUV) range are controversial [1,2]. One of the authors (H. D.) demonstrated VUV light (Wave length: 115-180 nm) penetrates in several millimeters of sodium with high transmittance for the first time [3]. Inspired by the experiment, the transmittance measurement of metallic sodium using VUV has been performed at BL5B in UVSOR [4]. In this year, we adopted calcium fluoride (CaF_2, Pier Optics Co, ltd.) for windows of the sodium sample (Diameter: 18 m^{φ}, Thickness: 2.0 mm^{t}) to decrease interaction between the sodium and the windows, which were seemed to be one of significant causes of decreasing drastically the transmittance.

Figure 1 shows intensities of 0^{th} light, 1^{st} light and transparent VUV, which denote the raw light radiated from UVSOR, the light passed through lithium fluoride (LiF) filter, and the transparent light passed through the LiF filter and the CaF_2 windows, respectively. Because of the band gaps, the LiF and the CaF_2 can be transparent to more than about 100 nm and about 120 nm in wave length, respectively. Therefore, the intensities of the 1^{st} light and the transparent VUV show the stepwise increases in the characteristic wave lengths, which are corresponded to those of the LiF and the CaF_2. Figure 2 shows the transmittance of the CaF_2 windows, which was obtained by dividing the intensity of the transparent VUV by that of the 1^{st} light. In this calculation, the 0^{th} light can't be used because it includes the short-range wave-length light. The measured transmittance of CaF_2 windows is almost consistent with the literature datum [5], and it concluded that there were no problems in the transmittance measurement and CaF_2 windows.

However, the transparency phenomenon of VUV in the metallic sodium has never been confirmed by our group. Because the reaction (deterioration) of the sodium on the surface of the windows proceeded gradually and the products might hinder the transparency of VUV, we need to improve the technique of making the sodium sample.

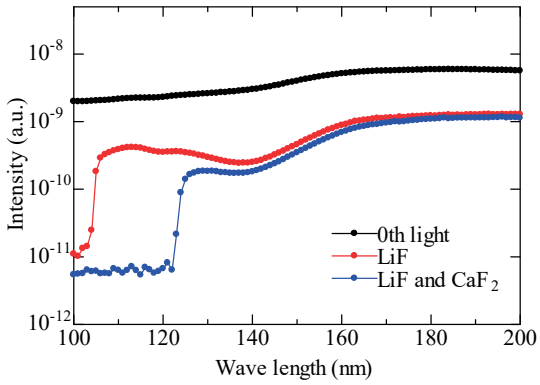


Fig. 1. Intensities of 0^{th} light at BL5B and of lights through LiF and CaF_2 windows ($2mm^{t}$), and transmittance of CaF_2 window.

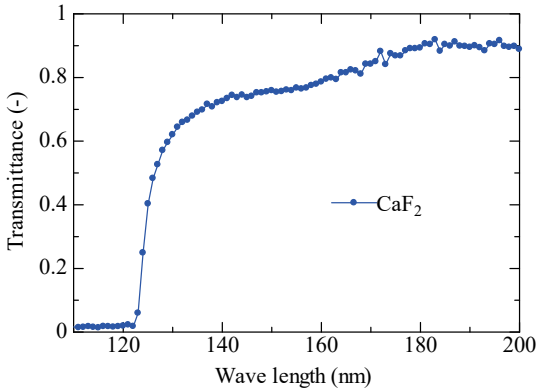


Fig. 2. Transmittance of CF_2 windows

[1] J. C. Sutherland *et al.*, Optical properties of sodium in the vacuum ultraviolet (ORNL-TM-1776, Oak Ridge National Laboratory, 1967).
[2] R. W. Wood, Phys. Rev. **44** (1933) 353.
[3] H. Daido *et al.*, Optics express **21** (2013) 28182.
[4] M. Kawaguchi, J. Saito, H. Daido and T. Suemoto, UVSOR Activity Report 2018 **46** (2019) 89.
[5] http://www.pier-optics.com/transparent.html

BL6U

Temperature-dependent Electronic Structure of a Quasi-2D Material η-Mo_4O_{11}

T. Kobayashi[1], E. Iwamoto[2], K. Sakamoto[2], M. Koyano[3], F. Matsui[4] and S. Suga[5]
[1]*Department of Material and Life Science, Osaka University, Suita 565-0871, Japan*
[2]*Department of Applied Physics, Osaka University, Suita 565-0871, Japan*
[3]*School of Materials Science, Japan Advanced Institute of Science and Technology, Nomi 923-1292, Japan*
[4]*UVSOR Synchrotron Facility, Institute for Molecular Science, Okazaki 444-8585, Japan*
[5]*Institute of Scientific and Industrial Research, Osaka University, Ibaraki 567-0047, Japan*

Angle resolved photoelectron spectroscopy (ARPES) with extremely high resolutions in both energy and momentum is indispensable to obtain detailed understanding of various phenomena in condensed matters physics, such as charge density wave (CDW), Rashba effect, properties of topological materials, and so on. These kind of studies may be effectively performed by momentum microscopy (MM) in the near future.

In order to check the performance of the beam line BL6U, where the MM is planned to be setup, we have measured the electronic structure of a quasi-2D material η-Mo_4O_{11} at different temperatures. By performing electrical resistivity measurements, η-Mo_4O_{11} has been reported to show transitions at T_{c1}=109 K and T_{c2}=30 K that are very likely due to CDW instabilities [1]. However, neither band gap opening nor band folding, which should be present in case of CDW transition, has been observed in the former ARPES study [2]. In the present study, we performed ARPES measurements at temperatures above and below the two CDW transitions to obtain more detailed information on the property of this material.

Figure 1 shows the Fermi surface of η-Mo_4O_{11} measured at 8.6 K. Straight lines indicating the presence of three 1D metallic bands in different direction are clearly observed. The observation of three 1D metallic bands is consistent with that reported in Ref. [2] but not with the electrical resistivity measurements [1] since the measurement temperature in Fig. 1 is lower than T_{c2}. The Fermi wave number of the metallic bands are ca. 35 % of the Brillouin zone. In Fig. 2, we show the energy distribution curves (EDC) measured at $T>T_{c1}$ (300 K), $T_{c1}>T>T_{c2}$ (60 K), and $T_{c2}>T$ (8.6 K). As well as the result in Fig. 1, no trace of CDW transition can be confirmed in Fig. 2. The peak just below the Fermi level shift a bit to lower binding energy and becomes shaper as the temperature decreases. The energy shift and the change in the Fermi wave vector (not shown) indicate hole-doping during the cooling. The closer the Fermi surface is to the half of the Brillouin zone the more likely the CDW transition occurs. In the present case, the Fermi surface is much smaller than the half of the Brillouin zone and thus the metallic behavior at all temperatures might be resulting from the hole-doping induced by the residual gas adsorption.

Since the in situ cleavage was successful to provide single crystal domains of the order of sub-mm, and because very complex band structures were detected in the present study, η-Mo_4O_{11} would be a suitable material for checking the performance of the MM in the near future.

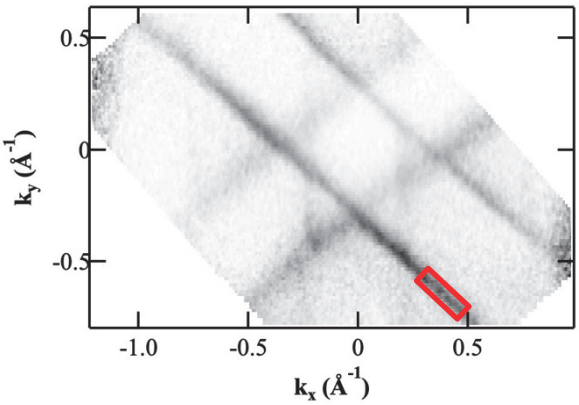


Fig. 1. Fermi surface of η-Mo_4O_{11} measured at 8.6 K.

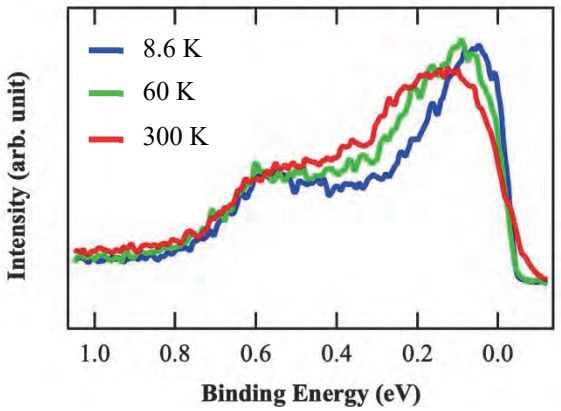


Fig. 2. EDC spectra obtained by integrating the data surrounded by the red rectangle shown in Fig. 1.

[1] H. Guyot *et al.*, J. Phys. C **16** (1983) L1227.
[2] G.-H. Gweon *et al.*, Phys. Rev. B **72** (2005) 035126.

BL6U

Angle-Resolved Photoemission Spectroscopy of Topological Insulators for Clarification of Origin of Pressure-Driven Superconductivity

Y. Kubozono[1], R. Eguchi[1], H. Goto[1], T. He[1], K. Kobayashi[1], T. Takahashi[1], H. Ozaki[2], K. Hayashi[2] and F. Matsui[3]

[1]*Research Institute for Interdisciplinary Science, Okayama University, Okayama 700-8530, Japan*
[2]*Nagoya Institute of Technology, Nagoya 466-8555, Japan*
[3]*Institute for Molecular Science, Okazaki 444-8585, Japan*

Two-dimensional angle-resolved photoelectron spectroscopy (ARPES) is a powerful tool to study the electronic structure of crystalline materials, in particular the unique electronic structures of topological materials such as topological insulators, Dirac / Weyl semimetals, and axion insulators have been extensively investigated during a past decade. The initial state binding energy (E) and the wave vector ($\boldsymbol{k}$) can be easily determined from the kinetic energy and the direction of the detected ARPES data. Some of topological insulators such as $Bi_{2-x}Sb_xTe_{3-y}Se_y$ [1] and Sr or Ag doped Bi_2Se_3 [2,3] provided the pressure-driven superconducting phases.

To understand the correlation between the electronic property and pressure-driven superconductivity, we must obtain the detailed information of electronic structures of topological insulators at ambient pressure. Admittedly, in case of $Bi_{2-x}Sb_xTe_{3-y}Se_y$, the Fermi level and Dirac point significantly shifted against x and y [4]. Therefore, the superconductivity of topological insulators induced by pressure must be investigated by associating exactly with their electronic structures, as well as with the structural transitions. In addition, the superconducting gap function (Cooper pair symmetry) of pressure-driven superconductivity in topological insulators must be clarified to show the topologically non-trivial nature of superconductivity, which requires the exact information of electronic structures at ambient pressure. For these purposes, the study on electronic structure by ARPES is indispensable for topological insulators. In this study, we measured the ARPES data of Ag doped Bi_2Se_3 ($Ag_xBi_{2-x}Se_3$; x = 0.05), Nb doped Bi_2Se_3 ($Nb_xBi_2Se_3$; x = 0.5), $Bi_{2-x}Sb_xTe_{3-y}Se_y$ (x = 1.0, y = 2.0) and those precursor sample, Bi_2Se_3 using the MBS A-1 Lens#5 analyzer installed at BL6U.

We measured the ARPES data of the non-doped Bi_2Se_3 single crystal recorded at room temperature. A clear band dispersion showing a single Dirac cone, and conduction / valence bands was recorded as previously reported [5]. This means that the measurement system is available for detecting the exact information of electronic structures of topological insulators.

We measured the ARPES of $Ag_xBi_{2-x}Se_3$ (x = 0.05) single crystal at 10 K. At the present stage, the ARPES of $Ag_xBi_{2-x}Se_3$ was not distinguished from that of Bi_2Se_3, *i.e.*, the Ag doping was ambiguous. The reason is not clear, but one possibility that the cleaved surface of single crystal of $Ag_xBi_{2-x}Se_3$ might not include Ag atom was suggested. In other words, the area where no Ag atoms are included may be selectively cleaved in the $Ag_xBi_{2-x}Se_3$ crystal.

Moreover, we measured the ARPES of $Nb_{0.5}Bi_2Se_3$. A clear superconducting transition at ~3 K was observed in the magnetic susceptibility for this material. Figure 1 shows the band dispersion of $Nb_{0.5}Bi_2Se_3$ measured at 10 K. Fermi energy is 55.5 eV in kinetic energy. A single Dirac cone and the top of the valence band were observed.

Now, we are trying to measure the ARPES of new topological insulators which was recently found to show the pressure-driven superconductivity.

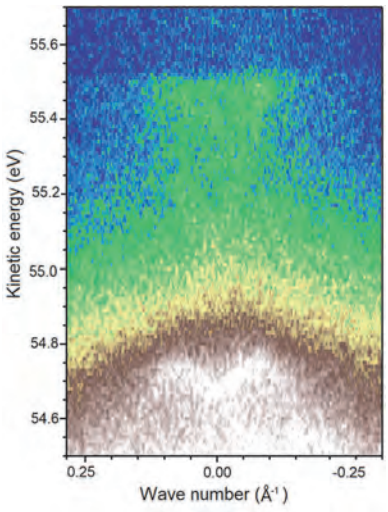


Fig. 1. Band dispersion of $Nb_{0.5}Bi_2Se_3$.

[1] T. He *et al.* Phys. Rev. B **100** (2019) 094525.
[2] Y. Zhou *et al*. Phys. Rev. B **93** (2016) 144514.
[3] T. He *et al.* Phys. Rev. B **97** (2018) 104503.
[4] T. Arakane *et al*. Nature Commun. **3** (2012) 636.
[5] Y. L. Chen *et al.* Science **329** (2010) 659.

BL6U

Photon-energy-dependence in the Photoelectron Angular Distribution from MoS_2

S. Tanaka[1], K. Ueno[2], H. Matsuda[3] and F. Matsui[3]

[1]*The institute of Scientific and Industrial Research, Osaka Univ., Ibaraki 567-0047, Japan*

[2]*Graduate School of Science and Engineering Saitama University, Saitama 338-8570, Japan*

[3]*UVSOR Synchrotron Facility, Institute for Molecular Science, Okazaki 444-8585, Japan*

2H-MoS_2 is one of the most typical transition metal dicalchogenides, and its electronic property is a fundamental issue for the fabrication of new functional low-dimensional electronic devices. In this report, we show a comparison in the momentum space between the ARPES measurement by using photons in the wide energy range (60-200 eV) and the DFT-calculation to demonstrate the validity of the photon-energy-dependent ARPES for identifying the characterization of the valence band of the materials.

The ARPES measurements were carried out at the room temperature, and the DFT calculation was made employing the QUANTUM ESPRESSO package (version 6.3), which had been installed in the computer at Research Center for Computational Science in IMS. Figures 1 show a part of the series of the photon-energy-dependence in the photoelectron angular distribution from MoS_2 at the same binding energy (1.8 eV). The first Brillouin zones are indicated as black lines. Shapes clearly change as a function of the photon energy; at 73-93 eV and 149 eV, a hexagon consisting of small triangles is shown; at 113 eV, a smaller hexagram is shown; and at 103 eV, both are shown. This behavior is not consistent with the calculated k_z value (not shown here), and thus cannot be interpreted to the dispersion along the k_z axis. Instead, this can be ascribed to the character of the band. Figures 2 show the calculated projected density of states for the Mo-4d and S-3p orbitals in the momentum space at the binding energy of -1.2 eV. The binding energy for the calculation was chosen so as to display shapes similar to the experiments. The discrepancy of 0.6 eV may partly be to the difference in the reference (in the ARPES, it is the Fermi level measured by using Au film, and in the DFT calculation it is the valence band maximum). It is clear that ARPES results at photon energies of 73-93 eV resembles to the band provided by Mo-4d while the hexagram shape obtained by ARPES at 103-113 eV resembles to the band of S-3p. Figure 3 shows the photoexcitation cross section of the atomic orbitals. The photoexcitation cross section of Mo-4d is higher than S-3p in the photon energy regions below ~70 eV and above ~170 eV. Although the crossing point at ~70 eV in Fig. 3 is significantly lower than ~100 eV which is derived from Figs. 1, a general trend shows a good agreement, and thus the characteristics of the band is well explained. More detailed analyses are in progress.

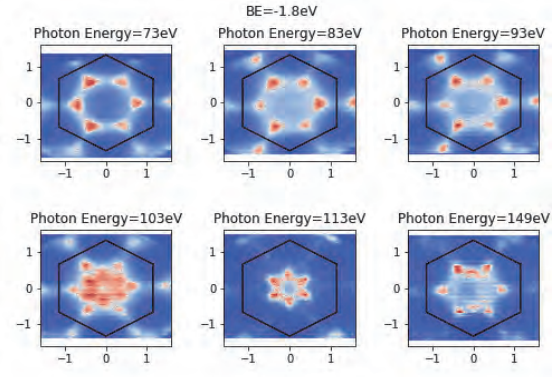


Fig. 1. Photoelectron angular distributions of the same binding energy from MoS_2 at various photon energies.

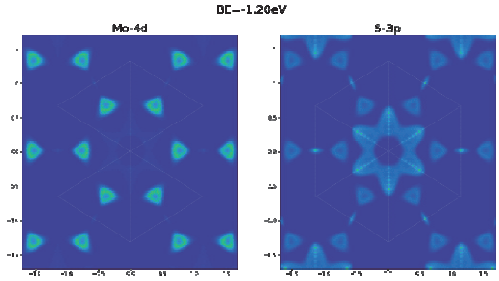


Fig. 2. Calculated density of states at BE=-1.2 eV which are projected into the Mo-4d and S-3p orbitals

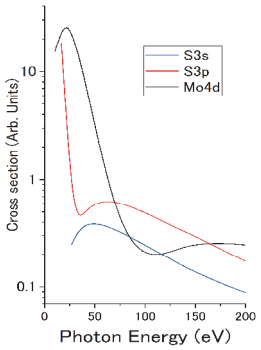


Fig. 3. Phototexcitation cross sections of S3s, S3p and Mo4d atomic orbitals [1].

[1] J. J. Yeh *et al.*, At. Data Nucl. Data Tables **32** (1985) 1.

BL6U

Anisotropy of Photoelectron Intensity Distribution upon Hole-Vibration Coupling in Perfluoropentacene Monolayer on Ag(111)

Y. Hasegawa[1], K. Maduwantha[2], R. Koswattage[2], T. Nakamura[3], F. Matsui[4] and S. Kera[1,4]
[1]*Department of Photo-Molecular Science, Institute for Molecular Science, Okazaki 444-8585, Japan*
[2]*Sabaragamuwa University of Sri Lanka, Belihuluoya 70140, Sri Lanka*
[3]*Department of Physics, Graduate School of Science, Osaka University, Toyonaka 560-0043, Japan*
[4]*UVSOR Synchrotron Facility, Institute for Molecular Science, Okazaki 444-8585, Japan*

Organic semiconductor thin films have been getting attention as next promising optical and electronic devices. Optimizing charge transfer between weakly connected materials is one of a key issue to improve the performance. Considering the charge transfer is affected by the coupling of the charge to specific vibrational modes of molecules, the impact of anisotropic deformation of a molecule upon ionization at the interface on the transfer efficiency should be investigated.

We have found perfluoropentacene (PFP) monolayer on inert crystalline substrate shows hole-vibration coupling upon angle-resolved ultraviolet photoelectron spectroscopy (ARPES) measurement and distinct angular distribution of highest occupied molecular orbital (HOMO) features depending on the vibronic couplings [1]. To address the origin of the photoelectron intensity distribution of the vibronic states, a precise experiment of the photoelectron momentum map (PMM) was carried out to evaluate the intensity modulation.

PFP monolayer of 2.5 Å was deposited onto a clean Ag(111) substrate. Low energy electron diffraction (LEED) and PMM were carried out at the sample temperature of 16 K. PMM was taken by means of acceptance-cone-tunable spectrometer equipped with A-1 analyzer (MBS) which enables mechanical deflector scan. Detail of the setup is reported elsewhere [2].

ARPES measurement of PFP monolayer on Ag(111) shows HOMO with fine structure, a main peak of HOMO, labeled H(00), followed by the vibrational progression of satellite peaks toward higher binding energy. Figures 1(a) and (b) are PMM taken from H(00) and the first satellite, H(01), respectively. The PMMs correspond to the photoelectron intensity integrated for the two different domains, where the molecular arrangements of A and C are shown in Fig. 1 (c). Note the one from arrangement A is marked by dashed oval. Figure 2 shows the line profiles of the PMMs taken from k_1 and k_2 direction marked by dashed and solid allows in Fig. 1, respectively. In direction of k_2 subtle difference of the intensity between H(00) and H(01) is observed whereas little difference is evaluated in direction of k_1. This observation indicates that the nuclei position is not fixed during the photoionization process as found in gas-phase system, meaning the breaking of sudden approximation in the thin film. Moreover the wavefunction of the molecular orbital is modulated only in a certain direction upon a specific hole-vibration coupling, thus designing a distortion of the molecular structure in real space upon ionization would be important to control device characteristics. The correlation between the distortion of the molecule upon vibronic excitation and the PMM would be further discussed beyond Franck-Condon approximation.

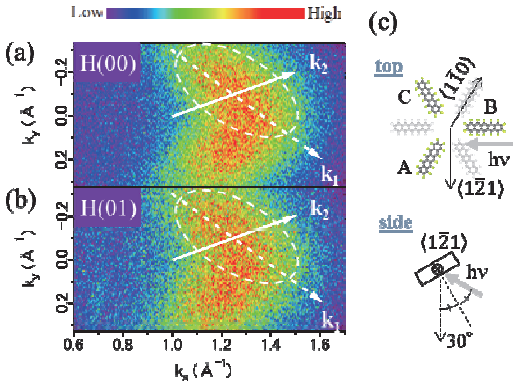


Fig. 1. PMM image taken at the HOMO of the (00) and (01) peaks (ΔE ~ 50 meV) of PFP/Ag(111) with hv = 50 eV. The color scaling and intensity are normalized at maximum intensity. (c) Geometry for the measurement.

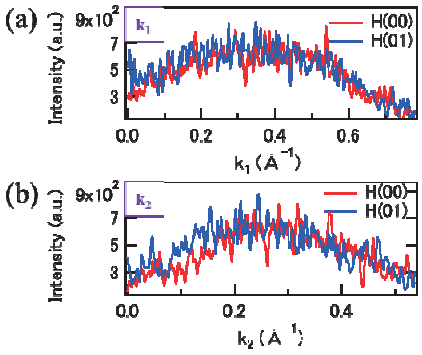


Fig. 2. Line profiles taken from H(00) and H(01) indicated by white arrows, (a) k_1 and (b) k_2 in Figs. 1(a) and (b), respectively. Origins of k_1 and k_2 in (k_x,k_y) are (1, -0.3) and (1.0, 0.0), respectively.

[1] S. Kera *et. al.*, Prog. Surf. Sci. **84** (2009) 135.
[2] H. Yamane *et. al.*, Rev. Sci. Instrum. **90** (2019) 093102.

BL6B, BL7B

Anisotropic Metal-Insulator Transition in RuAs

Y. Nakajima[1], Z. Mita[2], H. Watanabe[2,1], Y. Ohtsubo[2,1], T. Ito[3,4], H. Kotegawa[5], H. Sugawara[5], H. Tou[5] and S. Kimura[2,1]

[1]*Department of Physics, Graduate School of Science, Osaka University, Toyonaka 560-0043, Japan*
[2]*Graduate School of Frontier Biosciences, Osaka University, Suita 565-0871, Japan*
[3]*Nagoya University Synchrotron Radiation Research Center, Nagoya University, Nagoya 464-8603, Japan*
[4]*Graduate School of Engineering, Nagoya University, Nagoya 464-8603, Japan*
[5]*Department of Physics, Graduate School of Science, Kobe University, Kobe 657-8501, Japan*

Ruthenium mono-antimonide, RuAs, which is one of related materials to iron-pnictide superconductors, shows a metal-to-insulator (MIT) transition accompanied with structural change [1]. The metallic character at room temperature changes to an insulating one detected by an electrical resistivity measurement [2] through a two-step structural phase transition at about 250 K (T_{MI1}) and about 200 K (T_{MI2}). The orthorhombic crystal structure with space group *Pnma* at room temperature changes to the formation of a 3×3×3 superlattice of the original unit cell of the monoclinic structure with space group $P2_1/c$ below T_{MI2}. However, the origin of the two-step phase transition has not been clarified yet because the intermediate phase at temperatures between T_{MI1} and T_{MI2} has not been identified. So, to clarify the change of the electronic structure due to the two-step phase transition, we measured temperature-dependent polarized optical conductivity [$\sigma(\omega)$] spectra and revealed the anisotropic change of the electronic structure.

Optical reflectivity [$R(\omega)$] spectra as well as $\sigma(\omega)$ spectra of single-crystalline RuAs samples, with the largest size of about 0.1×0.5×0.2 mm^3, were measured along the *b* and *c* axes in the photon energy range from 15 meV to 30 eV to ensure an accurate Kramers-Kronig analysis (KKA). Infrared (IR) and terahertz (THz) measurements at the photon energy regions of 15 meV to 1.5 eV have been performed using conventional reflectivity measurement setups and IR and THz microscopes at BL6B. In the photon energy range of 1.2–30 eV, the $R(\omega)$ spectrum was measured only at 300 K at BL7B for accurate KKA.

Figure 1 shows the temperature dependence of the $\sigma(\omega)$ spectra at around 200 K (~T_{MI2}), where large spectral change is expected. In E // b_H, which is the *b* axis above T_{MI2}, the spectrum changes little above 200 K, but below the temperature, the intensity at ~ 0.1 eV decreases, and that at about 0.16 eV increases, suggesting the appearance of an energy gap. At 160 K, the energy gap structure becomes recognized spectrum at 210 K slightly changes from that at 230 K, where clearly, as shown in Fig. 1. On the other hand, in E // c_H, the spectrum at 210 K slightly changes from that at 230 K where the intensity below (above) 0.22 eV decreases (increases). The change becomes clearer with decreasing temperature, which indicates the energy gap opening. These results imply that the spectral change in E // b_H starts at T ≲ 210 K, but that in E // c_H gradually occurs between 210 and 230 K. This suggests that the temperature of the $\sigma(\omega)$ spectral change as well as the change of the electronic structure is anisotropic, i.e., the change along the b_H (c_H) axis occurs at lower (higher) temperature. The anisotropic change of the electronic structure is considered to be the origin of the two-step phase transition [3].

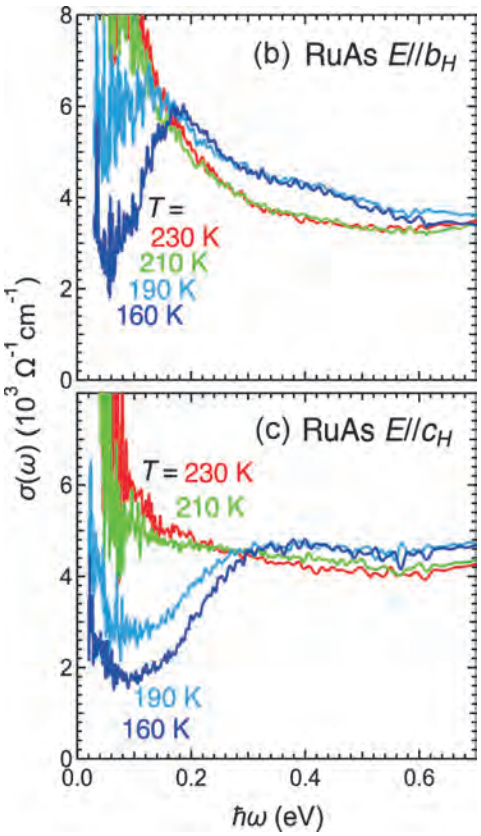


Fig. 1. Temperature-dependent polarized $\sigma(\omega)$ spectra of RuAs in E // b_H and E // c_H near the first-order phase transition temperature of ~200 K (T_{MI2}).

[1] D. Hirai *et al.*, Phys. Rev. B **85** (2012) 140509(R).
[2] H. Kotegawa *et al.*, Phys. Rev. Mater. **2** (2018) 055001.
[3] Y. Nakajima *et al.*, Phys. Rev. B **100** (2019) 125151.

BL6B

Infrared Reflectivity Spectrum for Au-codoped Mg_2Si:Bi Crystal

T. Tanimoto[1], M. Kitaura[2], H. Udono[3] and A. Ohnishi[2]
[1]*Graduate school of Science and Engineering, Yamagata University, Yamagata 990-8560, Japan*
[2]*Faculty of Science, Yamagata University, Yamagata 990-8560, Japan*
[3]*Department of Electrical and Electronics Engineering, Ibaraki University, Hitachi 316-8511, Japan*

Mg_2Si is a thermoelectric material with high figure of merit *ZT*. This material is composed of nontoxicity and abundant elements, and attract much attention as a KANKYO semiconductor [1]. The value of *ZT* is generally influenced by the carrier concertation. The increase in carrier concertation is mainly caused by impurity doping. The effect of such impurity doping on thermoelectric properties of Mg_2Si has been studied so far. The Bi atom is known as an effective element for electron doping in Mg_2Si. The electronic structure of Bi-doped Mg_2Si (Mg_2Si:Bi) has been studied [2]. Recently, it was reported that the carrier concentration above 10^{20} cm^{-3} is attained by multiple impurity doping [3]. On the other hand, the effect of impurity codoping on the carrier concertation has not yet been reported for Mg_2Si:Bi.

In the present study, the effect of Au codoping on the carrier concertation in Mg_2Si:Bi was investigated. In this work, infrared reflective spectra were measured at 300 K to determine the carrier concentration of an Au-codoped Mg_2Si:Bi crystal. In n-type semiconductors, infrared reflectivity spectra exhibit the structure due to the plasma reflection, which arises from collective excitation of free electrons [4]. The carrier concentration can be determined by analyzing the plasma reflection.

Au-codoped Mg_2Si:Bi crystals were grown from the melt by the Bridgeman method. Infrared reflectivity spectra were obtained using a FT-IR spectrometer at the beamline BL6B. The infrared reflectivity spectra were analyzed using the software RefFit [5]. The parameters of the plasma frequency ω_p, dielectric constant ε_∞, and damping constant Γ_p were determined by the fit of the Drude-model to the experimental data. Using these parameters, the carrier concentration *N* and relaxation time τ were also determined, and was compared to that determined by the Hall effect experiment.

Generally, it is hard to determine the absolute reflectivity correctly, because the absolute reflectivity is sensitive to roughness and contamination of the crystal surface. The absolute reflectivity was corrected using the refractive index and dielectric constant at 5000 cm^{-1} in the transparent region [4,6]. The infrared reflectivity spectrum for an Au-codoped Mg_2Si:Bi crystal, thus obtained, is shown in Fig. 1. The reflectivity spectrum exhibits a dip around 1100 cm^{-1}. The reflectivity is rapidly increased with decreasing wavenumber. This feature is explained as so-called Drude-like behavior. The reflectivity spectrum is almost agreement to the result of the curve fit analysis. The parameters obtained are listed in Table 1. The values of *N* and τ determined were also listed in Table 1. The value of *N* is approximately consistent with that (=5.0×10^{19} cm^{-3}) determined by the Hall effect experiment. On the other hand, the value of τ is larger than those in Ref. [3]. It is known that τ becomes small with increasing *N*. The value of *N* in our sample is one-order magnitude smaller, compared to those in Ref. 3. It is thus reasonable to attribute the difference in τ to that in *N*. The analysis of the infrared reflectivity spectrum apparently gives reasonable physical parameters dominating electric properties of n-type Mg_2Si.

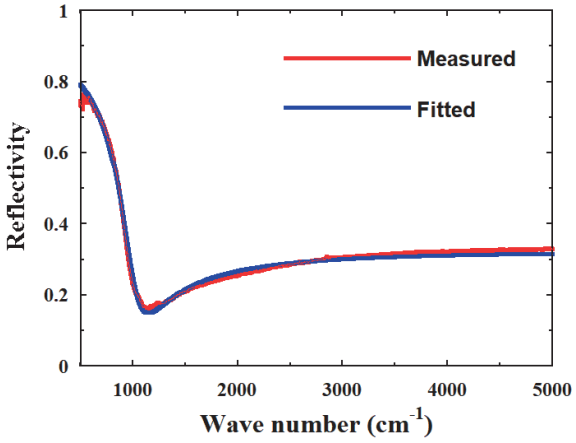


Fig. 1. Infrared reflective spectrum for an Au-codoped Mg_2Si:Bi crystal. Red and blue lines indicate the experimental data and the fit curve, respectively.

Table 1. Summary of the parameters in Drude-model, determined from the curve fit analysis.

ω_p (cm^{-1})	Γ_p (cm^{-1})	τ (s)	N (cm^{-3})
1026.2	310.1	1.1×10^{-13}	1.3×10^{19}

[1]K. Kambe *et al*., J. Electron. Mater. **43** (2014) 2212.
[2] N. Farahi *et al*., Dalton Trans. **43** (2014) 14983.
[3] J. Zhao *et al*., J. Mater. Chem. A. **39** (2015) 19774.
[4] D. McWilliams *et al*., Phys. Rev. **130** (1963) 2248.
[5] A. B. Kuzmenko, Rev. Sci. Instrum. **76** (2005) 083108.
[6] D. McWilliams *et al*., J. Opt. Soc. Am. **53** (1963) 298.

BL7U

d_{xy} Orbital Character of Hole Bands in $NdFeAs_{1-x}P_xO_{0.9}F_{0.1}$ Observed by Angle Resolved Photoemission Spectroscopy

Z. H. Tin[1], T. Adachi[1], A. Takemori[1], S. Miyasaka[1], S. Ideta[2,3], K. Tanaka[2,3] and S. Tajima[1]

[1]*Department of Physics, Osaka University, Osaka 560-0043, Japan*

[2]*UVSOR Synchrotron Facility, Institute for Molecular Science, Okazaki 444-8585, Japan*

[3]*School of Physical Sciences, The Graduate University for Advanced Studies, SOKENDAI, Okazaki 444-8585, Japan*

The iron-based superconductors (IBSs) has provided us new opportunity to investigate the unconventional superconductivity (SC). Among various systems of IBSs, 1111 system has highest T_c. In this 1111 system, however, it is difficult to synthesize the single crystals with high quality, and there are a few reports for study of angle resolved photoemission spectroscopy (ARPES). In this system, the electronic structure (Fermi surfaces (FSs)) can be controlled by the phosphorus doping on the arsenide site. Our previous result indicated that there are two superconducting states in $NdFeAs_{1-x}P_xO_{0.9}F_{0.1}$ and the critical P concentration is x~0.2 [1]. The previous result of ARPES using the *p*-polarization configuration shows that FS topology is changed by P doping at the same value of x=0.2 [2]. Theoretical investigation predicted that the hole pocket with *xy* orbital character is important in realizing high-T_c SC, but the hole bands with this orbital character have not been observed in our previous work [2,3]. In order to clarify the origin of FS topology change and the relationship between the *xy* hole band and high T_c, we perform the ARPES measurements on the single crystals of $NdFeAs_{1-x}P_xO_{0.9}F_{0.1}$($x$=0 and 0.2).

The ARPES was measured at 10K. (T_c=43 K and 24 K for x=0 and 0.2, respectively.) In the present work, the Fe-Fe direction of the single crystal is parallel to the analyzer slit of detector. The photoenergy of incident light was 18eV for high energy resolution, and the *s*-polarization configuration was used to detect the *xy*/*yz* orbital character bands around the Brillouin zone center.

As shown in Fig. 1, we observed the *yz* band (green dotted line) in $NdFeAsO_{0.9}F_{0.1}$. In addition, we have observed other hole band below -50 meV, which we assign to γ band. This hole band should have the *xy* orbital character, since there should be only one band with the *yz* character in the result of the theoretical calculation. This γ band may play an important role in full-gapped s± wave symmetry based on spin-fluctuation theory. However, this band does not cross Fermi level. Interestingly, the small flat band appears at zone center around the binding energy of -18 meV. This flat band may also have *xy* character.

In x=0.2 sample, the similar band dispersion has been observed. As shown in Fig. 2, this compound has 3 hole bands around zone center, and the energy levels of γ and flat bands are slightly different from those in x=0. The γ band shifts down by 10 meV with P doping, while the flat band shift upward by 6 meV. This behavior can be explained by the sensitivity of γ band to the structural parameter, h_{pn} and α. The h_{pn} (α) decreases (increases) with phosphorus doping. Our result is consistent with the shift down of γ band with decreasing h_{pn}. On the other hand, the flat *xy* band near Fermi level overlaps with the top of the *xz* hole band, which shows the systematic energy shift with P doping [2]. The present results suggested that the *yz*/*xz* band splitting is induced by the mixing of *xy*/*xz* orbital characters on the top of the hole band.

Finally, a suspicious intensity enhancement is observed on this flat band below T_c. This suggests that the flat band is related to the high-T_c SC. We need further investigation to clarify this mixing *xy* orbital character on the flat band.

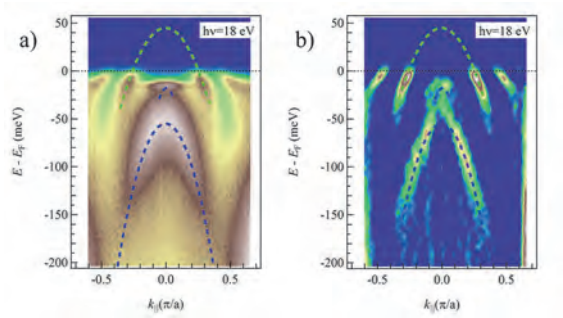


Fig. 1. ARPES results of $NdFeAsO_{0.9}F_{0.1}$ around zone center. The ARPES intensity plot (a) and its 2nd derivative plot (b) with respect to k, respectively.

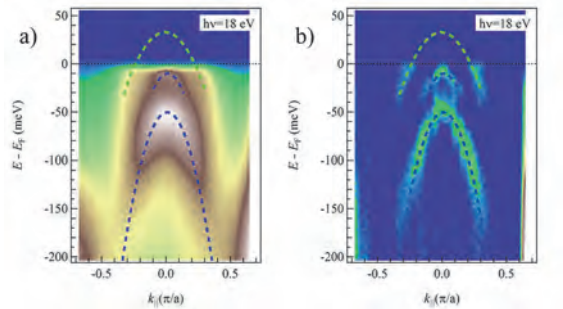


Fig. 2. ARPES results of $NdFeAs_{0.8}P_{0.2}O_{0.9}F_{0.1}$ around zone center. The ARPES intensity plot (a) and its 2nd derivative plot (b) with respect to k, respectively.

[1] S. Miyasaka *et al.*, J. Phys. Soc. Jpn. **82** (2013) 124706.

[2] A. Takemori *et al.*, Phys. Rev. B **98** (2018) 100501(R).

[3] K. Kuroki *et al.*, Phys. Rev. B **79** (2009) 224511.

BL7U

High-resolution ARPES Study of High-temperature Iron-based Superconductor Fe(Se,Te)

K. Nakayama[1], R. Tsubono[1], Y. Kubota[1], F. Nabeshima[2], T. Ishikawa[2], T. Shikama[2], A. Maeda[2], T. Takahashi[1,3,4] and T. Sato[1,3,4]

[1]*Department of Physics, Tohoku University, Sendai 980-8578, Japan*
[2]*Department of Basic Science, the University of Tokyo, Tokyo 153-8902, Japan*
[3]*Center for Spintronics Research Network, Tohoku University, Sendai 980-8577, Japan*
[4]*WPI Research Center, Advanced Institute for Materials Research, Tohoku University, Sendai 980-8577, Japan*

Since the discovery of topological insulators, the search for new material phases characterized by nontrivial topology of electronic wave functions is a hot topic in condensed-matter physics. A leading example is a topological superconductor in which gapless bound states appear at edges and/or vortex cores. The gapless bound states in topological superconductors consist of Majorana quasiparticles which have the unique property that the particle is own antiparticle, and are predicted to be useful for various applications such as fault-tolerant quantum computations. Therefore, the experimental demonstration of topological superconductivity is highly desired.

Recently, it was suggested that an iron-based superconductor Fe(Se,Te) (a superconducting transition temperature T_c of 14 K) hosts topological Dirac-cone surface states, and proximity-induced *s*-wave superconductivity therein leads to two-dimensional topological superconductivity with Majorana bound states in vortex cores [1].

In this study, to explore 'high-T_c' topological superconductivity, we performed angle-resolved photoemission spectroscopy (ARPES) measurements of compressive-strained Fe(Se,Te) thin films which show a 1.5 times higher T_c (~23 K) than bulk counterpart [2-4], and searched for the topological surface states responsible for topological superconductivity.

High-quality compressive-strained Fe(Se,Te) thin films with the thicknesses of approximately 400 layers were grown on CaF_2 substrate by pulsed laser deposition. High-resolution ARPES measurements were performed by using a MBS-A1 spectrometer at BL7U with linearly-polarized energy-tunable photons of 7-25 eV. The clean surface necessary for the ARPES measurements was obtained by cleaving the thin film *in situ* in an ultrahigh vacuum better than 1×10^{-10} Torr.

Since the topological Dirac-cone surface states are expected to emerge at the center of the Brillouin zone in Fe(Se,Te), we performed band-structure mapping near the Γ point with high energy and momentum resolutions by utilizing a low photon energy of 7 eV at BL7U. Figure 1(a) displays the ARPES intensity map at the Fermi level plotted as a function of two-dimensional wave vector, measured in the normal state (T = 30 K). One can find a strong intensity spot at the Γ point and a relatively large circular-shaped intensity distribution. Next, we determined the band dispersion along the momentum cut crossing the Γ point [Fig. 1(b)]. One can see a holelike band approaching the Fermi level in the vicinity of the Γ point, which produces the strong intensity spot in Fig. 1(a). One can also find another holelike band forming the circular Fermi surface seen in Fig. 1(a). In this study, we also performed photon-energy dependent ARPES measurements and tried to distinguish the topological surface states from the three-dimensionally-dispersive bulk states.

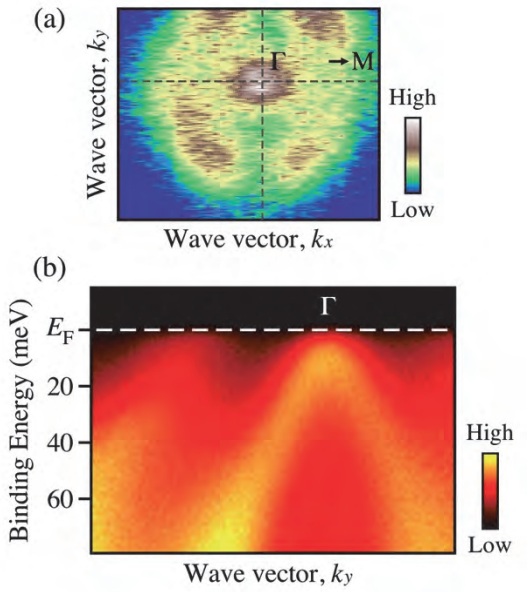


Fig. 1. (a) Fermi surface mapping plotted as a function of two-dimensional wave vector measured on compressive strained Fe(Se,Te) thin film (T_c = 23 K) at T = 30 K. (b) ARPES intensity plot as a function of binding energy and wave vector.

[1] P. Zhang *et al*., Science **360** (2018) 182.
[2] F. Nabeshima *et al*., Appl. Phys. Lett. **103** (2013) 172602.
[3] Y. Imai *et al*., Proc. Natl. Acad. Sci. USA **112** (2015) 1937.
[4] Y. Imai *et al*., Sci. Rep. **7** (2017) 46653.

BL7U

Pd-doping Dependent Energy Level of Dirac Point in $Ni_{1-x}Pd_xTe_2$ Observed by Angle Resolved Photoemission Spectroscopy

A. Kanayama[1], K. Yoshino[1], Z. H. Tin[1], S. Miyasaka[1], S. Tajima[1], S. Ideta[2,3] and K. Tanaka[2,3]

[1]*Department of Physics, Graduate School of Science, Osaka University, Toyonaka 560-0043, Japan*

[2]*UVSOR Synchrotron Facility, Institute for Molecular Science, Okazaki 444-8585, Japan*

[3]*School of Physical Sciences, The Graduate University for Advanced Studies, SOKENDAI, Okazaki 444-8585, Japan*

The Ni, Pd, and Pt dichalcogenides MX_2 (M=Ni, Pd, Pt; X=S, Se, Te) have several crystal structures such as the 2-dimensional (2D) CdI_2-type, the pseudo-2D $PdSe_2$-type and the 3-dimensional pyrite-type structures. We have studied MX_2 and their solid solution systems to explore the new physical properties. These systems show various physical properties coupled with the crystal structures.

Recently 2D CdI_2-type MTe_2 revisited from a viewpoint of Dirac fermion [1-3]. The experimental studies on $PdTe_2$ and $PtTe_2$ have indicated that these compounds have type II Dirac fermion state [1,2]. The results of angle resolved photoemission spectroscopy (ARPES) have revealed that the Dirac point exists at (0, 0, k_z) and the Dirac cone is strongly tilted along Γ-A direction (k_z-direction) in $PdTe_2$ and $PtTe_2$. The ARPES result for related material $NiTe_2$ indicates that this compound also has type II Dirac cone. The Dirac point exists just above Fermi level (E_F) (~ +0.2 eV) in $NiTe_2$, while they in Pd and Pt systems are located around -0.6 ~ -0.8 eV below E_F [1-3].

We have tried to control the energy level of Dirac point in the Pd-doped $NiTe_2$ system $Ni_{1-x}Pd_xTe_2$. In the end members, $NiTe_2$ and $PdTe_2$, the Dirac point is located above E_F (~ +0.2eV) and below E_F (~ -0.6 eV), respectively. We expected that the energy level of Dirac point can be turned near E_F by slightly Pd doping in $NiTe_2$ and the systematic change of Dirac pint energy level with Pd doping can be observed by ARPES measurements.

The single crystals of $Ni_{1-x}Pd_xTe_2$ (x=0, 0.05, and 0.10) were synthesized by a flux method in an evacuated silica tube. The results of the energy dispersive X-ray spectroscopy (EDX) indicated that the actual Pd concentration was the same as the nominal one. The ARPES spectra were measured at BL7U of UVSOR facility in Institute for Molecular Science using incident photons with $h\nu$=10-30 eV. All the measurements were carried out at ~10 K.

First of all, we measured the k_z-dependence of band structure by changing the incident photoenergy from 10 eV to 30 eV for x=0.05 and 0.10 samples. In all the single crystals, we observed the clear band crossing around (0, 0, 0.37c*) just below E_F indicating that these materials have Dirac point around this point. In the end member $NiTe_2$, the similar k_z-dependence of band structure has been observed. Below E_F, however, we did not observe the band crossing related with the Dirac point in $NiTe_2$. The present result has suggested that the Dirac point exists above E_F, as reported previously [3].

Next, we have focused the Pd-doping dependence of Dirac point energy level. Figures 1 and 2 show the ARPES intensity plot along $k_{//}$ (parallel to Γ-M direction) at (0, 0, 0.37c*) for x=0.05 and 0.10, respectively. Both samples have linear band dispersion indicating the existence of Dirac cone. The Dirac point, where the two bands with linear $k_{//}$ dispersion cross, shifts down with Pd doping, as shown in Figs. 1 and 2. This result indicates that in $NiTe_2$, the energy level of Dirac pint can be controllable by Pd doping.

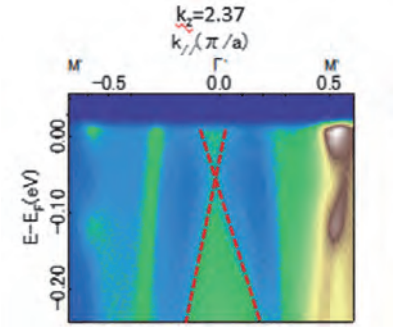


Fig. 1. ARPES intensity plot along $k_{//}$ (parallel to Γ-M direction) at (0, 0, 0.37c*) for x=0.05.

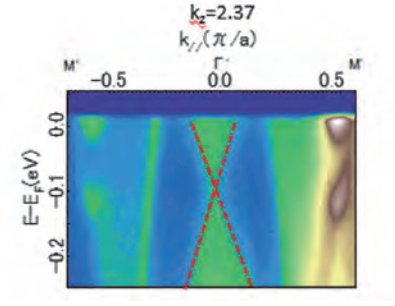


Fig. 2. ARPES intensity plot along $k_{//}$ (parallel to Γ-M direction) at (0, 0, 0.37c*) for x=0.10.

[1] H.-J. Noh *et al.*, Phys. Rev. Lett. **119** (2017) 016401.
[2] K. Zhang *et al.*, Phys. Rev. B **96** (2017) 125102.
[3] B. Ghosh *et al.*, Phys. Rev B **100** (2019) 195134.

BL7U

Three Dimensional Comparison between the ARPES Measurements and DFT Calculation for MoS_2

S. Tanaka[1], K. Ueno[2], S. Ideta[3] and K. Tanaka[3]

[1] *The institute of Scientific and Industrial Research, Osaka Univ., Ibaraki 567-0047, Japan*

[2] *Graduate School of Science and Engineering Saitama University, Saitama 338-8570, Japan.*

[3] *UVSOR Synchrotron Facility, Institute for Molecular Science, Okazaki 444-8585, Japan.*

2H-MoS_2 is one of the most typical TMDCs, and its electronic structure has been extensively studied by using angle-resolved photoelectron spectroscopy (ARPES). In these studies, comparison with the theoretical calculation was commonly made for revealing the electronic structure. However, most of the comparison has been made only on the highly symmetric lines in the Brillouin zone, and the other points are usually omitted. In this report, we made the comparison of the constant energy map derived from the photoelectron angular distribution in the ARPES measurement to those derived from the first principles calculation in the momentum space.

The experiments were carried out at the BL7U. The sample temperature was 9K and the photon energy used was 21 eV. The A-1 electron energy analyzer collects the photoelectron within the window of 30° along the photon-incident plane (defined as k_x axis hereafter) , and the volume map was obtained by changing the sample tilt angle which is perpendicular to the photon incidence plane (defined as k_y axis hereafter).

The energy band of MoS_2 was calculated within the density functional theory (DFT) framework, employing the QUANTUM ESPRESSO package (version 6.3), which had been installed in the computer at Research Center for Computational Science in IMS. The eigen energies are calculated at 64×64×16 grid points in the Brillouin zone. Then, the band energies are broadened by the convolution with the Gaussian-peak function with the width of 0.05 eV at each k-point; which is a usual procedure for obtaining a density of states curve. The dispersion along the k_z line is averaged by adding all 16 spectra at one (k_x, k_y) point. The final constant-energy maps for comparing the experiments were made by the broadening in the k-space with the Gaussian function with the width of 0.02 $Å^{-1}$.

Figure 1 show the comparison between the constant energy maps derived from the ARPES measurements (left-hand side) and those from the DFT calculations (right-hand side). The binding energies are scaled with respect to the valence band maximum. The energy here are determined so as that the calculation and experiments show similar shape and symmetry. The relation of energies used in Figs. 1 are phenomenologically given by the formula $E_{calc} = 0.078E_{exp}^2 + 1.43E_{exp}(eV)$. This indicates that there are errors of the binding energies in the DFT calculation of this work. In spite of this considerable disagreement in the electron energy, the overall shape and symmetry in the constant-constant energy map by ARPES is well represented by the calculation. This means that characteristics of the electron band is well reproduced by the DFT calculation, suggesting an advantage of the comparison in the k-space to a comparison of dispersions only on the highly symmetric lines in which the energetic agreements are necessary to match.

The method of the comparison in the three dimensions shown above, is instinctive and easy to understand. However, in order to achieve scientifically new results, it is required to take more detailed measurements combining e.g., the photon-energy-dependence and the polarization dependence, which are in progress.

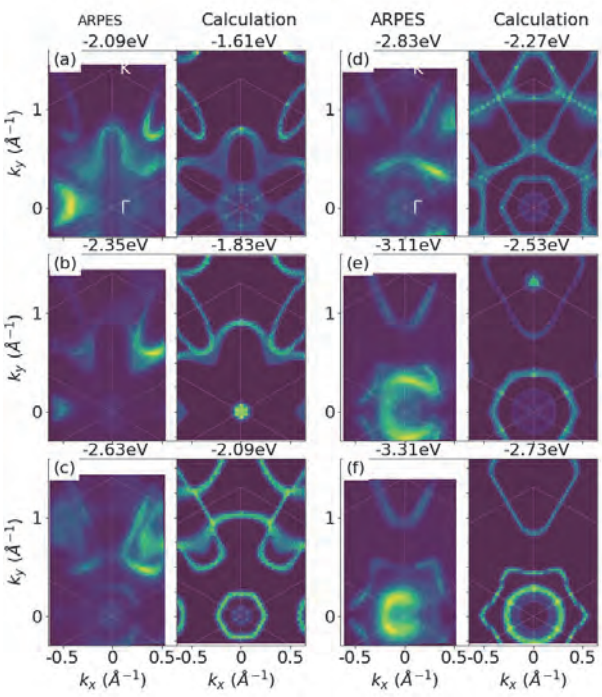


Fig. 1. Comparison of the constant energy maps between the ARPES measurements (left) and the DFT calculation(right).

BL7U

Charge Density Wave State of $CeTe_3$ Investigated by Angle-resolved Photoemission Spectroscopy

Y. Arai[1], K. Kuroda[1], Y. Wan[1], Y. Dong[1], Y. Fujisawa[2], S. Ideta[3], K. Tanaka[3]
Y. Okada[2] and T. Kondo[1]

[1]*ISSP, University of Tokyo, Kashiwa 277-8581, Japan*
[2]*Quantum Material Science Unit, OIST, Onna-son 904-0495, Japan*
[3]*UVSOR Synchrotron Facility, Institute for Molecular Science, Okazaki 444-8585, Japan*

In strongly correlated electron systems, the many-body effect often significantly reconstructs the electronic structure of matter in the vicinity of the Fermi energy; for example, charge density wave (CDW) opens a band gap, and Kondo effect leads to heavy quasi-particle bands. The conflict or interplay among such multiple many-body effects is of great interest in condensed matter physics. $CeTe_3$ with 4*f* orbitals exhibits CDW state, thus offers an excellent playground to study such an intriguing physics.

$CeTe_3$ is composed of an alternate stacking of Te planes and CeTe slabs as shown in Fig. 1 (a). Te planes mainly contribute to the Fermi surface and host the CDW state. The transition temperature of CDW is more than 400 K [1] and the lattice originally of square Te plans is distorted by as much as 0.2 Å [2], indicating that the CDW state is quite robust; this is further confirmed by a large CDW gap as large as 400meV observed by angle-resolved photoemission spectroscopy (ARPES) [3]. The electronic state of $CeTe_3$ is also characterized by the Kondo effect, which is observed in the electrical resistivity increasing below 10 K with a local maximum value at 6 K [1]. Since this temperature is associated with the coherence derived from the Kondo lattice, both CDW and Kondo effects are expected to affect the electronic structure below 6 K in $CeTe_3$.

Although ARPES is a suitable probe to investigate the electronic reconstruction due to CDW and Kondo effect, the previous research observed the band structure only down to 25 K, where only the CDW occurs. In this study, therefore, we have conducted the ARPES measurements down to 6 K comparable with the Kondo temperature, in order to realize the coexistence between the CDW and Kondo effect and study the relationship of these.

Figure 1(b) shows the Fermi surface mapping, where the ARPES intensities are integrated from E_F to E_F-200 meV. Due to the interlayer coupling between Te planes and Ce-Te slabs, Te plane bands are folded along the three-dimensional Brillouin zone [3]. We clearly observed that a CDW gap is opened along the Fermi surface, and its size increases from $k_y \sim 0$ Å^{-1} to $k_y = \pm 0.4$ Å^{-1} (Fig. 1(g)), reaching the maximum of about 400 meV. This result at 6 K is consistent with the previous ARPES studies at 25 K; this indicates that CDW in the Te plane is almost independent of the Kondo effect associated with Ce ions in the slab probably because the interaction between the Ce-Te slab structure and the Te planes is relatively weak.

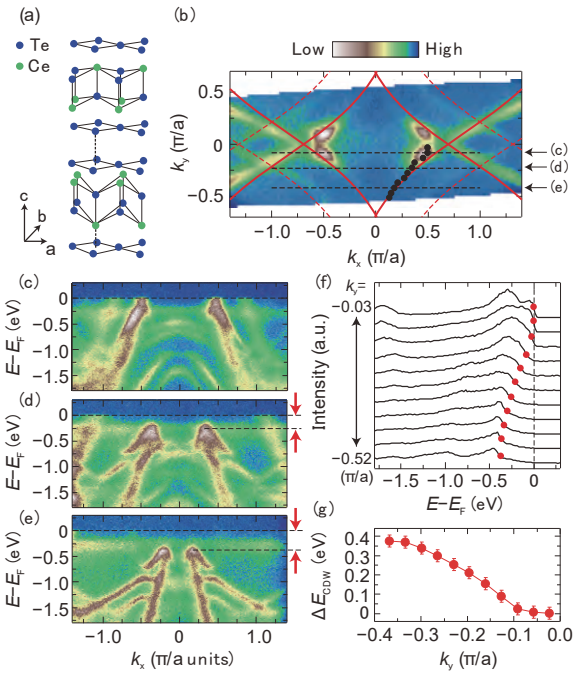


Fig. 1. Electronic structure in CDW state of $CeTe_3$. (a) Crystal structure of $CeTe_3$. Note that, unlike the convention, the *c* axis is set to be perpendicular to the Te planes. (b) Fermi surface map at 6 K measured by ARPES. Red lines represent calculated Fermi surface dominated by the Te plane, and red dotted lines are that folded about the 3D BZ [1]. (c-e) Band dispersions measured at black dotted lines in (b). Red arrows highlight CDW gaps. (f) Energy distribution curves along the Fermi surface corresponding to the black points in (b). Red points indicate the leading edge of the spectra. (g) *k* dependence of the CDW gap along (f).

[1] N. Ru *et al.*, Phys. Rev. B. **73** (2006) 033101.
[2] H. J. Kim *et al.*, Phys. Rev. Lett. **96** (2006) 226401.
[3] V. Brouet *et al.*, Phys. Rev. Lett. **93** (2004) 126405.

BL7U

High-resolution ARPES Study on the Electronic Structure of Heterointerfacial Superconductors

R. Tsubono[1], K. Nakayama[1], Y. Kubota[1], F. Nabeshima[2], T. Ishikawa[2], T. Shikama[2], A. Maeda[2], T. Takahashi[1,3,4] and T. Sato[1,3,4]

[1]*Department of Physics, Tohoku University, Sendai 980-8578, Japan*
[2]*Department of Basic Science, the University of Tokyo, Tokyo 153-8902, Japan*
[3]*Center for Spintronics Research Network, Tohoku University, Sendai 980-8577, Japan*
[4]*WPI Research Center, Advanced Institute for Materials Research, Tohoku University, Sendai 980-8577, Japan*

Since the discovery of superconductivity in a $LaAlO_3/SrTiO_3$ heterostructure consisting of band insulators [1,2], heterointerfaces have been an interesting research target for investigating unconventional superconductivity due to the low dimensionality, spatial inversion-symmetry breaking, and interfacial interactions. A recently-discovered interfacial superconducting system is the hybrid between a topological insulator Bi_2Te_3 and a parent compound of iron-based superconductors FeTe [see Fig. 1(a) for a schematic view of the heterostructure] [3]. Although both Bi_2Te_3 and FeTe are non-superconducting, the superconducting transition temperature T_c of Bi_2Te_3/FeTe heterostructure reaches ~12 K, which is about ten times higher than that of $LaAlO_3/SrTiO_3$. This finding triggered intensive investigations on Bi_2Te_3/FeTe, and, consequently, several peculiar properties have been reported in Bi_2Te_3/FeTe and related heterostructures. An intriguing finding is the lack of interfacial superconductivity in the selenide counterpart, Bi_2Se_3/FeSe. Understanding the origin of such a remarkable difference in the superconducting property between structurally identical Bi_2Te_3/FeTe and Bi_2Se_3/FeSe would provide a key to clarify the nature of exotic interfacial superconductivity. Therefore, a comparative study on the electronic states of Bi_2Te_3/FeTe and Bi_2Se_3/FeSe is of crucial importance.

In this study, we performed high-resolution angle-resolved photoemission spectroscopy (ARPES) and determined the electronic structure relevant to the interfacial superconductivity of Bi_2Te_3/FeTe and Bi_2Se_3/FeSe. ARPES measurements at BL7U were performed using a MBS-A1 spectrometer with energy-tunable photons. The energy and angular resolutions were set to be 5–20 meV and 0.3º, respectively. The sample was kept at $T = 30$ K during the ARPES measurements.

We plot in Fig. 1 the representative ARPES results obtained on the as-grown FeSe films. As seen from Fig. 1(b), the as-grown FeSe film has small Fermi surfaces centered at the Γ and M points in the Brillouin zone. These Fermi surfaces originate from holelike and electronlike energy bands of Fe 3*d* orbtials [see Fig. 1(c)], indicating the semimetallic character of FeSe. Upon interfacing Bi_2Se_3 layers, we observed clear differences in the FeSe-derived energy bands. We compared these results to those obtained in Bi_2Te_3/FeTe [4] and found an important insight into the origin of interfacial superconductivity.

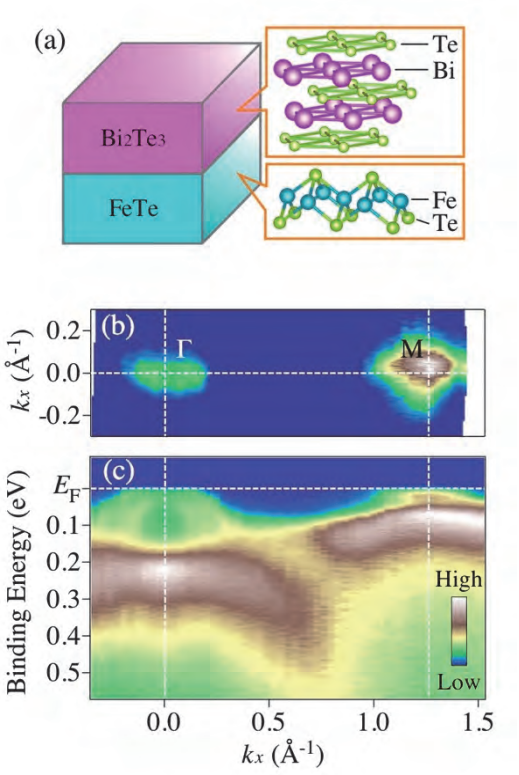


Fig. 1. (a) Schematic of Bi_2Te_3/FeTe heterostructure. (b) ARPES intensity mapping at the Fermi level plotted as a function of two-dimensional wave vector, measured at $T = 30$ K at $h\nu = 21$ eV in FeSe. (c) Experimental band dispersion measured along the ΓM high-symmetry line.

[1] A. Ohtomo and H. Y. Hwang, Nature (London) **427** (2004) 423.
[2] N. Reyren *et al.*, Science **317** (2007) 1196.
[3] Q. L. He *et al.*, Nat. Commun. **5** (2014) 4247.
[4] K. Owada *et al.*, Phys. Rev. B **100** (2019) 064518.

BL7U

Doping Dependence of the Superconducting Gap in Bi2223 Observed by Angle-Resolved Photoemission Spectroscopy

S. Ideta[1,2], T. Yoshida[3], A. Fujimori[4], S. Adachi[5], N. Sasaki[5], S. Yamaguchi[5], T. Watanabe[5] T. Noji[6] and K. Tanaka[1,2]

[1]*National Institutes of Natural Science, Institute for Molecular Science, Okazaki 444-8585, Japan*
[2]*The Graduate University for Advanced Studies, SOKENDAI, Okazaki 444-8585, Japan*
[3]*Graduate School of Human and Environmental Studies, Kyoto University, Kyoto 606-8501, Japan*
[4]*Department of Applied Physics, Waseda University, Tokyo 169-8555, Japan*
[5]*Graduate School of Science and Technology, Hirosaki University, Hirosaki 036-8561, Japan*
[6]*Department of Applied Physics, Tohoku University, Sendai 980-8579, Japan*

To understand the mechanism of high-T_c superconductivity in cuprates is one of the crucial issues. Especially, the energy gap seen in the superconducting (SC) and normal states is believed to be an important piece of evidence for the non-BCS behavior of the SC transition from the underdoped to overdoped regime in the high-T_c cuprate superconductors. In cuprates, two different representative energy gaps are present in the SC and normal states, namely, the SC gap and pseudogap [1-3]. Doping dependence of the SC gap has been considered as the direct evidence to reveal high-T_c superconductivity and sheds light on its nature.

Triple-layer Bi-based cuprate superconductor, $Bi_2Sr_2Ca_2Cu_3O_{10+\delta}$ (Bi2223), which shows the highest T_c (110 K) among the Bi-based cuprates, has two inequivalent CuO_2 planes with different hole carrier [4-6]. In this study, we have investigated the momentum and doping dependence of the energy gap anisotropy and found that the SC gap obtained from different doping showed a similar magnitude. We observed two bands corresponding to the outer (OP) and inner (IP) CuO_2 planes. Hole concentration was deduced from the IP and OP Fermi surfaces actually increases in going from the underdoped to overdoped samples.

High-quality single crystals of underdoped, optimally-doped, and overdoped $Bi_2Sr_2Ca_2Cu_3O_{10+\delta}$ (UD, Opt, and OD Bi2223, T_c = 80 K, 110 K, and 110 K, respectively) were grown by the TSFZ method. Underdoped Bi2223 samples were successfully obtained in the two-step annealing in order to control their doping levels [7]. ARPES experiments were carried out at BL7U of UVSOR-III Synchrotron. Clean sample surfaces were obtained for the ARPES measurements by cleaving single crystals *in-situ* in an ultrahigh vacuum better than 6×10^{-9} Pa. The measurements were performed at 10 K.

In order to estimate the doping and momentum dependence of the SC gap, as shown in Fig. 1, the SC gap (10 K) estimated along the Fermi surface is plotted as a function of the *d*-wave order parameter. For the IP band, the extrapolated SC gap from the nodal to the antinode (a black dotted line) shows a similar magnitude at the antinode. As for the OP band too, the SC gap at the antinode shows the same magnitude in spite of different doping. Note that we need to exclude the result of the OP-bonding band (BB) [8]. These results are similar to the double-layer cuprate $Bi_2Sr_2CaCu_2O_{8+\delta}$ observed by ARPES [9]. Here, the present ARPES study raises a question about the mechanism; why the SC transition temperature and hole carrier is different in Bi2223, the SC gap keeps the same magnitude at the antinode.

As future work, we need to investigate the pseudogap and the Fermi arc length above T_c in order to determine the relationship between the T_c and effective SC gap in Bi2223.

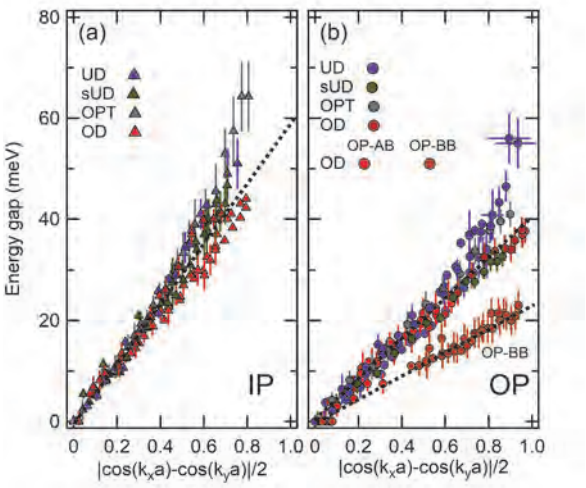


Fig. 1. Superconducting (SC) gap of Bi2223 with different doping. (a) SC gap of the IP band. (b) SC gap of the OP band.

[1] D. S. Marshall *et al*., Phys. Rev. B **76** (1996) 4841.
[2] A. G. Loeser *et al*, Science **273** (1996) 325.
[3] H. Ding *et al*., Nature (London) **382** (1996) 51.
[4] S. Ideta *et al*., Phys. Rev. Lett. **104** (2010) 227001.
[5] S. Ideta *et al*., Phys. Rev. B **85** (2012) 104515.
[6] S. Ideta *et al*., Physica C **470** (2010) S14-S16.
[7] S. Adachi *et al*., Physics Procedia **65** (2015) 53.
[8] S. Ideta *et al*., UVSOR Activity Report 2016 **44** (2017) 90.
[9] I. M. Vishik *et al*., PNAS **109** (2012) 18332.

BL7U

Angle-resolved Photoemission Study of MAX Phase Compound Ti_2SnC

T. Ito[1,2], M. Ikemoto[2], D. Pinek[3], M. Nakatake[4], S. Ideta[5,6], K. Tanaka[5,6] and T. Ouisse[3]

[1]*Nagoya University Synchrotron radiation Research center (NUSR), Nagoya University, Nagoya 464-8603, Japan*
[2]*Graduate School of Engineering, Nagoya University, Nagoya 464-8603, Japan*
[3]*Grenoble Alpes, CNRS, Grenoble INP, LMGP, F-38000 Grenoble, France*
[4]*Aichi Synchrotron Research Center, Seto, 489-0965, Japan*
[5]*UVSOR Synchrotron Facility, Institute for Molecular Science, Okazaki 444-8585, Japan*
[6]*The Graduate University for Advanced Studies, SOKENDAI, Okazaki 444-8585, Japan*

MAX phase compounds, i.e., $M_{n+1}AX_n$ where M is a transition metal, A belongs to groups 13-16 and X is the C or N element, have recently been attracted much attention due to their possible application for new class of two-dimensional systems called MXenes by removing A atoms [1]. On the other hand, the bulk electronic structure of MAX phase has been studied mostly by calculations, mainly because of lack of well-established single crystalline samples. In this study, we have performed angle-resolved photoemission spectroscopy (ARPES) on MAX phase compound Ti_2SnC [2] to directly investigate the electronic structure of this system.

ARPES measurements were performed at the UVSOR-III BL5U. Data were acquired at T = 25 K with hν = 22.5 eV which enables us to trace around the ΓKM plane with inner potential of V_0=10.7 eV estimated from the photon energy dependent measurement (not shown). It should be noted that each ARPES images were obtained without changing the photon incident angle relative to the sample surface by utilizing two-dimensional mapping lens mode of MBS A-1 analyzer.

Figure 1 shows the obtained Fermi surface (FS) image on the ΓKM plane (a) compared with the FS topologies calculated by DFT method (b,c). Around the corner of hole-like FS (β), a broad egg-shaped FS counter has been observed. To elucidate the detail electronic structure around the observed egg-shaped FS, the band structure near the Fermi level (E_F) and momentum distribution curve (MDC) at E_F along the k_x (#1) and k_y (#2) cut across the FS are shown in Fig. 2 (a) and (b), respectively. From the comparison with DFT calculation, the egg-shaped FS seems to be in consistent with Dirac-cone like dispersive features of γ - blanch. In addition, we have found the Dirac point (DP) or bottom of the upper Dirac cone locates around 250 meV from the present ARPES, while DP around 400 meV has been expected by DFT calculation. To pursue the relation between the complicated FS and the thermodynamic properties of Ti_2SnC, further studies are intended.

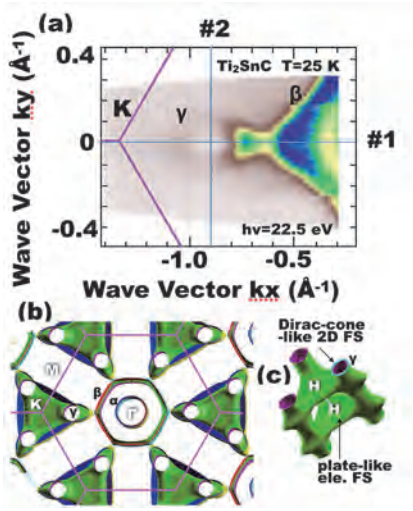


Fig. 1. Fermi surface (FS) image on ΓKM plane of Ti_2SnC (a). (b,c) FS calculated by DFT shown as projection along the [001] axis (b) and enlarged FS around the KH axis (c).

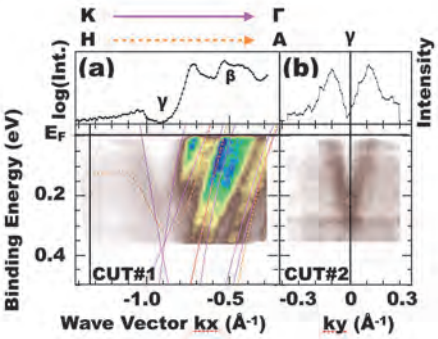


Fig. 2. Band structure near E_F (lower panel) and MDC spectra at E_F (upper panel) along the CUT#1 (a) and CUT#2 (b) indicated in Fig. 1(a) of Ti_2SnC. Dirac-cone like dispersive features have been observed on the γ - branch. Solid and dashed lines are DFT calculation along the ΓK and AH lines, respectively.

[1] M. Basoum, *MAX phases* (Wiley, Weinheim 2013).
[2] J. Y. Wu, Y. C. Zhou and J. Y. Wang, Mat. Sci. Eng. A **422** (2006) 266.

BL7B

Evaluation of Achromatic Vacuum-ultraviolet Lens

T. Shimizu, Y. Minami, K. Kuroda, K. Shinohara, D. Umeno and N. Sarukura
Institute of Laser Engineering, Osaka University, Suita 565-0875, Japan

Vacuum ultraviolet (VUV) has numerous scientific and technological applications including spectroscopy, environmental monitoring, surface micromachining, sterilization and so on. In the study of VUV materials, it has been found that fluoride materials can be applied as new VUV optics including lenses. For VUV lenses, the material must be transparent to the light in the VUV region, have chemical stability, have a high melting point, and be uniform and of good quality. In this study, an achromatic lens made of two materials was fabricated based on a design that minimizes chromatic aberration in the 150-300 nm range using fluoride crystals with high VUV transmittance.

A combination of $LiCaF_6$ and $BaLiF_3$ was used as materials for the convex and concave lenses of the VUV achromatic lens because it has the lowest chromatic aberration in combinations of fluoride crystals with high transmittance in the vacuum ultraviolet region. Chromatic aberration at 150 nm and 300 nm is corrected for in this design. In addition, since there is no lens adhesive that can transmit vacuum ultraviolet light, there is a gap between the convex and concave lenses, which is fixed by sandwiching them with a lens folder. The coating agent used for the anti-reflection coating, which suppresses reflections on the lens surface, is not applied because it cannot penetrate VUV light and may reduce the transmittance and degrade the vacuum due to vaporization.

The performance of VUV achromatic lenses is evaluated in the following three areas: transmittance, chromatic aberration, and focusing performance. For the transmittance measurement, VUV achromatic lenses were irradiated with synchrotron radiation of 50 to 1000 nm wavelengths at BL7B (Fig. 1). The transmittance can be measured by measuring the beam intensity of the incident light and the beam intensity after passing through the VUV achromatic lens. The transmittance of the VUV achromatic lenses was measured in the wavelength region of 100-300 nm. The absorption edge was found to be 123 nm, which is enough to transmit the light in the range of 150-300 nm, which was the target in the original design. We have concluded that the degradation of the absorption edges of $LiCaF_6$ and $BaLiF_3$ was caused by the quality of the crystals. In addition, since no AR coating was applied, it was confirmed that the overall transmittance was low due to the reflection of the lens surface.

The evaluation of chromatic aberration will be carried out in the second half of the experiment using BL3B.

In the future, a rigorous evaluation is required, and it is important to further increase the knowledge of achromatic lenses in the vacuum ultraviolet region. In addition, the development of an imaging spectrometer with a VUV achromatic lens is expected to be carried out in parallel for practical use.

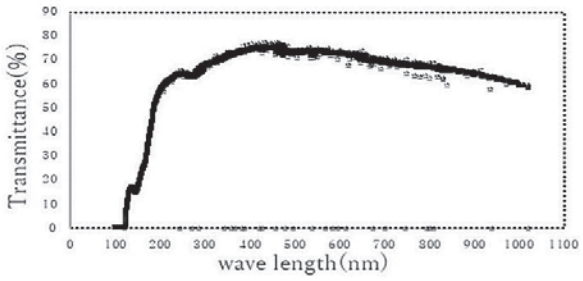


Fig. 1. Transmittance measurement results.

[1] K. Shimamura, H. Sato, A. Bensalah, H. Machida, N. Sarukura and T. Fukuda, J. Alloys Cmpds. **343** (2002) 204.
[2] M. V. Luong, M. J. F. Empizo, M. Cadatal- Raduban, R. Arita, Y. Minami, T. Shimizu, N. Sarukura, H. Azechi, M. H. Pham, H. D. Nguyen, Y. Kawazoe, K. G. Steenbergen and P. Schwerdtferger, Opt. Mater. **65** (2017) 15.
[3] R. Arita, Y. Minami, M. Cadatal-Raduban, M. H. Pham, M. J. F. Empizo, M. V. Luong, T. Hori, M. Takabatake, K. Fukuda, K. Mori, K. Yamanoi, T. Shimizu, N. Sarukura, K. Fukuda, N. Kawaguchi, Y. Yokota and A. Yoshikawa, Opt. Mater. **47** (2015) 462.
[4] T. Shimizu, M. V. Luong, M. Cadatal-Raduban, M. J. F. Empizo, K. Yamanoi, R. Arita, Y. Minami, N. Sarukura, N. Mitsuo, H. Azechi, M. H. Pham, H. D. Nguyen, K. Ichiyanagi, S. Nozawa, R. Fukaya, S. Adachi, K. G. Nakamura, K. Fukuda, Y. Kawazoe, K. G. Steenbergen and P. Schwerdtfeger, Appl. Phys. Lett. **110** (2017) 141902.
[5] M. V. Luong, M. Cadatal-Raduban, M. J. F. Empizo, R. Arita, Y. Minami, T. Shimizu, N. Sarukura, H. Azechi, M. H. Pham, H. D. Nguyen and Y. Kawazoe, Jpn. J. Appl. Phys. **54** (2015) 122602.
[6] K. Yamanoi, T. Murata, Y. Arikawa, T. Nakazato, M. Cadatal-Raduban, T. Shimizu, N. Sarukura, M. Nakai, T. Norimatsu, H. Nishimura, H. Azechi, S. Fujino, H. Yoshida, A. Yoshikawa, N. Satoh and H. Kan, Opt. Mater. **35** (2013) 1962.

Ⅲ-3

Chemistry



Highlight

BL1U

Controlling the Orbital Alignment in Atoms using Circularly Polarized Radiation Wave Packets

T. Kaneyasu[1,2], Y. Hikosaka[3], M. Fujimoto[2,4], H. Iwayama[2,4] and M. Katoh[2,5]

[1]*SAGA Light Source, Tosu 841-0005, Japan*
[2]*Institute for Molecular Science, Okazaki 444-8585, Japan*
[3]*Institute of Liberal Arts and Sciences, University of Toyama, Toyama 930-0194, Japan*
[4]*The Graduate University for Advanced Studies, SOKENDAI, Okazaki 444-8585, Japan*
[5]*Hiroshima Synchrotron Radiation Center, Hiroshima University, Higashi-Hiroshima 739-0046, Japan*

We report on a new application of the circularly polarized radiation provided by a helical undulator at a synchrotron light source - the coherent control of excited state alignment [1]. Our method is based on the use of undulator radiation to create longitudinally coherent wave packets with attosecond-controlled spacing [2]. The performance of our scheme is demonstrated by the photoexcitation of helium atoms in the extreme ultraviolet wavelength region by using the temporal coherent control technique.

The experiment was carried out at the beamline BL1U using the tandem undulator consisted of twin APPLE-II devices. We set the upstream and downstream undulators to provide left-circular polarization (LCP) and right-circular polarization (RCP), respectively. The central photon energy of the fundamental radiation was adjusted to ~24 eV, at which the period of the radiation is ~171 as. Each relativistic electron in the bunch which passes though the tandem undulator emits a pair of wave packets whose waveforms are well-characterized as time-separated 10-cycle oscillations. The spacing between the wave packets was tuned with attosecond precision by the phase shifter magnet.

Figure 1 illustrates the helium atom interacting with the radiation wave packets from the tandem undulator. As a result of the sequential interaction with the wave packets, helium atom is excited to the 1s6p coherent superposition state (transition frequency of ω), which consists of the M_j=±1 magnetic substates associated with the first (LCP) and second (RCP) parts of the wave packet pair, following the selection rules for dipole transitions. In an orbital picture, the $6p_{\pm}$ orbitals are coherently superposed, forming a 6*p* orbital aligned in the *xy*-plane. The orbital alignment is controlled by the delay time, where the tilt angle is set to ωτ/2 with respect to the *x*-axis. The detector setup allows us to determine the alignment of the 6*p* orbital because the fluorescence photons are preferentially emitted perpendicular to the alignment axis.

Figure 2 shows the fluorescence yield measured as a function of delay time in decays from the 1*s*6*p* to the 1*s*2*s* states, revealing a clear sinusoidal modulation. Reflecting the spatial distribution of the dipole emission as shown in the top panel of Fig. 2, we can expect the signal intensity oscillates at the resonant frequency of the 1*s*6*p* excited state depending on the delay time. The observed oscillation shows high visibility and is well reproduced by a sinusoidal curve. This supports the applicability of circularly polarized undulator radiation to control excited state alignment based on the temporal coherent control technique.

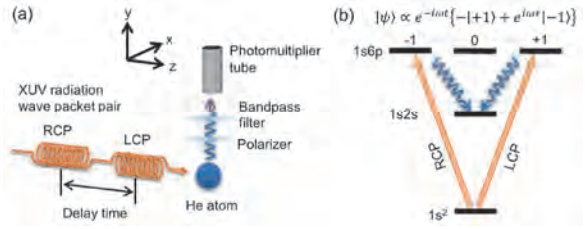


Fig. 1. (a) Interaction between the radiation wave packet pair and helium atom. The fluorescence photons are detected by the photomultiplier tube. (b) The helium atom is excited into the 1*s*6*p* superposition state which consists of the M_j=±1 substates associated with the first (LCP) and second (RCP) parts of the wave packet pair.

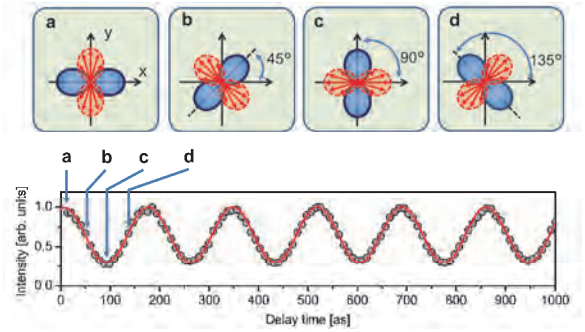


Fig. 2. Fluorescence yield measured as a function of the delay time. The gray circles are measured data and the red line shows the theoretical curve.

[1] T. Kaneyasu *et al.*, Phys. Rev. Lett. **123** (2019) 233401.
[2] Y. Hikosaka *et al.*, Nat. Commun. **10** (2019) 4988.

Highlight

BL3U

Mechanistic Investigation of Homogeneous Iron-Catalyzed Organic Reactions Based on Solution-Phase L-edge XAS

H. Takaya[1], M. Nagasaka[2] and K. Kashimura[3]

[1]*International Research Center for Elements Science, Institute for Chemical Research, Kyoto University, Uji 611-0011, Japan*

[2]*UVSOR Synchrotron Facility, Institute for Molecular Science, Okazaki 444-8585, Japan*

[2]*Faculty of Engineering, Chubu University, Kasugai 487-8501, Japan*

We have found that iron complexes of FeX_2SciOPP (X = Br or Mes) bearing a bulky phosphine ligand SciOPP showed excellent catalytic activities toward the cross-coupling of organometallic reagents of Mg, B, Al, and Zn with various aryl halides [1,2]. Such iron-based catalysts for organic reactions alternative to the conventional precious metal catalysts has been intensively investigated for the development of future sustainable production of chemical compounds. Solution-phase XAS analysis is highly useful for the mechanistic study of iron-catalyzed organic reactions to identify the catalytically active organoiron species with their electronic and molecular structures, because the conventional solution-phase NMR analysis cannot be used due to the paramagnetic nature of organoiron species along with the large paramagnetic shift and peak broadening in NMR spectrum. L-edge XAS of transition-metal catalysts has been expected to be highly useful to investigate the electronic structure of 3d orbitals which provide essential information to elucidate how to work the catalyst. However, solution-phase L-edge XAS measurement is generally difficult because the measurement has to be performed under a vacuum condition where the solution sample is vaporized with vigorous boiling. In this project, we used the specially designed flow-cell for the solution-phase L-edge XAS measurement of homogeneous organic solution of iron complex catalysts. In BL3U, a stainless-steel flow cell has been used for various experiments, but we should carefully avoid contamination of iron species from the environment. For this reason Prof. Nagasaka newly designed and prepared PEEK-made flow cell bearing ultra-thin 100 nm Si_3N_4 membrane X-ray window (Fig. 1. left). The solvent-resistant PEEK made body worked well with an excellent chemical resistance toward the various organic solvents such as THF, CH_2Cl_2, and benzene, these often used in iron-catalyzed cross-coupling reactions. However, the static electrical charge generated by the frictional interactions between PEEK wall and organic solvents caused undesired baseline shifts in the NEXAFS spectrum. To solve this problem, a gold-made electrode was attached to the Si_3N_4 membrane with earth connection (Fig. 1. right). This flow cell was introduced into the He-filled chamber which inserted into the X-ray optics line, and connected to a syringe pump through a Teflon tube. The THF solution samples of iron catalyst and isolate catalytic intermediates of FeX_2SciOPP **1**–**3** (X = Br or Mes) were prepared in an argon-filled glovebox, because the solution of iron complexes are quite sensitive to oxygen and water, and immediately react to give iron oxide and hydroxide. The XAS measurement was successfully carried out under a flow condition (flow rate: 50–200 μL/h) to give L-edge NEXAFS of **1**–**3** without the undesired baseline shift by the static electricity (Fig. 2.). However, the penetration of helium gas into the cell causing a bubbling noise could not be perfectly controlled. To solve this problem, Viton O-ring is changed to a fluorosilicone polymer with improving the flow line design and tube connection. This improved cell is testing in 2020 experiment.

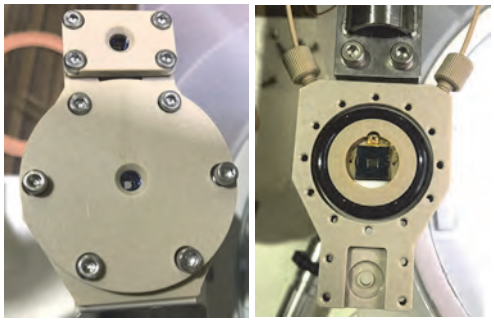


Fig. 1. Photos of the PEEK-made flow cell.

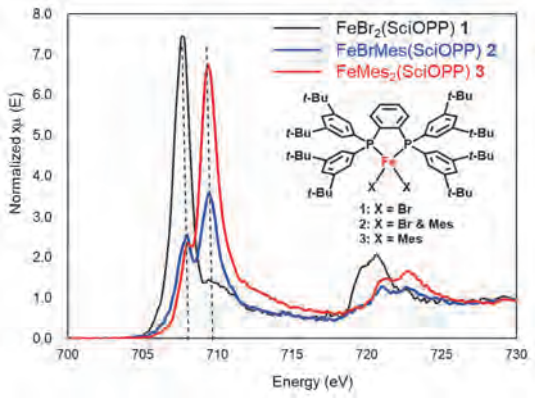


Fig. 2. Solution-phase NEXAFS spectrum of FeX_2(SciOPP) in THF.

[1] H. Takaya and M. Nakamura *et al.*, Bull. Chem. Soc. Jpn. **88** (2015) 410.
[2] R. Agata, H. Takaya, and M. Nakamura *et al.*, Bull. Chem. Soc. Jpn. **92** (2019) 381.

BL1U

Supramolecular Chirality Induction by Optical Vortex UV Light to Magnetic Azo-metal Complexes

T. Akitsu[1], S. Yamazaki[1], M. Yoshida[1], T. Haraguchi[1], M. Fujiki[2], M. Fujimoto[3] and M. Katoh[3,4]

[1]*Faculty of Sciences, Tokyo University of Science, Tokyo 162-8601, Japan*
[2]*Graduate School of Materials Sciences, NAIST, Ikoma 630-0192, Japan*
[3]*UVSOR Synchrotron Facility, Institute for Molecular Science, Okazaki 444-8585, Japan*
[4]*HiSOR Facility, Hiroshima University, Higashi-Hiroshima 739-0046, Japan*

For several years, we have studied on photochemical materials using optical vortex UV light have attracted attention. In contrast to circularly polarized light (associated with spin angular momentum), a light vortex having a spiral wave front (associated with orbital angular momentum) may provide mechanical torque onto the surface of (photofunctional) materials irradiated. In this context, we attempted molecular orientation control by irradiating linearly and/or circularly polarized (and optical vortex) UV light to polymer films containing (achiral) dinuclear Schiff base metal complexes without photoisomerization moiety in previous study [1,2]. Herein, we have designed new metal complexes having rigid Y-shaped structure with photoisomerization moiety expected to occur Weigert effect to be aligned by polarized UV light. Newly prepared PMMA films from DMF solvent were also employed for enhancing molecular orientation phenomenon induced by several types of UV light irradiation not on the surface but even in the films.

By using laboratory light source, linearly or circularly polarized UV light was irradiated to the PMMA films containing the metal complexes. For example, after linearly polarized UV light irradiation, optical anisotropy of Zn or Cu complexes-PMMA sample was observed as depicted in Fig. 2. Similarly, after circularly polarized UV light irradiation, new CD bands appeared, which suggested chirality attributed not to achiral molecules but to supramolecular arrangement induced by light. Thus, the Zn complex-PMMA was more sensitive to light.

At UVSOR, optical vortex with l = +1, -1 orbital angular momentum at 280 nm from linearly polarized light was irradiated to the same sample. CD spectra (Fig. 3) were analyzed with sine curve fiting to extract major linearly polarized light component and minor orbital angular momentum component.

[1] H. Nakatori, T. Haraguchi and T. Akitsu, Symmetry **10** (2018) 147.
[2] M. Takase, S. Yagi, T. Haraguchi, S. Noor and T. Akitsu, Symmetry **10** (2018) 760.

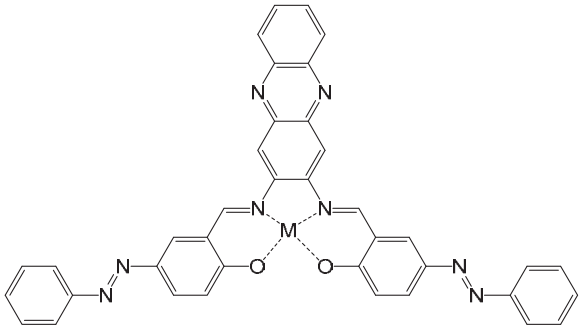


Fig. 1. Molecular structures of metal complexes (M= Cu(II) and Zn(II)).

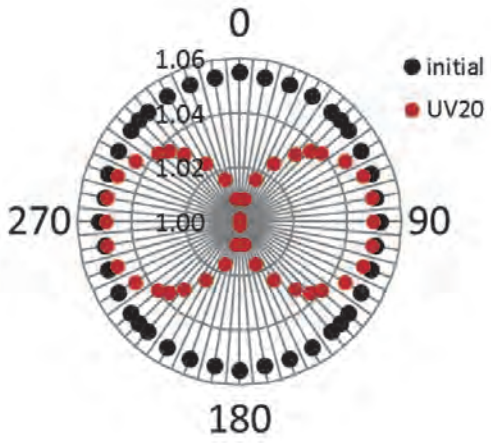


Fig. 2. Angular dependence of absorbance of polarized UV-vis spectra at 385 nm for the Zn complex-PMMA sample.

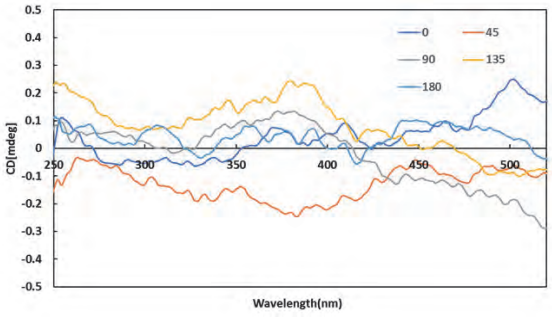


Fig. 3. CD spectra for the Zn complex-PMMA sample after optical vortex irradiation. KBr disk were rotated at five points to cancel artifact CD peaks.

BL1U

Time-Domain Ramsey Interferometry on Rydberg-Electron Wave Packets Generated in Helium Atoms

Y. Hikosaka[1], T. Kaneyasu[2,3], M. Fujimoto[3], H. Iwayama[3] and M. Katoh[3,4]
[1]*Institute of Liberal Arts and Sciences, University of Toyama, Toyama 930-0194, Japan*
[2]*SAGA Light Source, Tosu 841-0005, Japan*
[3]*Institute for Molecular Science, Okazaki 444-8585, Japan*
[4]*Hiroshima Synchrotron Radiation Center, Hiroshima University, Higashi-Hiroshima 739-0046, Japan*

Quantum state control of matter by the coherence of light has attracted great interest in various fields such as physics, chemistry, and information processing. The forefront of this coherent control research is rapidly evolving to the extreme ultraviolet wavelength range and attosecond time resolution, thanks to the developments of laser high-harmonic generations and seeded free electron lasers. On the other hand, while synchrotron radiation is high-brightness light covering a wide wavelength range up to X-rays, its longitudinal coherence is significantly lower than that of a laser. Thus synchrotron radiation has not been considered as a tool for coherent control. We demonstrate here the capability of synchrotron radiation to perform coherent control by achieving time-domain Ramsey interferometry on Rydberg wave packets generated in He atoms.

Our scheme for the coherent control by synchrotron radiation uses light wave packet pairs contained in the radiation pulses from two undulators [1,2]. The experiments were performed at the beamline BL1U. The two APPLE-II undulators inserted in series in the U1 straight section of the storage ring were both set to linear polarization mode, and light wave packet pairs of extreme ultraviolet (central photon energy of 24 eV and 10% bandwidth) were emitted. The delay time between the light wave packets was adjusted with an attosecond precision in the range of 2-50 fs, by the three-pole wiggler magnet installed between the two undulators. The central part of the undulator radiation was cut out by an aperture with a diameter of 0.4 mm at 8.2 m downstream from the downstream undulator, and irradiated with He gases. The bandwidth of the undulator spectrum covers the Rydberg states with principal quantum numbers from 3 to ∞. Visible/ultraviolet fluorescence emitted in the decays of the populated Rydberg states in He was detected by a photomultiplier tube.

Figure 1 shows the total fluorescence yield measured as a function of the delay time between the light wave packets. It is observed that the fluorescence yield, reflecting the amount of Rydberg states populated by the irradiation, oscillates with a period of about 170 as and its amplitude is modulated. The delay time response of the fluorescence yield is understood in terms of interference of the Rydberg-electron wave packets generated by the light wave packet pair. When the fluorescence from individual Rydberg states was selected in the observation, the relative fluorescence intensities of these states showed remarkable changes depending on the delay time [1]. This observation proves that the populations of the Rydberg states can be controlled by tuning the delay of the light wave packet pair.

[1] Y. Hikosaka *et al*., Nat. Commun. **10** (2019) 4988.
[2] T. Kaneyasu *et al.*, Phys. Rev. Lett. **123** (2019) 233401.

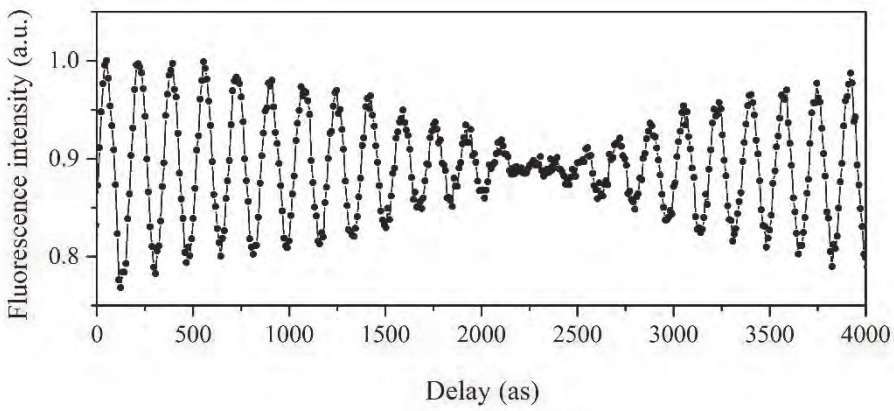


Fig. 1. Intensities of fluorescent photons from He, measured as a function of the time delay between the light wave packets generated by a tandem undulator [1]. Delay time of the horizontal axis is measured from the original delay (~2.1 fs) between the light wave packets.

BL1U

Energy-Dependence of Photoelectron Circular Dichroism of Chiral Molecules

H. Kohguchi[1], Y. Hikosaka[2], T Kaneyasu[3], S. Wada[1], M. Fujimoto[4], M. Katoh[4] and Y-I. Suzuki[5]

[1]*Graduate School of Science, Hiroshima University, Higashi-Hiroshima 739-8526, Japan*
[2]*Institute of Liberal Arts and Sciences, University of Toyama, Toyama 930-0194, Japan*
[3]*SAGA Light Source, Tosu 841-0005, Japan*
[4]*UVSOR Synchrotron Facility, Institute for Molecular Science, Okazaki 444-8585, Japan*
[5]*School of Medical Technology, Health Sciences University of Hokkaido, Tobetsu 061-0293, Japan*

Photoelectron circular dichroism (PECD) is expected to be a powerful tool for chiral recognition because of the high efficiency due to electric dipole interaction of chiral molecules with radiation. The PECD emerges as forward-backward asymmetry in the photoelectron scattering distribution of enantiomers with respect to propagation of circular polarized light. The origin of PECD has been simply described as an incomplete compensation of the scattering amplitudes of partial photoelectron waves due to the chiral molecular framework. Although a good agreement of the experiments and theoretical model calculations was shown for typical chiral molecules in the previous studies with VUV light, a recent finding of PECD in the higher photon energy region was explained by a different mechanism, indicating the significance of the energy-dependence to understand PECD. In this research project, we have planned to measure PECD in a wide photon energy region to establish an effective model to describe the physical origin of PECD.

We conducted the measurement of PECD at BL1U with a velocity-mapping photoelectron imaging detector [1]. Since this was our first experimental action, detection efficiency and energy- and angular-resolution were carefully inspected based on the comparison with the literature results of typical PECD systems: camphor and methyl-oxirane. Undulator radiation was used to ionize the vapor sample, which was introduced into the vacuum chamber as an effusive beam. Photon energy was varied in the 10 - 20 eV region, which generated photoelectrons with the kinetic energy of 0 - 8 eV. A set of PECD data consisted of the scattering images with circularly polarized radiation. The controllability of the polarization and the photon energy in the BL1U undulator was quite useful for obtaining the difference image data between the right/left-handed circularly polarized radiations under the constant measurement conditions.

Our measurements well reproduced the PECD images of camphor and methyl-oxirane in the previous studies. Examples of the observed results of camphor are shown in Fig. 1. The forward-backward asymmetry with respect to the light propagation direction (vertical in Fig. 1), which is experimental evidence of PECD, exhibited opposite signs for *l*- and *d*-camphor enantiomers. The radial distributions indicating the state-specific PECD showed a good agreement with the previous measurements. The photon energy dependence of the PECD images was also confirmed in this measurement (Fig. 1). Further analysis was limited at present by a relatively large photon energy width ($\Delta E/E \approx 10$ %), which smears PECD due to overlapping of the photoelectron bands.

Feasibility of the PECD measurements with BL1U was positively demonstrated in the present study. We found possible modifications to BL1U to improve the quality of the PECD data.

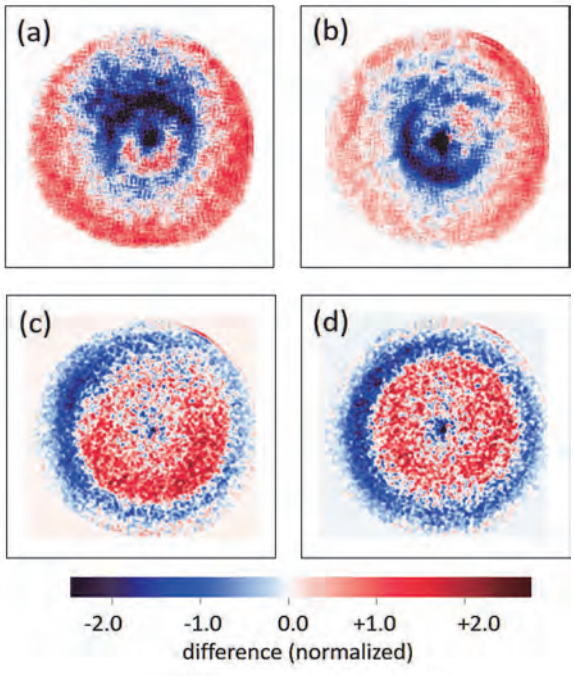


Fig. 1. Photoelectron circular dichroism of *l*- and *d*-camphor enantiomers measured at BL1U. (a) and (c); *d*-camphor, (b) and (d); *l*-camphor. Photon energy-dependence is shown as the difference between the image data with hv= 120 nm ((a) and (b)) and hv= 60 nm ((c) and (d)).

[1] T.Kaneyasu *et al*., Phys. Rev. A **95** (2017) 023413.

BL1B, BL6B

Low-Frequency and THz Region Spectroscopy on Various Organic Molecules to Elucidate Microwave-Enhanced Organic Reactions

H. Takaya[1], T. Yamada[2], K. Tanaka[3] and F. Teshima[3]

[1]*International Research Center for Elements Science, Institute for Chemical Research, Kyoto University, Uji 611-0011, Japan*

[2]*Faculty of Science and Engineering, Keio University, Yokohama 223-8522, Japan*

[3]*UVSOR Synchrotron Facility, Institute for Molecular Science, Okazaki 444-8585, Japan*

THz and Low-frequency region spectroscopic analysis was performed on various organic compounds to investigate the dynamic behavior of organic molecules under microwave irradiation.

Microwave-enhanced chemical process has been recently focused intensely because the high-speed and high-selective molecular conversion provide a highly efficient chemical process which never accessible by using the conventional heating techniques such as oil bath and electric heater. Prof. Yamada and his colleagues found that axially chiral biaryl compounds such as 1-methyl-6*H*-naphtho[2,1-*c*]chromen-6-one **1** show microwave-enhanced racemization behavior under the irradiation of 2.45 GHz microwave, where the corresponding enantiomerically pure atropisomer efficiently undergoes racemization through the rotation around the biaryl axial linkage [1]. Theoretical simulation demonstrated that the rotation-induced atropisomerism closely corresponds to molecular dynamics coupled with THz to low-frequency vibration modes (5–800 cm^{-1}). We considered that microwave irradiation could excite the internal rotation through such vibration modes and the molecular dynamics under microwave irradiation can be detected by THz and low-frequency region vibration spectroscopy. For this reason, we examined the THz-low frequency spectroscopic analysis of various biaryl organic compounds including **1**.

All the samples of biaryl compounds were once dissolved into the appropriate solvents such as CH_2Cl_2 and THF and directly dropped onto a THz-transparent diamond window to set the sample stem which insets into the vacuum chamber. The THz-low-frequency measurement carried out under the standard condition of the beamline using HDL-5 Infrared Laboratories I.R detector bolometer in the range of 30–130 and 130–680 cm^{-1} with appropriate beam splitters of Mylar and KBr/Ge, respectively. The resulting raw spectrum was processed by dividing the reference spectrum of diamond plate for baseline correction. Theoretical simulation of the spectrum was performed by DFT at M06-2x/6-311G+(d,p) level of theory using vibrational frequency scale factor for this level (0.967) [2]. The spectrum of compound 1 is shown in Fig. 1. with the corresponding DFT-simulated spectrum where the spectrum in the Mid-infrared range from 350–680 is qualitatively agreed with the real specrum.

[1] S. Tashima, K. Nushiro, K. Saito and T. Yamada, Bull. Chem. Soc. Jpn. **89** (2016) 833.

[2] Computational Chemistry Comparison and Benchmark DataBase (CCC BDB), https://cccbdb.nist.gov/vibscalejust.asp

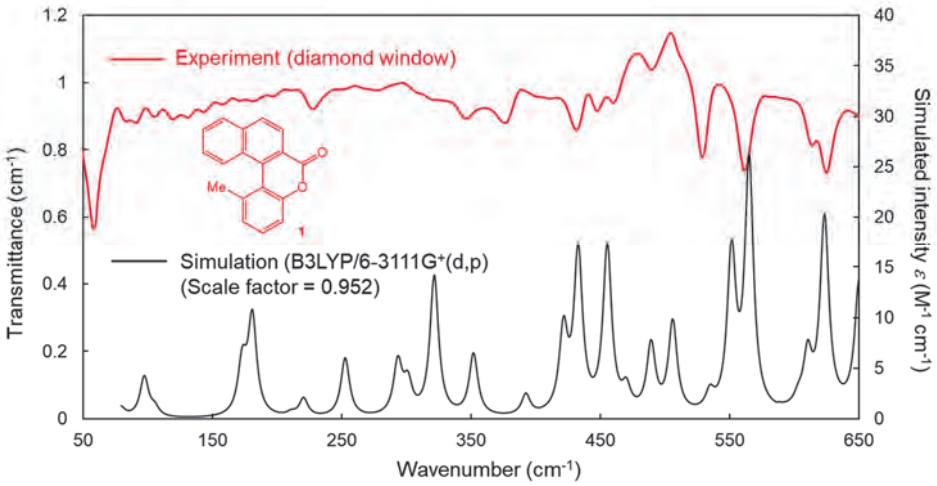


Fig. 1. Low-Frequency IR Spectrum of **1**: Experimental (red solid line) and DFT-simulated with smearing (blak solid line).

BL3U

π-π Interactions Between Liquid-Crystal Molecules Studied by *in-situ* X-ray Absorption Spectroscopy

H. Iwayama[1, 2] and M. Nagasaka[1, 2]

[1]*Editorial Board, UVSOR Synchrotron Facility, Institute for Molecular Science, Okazaki 444-8585, Japan*

[2]*School of Physical Sciences, The Graduate University for Advanced Studies, SOKENDAI, Okazaki 444-8585, Japan*

The liquid crystal is one of the most important materials for display devices. In the case of nematic liquid crystals, the rod-shaped organic molecules have no position order, but they self-align to have long-range directional order with their long axes roughly parallel. Since X-ray absorption spectroscopy (XAS) is sensitive to a local atomic geometry and the chemical state of the atom of one specific element, XAS spectroscopy is suitable to investigate structures of liquid crystals materials. However, XAS measurement of liquid-crystal materials is limited to one in a solid phase due to the requirement of high vacuums of a sample chamber. Considering the fact that they work as display device in a liquid-crystal phase, we need to measure XAS in a liquid-crystal phase. Recently, our colleague, Nagasaka developed a liquid cell, which allows us to measure XAS spectra of liquid samples [1]. In our work, we measure XAS of liquid-crystal materials in the liquid-crystal phase.

Our sample is 4-Cyano-4'-pentylbiphenyl (5cb), which is one of the most popular liquid-crystal materials. A schematic draw of 5cb molecules is shown in Fig. 1. The phase transition temperature of liquid to liquid-crystal and liquid-crystal to solid are 35 and 22.5 °C, respectively. The XAS measurements were carried out at UVSOR BL3U. After liquid-crystal cell which is composed of two Si_3N_4 membranes was filled with the liquid-crystal sample, the thickness of liquid-crystal sample was optimized by controlling the He gas pressure around the cell. The photon energy was calibrated by using the C-K edge XAS spectrum of the proline thin layer.

Figure 2 shows a C K-edge XAS spectrum of 5cb sample at 26 °C, which correspond to the liquid-crystal phase. We observed several peaks and a strong peak at 285 eV. To understand XAS spectrum and perform a peak assignment, we need theoretical calculation. We introduced a quantum chemical calculation software, StoBe, which is based on the density functional theory and can calculate core hole states. A calculated spectrum is also shown in Fig. 2 and reproduces experimental results well. By analyzing the calculation, it is revealed that the strong peak at 285 eV correspond to a core excitation of C 1s to π* orbitals of phenyl group.

Figure 3 shows peaks at 285 eV for each phase. We observed high energy shift of the peak at the phase transition between solid and liquid-crystal phases. This phase dependence of core excitations reflects the change of molecular alignments between each phase. Our results show the phase transition between solid to liquid-crystal phases weaken π-π interaction between molecules.

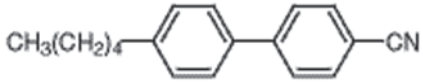


Fig. 1 Schematic draw of 4=Cyano-4'- pentylbiphenl (5cb) molecules.

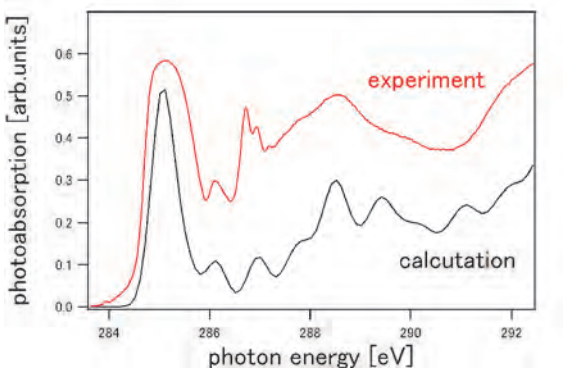


Fig. 2 Experimental and calculated C K-edge spectra of 5cb molecules. Experimental spectra were measured at 26 °C (liquid-crystal phase).

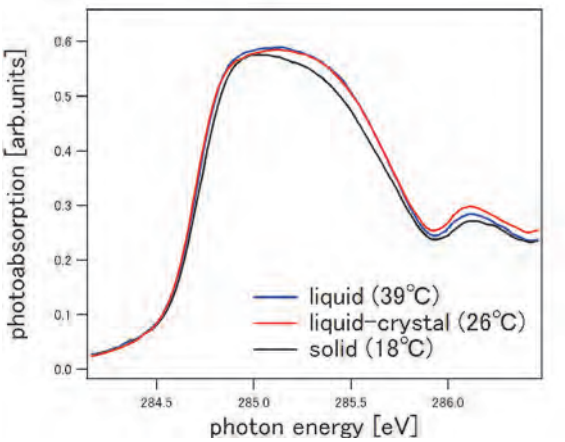


Fig. 3 C K-edge XAFS spectra of 5cb molecules at 18 (solid), 26 (liquid-crystal) and 39 °C (liquid).

[1] M. Nagasaka, H. Yuzawa and N. Kosugi, J. pectrosc. Relat. Phenom. **200** (2015) 293.

BL3U

Oxygen K-edge X-ray Absorption Spectroscopy of Aqueous Acetonitrile Solution at Different Concentrations

M. Nagasaka[1,2], H. Yuzawa[1] and N. Kosugi[1,2]
[1]*Institute for Molecular Science, Okazaki 444-8585, Japan*
[2]*The Graduate University for Advanced Studies, SOKENDAI, Okazaki 444-8585, Japan*

Aqueous acetonitrile solution shows microheterogeneity, where two liquids seem to be mixed in a macroscopic scale but are inhomogeneous in microscopic scale [1]. Soft X-ray absorption spectroscopy (XAS) is an effective method to investigate molecular interactions of aqueous acetonitrile solutions since molecular interactions of acetonitrile can be revealed by the C and N K-edge, and the interaction of solvent water molecules is separately revealed by the O K-edge. Recently, several groups measured O K-edge XAS of aqueous acetonitrile solutions. By increasing the molar fraction of acetonitrile, the main-edge peak (538 eV) becomes sharper in profile, which means that isolated water molecules exist in aqueous solutions [2]. However, their studies reported molecular interaction of solvent water only in a limited concentration region. In this study, we have investigated molecular interactions of solvent water in the wide concentration regions by using O K-edge XAS [3].

The experiments were performed at soft X-ray beamline BL3U. XAS spectra of liquid samples were measured by a transmission-type liquid flow cell [4].

Figure 1(a) shows O K-edge XAS spectra of aqueous acetonitrile solutions $(CH_3CN)_x(H_2O)_{1-x}$ at different concentrations from x = 0.0 to 0.9 by 0.05 step. By increasing the molar fraction of acetonitrile (x), the pre-edge peaks (535 eV) related to the $4a_1$ states show lower energy shifts and the main-edge peaks related to the $2b_2$ states show sharper profile. The sharp profile in the main-edge peak is caused by decreasing molecular interactions among water molecules. This sharp profile starts to grow above x = 0.2, which means that water molecules form the dipole (DP) structure with acetonitrile at $x > 0.2$.

Figure 1(b) shows the energy shifts of the pre-edge peaks at different concentrations from those of liquid water ($x = 0.0$). The larger energy shift at higher molar fraction of acetonitrile is caused by the formation of an isolated water molecule enclosed in liquid acetonitrile as shown in the inset. The concentration-dependent energy shift is gentle at $0.7 > x$ but is larger at $x > 0.7$. It suggests that the population of isolated water molecules embedded in liquid acetonitrile is rapidly increased at $x > 0.7$.

We have also measured C and N K-edge XAS of aqueous acetonitrile solution at different concentrations for studying molecular interaction of acetonitrile in aqueous solution [3]. In the middle concentration region, the acetonitrile clusters are fully surrounded by water with the DP interactions, which is the key structures to emerge the microheterogeneity. The energy shifts of the pre-edge peaks in O K-edge XAS also confirm the DP interactions between acetonitrile and water, which forms isolated water molecules in acetonitrile-rich regions.

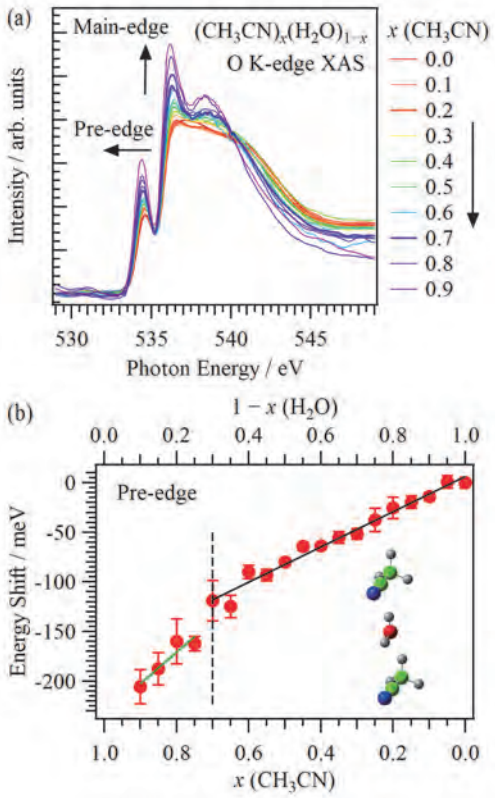


Fig. 1. (a) O K-edge XAS spectra of aqueous acetonitrile solution at different concentrations. The pre-edge and main-edge peaks are changed to the direction of arrows by increasing the molar fraction of acetonitrile (x). (b) Energy shifts of the pre-edge peaks at different concentration from those of liquid water (x = 0.0). The inset shows a water molecule enclosed in two acetonitrile molecules.

[1] Y. Marcus, J. Phys. Org. Chem. **25** (2012) 1072.
[2] N. Huang *et al*., J. Chem. Phys. **135** (2011) 164509.
[3] M. Nagasaka, H. Yuzawa and N. Kosugi, J. Phys. Chem. B **124** (2020) 1259.
[4] M. Nagasaka *et al*., J. Electron Specrosc. Relat. Phenom. **224** (2018) 93.

BL3U

Hydrated Water Structure of *N,N*-Dimethylglycine Studied by Soft X-Ray Absorption Spectroscopy

N. Fukuda[1], S. Ohsawa[1], H. Yuzawa[2], M. Nagasaka[2,3] and K. Okada[1]

[1]*Graduate School of Science, Hiroshima University, Higashi-Hiroshima 739-8526, Japan*

[2]*Institute for Molecular Science, Okazaki 444-8585, Japan*

[3]*School of Physical Sciences, The Graduate University for Advanced Studies, SOKENDAI, Okazaki 444-8585, Japan*

Living cells protect themselves from external stress such as hydrostatic pressure and drought by regulating the amount of solutes called osmolytes [1]. Several organic osmolytes have a characteristic feature of the form as a zwitterion. Found most commonly in cells are fully *N*-substituted amino acids, although partially- and non-substituted amino acids also take a zwitterionic form. Glycine betaine (also known as *N,N,N*-trimethylglycine or TMG) is among the most common species in cells, and its amount dominates much over *N*-methylglycine (NMG) and *N,N*-dimethylglycine (DMG). Many recent studies have revealed that the higher-order structure of proteins is protected through the indirect interaction between the hydrated proteins and osmolytes. Studying the difference in hydration structure between TMG and DMG gives a clue to understand why biological systems prefer fully *N*-substituted amino acids over partially substituted counterparts. The hydration of DMG has not yet investigated in this sense. We therefore focus in this report on the electronic structure of the hydrated water molecules of DMG compared with that of TMG by soft X-ray spectroscopy.

Photoabsorption spectra at the oxygen K-edge were measured in the transmission mode at room temperature. Aqueous solutions of DMG and TMG with concentrations up to 1.0 M were introduced by means of a tubing pump into a liquid flow cell [2] installed on the soft X-ray beamline BL3U. The flow cell for this study was equipped with a pair of windows made of thin silicon nitride membrane. The incident photon energy was calibrated to the peak at 530.88 eV of a polymer film [3].

Figure 1 shows the O 1s absorption spectra of liquid water, DMG and TMG aqueous solutions enlarged at the water $4a_1$ resonance band. The peak top at 534.6 eV is shifted by +0.20 and −0.05 eV for DMG and TMG solutions, respectively. The apparent shift observed for the TMG solution is consistent with our previous measurement [4]. The hydration structure is extracted by deconvolution of the band consisting of the hydrated and bulk water components thanks to the chemical shift present in the inner-shell excitation of molecules under different chemical environments. The second and fourth derivatives (not shown) of the absorption spectra of liquid water suggest that there exist two components in the $4a_1$ resonance band. The derivatives for the DMG and TMG solutions indicate that additional components are necessary to reproduce the spectra. The latter components can be ascribed to the hydrated water acting as a hydrogen-bond donor or acceptor to interact with the solutes. The validity of the present analysis is supported by the fact that the area of the components increases with the concentration.

The apparent blue shift for the DMG solution is reasonably explained by the presence of the hydrated water acting as a hydrogen-bond acceptor. Because its component is placed at the higher energy side of the band, the intensity around it is higher than that of liquid water and of the TMG solution. A further analysis is in progress and the results will be published elsewhere.

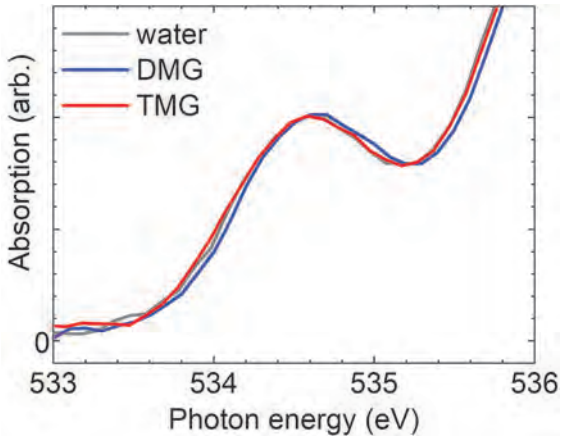


Fig. 1. Enlarged O 1s photoabsorption spectra of liquid water, 1.0-M DMG and 1.0-M TMG aqueous solutions in the 533–536 eV region.

[1] P. H. Yancey, M. E. Clark, S. C. Hand, R. D. Bowlus and G. N. Somero, Science **217** (1982) 1214.

[2] M. Nagasaka, T. Hatsui, T. Horigome, Y. Hamamura and N. Kosugi, J. Elec. Spectrosc. Relat. Phenom. **177** (2010) 130.

[3] M. Nagasaka, H. Yuzawa, T. Horigome and N. Kosugi, J. Elec. Spectrosc. Relat. Phenom. **224** (2018) 93.

[4] S. Ohsawa, N. Fukuda, H. Iwayama, H. Yuzawa, M. Nagasaka and K. Okada, UVSOR Activity Report 2018 **46** (2019) 115.

BL3U

X-ray Absorption Measurements Applied to Aqueous Solutions of Carboxylate Ions, in the Vicinity of the O K-edge Ionization Thresholds

D. Céolin[1], T. Saisopa[2], K. Klaiphet[2], J. Borsup[2], P. Songsiriritthigul[2], H. Yuzawa[3] and N. Kosugi[4]

[1]*Synchrotron SOLEIL, L'Orme des Merisiers Saint-Aubin BP 48 91192 Gif-sur-Yvette Cedex, France*
[2]*Research Network NANOTECH-SUT on Advanced Nanomaterials and Characterization and School of Physics, Suranaree University of Technology, Nakhon Ratchasima 30000, Thailand*
[3]*UVSOR Synchrotron Facility, Institute for Molecular Science, Okazaki 444-8585, Japan*
[4]*Institute of Materials Structure Science, KEK, Tsukuba 305-0801, Japan*

It is well established in organic chemistry that the reactivity of a specific group can be predicted considering several additive or competing effects influenced by the energy position and occupation of the frontier orbitals. In this context, it is interesting to evaluate the role of the molecular skeleton on which a carboxylate group is fixed (R in R−COO^-), and how its inductive or mesomeric properties might influence the reactivity of the system.

One method to determine the energy position of the unoccupied orbitals of carboxylate is to perform XAS measurements. This was done for instance on aqueous solutions of acetate salts – with the motivation to probe the pairing efficiency of −COO^- with different types of positive ions [1].

At the beamline BL3U, and using the liquid cell in transmission mode, we measured XAS in the vicinity of the O *K*-edge ionization threshold on sodium formate, acetate, propionate, trifluoroacetate and benzoate (R = H, CH_3, C_2H_5, CF_3 and C_6H_5 respectively). See Fig. 1 (C_2H_5 spectrum is not shown but the resonances position is similar to those of CH_3).

The resonance located at hν = 535 eV is attributed to the O1s excitation of water to its first empty orbital. The O1s → π^*_{CO} resonances associated with the −COO^- group are located between 531.5 eV and 533.5 eV, and the small structure at 530.9 eV is due to surface oxidation of Si_3N_4 membranes. To give a preliminary interpretation of these results, we looked at the inductive and mesomeric properties of R. With R = H taken as a neutral reference, CF_3 and C_6H_5 are electron withdrawing groups (-I), and CH_3 and C_2H_5 are electron donating groups (+I). CF_3 withdraws electrons because of the very strong electronegativity of the fluorine atoms. C_6H_5 is also generally considered as -I compared with hydrogen due to the sp^2 hybridization of the carbon atom of the phenyl ring bonded to −COO^-. On the contrary, for CH_3 and C_2H_5, the carbon bonded to the carboxylate has a sp^3 hybridization and is considered as electron donating. The sp^2 hybridized orbitals have a larger s-character than the sp^3 ones, and contrary to the 2p-electrons, the 2s-electrons have the property to be more tighten to the nucleus. This leads to less diffuse sp^2 hybridized orbitals and to an increase of their electronegativity. To explain the strong shift of the C_6H_5 group, one can invoke its mesomeric property (see Fig. 2). Despite more complex and probably weaker, a similar effect might be considered for CF_3 as well due to possible hyperconjugation process [2].

All effects taken into account, it seems that the total charge density located in the vicinity of the oxygens of the carboxylate group plays a crucial role on the resonances position. Induction has an influence on the σ-skeleton of the molecule, and thus might modify the spatial extension of the oxygen lone-pairs carried by −COO^-, and electron delocalization through the π-system clearly increases the negative charge on the oxygen of carboxylate. These hypotheses need to be confirmed, and their relation with the resonances position will be the subject of theoretical investigations.

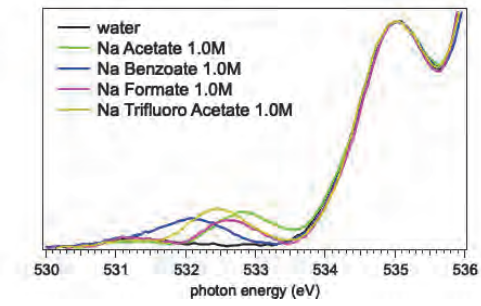


Fig. 1. X-ray absorption spectra of 1 M aqueous solutions of sodium formate, acetate, propionate, trifluoroacetate and benzoate, in the vicinity of the O *K*-edge ionization thresholds. Normalization is done on the peak maximum at 535 eV.

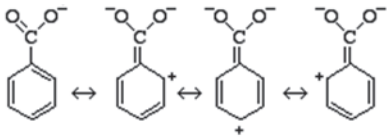


Fig. 2. Resonating forms of benzoate.

[1] J. S. Uejio *et al*., PNAS **105** (2008) 6809, E. F. Aziz *et al*., J. Phys. Chem. B **112** (2008) 12567, T. Petit *et al*., Structural Dynamics **1** (2014) 034901.
[2] L. M. Stock, M. R. Wasielewski, *Progress in Physical Organic Chemistry 13*, chapter 4 (John Wiley & Sons, Inc., 1981).

BL3U

NEXAFS Study of μ-Nitrido-Bridged Iron Phthalocyanine Dimer with Graphite Surface

Y. Yamada [1,2,3] and M. Nagasaka[4]

[1]*Department of Chemistry, Graduate School of Science, Nagoya University, Nagoya 464-8602, Japan*
[2]*Research Center for Materials Science, Nagoya University, Nagoya 464-8602, Japan*
[3]*PRESTO/JST, Kawaguchi 332-0012, Japan*
[4]*Institute for Molecular Science, Okazaki 444-8585, Japan*

Direct C-H activation of light alkanes such as methane and ethane under mild reaction condition is an important challenge in the field of catalytic chemistry because efficient conversion of light alkanes into valuable chemical raw materials can contribute to reduce our dependence on petroleum resources. μ-Nitrido-bridged iron phthalocyanine dimer (**1** in Fig. 1) is one of the most potent molecule-based catalysts for direct C-H activation of methane and ethane [1,2]. It can catalytically convert light alkanes into corresponding alcohols, aldehydes, and carboxylic acids in an acidic aqueous solution at a lower temperature below than 100 °C in the presence of H_2O_2. Recently, we found that the catalytic methane oxidation activity of **1** was significantly enhanced by adsorption on graphite surface. In order to clarify the mechanism of this enhancement, we investigated the structure of **1** on graphite surface, as well as the interaction between **1** and graphite by XAFS study.

1 was adsorbed on a highly oriented pyrolytic graphite (HOPG) to prepare **1**/HOPG as shown in Fig. 1. N K-edge NEXAFS measurements were performed at the soft X-ray beamline BL3U of UVSOR [3]. For these measurements, **1**/HOPG was fixed with double-sided conductive carbon tape onto a stainless sample holder. The holder was fixed on a rotatable linear and installed into a vacuum chamber ($< 1 \times 10^{-5}$ Pa). The N K-edge NEXAFS spectra were obtained in total electron yields by measuring a sample drain current.

Figure 2 (a) shows a comparison of the NEXAFS spectra obtained at three different incident angles (θ = 90°, 55°, and 30° from the HOPG surface). The peaks at around 398 eV are assignable to the excitation of N 1s core electrons to the C=N π* orbitals of the phthalocyanine. Considering that the C=N π* transition moment is perpendicular to the p-surface of the phthalocyanine, the high intensity of the π* peak at θ = 30° implies that the π-surface was parallel to the HOPG surface. Figure 2 (b) shows incident-angle dependence of the C=N π* peak intensity at 398 eV with the simulated curve calculated from the tilted angle of the C=N π* transition moment from the normal of the HOPG surface [4]. As a result of the fitting procedure, the tilted angle of the C=N π* transition moment is approximately 0 from the surface normal. This indicates that the phthalocyanine π-surface was parallel to the HOPG surface as shown in Fig. 1b.

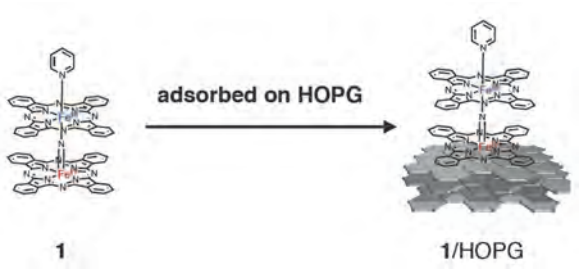


Fig. 1. Adsorption of **1** on a HOPG substrate.

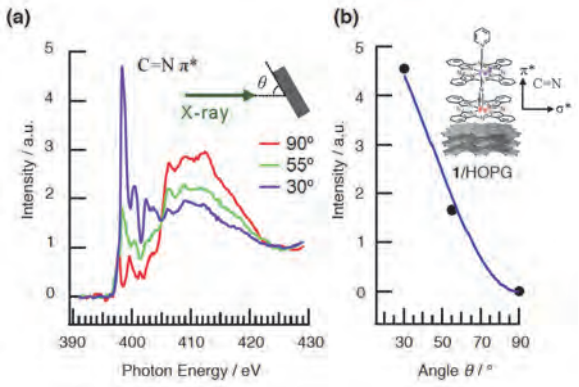


Fig. 2. (a) Comparison of the NEXAFS spectra of **1**/HOPG at three different incident angles (θ = 90°, 55°, and 30°). (b) Dependence of the C=N π* peak intensity (398 eV) on the incident angle with the simulated curve.

[1] P. Afanasiev and A. B. Sorokin, Acc. Chem. Res. **49** (2016) 583.
[2] Y. Yamada, K. Morita, N. Mihara, K. Igawa, K. Tomooka and K. Tanaka, New J. Chem. M. **43** (2019) 11477.
[3] T. Hatsui, E. Shigemasa and N. Kosugi, AIP Conf. Proc. **705** (2004) 921.
[4] Y. L. Huang, W. Chen, S. Chen and A. T. S. Wee, Appl. Phys. A. **95** (2009) 107.

BL3U

Oxygen K-edge X-ray Absorption Spectroscopy of Aqueous Ethanol Solution at Different Concentrations

M. Nagasaka[1,2], M. Bouvier[1], H. Yuzawa[1] and N. Kosugi[1,2]
[1]*Institute for Molecular Science, Okazaki 444-8585, Japan*
[2]*The Graduate University for Advanced Studies, SOKENDAI, Okazaki 444-8585, Japan*

Aqueous ethanol (EtOH) solution is a model to explore competition between hydrophilic (namely, HB: hydrogen bond) and hydrophobic interactions and is important to understand several physical, chemical, and biological phenomena [1]. Soft X-ray absorption spectroscopy (XAS) is an effective method to investigate HB with water molecules [2]. Recently, several groups measured O K-edge XAS of aqueous EtOH solutions [3,4], but they reported spectra only in a limited concentration region. In this study, we have investigated HB interaction between EtOH and water in the wide concentration region by O K-edge XAS.

The experiments were performed at soft X-ray beamline BL3U. XAS of liquid samples were measured by a transmission-type liquid flow cell [5]. Liquid samples are exchanged in situ by using a tubing pump without changing the sample position.

Figure 1(a) shows O K-edge XAS spectra of aqueous EtOH solutions at different concentrations at 25 °C. In the XAS spectrum of liquid water (x = 0.0), the pre-edge peak at 535 eV corresponds to the transition of O 1s electron to an unoccupied $4a_1$ orbital and reflects HB interaction between water molecules [2]. On the other hand, the pre-edge feature of liquid EtOH (x = 1.0) is embedded in the main peak at 538 eV, as observed in the previous study [3, 4]. As observed in the inset of Fig. 1(a), the pre-edge region shows isosbestic points at 534.9 and 535.9 eV. It indicates that the pre-edge region consists of two spectral contributions from EtOH and water, which is also suggested by the previous study [3].

Figure 1(b) shows spectral fractions of EtOH and water in the pre-edge region at different molar factions of EtOH (x) obtained by fitting the superposition of pure EtOH (x = 1.0) and pure water (x = 0.0). The spectral fraction of water is decreased and that of EtOH is increased by increasing the molar fraction of EtOH (x). However, these changes show nonlinear features, where the changes of EtOH is crossed with that of water at x = 0.65. It is a different trend from O K-edge XAS of aqueous methanol (MeOH) solutions, where the spectral fraction of MeOH is changed linearly and is crossed at x = 0.5 [6]. Since the ethyl group is larger than the methyl group, the HB interaction between water molecules would be increased by the stronger hydrophobic interaction in EtOH than in MeOH, resulting the higher ratio of water spectral fraction at the EtOH-rich concentration region.

In the future, we will discuss hydrophobic interactions of the ethyl group in EtOH more directly from the C K-edge XAS spectra.

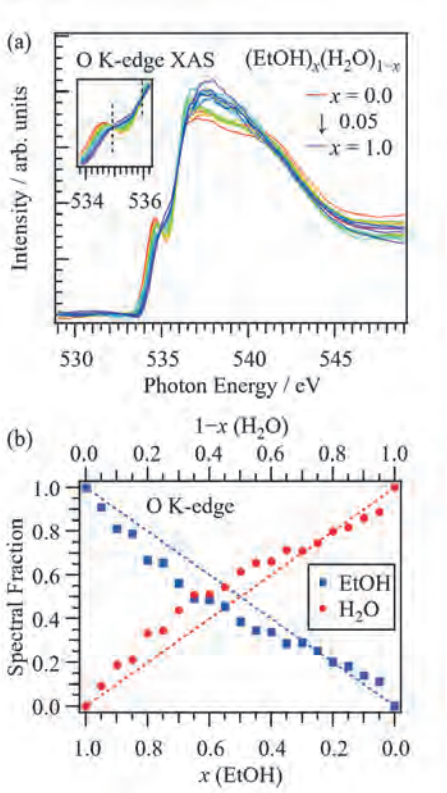


Fig. 1. (a) O K-edge XAS spectra of aqueous EtOH solutions at different concentrations from x = 0.0 to 1.0 by 0.05 step. The inset shows the expansion of the pre-edge region. (b) Spectral fractions of EtOH and water in the pre-edge region as a function of the molar fraction of EtOH (x) obtained by fitting the superposition of pure EtOH (x = 1.0) and pure water (x = 0.0).

[1] A. Ghoufi *et al.*, J. Phys. Chem. B **120** (2016) 793.
[2] J. W. Smith and R. J. Saykally, Chem. Rev. **117** (2017) 13909.
[3]I. Juurinen *et al.*, J. Phys. Chem. B **118** (2014) 8750.
[4] R. K. Lam *et al.*, J. Chem. Phys. **144** (2016) 191103.
[5] M. Nagasaka *et al.*, J. Electron Specrosc. Relat. Phenom. **224** (2018) 93.
[6] M. Nagasaka *et al.*, J. Phys. Chem. B **118** (2014) 4388.

BL3U

Observations of Micelle Formation in Aqueous Organic Solutions Using Soft X-ray Absorption Spectroscopy

J. J. Lin[1], G. Michailoudi[1], Kamal Raj R.[1], H. Yuzawa[2], M. Nagasaka[3,4] and N. L. Prisle[1]

[1]*Nano and Molecular Systems research unit, University of Oulu, P.O. Box 3000, 90014 University of Oulu, Finland*

[2]*UVSOR Synchrotron Facility, Institute for Molecular Science, Okazaki 444-8585, Japan*

[3]*Institute for Molecular Science, Okazaki 444-8585, Japan*

[4]*School of Physical Sciences, The Graduate University for Advanced Studies, SOKENDAI, Okazaki 444-8585, Japan*

Amphiphilic compounds in aqueous solutions are known to self-assemble into structures known as micelles above some critical micelle concentration (CMC). The role of amphiphiles in cloud droplet nucleation is still debated, with the specific impact of micelles unaccounted for in cloud formation models [1]. The uncertainties involving the formation of cloud droplets from organic cloud nuclei are some of the largest in the understanding of anthropogenic climate forcing [2].

Aqueous solutions of sodium hexanoate were studied using X-ray absorption spectroscopy (XAS) at the BL3U beamline using the liquid flow cell setup. The range of reported CMC values for sodium hexanoate is 0.53–1.7 M [3]. A value of 0.9 M was assumed and solutions at 0.75 and 3 times the CMC value (i.e. 0.68 and 2.7 M) were made for this study. For each concentration, the solutions were made at the pK_a of hexanoic acid as well as one pH unit above and below the pK_a.

The sensitivity of XAS to chemical environment provides information about the bulk properties of the aqueous components. XAS measurements were made at the carbon K-edge in order to specifically capture the aliphatic R(CH)R' and carboxylic C(=O)OH carbon absorption peaks. The measured photon energy range was from 280 to 300 eV with resolution of 0.02 eV from 285 to 290 eV and 0.1 eV for the rest of the energy range. Measurements were also made on pure water in the liquid cell in order to remove the carbon signal from contamination in the beamline and the liquid cell. The energy of the incident X-rays was regularly calibrated using XAS measurements on a thin polymer film (ProLINE) which has a well-defined absorption peak. The temperature of the liquid samples was controlled to 25 °C.

Measured absorption spectra are shown in Fig. 1. Background absorption has been removed by subtracting the pure water spectrum, and each spectrum has been calibrated using the polymer film spectra taken immediately before and after the sample spectrum. For most of the spectra, a main peak is observed at around 289 eV. In general, the absorption of the sample decreases with increasing sodium hexanoate concentration and decreasing pH value. Changes in concentration and pH also affect the pre-peak to main peak ratio. A large drop in absorption is observed going from pH ~6 to pH ~5 for both sodium hexanoate concentrations. At low pH values, the absolute absorption values of 0.75 CMC solutions are roughly the same as the 3 CMC solutions. For the 3 CMC sodium hexanoate solutions, the main absorption peak mostly disappears.

Additional analysis of the spectra is ongoing, including comparison to previous measurements at BL3U of similar organic compounds in aqueous solution [4]. Detailed fitting of the spectra will be carried out to identify the underlying absorption peaks. Complementary measurements and theoretical prediction for these systems are also in progress.

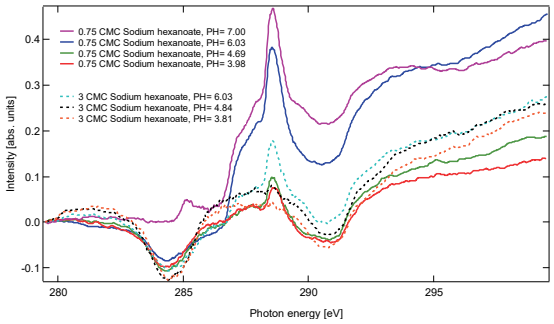


Fig. 1. Preliminary absorption spectra for aqueous sodium hexanoate solutions at 0.75 and 3 times the critical micelle concentration and for various pH values.

[1] N. L. Prisle *et al.*, Atmos. Chem. Phys. **10** (2010) 5663.

[2] O. Boucher *et al.*, *Clouds and Aerosols.* In: *Climate Change 2013: The Physical Science Basis. Contribution of Working Group I to the Fifth Assessment Report of the Intergovernmental Panel on Climate Change* (Cambridge University Press, Cambridge and New York City, 2013).

[3] P. Mukerjee and K. J. Mysels, *Critical Micelle Concentrations of Aqueous Surfactant Systems* (U.S. National Bureau of Standards, Washington, D.C., 1972).

[4] J.J. Lin *et al.*, *in prep*.

BL3B

Optical Investigation on Fluoro-olefins in Vacuum-Ultraviolet for New Refrigerant Gas Development

K. Yamanoi[1,2], Y. Sakata[1], H. Iwayama[3], Y. Hasumoto[1,2], T. Takakuwa[1,2], O. Yamamoto[1,2] and M. Noumi[1,2]

[1]*Osaka university, Suita 565-0871, Japan*
[2]*DAIKIN Industries Ltd, Settsu 566-8585, Japan*
[3]*UVSOR Synchrotron Facility, Institute for Molecular Science, Okazaki 444-8585, Japan*

Chlorofluorocarbon (CFC), hydrochlorofluorocarbon (HCFC), and hydrofluorocarbon (HFC) have been used as a refrigerant. These gases have high global warming potential (GWP) over 100. Recently, the hydrofluoroolefin (HFO) gases are expected as new low environmental load refrigerant due to its low GWPs since olefin gas is unstable and easily decompose by ultraviolet light in nature. In order to put HFO into practical use as a refrigerant, it is necessary to clarify the physical characteristics of HFO such as UV absorption and decomposition process. In this study, we measured the vacuum ultraviolet (VUV) absorption and fluorescence of tetrafluoroethylene (TFE). The absorption and fluorescence spectra measurements were carried out in BL3B in UVSOR Synchrotron Facility. TFE gas was filled in the cell having MgF_2 windows at 100 Pa. The optical path length in the cell is 35 mm. The sample-gas filled cell was placed in the vacuum chamber and VUV light was irradiated through the MgF_2 windows and detected by a photodiode. The photoluminescence was measured by the spectrometer at 90 degree from incident beam. Figure 1 shows the photograph of the sample cell and schematics of the experimental setup.

Figure 2 shows the transmission spectra of TFE at 100 Pa. We could clearly observed the absorption at about 145 nm and 190 nm. The absorption at 145 nm is attributed to the stretching and twisting of carbon double band and the 190 nm is the transition from π to π*, respectively [1].

Figure 3 shows the photoluminescence spectra of TFE at 100 Pa excited by 145 nm. The broad fluorescence from 250 to 350 nm with 276-nm peak was observed. This emission is CF_2 singlet transition [2].

In conclusion, we could observe the optical properties of TFE in VUV region. The results let us know the possibility of the UV- or VUV-induced decomposition dynamics of fluoro-olefins using optical technique such as pump and probe method.

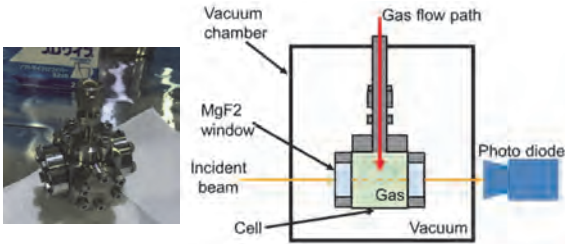


Fig. 1. Photograph of the sample cell and schematics of the experimental setup.

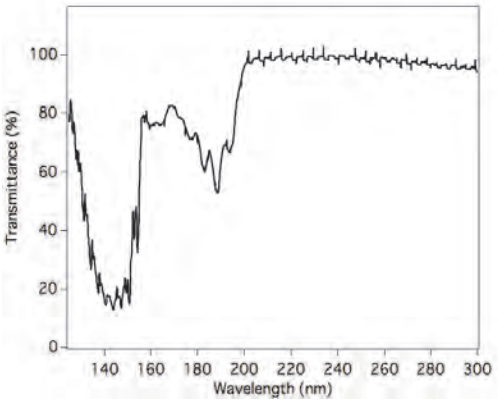


Fig. 2. Transmission spectra of TFE.

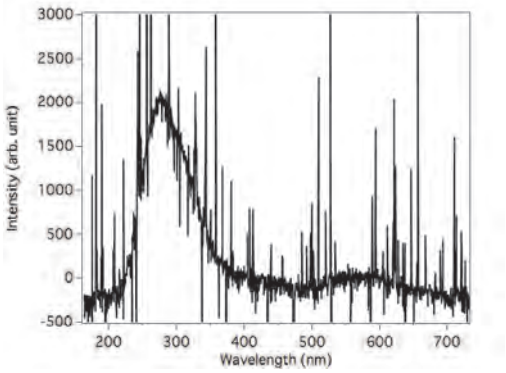


Fig. 3. Photoluminescence spectra of TFE.

[1] G. Belange *et al.*, J. Chem. Phy **55** (1971) 2055.
[2] B. A. Williams *et al.*, Chem. Phy. Let. **309** (1999) 75.

BL4B

Electron Coincidence Spectroscopy for Poly(Methylmethacrylate) Thin Film

Y. Hikosaka[1] and S. Wada[2]

[1] *Institute of Liberal Arts and Sciences, University of Toyama, Toyama 930-0194, Japan*

[2] *Department of Physical Science, Hiroshima University, Higashi-Hiroshima 739-8526, Japan*

Irradiation of soft x-ray to an organic thin film may lead a core electron ejection from a specific atom in the molecular constituent. The core hole thus generated decays mainly by emitting an Auger electron. The spectrum of the Auger electron contains useful information of the valence orbitals relevant to the decay process. In case that the constituent molecule contains the same element at different sites, Auger structures associated with these core holes overlap each other in the conventional Auger spectrum. The atomic site where the core hole has been formed can be identified by the chemical shift of the photoelectron ejected on the core-hole creation. Accordingly, Auger structures associated with individual core holes can be filtered out by coincidence observations with chemical-shifted photoelectrons. Such photoelectron-Auger electron coincidence spectroscopy can be performed with high efficiency by using a magnetic bottle electron spectrometer [1]. The adaptability of the spectrometer to solid samples is already verified [2].

In this study, photoelectron-Auger electron coincidence measurements were made for poly(methyl methacrylate) (PMMA) thin films on a copper wire. The magnetic bottle electron spectrometer employed in this study is equipped with an electrostatic retarder [3], to improve the energy resolving power. PMMA has carbon atoms in different chemical environments within a single unit (see inset of Fig. 1). Figure 1 shows a C1s photoelectron spectrum of PMMA measured at a photon energy of 482.4 eV. At least three photoelectron peaks are identified in the spectrum, and their assignments are indicated with labels of the same colors as used in the chemical formula (inset). The Auger spectra observed in coincidence with the photoelectrons for these three peaks are plotted in Fig. 2, where the colors of the spectra follow those allocated in Fig. 1. Tangible differences in spectral feature are identified among the coincidence Auger spectra. Calculation is under way, to interpret the spectral features.

[1] J. H. D. Eland *et al.*, Phys. Rev. Lett. **90** (2003) 053003.

[2] Y. Hikosaka *et al.*, J. El. Spectrosc. Rel. Phenom. **213** (2016) 17.

[3] Y. Hikosaka *et al.*, J. El. Spectrosc. Rel. Phenom. **192** (2014) 69.

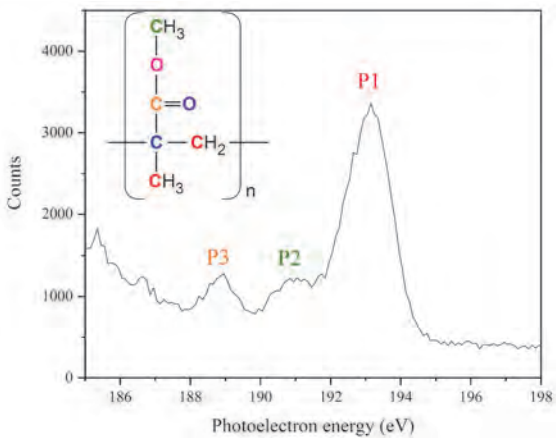


Fig. 1. C1s photoelectron spectrum of PMMA measured at a photon energy of 482.4 eV.

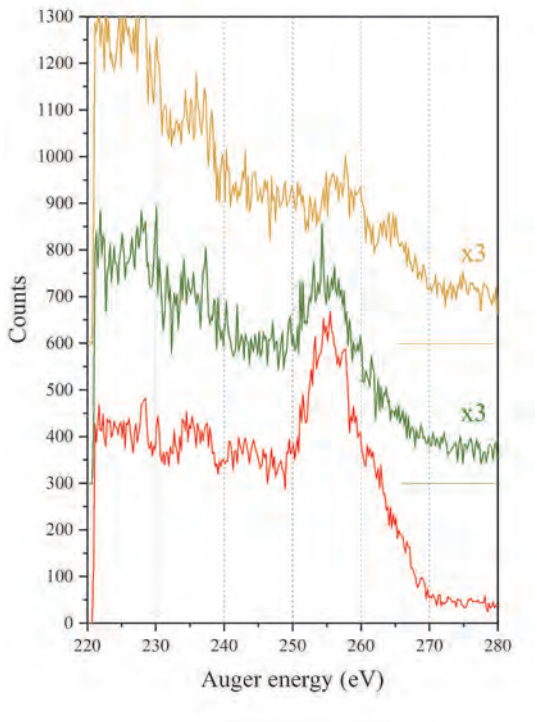


Fig. 2. Auger spectra observed in coincidence with C1s photoelectrons.

BL5B

Evaluation of Polarization Characteristic of Monochromatized Synchrotron Radiation by Observing Zeeman Quantum Beat

Y. Hikosaka[1], H. Iwayama[2] and T. Kaneyasu[3]

[1]*Institute of Liberal Arts and Sciences, University of Toyama, Toyama 930-0194, Japan*

[2] *Institute for Molecular Science, Okazaki 444-8585, Japan*

[3] *SAGA Light Source, Tosu 841-0005, Japan*

Evaluation of the polarization characteristic of monochromatized synchrotron radiation is an important concern in synchrotron radiation researches. The optical components of monochromators and beamlines modify the original polarization state of the synchrotron radiation. The effect of the modification is pronounced in the extreme ultraviolet (XUV) range, as steeper incidence angles to the optical elements are usually adopted for the monochromatization. The diagnosis of the polarization state of XUV light can be preciously made with an optical method using polarimeters. Such a measurement, however, requires stringent alignments of the polarimeters, and the fabrication and manipulation of an effective polarimeter system are still challenging. Over the optical method, observation of a material process responding to light polarization has an advantage in easy measurement. Angler distribution of photoelectrons emitted from gas samples has been conveniently utilized for evaluating the polarization.

Here we propose that the polarization characteristic of monochromatized synchrotron radiation in the XUV range can be evaluated by observing quantum beat of Zeeman-split Rydberg states in He [1]. A fluorescence decay curve measured at the He 1s→6p excitation energy is presented in Fig. 1 (black dots), where UV fluorescence photons emitted on the 6p→2s decay is detected by a photomultiplier. The photomultiplier was placed at right angles to both the polarization and propagation of the monochromatized synchrotron light, and a magnetic field of 21.1 mT was applied along the light propagation axis.

The fluorescence decay curve exhibits a quantum beat oscillation superposing on the exponential-decay form. This observation manifests the coherent excitation to the Zeeman-split M_j=±1 levels. The decay curve can be fitted with the formula

$$I(t) \sim [1 + P\cos\Delta\omega t] \exp(-\gamma t) \qquad (1)$$

where P, $\Delta\omega$, and γ are the polarization degree, the transition frequency of the initial excitation, and the lifetime of the excited state, respectively. This equation indicates that visibility of the oscillation superposing on the exponential decay reflects directly the degree of the light polarization. The solid red curve in Fig. 1 is the best fit to the observation, where the temporal resolution of the measurement was assumed as the Gauss function of 2.9 ns FWHM. The fitting indicates the degree of the linear polarization to be P=0.60±0.05. The polarization degree may be too poor, even as the light provided by the bending magnet beamline of the large acceptance in the vertical direction. It is practically anticipated that the fitting result underestimates the actual polarization degree. This is because the fitting does not take into account the large detection solid angle for the present fluorescence observation, while the phase of the quantum beat varies according to the detection angle and the overlap of the quantum beats with different phases in the detection solid angle reduces the visibility of the observed quantum beat oscillation. More accurate estimation of the polarization degree can be achieved by observing fluorescence with a smaller detection solid angle, which is fully feasible considering the favorable count rates in the present investigation.

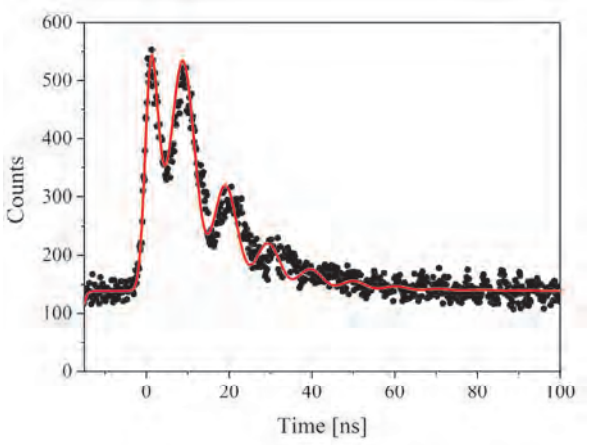


Fig. 1. Fluorescence decay curve (dots) of the 1s6p excited state in helium, measured with a magnetic field of 21.1 mT. It was obtained by an accumulation around 10 min. The red solid curve is the best fit to the observation (see text).

[1] Y. Hikosaka *et al*., submitted.

BL5B

Visible Fluorescence Studies on the Inner-shell Excitations in Kr and Xe

T. Kaneyasu[1,2], Y. Hikosaka[3], M. Fujimoto[2,4] and H. Iwayama[2,4]
[1]*SAGA Light Source, Tosu 841-0005, Japan*
[2]*Institute for Molecular Science, Okazaki 444-8585, Japan*
[3]*Institute of Liberal Arts and Sciences, University of Toyama, Toyama 930-0194, Japan*
[4]*The Graduate University for Advanced Studies, SOKENDAI, Okazaki 444-8585, Japan*

The inner-shell excitations of atoms and molecules have been studied in detail along with the development of synchrotron light sources and beamline techniques. Usually the excitation spectra are obtained by detecting the charged particles emitted in the energy relaxation process following the inner-shell excitation. In particular, the ion yield spectroscopy allows one to obtain excitation spectrum which is normally equivalent to the photoabsorption.

We report on visible fluorescence studies on the Kr 3d and Xe 4d excitations. The visible fluorescence photons are emitted in decays of the singly charged ionic states formed by spectator Auger decay of the inner-shell excited state. We show that the fluorescence yield is enhanced at a particular excited state, dependent on the wavelength of the visible fluorescence.

Figures 1 and 2 show the Kr 3d and Xe 4d excitation spectra obtained by the ion and fluorescence yield spectroscopies. The visible fluorescence photons were detected by a photomultiplier tube equipped with a bandpass filter. The assignments of the peaks are indicated in the top panels. It is obvious that the peak structures corresponding to the inner-shell excitations appear more clearly in the fluorescence spectra. This is a consequence of the selective detection of the Auger final states which cannot be populated via valence ionization or normal Auger decay following the inner-shell ionization.

When the wavelength of the fluorescence photon is selected by the bandpass filter, the spectral shapes drastically change. In the Kr 3d excitations, while the $3d^{-1}_{5/2}5p$ state is enhanced when the 460-nm-wavelength photons are detected, the intensity of the $3d^{-1}_{3/2}5p$ becomes large in the 450-nm-wavelength spectrum. This spectral feature agrees with the previous measurement [1], and is qualitatively explained by the spectator Auger decay from a specific initial state to a specific final state. Similar behavior is observed in the Xe 4d excitations as in Fig. 2. The measurement approach presented here can be used to investigate the cascade decay following the inner-shell excitation [2]. Additionally, such a detection scheme will allow us to selectively observe the inner-shell excitations even with the use of nonmonochromatized radiation.

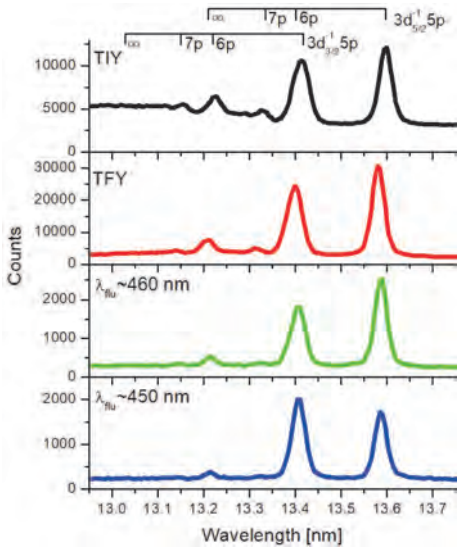


Fig. 1. Total ion yield (TIY), total visible fluorescence yield (TFY) and wavelength-selected fluorescence spectra in the Kr 3d excitation regime.

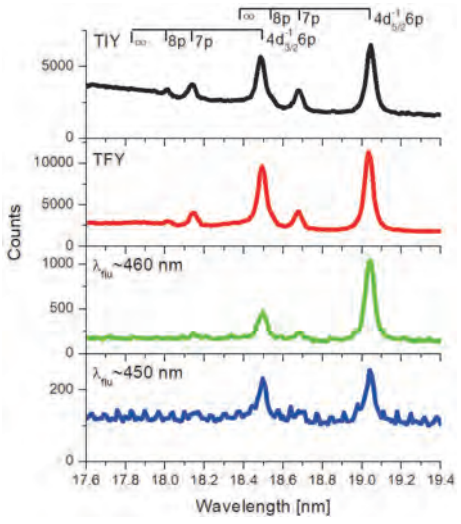


Fig. 2. Total ion yield (TIY), total visible fluorescence yield (TFY) and wavelength selected fluorescence spectra in the Xe 4d excitation regime.

[1] A. Sankari *et al*., Phys. Rev. A **77** (2008) 032720.
[2] R. Flesch *et al*., Phys. Rev. A **61** (2000) 062504.

BL6B

Cancelation of Orbital Degeneracy in $Me_4N[Pt(dmit)_2]_2$

T. Yamamoto[1,2,3], K. Takasugi[1], T. Naito[1,2], T. Teshima[4], K. Tanaka[4], M. Nomura[3] and R. Kato[3]

[1]*Graduate School of Science and Technology, Ehime University, Matsuyama 790-8577, Japan.*
[2]*Geodynamics Research Center, Advanced Research Unit for High-Pressure, and Research Unit for Superconductivity, Ehime University, Matsuyama 790-8577, Japan.*
[3]*RIKEN, Wako 351-0198, Japan.*
[4]*UVSOR Synchrotron Facility, Institute for Molecular Science, Okazaki 444-8585, Japan*

Orbital degrees of freedom and Jahn-Teller effect in the inorganic and organic complex compounds have been investigated by chemists and physicist. Orbital degeneracy in metal-dithiolene complexes has attracted a growing interest since the discoveries of the single-component metal and the photoconductivity. However, only a few efforts have been devoted to revealing the orbital degrees of freedom. We have focused on $X[Pt(dmit)_2]_2$ (dmit = 1,3-dithiole-2-thione-4,5-dithiolate and X = monovalent cation) as a candidate of orbital degeneracy. In the past study performed at BL6B and Instrumental center, we revealed that the disproportionation reaction of the X = Me_4Sb and Me_4P salts was ascribed to the cancelation of the orbital degeneracy [1]. However, the behavior of the C=C stretching modes of the X = Me_4Sb salt was not always identical to that of the X = Me_4P salt although the crystal structures were isostructural to each other. This result suggested that the inter–molecular interaction depends on the size of counter cation. We moved our focus on the X = Me_4N salt because the cation size is the smallest among three compounds and the transfer integral in a dimer is the smallest. In the present study at BL6B, we analyzed the behavior of the C=C stretching modes in the X = Me_4N salt.

Figure 1 shows the infrared spectra obtained by the transmission method. The B mode in the high–temperature phase was changed into the B1 and B2 modes in the low–temperature phase. The C mode was changed into the C1 and C2 modes. The assignments of these vibrational modes are identical to those of the X = Me_4Sb and Me_4P salts [1]. The B and C modes belong to $[Pt(dmit)_2]_2^{-1}$. The B1 and C1 modes belong to the charge–rich dimer ($[Pt(dmit)_2]_2^{-1-\Delta}$), and the B2 and C2 modes belong to the charge–poor dimer ($[Pt(dmit)_2]_2^{-1+\Delta}$). This temperature dependence is the evidence for the disproportionation reaction. Similar to the previous results on the X = Me_4Sb and Me_4P salts, the orbital degeneracy at the high–temperature phase of the X = Me_4N salt was canceled in the low–temperature phase.

The intensities of the A1 and A2 modes were inversely proportional to the temperature, which indicates that the A1 mode is assgined to one of the C=C stretching modes of a charge–rich dimer. On the other hand, the A1 mode of the X = Me_4Sb salt was negligible in the transmission spectra [1]. The intensity of the X = Me_4P salt was smaller and larger than those of the X = Me_4N and Me_4Sb salts, respectively [1]. Therefore, the A1 mode belong to the symmetric vibration. Owing to the asymmetric deformation in the charge–rich dimer, the mutual exclusion rule cannot be exactly applicable to both IR and Raman spectra. The difference in the intensities of the A1 modes among three compounds suggests that the degree of deformation of the X = Me_4N salt is larger than those of the X = Me_4N and Me_4Sb salts. This result indicates that the molecular deformation suppresses the instability of the highest occupied orbital arising from the decrease in the transfer integral in the charge–rich dimer.

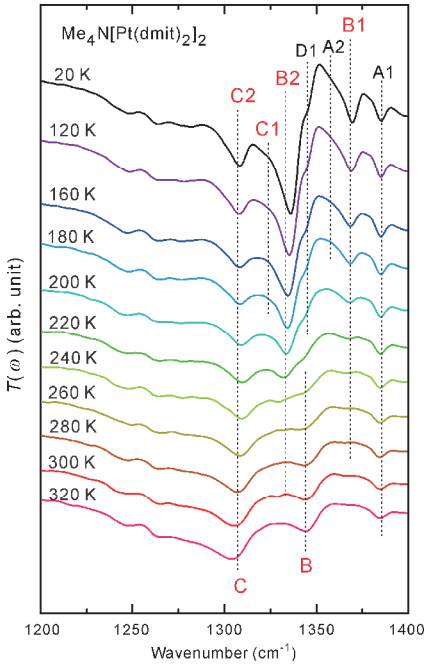


Fig. 1. Transmission spectra of $Me_4N[Pd(dmit)_2]_2$.

[1] T. Yamamoto *et al.*, UVSOR Acrtivity Report 2018 **46** (2019) 126.

Ⅲ-4

Surface, Interface and Thin Films



Highlight

BL6U

The Photoelectron Momentum Microscope

F. Matsui[1], S. Makita[1], H. Matsuda[1], T. Yano[1], E. Nakamura[1], K. Tanaka[1,2], T. Ohigashi[1,2], H. Horigome[1], S. Ideta[1,2], Y. Hasegawa[2], S. Suga[3] and S. Kera[1,2]

[1]*UVSOR Synchrotron Facility, Institute for Molecular Science, Okazaki 444-8585, Japan*
[2]*The Graduate University for Advanced Studies, SOKENDAI, Okazaki 444-8585, Japan*
[3]*The Institute of Scientific and Industrial Research, Osaka University, Ibaraki 567-0047, Japan*

The importance of characterizing microstructure electronic properties cannot be overemphasized. The demand for photoelectron micro-spectroscopy and spectro-microscopy is growing rapidly. Photoelectron spectroscopy resolved in three-dimensional momentum space with a microscopic field of view is realized by combining a so-called Momentum Microscope with a soft X-ray synchrotron radiation source. This method opens the door to direct observation of the Fermi surface of μm-sized crystals, which was difficult with conventional ARPES-type hemispherical analyzers. A new experimental station for Momentum Microscopy has been built at BL6U, an undulator-based soft X-ray beamline. In fact, this successful combination of a single HDA-type Momentum Microscope at the synchrotron facility is the first case in the world. As shown in Fig.1, the system consists of a photoemission electron microscope (PEEM) lens, a hemispherical deflection analyzer (HDA) for imaging-type energy filter, and a 2D detector with a CMOS camera. This experimental station specializes in characterizing the electronic structure of surface atomic sites, thin films, molecular adsorbates, and bulk crystals.

The details of the specification evaluation result are described elsewhere [1]. In brief, the energy resolution of the analyzer was estimated to be 22.74 meV at pass energy of 20 eV. The spatial resolution in the microscopy mode was evaluated to be about 50 nm. The momentum resolution of 0.012 $Å^{-1}$ has been achieved. The position of sample stage facing to the analyzer is precisely controlled by a hexapod. Samples can be cooled down to 10 K and heated up to 400 K.

Figure 2 shows the optical and PEEM images of a piece of micro channel plate (MCP) fragment. The pore size was 10 μm and the interval of each pore was 11.6 μm. The top surface of the MCP is clearly imaged, despite the nearby deep holes and useful for the lateral length calibration. It is interesting to note that excited photoelectrons are detected from one side of the hole wall. Figure 3 shows the preliminary results of valence band photoelectron 2D angular patterns excited by He lamp and synchrotron radiation. The six bright spots correspond to the π band at the vicinity of Dirac cone. The center double ring structure originates from the substrate Ru 4*d* band.

We greatly acknowledge Dr. Markus Breusing, Dr. Marko Wietstruk, and Dr. Mirko Weidner (SPECS) and Dr. Dai Yamaguchi (Tokyo Instruments Inc.) for their contribution in the construction of the BL6U Momentum Microscope experimental station.

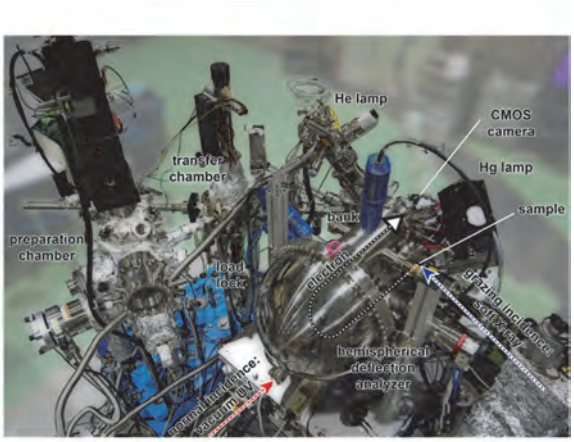


Fig. 1. Photograph of the Momentum Microscopy station at BL6U.

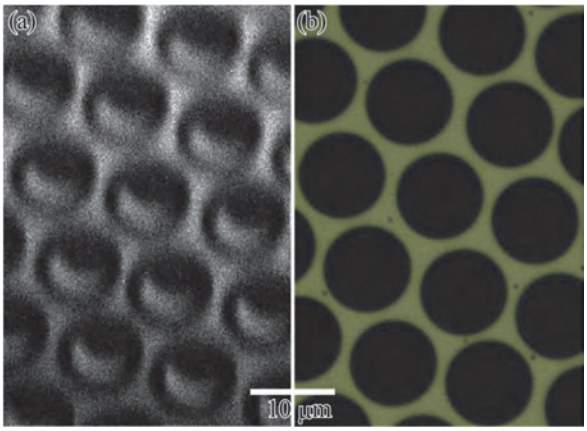


Fig. 2. (a) Optical photograph and (b) PEEM image of a honeycomb pattern.

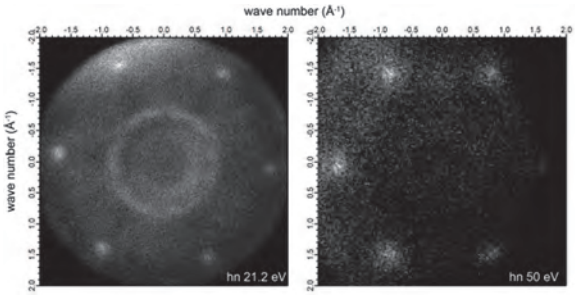


Fig. 3. Photoelectron angular distribution of valence band from graphene grown on the Ru(111) surface excited by (a) He lamp and (b) synchrotron radiation.

[1] F. Matsui *et al*., Jpn. J. Appl. Phys. **59** (2020) 067001.

BL2A

NEXAFS Spectroscopy of Magnesium Oxide Powder

E. Kobayashi[1], K. K. Okudaira[2], T. Kikuchi[2], M. Imamura[3], K. K. Bando[3], S. Yoshioka[4] and O. Takahashi[5]

[1]*Kyushu Synchrotron Light Research Center, Tosu 841-0005, Japan*
[2]*Chiba University, Chiba 263-8522, Japan*
[3]*National Institute of Advanced Industrial Science and Technology, Tsukuba 305-8565, Japan*
[4]*Graduate School of Engineering, Kyushu University, Fukuoka 819-0395 Japan*
[5]*Graduate School of Science, Hiroshima University, Higashi-Hiroshima, 739-8526, Japan*

Magnesium oxide (MgO) has been widely used as catalytic, optical and electrical applications [1]. In recent years, the performance of not only organic photovoltaics but also perovskite solar cells has been successfully improved by employing MgO nanolayers as electrodes [2,3].

In order to further improve the characteristics of such solar cells, it is necessary to understand the surface and bulk electronic states. Near-edge X-ray absorption fine structure (NEXAFS) spectroscopy is a powerful tool for investigating the electronic structures of materials. The NEXAFS spectra can be obtained by electron yield (EY) mode or fluorescence yield (FY) mode. The former is sensitive to the surface and the latter is sensitive to the bulk.

In this study, we measured Mg *K*-edge NEXAFS spectra of MgO using both total electron yield (TEY) and partial fluorescence yield (PFY) modes in order to investigate the change in surface and bulk states with particle size.

Two MgO powders with different particle size were prepared. One is the size of 50 nm or less (MgO_A). The other is 50 nm average (MgO_B). NEXAFS spectra of the MgO powders were measured at the beamline 2A of the UVSOR in the Institute of Molecular Science. For TEY, the drain current from the sample was measured. For PFY fluorescence X-rays were collected using an energy dispersible silicon drift detector (SDD). All experiments were performed at room temperature.

Figure 1 shows the Mg *K*-edge NEXAFS spectra of MgO powder obtained from TEY and PFY. In the spectrum measured in the TFY mode, the spectra of MgO_A and MgO_B showed almost the same shape. Their spectra were different from the $Mg(OH)_2$ spectra measured as a reference. On the other hand, in the spectrum measured in the TEY mode, the spectra of MgO_A and MgO_B were different. The spectrum of MgO_A was almost similar to the spectrum of $Mg(OH)_2$ measured as a reference. These results indicate that the bulk of MgO_A is MgO, but the surface is $Mg(OH)_2$. Since MgO_A has a smaller particle size than MgO_B, the surface has high activity. Therefore, $Mg(OH)_2$ formed on the surface of MgO_A with water in the atmosphere.

As a next step we will clarify the electronic structure of the interface between organic semiconductors and MgO nanolayers.

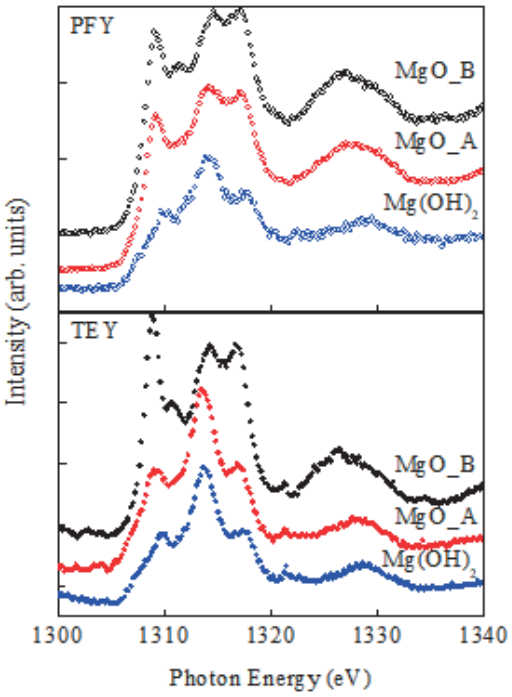


Fig. 1. Mg *K*-edge NEXAFS spectra of MgO powder.

[1] E. A. Colbourn, Surf. Sci. Rep.**15** (1992) 281.
[2]H. J. Bolink, H. Brine, E. Coronado and M. Sessolo, J. Mater. Chem. **20** (2010) 4047.
[3] J. Ma, G. Yang, M. Qin, X. Zheng, H. Lei, C. Chen, Z. Chen, Y. Guo, H. Han, X. Zhao and G. Fang, Adv. Sci. **4** (2017) 1700031.

BL2B

Electronic Structure of ZnO Nanoparticles Deposited on ITO

K. K. Okudaira and T. Kikuchi

Association of Graduate Schools of Science and Technology, Chiba University, Chiba 263-8522, Japan

Organic photovoltaic cells (OPV) have been attracting interest concerning both fundamental research and practical application for low-cost, large-area, lightweight and flexible devices. In recent years, various solution-processed bulk-heterojunction photovoltaic devices have been reported using p-type conjugated polymers, either in combination with n-type inorganic semiconductor nanoparticles. These hybrid polymers: inorganic - nanoparticle bulk heterojunctions can take advantage of the beneficial properties of both types of materials: solution processing of polymer semiconductors and high electron mobility of inorganic semiconductors.

The characteristics of OPV such as efficiency and filling factor are considered to be dependence on the electronic structure of not only organic semiconductor but also n-type inorganic semiconductor nanoparticles.

In this work we deposited ZnO nanoparticles (NPs) thin films on ITO and clarify the electronic structure of ZnO NPs using hν-dependence of ultraviolet photoelectron spectroscopy (UPS) measurements.

We synthesized ZnO NPs with different particle size. The size of nanoparticles synthesized by ref [1] is about 5 nm. On the other hand, the size of ZnO nanoparticle synthesized by ref [2] is about 80 nm, which is ten times larger than that synthesized by the first methods. Here after we refer the ZnO nanoparticles by the first method and the second method to ZnOs and ZnO200, respectively. UPS measurements were performed at the beam line BL2B of the UVSOR storage ring at the Institute for Molecular Science. UPS were measured with the photon energy (hν) of 28 eV and 40 eV. The ZnO NP thin films were prepared by spin-cast on ITO. The ZnO NP thin films were annealed at 120 °C.

We observed hν)dependence of UPS of ZnO NPs with different particle size (ZnOs and ZnO200) on ITO (Fig. 1). In the UPS three broad peaks appear about Eb (binding energy) of about 5 eV, 7.5 eV, and 10 eV. These peaks around 5 eV and 7.5 eV are assigned to the states which are hybridized Zn 4s and O 2p orbitals. By considering the photoionization cross section of O 2p and Zn 4s of hν of 28 eV and 40 eV, the peak at lower binding energy and that at higher binding energy is made of mainly by O 2p and Zn-4s, respectively. The peak at Eb of about 10 eV is the emission of the Zn 3d band. These assignments are good agreement with ref [3]. In Fig. 2 the annealing processes do not affect the UPS of ZnOs as well as ZnO200. On the other hand, the relative peak intensity of the peak about 10 eV to that about 5 eV of ZnOs is larger than that of ZnO200. It is considered that the two synthetic methods provide the different surface structures such as the introduction of hydroxyl group.

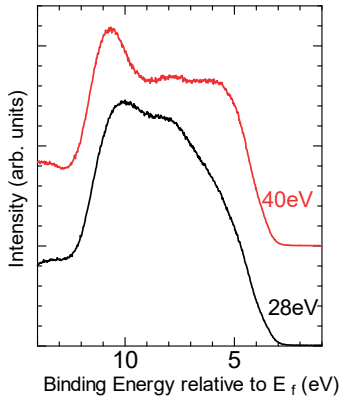


Fig. 1 UPS of ZnO NPs (ZnOs) at hν of 28 eV and 40 eV.

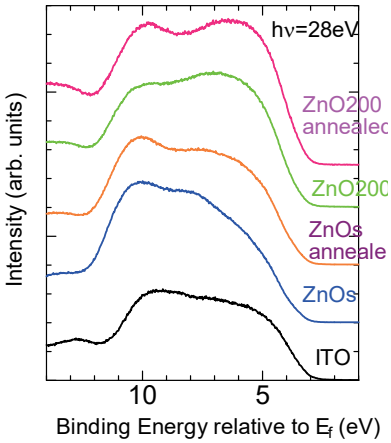


Fig. 2 UPS of ZnO nanoparticles (ZnOs and ZnO200) at hν of 28 eV.

[1] N. M. Shamhari, B. S. Wee, S.F. Chin and K. Y. Kok, Acta Chim. Slov. **65** (2018) 578.
[2] H. Du, F. Yuan, S. Huang, J. Li and Y. Zhu, Chem. Lett. **33** (2004) 770.
[3] W. Ranke, Solid State Commun. **19** (1976) 685.

BL3U

Cobalt Oxide Catalyst in Carbonate Aqueous Solution Studied by Operando C K-edge XAFS Measurement

T. Moriyama[1], M. Nagasaka[2], H. Yuzawa[2] and M. Yoshida[1,3]
[1]*Faculty of Engineering, Yamaguchi University, Ube 755-8611, Japan*
[2]*Institute for Molecular Science, Okazaki 444-8585, Japan*
[3]*Blue energy center for SGE technology (BEST), Yamaguchi University, Ube 755-8611, Japan*

Electrochemical water splitting with renewable energies is attracting attention as a sustainable hydrogen production technique. In the electrolysis of water, overvoltage of the oxygen evolution reaction (OER) is a problem, and the development of a highly active OER electrocatalyst is strongly required. In this situation, a nickel carbonate (Ni-C_i) was reported recently as an OER catalyst with high activity [1]. Meanwhile, we revealed the function of similar cobalt OER catalysts by operando X-ray absorption fine structure (XAFS) observation [2]. Therefore, we attempted to clarify the structure and reaction mechanism of the Ni-C_i catalyst by performing operando soft X-ray XAFS measurements.

A electrochemical cell was equipped with a Pt counter electrode and an Ag/AgCl reference electrode for all electrochemical experiments. The Ni-C_i thin films were electrodeposited on Au thin film in potassium carbonate aqueous solution containing $Ni(NO_3)_2$ at 1.7 V vs. RHE. The operando O *K*-edge and C *K*-edge XAFS spectra for Ni-C_i were taken under electrochemical control with transmission mode at BL3U in the UVSOR Synchrotron, according to the previous works [3].

First, we checked the electrochemical OER activity for Ni-C_i catalyst and confirmed that the catalyst can decompose water efficiently. The surface states and chemical composition were also measured by SEM, EDX, stylus profilometer.

Next, operando O-*K* edge XAFS spectra were measured for Ni-C_i catalyst under electrochemical condition. In this spectra, a peak coincided with that of γ-NiOOH of the reference sample was observed at around 528.6 eV, indicating that the Ni-C_i catalyst changed its structure to γ-NiOOH during the OER process.

Finally, operando C-*K* edge XAFS measurements were performed, as shown in Figure 1. At the non-active potential of 1.2 V, a peak was observed at around 290.3 eV near the peak position of carbonate ion, suggesting that the carbonate ion was adsorbed on the Ni-C_i catalyst. Furthermore, when the electrode potential changed from 1.2 V to 1.7 V, the carbonate peak shifted to a higher energy side. This phenomenon is presumed to be due to the direct adsorption of carbonate ion on the γ-NiOOH as active species. Thus, we suggest that the adsorption of carbonate ion is likely to contribute the stabilization of γ-NiOOH and that the Ni-C_i catalyst has high OER activity by the existence of γ-NiOOH with highly active reaction sites.

In conclusion, we revealed the function of Ni-C_i electrocatalyst by operando O *K*-edge and C *K*-edge XAFS measurements. It was exhibited that the carbonate species was adsorbed on the γ-NiOOH structure to stabilize the active reaction sites, and the interface of γ-NiOOH and adsorbed carbonate ion is likely to function as efficient OER site.

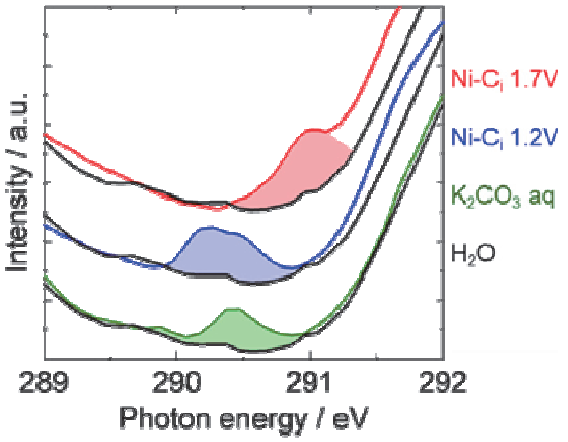


Fig. 1. Operando C *K*-edge XAFS spectra for Ni-C_i at 1.2 V (non-active state) and 1.7 V (active state) vs. RHE, together with the saturated K_2CO_3 aqueous solution.

[1] (a) M. Ma, Y. Liu, X. Ma, R. Ge, F. Qu, Z. Liu, G. Du, A. M. Asiri, Y. Yao and X. Sun, Sustainable Energy Fuels **1** (2017) 1287.
(b) K. S. Joya, Y. F. Joya and H. J. M. de Groot, Advanced Energy Materials **4** (2014) 1301929.
[2] K. Yamada, T. Hiue, T. Ina, K. Wang, H. Kondoh, Y. Sakata, Y. L. Lee, T. Kawai and M. Yoshida, Anal. Sci. **36** (2020) 35.
[3] (a) M. Nagasaka, H. Yuzawa, T. Horigome and N. Kosugi, Rev. Sci. Instrum. **85** (2014) 104105.
(b) M. Yoshida, Y. Mitsutomi, T. Mineo, M. Nagasaka, H. Yuzawa, N. Kosugi and H. Kondoh, J. Phys. Chem. C **119** (2015) 19279.

BL3U

In Situ XAFS Study of Pt Subnanoparticles on the Oxygen Reduction Reaction

A. Kuzume[1], M. Nagasaka[2] and K. Yamamoto[1]

[1]*JST-ERATO, Yamamoto Atom Hybrid Project, Institute of Innovative Research, Tokyo Institute of Technology, Yokohama 226-8503 Japan*

[2]*Institute for Molecular Science, Okazaki 444-8585, Japan*

Subnanoparticles (SNPs) is a new-generation material with a particle diameter of about 1 nm, composing only several tens of atoms. Due to its small number of constituent atoms (atomicity), it exhibits unique properties not commonly found in bulk and nanomaterials. However, it was difficult to understand the detailed characteristics and chemical activity of SNPs because of its difficulty in synthesis and analysis.

In our laboratory, we have established a liquid-phase SNPs synthetic method using a dendritic polymer called 4th generation Tetraphenylmethane-core, phenylazomethine dendrimer (TPM-DPA-G4) as a template macromolecule, which can control the atomicity precisely [1-3]. With this technique, scalable synthesis of SNPs is possible, and thus detailed analyses of physical, chemical and electric properties, as well as chemical activities, of SNPs is expected [4].

Pt SNPs have been synthesized using the method described above and were found to exhibit unique catalytic activities on electrochemical oxygen reduction reaction (ORR), which is the key cathodic reaction for the fuel cell development. Pt SNPs were found to exhibit discrete catalytic activity on ORR, depending on the atomicity [5-7]. To evaluate its specificity, it is necessary to monitor changes in the electron state of SNPs during the electrochemical reaction. In this study, in situ XAFS measurements of Pt SNPs on O K-edge were performed at BL3U in UVSOR facility to elucidate precise atomicity-dependent ORR activity by monitoring the state of Pt oxide on the surface of SNPs under electrochemical condition.

The home-made in situ XAFS cell with the electrochemical setup was used [8], where Pt SNPs were cast on a carbon-film modified on the silicon nitride substrate (10 mm x 10 mm). A Pt wire and Ag/AgCl electrode were used as a counter and reference electrode. Air-saturated 0.1M $HClO_4$ solution (prepared with MERCK Suprapur $HClO_4$ and ultrapure water from the Milli-Q system) were constantly supplied during the in situ measurement by the peristaltic pump.

Figure 1 shows the potential dependent in situ XAFS spectra of O K-edge on Pt_{12} SNPs. It was not easy to identify the potential dependence in the series of spectra due to significantly low signal intensity of O species adsorbed on Pt surface. Difficulty in the characterization of SNPs is mainly originated from their size. In general, the signal intensity of SNPs in the vibration spectroscopic study, such as infrared and Raman spectroscopy, is far below the detection limit with the conventional technique and requires improvement in sensitivity to detect SNPs [9]. To increase the signal intensity of XAFS spectra, one needs to increase the amount/surface coverage of Pt SNPs in our electrochemical XAFS setup. However, due to the principle of the measurement, one needs to keep the thickness of the sample as low as possible to increase the transmission rate. This trade-off situation makes it difficult to detect O species on Pt SNPs.

In conclusion, our preliminary results indicated that the transmission detection configuration needs to be changed to the fluorescence mode, where one can simply increase the amount of Pt SNPs to improve the detection sensitivity.

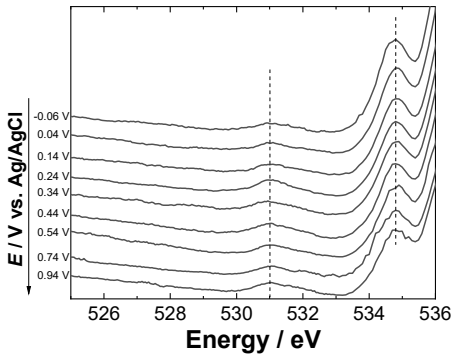


Fig. 1. Potential dependent in situ O K-edge XAFS spectra of Pt_{12} SNPs in 0.1M $HClO_4$ versus Ag/AgCl.

[1] A. Kimoto, K. Masachika, J.S. Cho, M. Higuchi and K. Yamaomto, Org. Lett. **6** (2004) 1179.
[2] O. Enoki, H. Katoh and K. Yamamoto, Org. Lett. **8** (2006) 569.
[3] K. Yamamoto, M. Higuchi, S. Shiki, M. Tsuruta and H. Chiba, Nature **415** (2002) 509.
[4] K. Yamamoto and T. Imaoka, Acc. Chem. Res. **47** (2014) 1127.
[5] K. Yamamoto, T. Imaoka, W.J. Chun, O. Enoki, H. Katoh, M. Takenaga and A. Sonoi, Nat. Chem. **1** (2009) 397.
[6] T. Imaoka, H. Kitazawa, W.J. Chun and K. Yamamoto, Angew. Chem. Int. Ed. **54** (2015) 9810.
[7] T. Imaoka, Y. Akanuma, N. Haruta, S. Tsuchiya, K. Ishihara, T. Okayasu, W.J. Chun, M. Takahashi and K .Yamamoto, Nat. Commun. **8** (2017) 688.
[8] M. Yoshida, Y. Mitsutomi, T. Mineo, M. Nagasaka, H. Yuzawa, N. Kosugi and H. Kondoh, J. Phys. Chem. C **119** (2015) 19279.
[9] A. Kuzume, M. Ozawa, Y. Tang, Y. Yamada, N. Haruta and K. Yamamoto, Sci. Adv. **5** (2019) eaax6455.

BL3B

Clarify of Formation Process and Optical Properties Evaluation of Ultra-Violet Emitting Zinc Aluminate Phosphor Thin Films

H. Kominami[1], M. Arimura[1], K. Imagawa[1], K.Warita[2], S. Nishibori[2], M. Endo[2], T. Kawashima[2], N. Sonoda[2], S. Kodama[3] and S. Kurosawa[3,4]

[1]*Graduate School of Integrated Science and Technology, Shizuoka University, Hamamatsu 432-8651, Japan*
[2]*Faculty of Engineering, Shizuoka University, Hamamatsu 432-8651, Japan*
[3]*New Industry Creation Hatchery Center (NICHe), Tohoku University, Sendai 980-8579, Japan*
[4]*Faculty of science, Yamagata University, Yamagata 990-8560, Japan*

The UV light is used for various applications depending on the wavelength as well as the sterilization described above. The lights of 200-280 nm (UV-C) region as for the sterilization, 280-320 nm (UV-B) region as the treatment of the skin disease, 320-400 nm (UV-A) region as application of purification of water and air, and photocatalysts. Recently, from the viewpoint of consideration to the environment, the mercury free UV emission devices have been demanded for the application of catalyst and medical situations. In our previous work, it was clarified that $ZnAl_2O_4$ phosphor was suitable for the UV field emission lamp because of its stability and luminescent property. It shows strong UV emission peaked around 250 nm which suitable for sterilization.

Conventionally, powder samples have been prepared and evaluated, but it was difficult to analyze transmittance and refractive index due to the influences of surface scattering, so it would be possible to evaluate these basic physical properties by preparing thin film samples. In this research, ZnO films were deposited on sapphire substrates by sputtering and $ZnAl_2O_4$ thin films were prepared by thermal diffusion. These films were evaluated the orientation and crystallinity. Quality of thin films were evaluated by relationships between UV emission intensity and penetration depth of electron beam, and also the distribution of Zn and Al was studied using cross sectional FE-EPMA to analyze the emitting layer.

Figure 1 shows the XRD patterns of thin films prepared on a-plane sapphire substrate. Before annealing, any diffraction peaks of ZnAl2O4 were not observed, however ZnO (002) peak was confirmed near 34°. After annealing, diffraction peak of $ZnAl_2O_4$ (333) appeared, and selective growth was confirmed. FWHM of diffraction peaks of $ZnAl_2O_4$ (333) decrease according to inarticulate interface of each layer, the multilayer film containing constituent elements was formed by sputtering on quartz substrate, and tried to prepare the $ZnAl_2O_4$ thin film by thermal diffusion.

Figure 2 shows PL spectra of $ZnAl_2O_4$ thin film annealed for 15 hours excited by VUV. From the spectra, ZnO emission around 380 nm and 520 nm (caused from exiton and oxygen vacancy, respectively) were not observed. It indicates that ZnO layer were diffused to substrate completely and re-evaporated. It is thought that the 50 hours or more thermal annealing is necessary for obtain the good quality $ZnAl_2O_4$ thin film preparation.

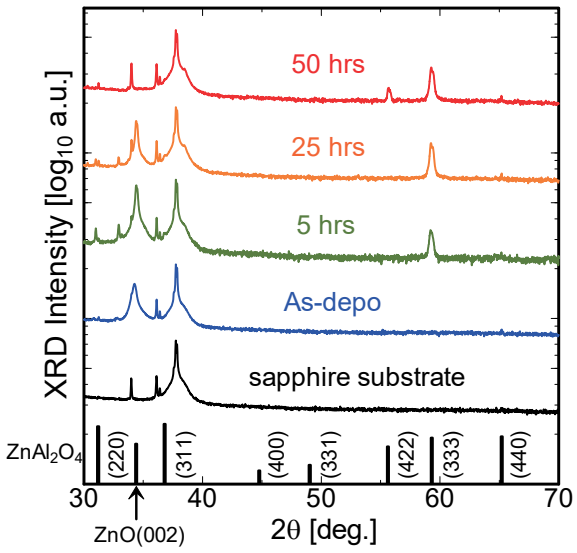


Fig. 1 XRD patterns of films on a-plane sapphire substrate before and after annealing for several hours.

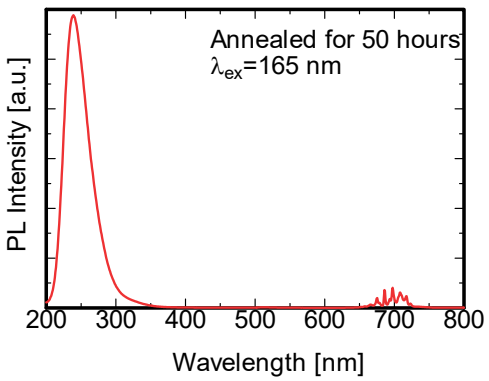


Fig. 2 PL spectra of $ZnAl_2O_4$ thin film.

BL4U

Microscopic Electronic Structure of Vanadium Nitride/Oxide Supercapacitors

H. W. Shiu[1], L. C. Yu[1], Y. L. Lai[1], T. Ohigashi[2], Y.-G. Lin[1] and Y. J. Hsu[1]
[1]*National Synchrotron Radiation Research Center, Hsinchu 300, Taiwan*
[2]*Institute for Molecular Science, Okazaki 444-8585, Japan*

How to provide an environmentally friendly energy system with high performance and low cost has become an important issue due to the rapid growth of electric vehicles and portable electronic devices. Supercapacitors (SCs), also called electrochemical capacitors, have attracted a lot of attentions due to their specific advantages of fast power release and long cycle-life [1]. However, the existing commercialized carbon electrode has the bad traits of low specific capacitance. Accordantly, the main research targets of SCs mainly focused on the development of pseudo-capacitive electrode materials. Transition metal oxide, nitride, sulfide and conducting polymers have been experimentally demonstrated as a promising electrode material for the next generation SCs [2].

Recently, the earth-abundant and inexpensive materials i.e. vanadium oxides (VOx), have been intensely investigated as cathode materials for SCs. The multiple stable oxidation states and layered structure enable it to have a higher storage capability. A similar material named Vanadium nitride (VN) holds great promise as an advanced electrode for asymmetric super capacitors due to its large specific capacitance (1340 F/g) and superb electrical conductivity (106/Ωm). In our previous studies we also observed that the capacitance retention is enhanced as high as 90% at high current density. Only 5.9% decay was observed at 1000 cycles.

In order to understand the mechanism of the enhancement of the specific capacitance and the capacitance retention, we synthesized a set of VON and VN through the electrochemical deposition in an electrolyte solution containing Na_2SO_4 and NH_4VO_3 for 6 hours and post-treatment at 500 to 700 degree Celsius under NH_3 condition. A systematically study for the set of materials was made by scanning transmission X-ray microscopy (STXM) and Near-edge X-ray absorption fine structure (NEXAFS) at UVSOR BL4U and TLS 09A2, respectively.

Figure 1 shows the XAS spectra of VON and VN powders transferred onto Si substrate measured at TLS BL 09A2 with the photon beamsize of 100 μm. The "average" spectrum of VN has no oxygen feature and the characteristic peaks of V L-edge shifted to lower photon energy which clearly indicated that the valence state is altered to the lower oxidation state.

To investigate the chemical distribution of the VON powders, multiple sets of STXM images at different photon energy have been measured. The results display the STXM element mapping as shown in Fig. 2 (a). All of the VON samples exhibit nano-rod structure with the dimension of ~ 150 nm in diameter and ~ 1 μm in length.

Figure 2 (b) shows the XAS spectra near the V L-edge and O K-edge extracted from Fig. 2 (a). The two major peaks at ~ 518 and 525 eV are the V L_{III} and L_{II} peaks, respectively. Different from the broadened peak of V L_{II}-edge, the three considerable peaks were observed at V L_{III}-edge correspond to the transition from V $2p_{3/2}$ to t_{2g} (π^*), t_{2g} (d*) and e_g (σ^*), respectively. The two clear features between 527 to 534 eV are the transition from O 1s to the hybridized O 2p/V 3d, i.e. t_{2g} and e_g orbitals. Significant intensity changes between those two peaks (O K-edge, $t2_g$ and e_g) may result from the ununiform valence state of N-V-O bound and polarization effect [3]. Further experiments are needed to confirm this observation.

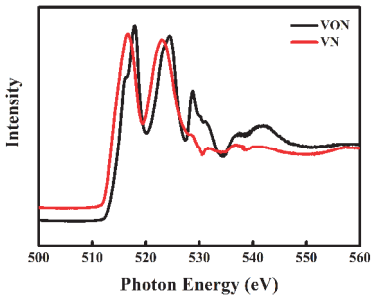


Fig. 1. V L-edges and O K-edge XAS spect ra of VON and VN measured at Taiwan Light Source (TLS).

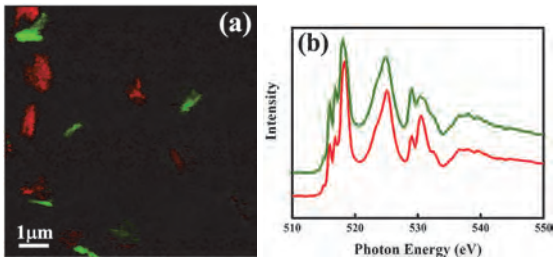


Fig. 2 (a) Color-coded composite mapping of VON powder identified by the O K-edge spectra (e_g/t_{2g}) and (b) the corresponding micro-spectra of red and green areas.

[1] Y. Yang, G. Ruan, C. Xiang, G. Wang and J. M. Tour, J. Am. Chem. Soc. **136** (2014) 6187.
[2] H. Pang, C. Wei, X. Li, G. Li, Y. Ma, S. Li, J. Chen and J. Zhang, Sci. Rep. **4** (2014) 3577.
[3] D. Maganas, M. Roemelt, M. Hävecker, A. Trunschke, A. Knop-Gericke, R. Schlögl and F. Neese, Phys. Chem. Chem. Phys. **15** (2013) 7260.

BL4B

Absorption Spectra of Amorphous Chalcogenide Thin Films in the Vacuum Ultraviolet Region

K. Hayashi
Department of Electrical, Electronic and Computer Engineering, Gifu University, Gifu 501-1193, Japan

Amorphous chalcogenide semiconductor materials are very photosensitive materials and show a variety of photo-induced phenomena. Therefore, these materials are expected as materials for optoelectronic devices. A lot of work have been done on the photo-induced phenomena of these amorphous semiconductor materials and various mechanisms have been proposed for these photo-induced phenomena [1-3]. However, the details of the mechanisms are still unknown. For device applications, it is necessary to sufficiently understand the fundamental properties of these materials. These phenomena have been studied by exciting outer core electrons by irradiating light with the energy corresponding to the optical bandgap or sub-bandgap. The interest has been attracted for the change of the optical properties in the energy region of the visible light. We are interesting for the changes of the optical properties in the higher energy region. To our knowledge, little attention has been given to photo-induced changes at the vacuum ultra-violet (VUV) absorption spectrum. In this report, we report the VUV absorption spectra of as-deposited evaporated amorphous Se and As_2Se_3 thin films.

Samples used for the VUV absorption spectrum were amorphous Se and As_2Se_3 thin films prepared onto aluminum thin films by conventional evaporation technique. Typical thickness of the amorphous film and the aluminum film were around 200 nm and 100 nm, respectively. The aluminum film of the thickness of 200 nm was also used in order to eliminate the higher order light from the monochromator in the VUV region. The measurements were carried out at room temperature at the BL4B beam line of the UVSOR facility of the Institute for Molecular Science. And the spectrum was measured by using the silicon photodiode as a detector. A pinhole of 1.5 mm in a diameter was inserted between the monochromator and sample to remove stray light. The intensity of the VUV light was monitored by measuring the total photoelectron yield of a gold mesh. The positions of the core levels for the samples were calibrated by referencing to the 2p core level absorption peak of the aluminum film.

Figure 1 shows the VUV absorption spectra of as-deposited amorphous Se and As_2Se_3 thin films at room temperature. The structure observed in this energy region from 40 to 55 eV is due to the transitions from the As 3d core level. On the other hand, the structure observed in this energy region from 55 to 70 eV is due to the transitions from the Se 3d core level. As shown in the figure, each spectrum is very broad and multiple shoulders are observed. The structure in the spectrum of amorphous As_2Se_3 is good agreement with previous report [4]. On the other hand, the spectrum shape of the main peak of amorphous Se is slightly different from the previous report. It can be attributed to the spin-orbit splitting of the 3d core level of each atom as observed by XPS. It is not clear about the origin of broad spectra and shoulders. I think that these origins are related to the local structures of the amorphous network. The detailed experiments and analysis will be done in the next step.

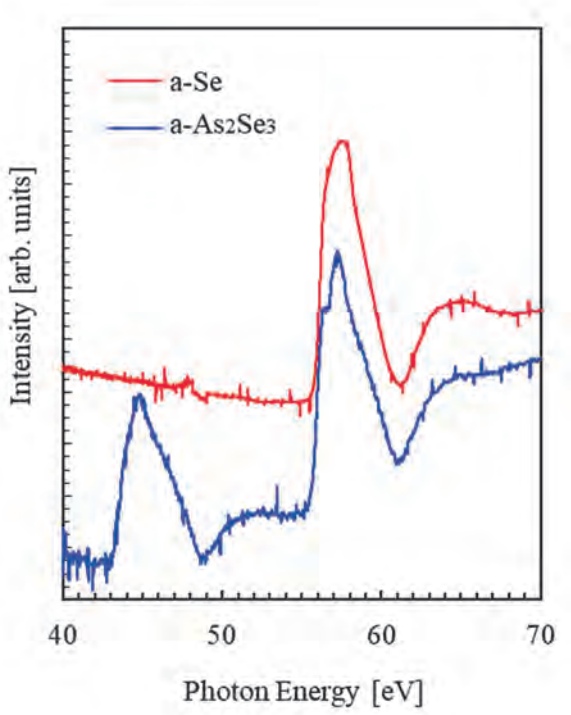


Fig. 1. VUV absorption spectra of as-deposited amorphous Se and As_2Se_3 thin films at room temperature.

[1] K. Tanaka, Rev. Solid State Sci. **4** (1990) 641.
[2] K. Shimakawa, A. Kolobov and S. R. Elliott, Adv. Phys. **44** (1995) 475.
[3] K. Tanaka, Encyclopedia of Nanoscience and Nanotechnology **7** (2004) 629.
[4] J. Bordas, Phil. Mag. **34** (1976) 501.

BL4B

Tuning Surfaces and Interfaces of FeNi Alloy Thin Films by Nitrogen Surfactant Effects

T. Miyamachi[1], K. Kawaguchi[1], Y. Takahashi[1,2], T. Iimori[1], T. Hattori[1], T. Koitaya[3,4], K. Yamamoto[3,4], M. Kotsugi[2], T. Yokoyama[3,4] and F. Komori[1]

[1]*Institute for Solid State Physics (ISSP), The University of Tokyo, Kashiwa 277-8581, Japan*
[2]*Faculty of Industrial Science and Technology, Tokyo University of Science, Tokyo 125-8588, Japan*
[3]*Department of Materials Molecular Science, Institute for Molecular Science, Okazaki 444-8585, Japan*
[4]*Department of Structural Molecular Science, The Graduate University for Advanced Studies, SOKENDAI, Okazaki 444-8585, Japan*

A rare-metal-free ferromagnetic $L1_0$-type FeNi ordered alloy attracts much attention due to its expected strong uniaxial magnetic anisotropy. Previous studies reported the preparation of $L1_0$ FeNi films by several thin film growth techniques such as layer-by layer molecular beam epitaxy (MBE) and pulse laser deposition (PLD). However, the perpendicular magnetic anisotropy of $L1_0$ FeNi has not been achieved so far possibly due to an imperfect layer-by-layer stacking and intermixing at the Fe/Ni interface during growth processes, which results in the low structural ordering.

To realize high-quality FeNi alloy thin films, we incorporate nitrogen surfactant effects of monatomic layer magnetic nitrides into the alternate Fe and Ni deposition. The nitrogen surfactant epitaxy intends to suppress the interdiffusion at the Fe/Ni interface during the deposition and annealing processes and keeps atomically flat surface/interface. The validity of this approach on structural and magnetic properties of FeNi alloy thin films were confirmed for 1 monolayer (ML) Fe on Ni_2N/Cu (001), which is the initial fabrication step, by scanning tunneling microscopy (STM) and x-ray absorption spectroscopy/x-ray magnetic circular dichroism (XAS/XMCD). We observed structural changes of the system from Fe/Ni_2N/Cu(001) to FeN/Ni/Cu(001) induced by the nitrogen surfactant effect while keeping the high quality Fe/Ni interface even after annealing process at 420 K, and resultingly the enhancement of the perpendicular anisotropy [1,2].

In this work, we grow thicker FeNi alloy thin films up to tri- and quadruple-layers (NiN/Fe/Ni and FeN/Ni/Fe/Ni) and investigate the impact of surface/interface modifications with increasing the film thickness on their electronic and magnetic properties by STM and XAS/XMCD [3].

The Ni_2N was grown on Cu(001) by following fabrication processes of a monatomic layer iron nitride (Fe_2N) [4]. The quality of the Ni_2N was prechecked by STM and LEED before XAS/XMCD measurements. Then, 1 ML Fe and Ni were alternatingly deposited at ~ 150 K to grow tri- and quadruple-layers. XAS/XMCD measurements were performed at BL4B in UVSOR by total electron yield mode at B = 0 - ± 5 T and T = 7.9 K. The XMCD spectra are obtained at the normal (NI: θ = 0°) and the grazing (GI: θ = 55°) geometries. Magnetization curves were recorded by plotting the L_3/L_2 XAS intensity as a function of the magnetic field.

We find from the magnetization curve that the magnetization easy axis of the trilayer is toward the out-of-plane direction. This indicates that the out-of-plane magnetocrystalline anisotropy of the trilayer is large enough for overcoming the in-plane film shape anisotropy. On the other hand, the quadruple layer shows the strong in-plane magnetic anisotropy. The results could be interpreted from the modification of the topmost surface layer from NiN (trilayer) to FeN (quadruple layer), which presumably prefers the in-plane magnetization [5].

[1] T. Miyamachi *et al*., UVSOR Activity Report 2018 **46** (2019) 138.
[2] T. Miyamachi *et al*., UVSOR Activity Report 2018 **46** (2019) 139.
[3] K. Kawaguchi *et al.*, Phys. Rev. Materials *accepted.*
[4] Y. Takahashi *et al*., Phys. Rev. Lett. **116** (2016) 056802.
[5]Y. Takahashi *et al*., Phys. Rev. B **95** (2017) 224417.

BL4B

Magnetic Properties of FeCo Alloy Thin Films Grown by Nitrogen Surfactant Epitaxy

T. Miyamachi[1,2], Y. Takahashi[1,3], T. Hattori[1], T. Koitaya[4,5], K. Yamamoto[4,5], M. Kotsugi[3], T. Yokoyama[4,5] and F. Komori[1]

[1]*Institute for Solid State Physics, The University of Tokyo, Kashiwa277-8581, Japan*
[2]*The University of Electro- Communications, Chofu 182-8585, Japan*
[3]*Tokyo University of Science, Tokyo 125-8588, Japan*
[4]*Institute for Molecular Science, Okazaki 444-8585, Japan*
[5]*The Graduate University for Advanced Studies, SOKENDAI, Okazaki 444-8585, Japan*

An $L1_0$-type FeCo ordered alloy is theoretically predicted to show an extraordinary large perpendicular magnetic anisotropy among transition metal alloys, attracting great attention as a rare earth-free permanent magnet. The precisely controlled thin film growth of alternating Fe and Co atomic layers using pulsed laser deposition have been used for the preparation of $L1_0$ FeCo thin films [1]. However, the degree of order of the $L1_0$ structure is still low due to atomic-scale structural and magnetic disorder at the Fe/Co interface and resultingly the perpendicular magnetization has not yet been achieved.

Toward realizing high quality FeCo alloy thin films, we here focus on the fabrication method utilizing nitrogen surfactant effects of monatomic layer iron and cobalt nitrides (Fe_2N and Co_2N). The validity of the nitrogen surface epitaxy on the growth of $L1_0$-type alloy thin films has been demonstrated for FeNi alloy thin films [2]. High lateral lattice stability of magnetic nitrides [3], and the surfactant nitrogen during the deposition of Fe and Co atomic layers can effectively suppress the interdiffusion at the Fe/Co interface, leading to atomically flat and homogeneous surface and interface in FeCo alloy thin films.

We here performed combined study of scanning tunneling microscopy (STM) and x-ray absorption spectroscopy/x-ray magnetic circular dichroism (XAS/XMCD) to investigate structural and magnetic properties of 1 monolayer (ML) Co on Fe_2N/Cu (001), the initial step for the fabrication of FeCo alloy thin films grown by the nitrogen surfactant epitaxy. The advantage of this complementary experimental approach is that macroscopic observations of element specific and quantitative electronic and magnetic properties by XAS/XMCD can be linked with microscopic origins of the Fe/Co interface characteristics revealed by STM [4].

The monatomic layer of Fe_2N was grown on Cu(001) in the following processes: (1) N^+ bombardment onto a clean Cu(001) surface with a beam energy of 500 eV, (2) Fe deposition onto N/Cu(001) at room temperature, and (3) subsequent annealing up to ~ 670 K [3]. 1 ML Co was thereafter deposited at a low temperature (~ 150 K).

XAS/XMCD measurements were performed at BL4B in UVSOR by total electron yield mode at B = 0 - ± 5 T and T = 6.6 K. The XMCD spectra are obtained at the normal (NI: $\theta = 0°$) and the grazing (GI: $\theta = 55°$) geometries by detecting $\mu_+ - \mu_-$, where μ_+ (μ_-) denotes the XAS recorded at Fe and Co L adsorption edges with the photon helicity parallel (antiparallel) to the sample magnetization. Note that θ is the angle between the sample normal and the incident x-ray. Magnetization curves were recorded by plotting the L_3 XAS intensity normalized by the L_2 one as a function of the magnetic field.

We first confirmed from XMCD measurements the strong in-plane magnetic anisotropy of bare Fe_2N as previously reported [3]. STM measurements revealed the formation of Co_2N/Fe/Cu (001) via nitrogen surfactant effect by adding 1 ML Co. Accordingly, relative increase in the out-of-plane magnetization of Fe to the in-plane magnetization was observed. These results indicate that the nitrogen surfactant effect efficiently suppresses the interdiffusion at the Fe/Co interface and keeps atomically flat surface/interface in FeCo atomic layers, presumably reflecting the intrinsic out-of-plane magnetization of $L1_0$ FeCo.

[1] H. Ito *et al*., AIP Advances **9** (2019) 045307.
[2] K. Kawaguchi *et al*., Phys. Rev. Materials, *accepted*.
[3]Y. Takahashi *et al*., Phys. Rev. B **95** (2017) 224417.
[4] S. Nakashima *et al*., Adv. Funct. Mater. **29** (2019) 1804594.

BL4B

Molecular Orientation and Magnetic Properties of Iron Phthalocyanine Thin Films Grown on Passivated Silicon Surfaces

S. Ohno[1], K. Yamamoto[2], T. Koitaya[2] and T. Yokoyama[2]
[1]*Fuclty of Engineering, Yokohama National University, Yokohama 240-8501, Japan*
[2]*Institute for Molecular Science, Okazaki 444-8585, Japan*

Iron phthalocyanine (FePc) is one of the prototype molecules to study magnetic properties of molecular thin films. It is a planner molecule which has an Fe^{2+} iron at the center. It has been shown that the first Hund's rule is violated in FePc, resulting in the ground state of S=1 rather than S=2 [1]. It has been reported that highly unquenched orbital moment is caused by the ^3E_g ground state with the half-filled e_g state at the Fermi level for FePc thin films grown on gold surfaces [2].

In the present work, we studied both molecular orientation and magnetic properties of FePc thin films grown on passivated silicon surfaces, such as water-adsorbed Si(001) (H_2O/Si(001)), oxidized Si(001) (SiO_2/Si(001)) and oxidized silicon wafer covered with monolayer graphene (Gr/SiO_2).

BL4B soft X-ray beamline was used for X-ray Absorption Near Edge Structure (XANES) spectroscopy measurements in N K-edge region and X-ray Magnetic Circular Dichroism (XMCD) measurements in Fe L-edge region.

Figure 1 shows angle-dependent linearly polarized XANES spectra at the N K-edge. The peaks A, B, and C are assigned to π* resonances and D, E, and F are assigned to σ* resonances [2]. In the present cases, the tilted angles of the molecular plane are estimated to be ~35-65° on average. These suggest that the FePc molecules are not perfectly aligned parallel to the surface nor perpendicular to the surface.

Figure 2 shows MCD spectra of FePc/Gr/SiO_2 at the Fe L-edge. We have evaluated the orbital magnetic moment (m_L) and the spin magnetic moment (m_S) using the sum rules. The values of m_L are estimated to be ~0.1-0.8 μ_B, depending on the thickness and substrate. In several cases, the values are even larger than the reported values (~0.2-0.5 μ_B) obtained for FePc/Au [2].

The present results indicate that the properties of FePc thin films grown on H_2O/Si(001) and SiO_2/Si(001) are similar in the molecular orientation as well as the magnetic moment. In contrast, the MCD spectra exhibit quite different features in the case of FePc thin films grown on Gr/SiO_2. For instance, the two distinct peaks are observed in the L_{III} region, as shown in Fig. 2. These may correspond to the a_{1g} and e_g states observed for the well-ordered films [2]. The role of monolayer graphene is found to be substantial to modify both molecular orientation and magnetic properties.

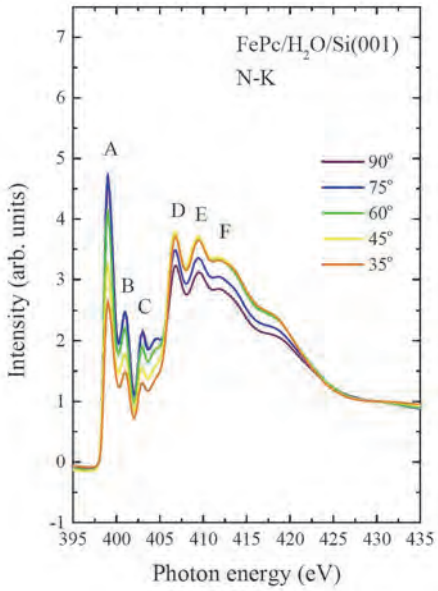


Fig. 1. Angle-dependent linearly polarized XANES spectra of FePc/H_2O/Si(001) at the N K-edge.

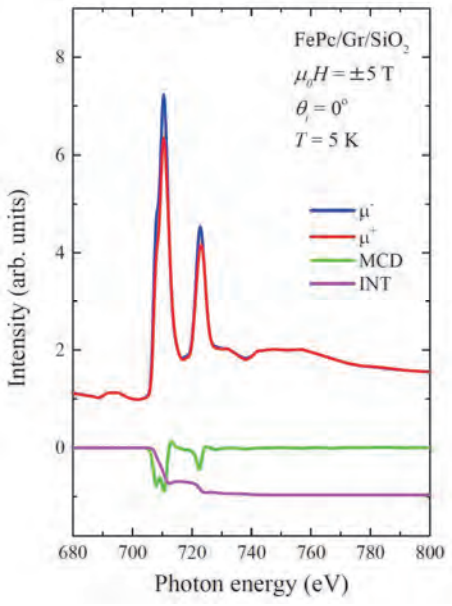


Fig. 2. MCD spectra of FePc/Gr/SiO_2 at the Fe L-edge.

[1] M.D. Kuz'min *et al.*, Phys. Rev. B **79** (2009) 024413.
[2] J. Bartolomé *et al.*, Phys. Rev. B **81** (2010) 195405.

BL5U

Polarization Dependent Interfacial Electronic Structure of Ultra-thin Fe Layers on Rashba-splitted Au (111) Surfaces

J. Okabayashi[1], K. Tanaka[2] and S. Mitani[3]

[1]*Research Center for Spectrochemistry, The University of Tokyo, Tokyo 113-0033, Japan*
[2]*UVSOR Synchrotron Facility, Institute for Molecular Science, Okazaki 444-8585, Japan*
[3]*National Institute for Materials Science, Tsukuba 305-0047, Japan*

When ferromagnetic transition metals (TMs) are deposited on the Rashba-type spin-orbit coupled surface, novel properties such as perpendicular magnetic anisotropy (PMA) are emerged at the interfaces, which are derived from the symmetry broken spin-orbit effects. The gold Au (111) surfaces have been investigated extensively by means of scanning tunneling microscopy and angle-resolved photoemission spectroscopy (ARPES) because this surface exhibits the large Rashba-type spin-orbit splitting of 110 meV [1]. It provides the wide varieties for the topological physics and spin-orbit coupled sciences at the surfaces and interfaces. Recently, the interfaces between Au(111) and other heavy elements such as Bi or Ag have been extensively investigated [2,3]. Here, we focus on the interfaces between ferromagnetic materials and Au(111) interfaces because the thin Fe layers on the heavy elements are expected to exhibit the PMA induced by the Rashba-type spin-orbit interaction.

The spin-orbit coupling between the ferromagnetic 3*d* TMs Fe or Co and 5*d*, 6*sp* heavy metal elements of non-ferromagnetic materials such as Pt and Au has been utilized for the PMA through the proximity at the interfaces. It is believed that the future researches concerning not only spins but also orbitals are recognized as the *spin-orbitornics*. Therefore, to clarify the origin of the PMA at these interfaces is a crucial role. The relationship between Au (111) Rashba-type spin-orbit interaction and PMA in 3*d* TMs has not been clarified explicitly. In order to investigate the orbital-resolved states in the Fe films showing the PMA, ARPES at the interfaces becomes powerful techniques through the photon-energy and polarization dependences in each 3*d* orbital. By using ARPES, we aim to understand the orbital-resolved electronic structures at the magnetic interfaces on the Rashba-type Au (111) surface in order to develop the researches of novel PMA using spin-orbit coupled interfaces.

We prepared the clean Au (111) surface for the Fe deposition. The commercialized single-crystalline 100-nm-thick Au (111) films on sapphire substrate were used. At the beamline BL5U in UVSOR, we repeated the Ar-ion sputtering at 1 kV accelerating voltage and subsequent annealing at 400 °C under the high vacuum conditions. After the sample preparation, the Fe layer was deposited at room temperature and then annealed. By *in-situ* transferring the samples into the ARPES chamber, we performed ARPES at 10 K using the photon energies of 60 and 120 eV because of the large cross-section of Au (111) surface states and detections of Fe 3*s* and Au 4*f* intensity ratios, respectively.

Figures 1 (a) and (b) display the photoemission spectra in Fe layers on Au (111) with horizontally and vertically polarized beams at 60 eV. As shown in Fig. 1a, the intensity ratio changes due to the difference of orbital symmetry. The Au (111) surface clearly exhibits the Rashba-type surface states. The Fe 3*d* states appear near the Fermi level (E_F) and the surface states disappear. As shown in Fig. 1 (c), band dispersion image plots taken by horizontal and vertical polarized beams exhibit asymmetric feature, which can be explained by the Fe 3*d* orbital-resolved states through the overlap between Fe and Au. Horizontal and vertical cases detect preferentially out-of-plane and in-plane orbitals, respectively. Furthermore, we confirmed the PMA at Fe/Au interface by x-ray magnetic circular dichroism and Mössbauer spectroscopies. Therefore, the interfacial chemical reaction between Fe and Au brings the novel properties on the ultrathin Fe electronic structures.

We acknowledge Dr. S. Ideta in IMS for technical supports of data analyses. This work was in part supported by KAKENHI Kiban(S) project.

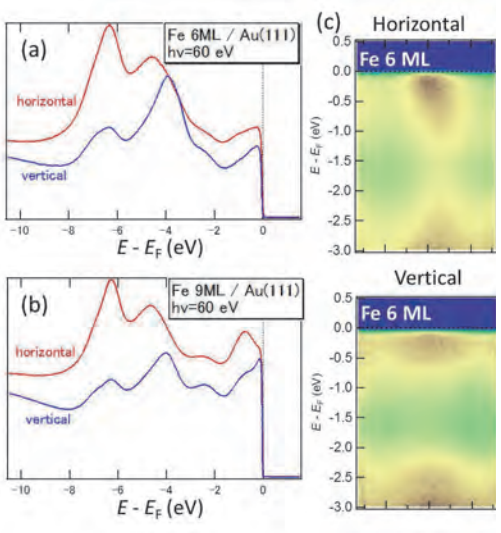


Fig. 1. Polarization dependence in Fe valence-band photoemission spectra taken at 60 eV for (a) 6 ML and (b) 9 ML. (c) Band-dispersion mapping of Fe 6 ML case for horizontal and vertical beams taken at 60 eV.

[1] S. LaShell *et al.*, Phys. Rev. Lett. **77** (1996) 3419.
[2] C. Tusche *et al.*, Ultramicroscopy **159** (2015) 620.
[3] B. Yan *et al.*, Nature Commun. **6** (2015) 10167.

BL5U

Electronic Structure of Ultrathin Bismuth Films Fabricated on InSb(111)

Y. Ohtsubo[1,2], J. K. Modak[2], T. Nakamura[2] and S. Kimura[1,2]
[1]*Gradudate School of Frontier Biosciences, Osaka University, Suita 565-0871, Japan*
[2]*Department of Physics, Graduate School of Science, Osaka University, Toyonaka 560-0043, Japan*

The electronic structure of elemental bismuth (Bi) has been studied extensively in this decade because of its ambiguous three-dimensional topological order driven by the large size of spin-orbit interaction in valence bands [1]. Moreover, ultrathin Bi film down to few monatomic layers is also predicted as a two-dimensional topological insulator [2] and hence is gathering much attention. Although growth of Bi ultrathin films with several layers has been achieved on various substrates [3-5], most of them are strongly influenced from substrates, such as the significant structural deformation on SiC [3] and intermixing with the metallic states of the Bi_2Te_3 substrate [4]. In this project, we tried to grow ultrathin Bi films with a few layers on InSb(111), which has the lattice constant very close to the Bi crystal and no electronic states around the Fermi level. These characteristics of InSb suggest that it is a suitable substrate to realize free-standing Bi ultrathin films down to 1-2 bilayers (BL).

The InSb(111) substrates were cleaned in an ultra-high vacuum chamber by repeated cycles of Ar ion sputtering with the ion energy of 1 keV and annealing with the temperature of 550 K until a sharp RHEED pattern was observed. Subsequent evaporation of Bi was performed on the substrate at room temperature using a home-made Knudsen cell, resulting in sharp and low-background patterns as shown in Fig. 1 (a). It suggests that high-quality Bi(111) films were obtained by this method. The Bi evaporation rate was checked *in-situ* by monitoring the intensity oscillation of the RHEED diffraction rods. Accordingly, we could fabricate the ultrathin Bi(111) films with the thicknesses from 1 to 5 BLs. The film thicknesses were cross-checked by core-level photoelectron peak areas of Bi, In, and Sb, showing a consistent behavior to the RHEED oscillation.

Figure 1 (b) shows the Fermi contour of the 5-BL Bi(111) film grown on InSb(111) obtained by ARPES. The six-fold tear-drop like contours and nearly circular one at the center of the surface Brillouin zone are consistent with the earlier results [1,5]: the latter should be hexagonal, but it is difficult to distinguish hexagon and circle with the current angular resolution. This agreement suggests that the obtained Bi(111) film, especially its electronic structure around the Fermi level, is free from any modulations by substrates. At the lower thicknesses, the shape of the Fermi contour as well as the surface-band dispersions changed according to the thicknesses. Detailed analysis of such changes, especially a comparison with theoretical calculations are ongoing in order to examine whether the fabrication of the free-standing Bi(111) films with 1-2 BLs, a promising playground to study the topological edge states of two-dimensional topological insulators, could be achieved or not.

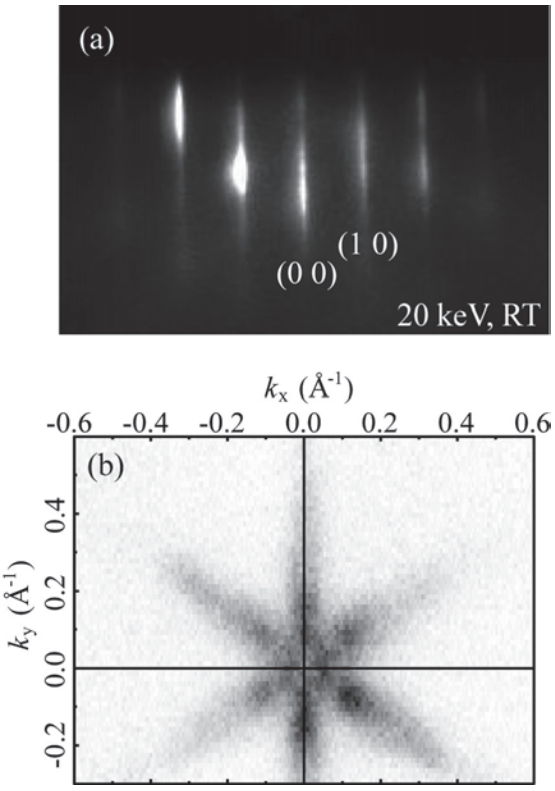


Fig. 1. (a) RHEED pattern of the Bi(111) film (5 BL) on InSb(111). (b) Fermi contour of the same sample taken by ARPES ($h\nu$= 60 eV, 7 K).

[1] L. Fu and C. L. Kane, Phys. Rev. B **76** (2007) 045302. S. Ito *et al.*, Phys. Rev. Lett. **117** (2016) 236402. Y. Ohtsubo and S. Kimura, New J. Phys. **18** (2016) 123015 and references therein.
[2] S. Murakami, Phys. Rev. Lett. **97** (2006) 236805.
[3] F. Reis *et al.*, Science **357** (2017) 287.
[4] T. Hirahara *et al.*, Phys. Rev. Lett. **107** (2011) 166801.
[5]T. Hirahara *et al.*, Phys. Rev. Lett. **97** (2006) 146803.

BL5U, BL7U

Thermal Effect of the Surface Reconstruction of the Topological Kondo Insulator SmB_6

Y. Ohtsubo[1,2], T. Nakamura[2], T. Nakaya[2], F. Iga[3] and S. Kimura[1,2]
[1]*Graduate School of Frontier Biosciences, Osaka University, Suita 565-0871, Japan*
[2]*Department of Physics, Graduate School of Science, Osaka University, Toyonaka 560-0043, Japan*
[3]*College of Science, Ibaraki University, Mito 310-8512, Japan*

Topological Kondo Insulators (TKI) are gathering much attention in these days as an interesting playground to study the concert effect of the spin-polarized topological surface states and strong electron correlation resulting in the metal-insulator transition of Kondo insulators [1]. Samarium hexaboride (SmB_6) is the first and the most extensively studied candidate of TKI. It has been revealed that the (001) surface of a cleaved SmB_6 single crystal hosts the metallic and spin-polarized surface states as expected from topological classification [1,2]. However, the topological order of SmB_6 itself is still under debate because of the multiple possible interpretations of the metallic surface bands [3,4] as well as the various surface atomic structures randomly appear on the cleaved surfaces [5].

In this project, we have revisited the surface atomic and electronic structures of SmB_6(001) by using the *in-situ* cleaning method in an ultra-high vacuum (UHV) chamber. The (001) faces of SmB_6 single crystals were polished under air atmosphere and then cleaned in the UHV chamber by repeated cycles of Ar^+ sputtering (ion energy: 1 keV) and annealing. The annealing temperature was set at several temperatures from 600 to 1400 °C and the surface atomic and electronic structures were checked at each temperature by LEED and ARPES measurements, respectively.

As shown in Fig. 1 (a), we found the (2×1) surface reconstruction with the annealing temperature of 800 °C. The fractional order spots became weak and diffused with the elevated annealing temperature up to 1000 °C. Afterward, at the highest annealing temperature (1400 °C), the fractional-order spots appeared again with the sharper shape than those after 800 °C annealing, (see Fig. 1 (b)). These (2×1) surface reconstructions are consistent with the known surface structures [3,5-7].

Figure 1 (c) shows the B-1*s* core-level photoelectron spectra corresponding to the LEED patterns shown in Figs. 1 (a, b). At 800 °C (the lower spectrum), a satellite peak around 16.7 eV is shown, suggesting the surface reconstruction by boron, which would originate from displacements of B_6 clusters. In contrast, at 1400 °C (the upper), no such satellite observed in the spectrum. It suggests that the latter (2×1) surface reconstruction does not originate from the surface boron but from the other reasons such as periodic desorption of Sm atoms from the surface atomic layers.

These two different (2×1) surfaces on SmB_6(001) could reconcile the wide variety of surface preparation conditions reported so far [6,7]. Further analysis on the surface electronic structure around the Fermi level, especially the influence from the newly distinguished surface reconstructions, is ongoing.

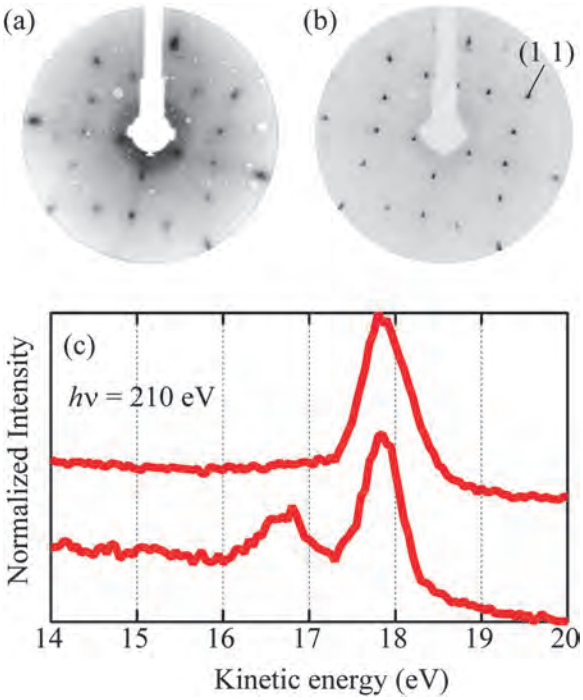


Fig. 1. (a, b) LEED patterns (The pass energy: E_P = 44 eV) of the SmB_6(001)-(2×1) surfaces annealed at (a) 800 °C and (b) 1400 °C. (c) B-1*s* core-level spectra taken from the SmB_6(001)-(2×1) surfaces; the lower (upper) one is from the surface annealed at 800 (1400) °C.

[1] M. Dzero *et al.*, Phys. Rev. Lett. **104** (2010) 106408.
[2] N. Xu *et al.*, J. Phys.: Condens. Matt. **28** (2016) 363001 and references therein.
[3] P. Hlawenka *et al.*, Nat. Commun. **9** (2018) 517.
[4] Y. Ohtsubo *et al.*, Nat. Commun. **10** (2019) 2298.
[5] S. Rößler *et al.*, PNAS **111** (2014) 4798.
[6] H. Miyazaki *et al.*, Phys. Rev. B **86** (2012) 075105.
[7] M. Ellguth *et al.*, Philos. Mag. **96** (2016) 3284.

BL6U

Photoemission Tomography Utilizing One-dimensionally Ordered Film of High-mobility Organic Semiconductors

M. Iwasawa[1], S. Kobayashi[1], Y. Hasegawa[2], M. Nozaki[3], S. Kurihara[3], S. Otaki[3], K. Niki[3], M. Sasaki[1], F. Matsui[2], S. Kera[2] and Y. Yamada[1]

[1]*Institute of Applied Physics, University of Tsukuba, Tsukuba 305-8573, Japan*
[2]*Institute for Molecular Science, Department of Photo-Molecular Science, Okazaki 444-8585, Japan*
[3]*Institute of Applied Physics, Chiba University, Tsukuba 305-8573, Japan*

Recently, the researches of the photoelectron tomography (PT) of the organic semiconductor films have rapidly been increased with many successes to obtain the information of the character of the initial-state wavefunction. However, the researches have still been limited to the model molecules with simple molecular shape. In this work, we tried to apply PT to rather practical organic semiconductor molecules with high mobility, in order to clarify the mechanism of their charier transport.

In the present study, we especially focused on the practical molecules with rather simple structure, such as picene and Dph-BTBT. The single crystals and films of these molecules are known to show lather high mobility up to the range of 10^1 cm^2/Vs. Recent theoretical calculation have shown that, while the hole mobility in the case of picene can be rather fairly explained considering the HOMO, that in the case of BTBT cannot be understood only by HOMO. In the case of BTBT, HOMO-1 must be taken into account, despite the energy difference between HOMO and HOMO-1 of BTBT is much larger than that of picene. The PT analysis can shied the light on the nature of the molecular orbital which is responsible in the carrier transport.

We utilized well-defined thin film of picene and Dph-BTBT film utilizing anisotropic Ag(110) substrate. The molecular arrangements in these films were directly determined LEED and STM. PT of these system were done at BL6U of UVSOR. In the PT measurements, we utilized mesh electrode in front of the sample which was at +500 V with respect to the sample, in order to increase the acceptance angle of the photoelectron to probe wider area in the reciprocal space.

Figure 1 (a) shows the one-dimensional structure of the picene films on Ag(110) substrate, where the molecular axis of picene is aligned [1-10] direction of the substrate. Figure 1 (b) is corresponding photoelectron angular distribution (PAD) mapping patterns for HOMO and HOMO-1. The obtained patterns well correspond to the Fourier transform (FT) of the each molecular orbitals as shown in the inset. We then extract the energy distribution curve (EDC) from the portion of the rectangles in the PAD mapping, as shown in Fig. 1 (c) Although the area averaged EDC showed overlapped spectrum, selected-area accumulation clearly shows the EDC of HOMO and HOMO-1.

Figure 2 shows the results of Dph-BTBT. In contrast to the case of picene, the molecular long axis of Dph-BTBT/Ag(110) was not in the [1-10] direction and two different domains were found. In this case, the energy of the HOMO and HOMO-1 levels are well separated and their PAD are rather similar, in contrast to the case of picene. However, we can clearly separate the photoelectrons from these levels in PAD mapping, which will be useful in the discussion of the overlapping of these orbitals.

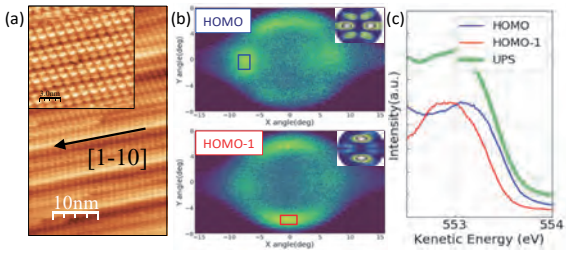


Fig. 1 (a) STM image of several layer of Picene/Ag (110). (b) PAD images of HOMO and HOMO-1 (c) selectred-area EDC of HOMO and HOMO-1.

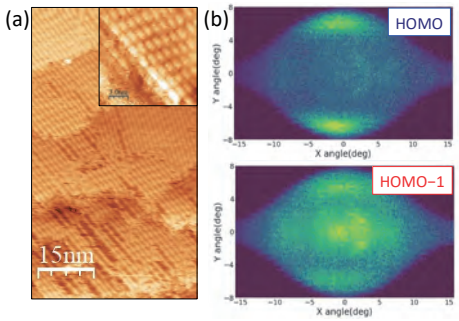


Fig. 2 (a) STM image of monolayer of Dph-BTBT/Ag (110). (b) PAD images of HOMO and HOMO-1.

BL6U

ARPES and RAES Study of Nanographene on Pt(111)

O. Endo[1,3], F. Matsui[2], W.-J. Chun[3], M. Nakamura[4], K. Amemiya[5] and H. Ozaki[1]

[1]*Department of Applied Chemistry, Faculty of Engineering, Tokyo University of Agriculture and Technology, Koganei 184-8588, Japan*

[2]*UVSOR Synchrotron Facility, Institute for Molecular Science, Okazaki 444-8585, Japan*

[3]*Graduate School of Arts and Sciences, International Christian University, Mitaka 181-8585, Japan*

[4]*Department of Applied Chemistry and Biotechnology, Faculty of Engineering, Chiba University, Chiba 263-8522, Japan*

[5]*Photon Factory, High Energy Accelerator Research Organization (KEK-PF), Institute of Materials Structure Science (IMSS), Tsukuba 305-0801, Japan*

Graphene, a single sheet of carbon, is one of typical 2D materials which exhibits a peculiar band structure. Nanographene (NG), which is cut from graphene into nano-size, is expected as a material for next generation devices due to the confined electronic structure and an open band gap. In this study, Angular Resolved Photo Emission Spectroscopy (ARPES) and Resonant Auger Electron Spectroscopy (RAES) were performed to investigate the electronic structure of NG.

NG was obtained by the thermal decomposition of benzene on the Pt(111) surface at the substrate temperature of either 1100 K (HT) or 800 K (LT). All the spectra were measured at BL6U of UVSOR.

Figure 1 shows the band dispersion along the Γ-K direction of the NGs on Pt(111). Both the NGs obtained at HT(a) and LT(b) exhibit the π band, and therefore, the π band is formed for the NG obtained at LT with the size of as small as 10 nm diameter, which was confirmed by scanning tunneling microscopy. The size of NG obtained at HT is estimated > 100 nm diameter. The NG lattice is rotated ca. 30° with respect to the Pt lattice. The bottom of the π band is located at 7.8 eV from E_F, which is shallower than that of graphite (8.16 eV) [1]. This indicates the electron transfer to the Pt substrate [2,3]. Figures 2 (a) and (b) show the C1s XPS spectra. In addition to the principal peaks at BE = 283.9 eV (sp2 carbon of graphene), a shoulder at 284.2 eV is enhanced for the NG obtained at LT. This shoulder suggests the existence of the sp3 carbon, which forms the C-Pt bond [4]. This is consistent with the Pt4f XPS spectra shown in Figs. 2(c) and (d), which exhibit a smaller surface-related band at 70.7 eV for the NG obtained at LT. Figure 3 shows the RAE spectra excited at the photon energy of 1s→π* transition. Although the angular dispersion is observed for the NG obtained at HT, which is similar to graphite [5], the auger electrons are focused at the Γ point for the NG obtained at LT. Similar dispersion patterns are observed for all the excitation energies in the C K-edge region.

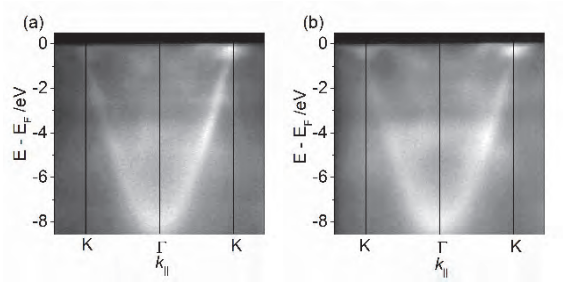


Fig. 1. π band of NG obtained at (a)HT and (b)LT.

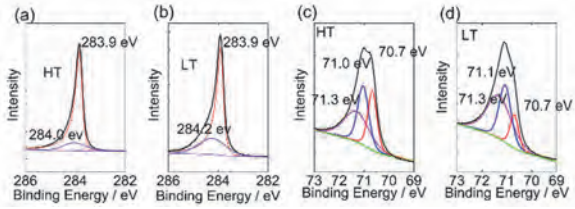


Fig. 2. C1s XPS of NG obtained at (a)HT and (b)LT. Pt 4f XPS of NG obtained at (c)HT and (d)LT.

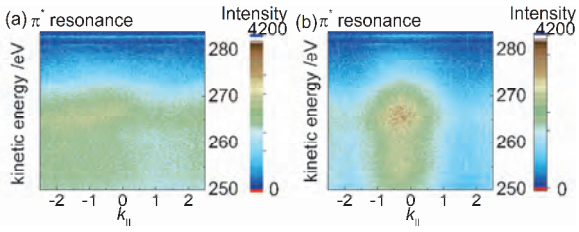


Fig. 3. RAES at C K-edge of NG obtained at (a)HT and(b)LT.

[1] F. Matsui *et al*., Phys. Rev. B **97** (2018) 045430.
[2] G. Giovannetti *et al*., Phys. Rev. Lett. **101** (2008) 026803.
[3] P. Sutter *et al*., Phys. Rev. B **80** (2009) 245411.
[4] S. Rajasekaran *et al*., Phys. Rev. B **86** (2012) 075417.
[5] F. Matsui *et al*., JPS 2019 Autumn meeting.

BL7U

High-resolution Angle-resolved Photoemission Study on $MnBi_2Te_4/Bi_2Te_3$

S. Kusaka[1], K. Sumida[1], T. Fukasawa[1], S. Ichinokura[1], S. Ideta[2], K. Tanaka[2] and T. Hirahara[1]
[1]*Department of Physics, Tokyo Institute of Technology, Tokyo 152-8551, Japan*
[2]*UVSOR Synchrotron Facility, Institute for Molecular Science, Okazaki 444-8585, Japan*

Topological insulators (TI) are extensively studied recently due to its peculiar properties [1]. The Dirac-cone surface states of TI are protected by time-reversal symmetry (TRS) and backscattering among these surface states is prohibited. But when TRS is broken by application of a magnetic field or incorporating magnetic materials, a gap opening in the Dirac cone is expected and an intriguing phase called the quantum anomalous Hall state can be realized [2]. This phase is expected to show even more exotic phenomena such as the topological magnetoelectic effect. To realize such state, two types of sample fabrication techniques have been employed up to now: (1) magnetic doping while growing the single crystal or thin film of TI [3], and (2) magnetic impurity deposition on the surface of TI [4]. While method (1) was successful and showed evidence of the TRS violation, no one has succeeded using method (2), which should be a more direct way to examine the interaction between the topological surface states and magnetism. We have previously found another novel technique to induce magnetism into TI, namely the magnetic extension effect [5]. By depositing Mn and Se on Bi_2Se_3, we found that Mn and Se are incorporated in the topmost Bi_2Se_3 layer and a novel heterostructure $MnBi_2Se_4/Bi_2Se_3$ is formed [5]. This heterostructure showed a clear Dirac cone gap of 85 meV and the gap persisted up to room temperature. From magnetic measurements it was revealed that ferromagnetism also persists up to room temperature in this system. Taking all these facts into account, it can be said that this system is promising to observe the quantum anomalous Hall effect at room temperature. However, the Dirac cone gap is not at the Fermi level and there is no systematic method to control the Fermi level position in Bi_2Se_3.

Therefore in this study, we have employed Bi_2Te_3 as the parent TI and have deposited Mn and Te on Bi_2Te_3 to see if magnetic extension can also occur for this system. Our structural analysis based on LEED-IV measurements ensured that the heterostructure we fabricated was $MnBi_2Te_4/Bi_2Te_3$. The band dispersion measured at 10 K is shown in Fig. 1. In contrast to the $MnBi_2Se_4/Bi_2Se_3$ sample, there was no gap opening in the surface Dirac cone of $MnBi_2Te_4/Bi_2Te_3$ even at 10 K. We have also performed X-ray magnetic circular dichroism measurements on this heterostructure and found that it is paramagnetic down to 5.6 K, the lowest temperature we can reach in the experimental system. Thus the absence of the Dirac cone gap and its correspondence with the magnetic properties is clear-cut in this system. The remaining questions are: (1) why is this structure paramagnetic down to 5.6 K in contrast to the theoretical calculations that predict a Curie temperature of 12 K [6] with a 77 meV Dirac cone gap [7]? (2) why is the magnetic property of this system so different from that of $MnBi_2Se_4/Bi_2Se_3$? We hope to resolve these questions in the near future from further investigation.

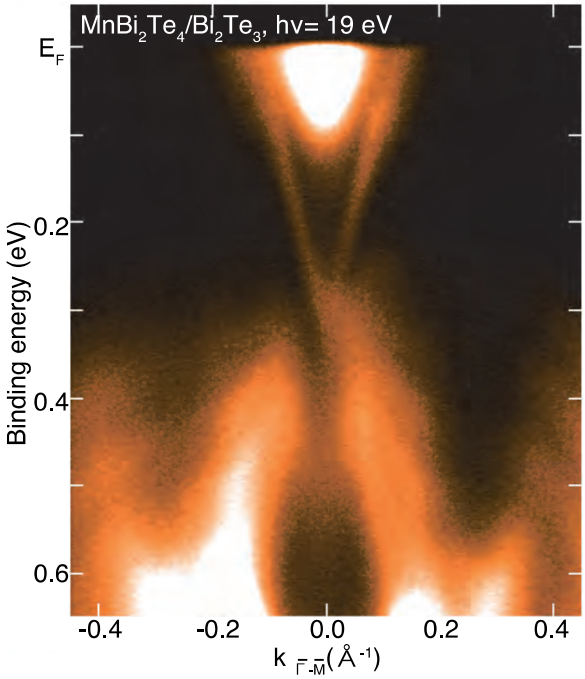


Fig. 1. Band dispersion image of the $MnBi_2Te_4/Bi_2Te_3$ heterostructure measured at 10 K.

[1] M. Hasan and C. Kane, Rev. Mod. Phys. **82** (2010) 3045.
[2] X.-L. Qi and S.-C. Zhang, Rev. Mod. Phys. **83** (2011) 1057.
[3] For example, C. Z. Chang *et al.,* Science **340** (2013) 167.
[4] For example, M. Ye *et al.,* Phys. Rev. B **85** (2012) 205317.
[5] T. Hirahara *et al.,* Nano Lett. **17** (2017) 3493.
[6] M. Otrokov *et al.,* Phys. Rev. Lett. **122** (2019) 107202.
[7] M. Otrokov *et al.,* 2D Materials **4** (2017) 025082.

BL7U

Evolution of Electronic Structure of Pentacene Monolayer on Graphite Probed by Low-Energy ARUPS

Y. Hasegawa[1], T. Nakamura[2], M. Meissner[1], T. Yamaguchi[1], S. Ideta[1], K. Tanaka[1] and S. Kera[1]
[1]*Department of Photo-Molecular Science, Institute for Molecular Science, Okazaki 444-8585, Japan*
[2]*Department of Physics, Graduate School of Science, Osaka University, Toyonaka 560-0043, Japan*

Thin films of small organic semiconductor molecules on layered substrates have been widely studied to explore new electronic property and application. The electronic state of the organic thin film can be modified by the subtle change of intermolecular and molecule-substrate interaction which is dominated by weak van der Waals forces. Although impacts of such weak interaction on the electronic state are important to study the mechanism, it has been hardly investigated due to complex and inhomogeneous organic molecular structure.

We have revealed the precise growth of well-ordered thin film of small organic semiconductor molecules on the graphite substrate and investigated the system by means of angle-resolved ultraviolet photoelectron spectroscopy (ARPES) using low-photon energy (hv) excitation (LE-ARUPS). Utilizing the system, we have found modification of the wavefunction despite the weak interaction between the molecule and the substrate [1]. Here, the impact of the structural transition of two-dimensional molecular arrangement in the monolayer of the pentacene/graphite on the electronic structure is investigated by changing the sample temperature. The sample was prepared in a custom UHV chamber. A single crystal graphite (SCG) substrate was cleaned by annealing at 900 K for several hours. Pentacene film of 3 Å was deposited onto the substrate at room temperature. Low-energy electron diffraction (LEED) measurement was performed separately as independent experiments.

First, the structural transition of pentacene monolayer was investigated by taking LEED pattern as shown in Fig. 1. Transition of the LEED pattern from sharp spot to filled hexagon-like pattern with increasing the temperature indicates that the pentacene monolayer with densely packed molecule is formed below the transition temperature (135 K), whereas the monolayer consisting both of molecules which is aligned with a mean distance from adjacent molecules and densely packed molecules with relatively small grains are formed above the transition temperature.

Energy and momentum (E-k) maps of both phases observed by LE-ARPES are shown in Fig. 2. In the E-k maps, flat bands originated from highest occupied molecular orbital (HOMO) of pentacene, consisting of a main peak (00) with the vibrational progressing of satellite peaks toward higher binding energy, (01) and (02), is observed as in the previous works [2]. Below the transition temperature, in addition to the energy shift toward higher energy side, dispersed band at around Γ-point marked by dashed line which is not deribed from a clean graphite is observed (Fig. 2 (a)). This feature is detected only in a certain hv energy region from 7.4 eV to 7.8 eV [1] and shifts with increasing the kinetic energy, indicating that it is possibly originated from resonant excitation of an unoccupied band newly formed for the pentacene molecule and the SCG substrate. This band disappears above the transition temperature, indicating that the electronic state is sensitive to the interfacial structure. These observations suggest that the electronic wave function of pentacene monolayer is connected to that of graphite coherently which causes strong modification of their unoccupied state. The method realizes that the possibility to probe a tailoring of electronic state via weak interaction.

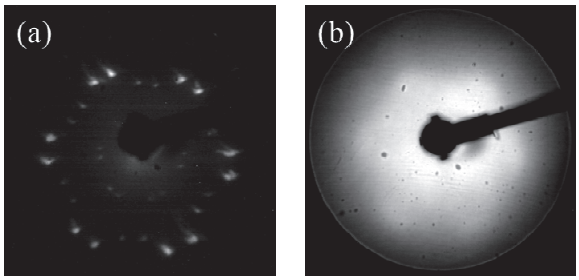


Fig. 1. LEED pattern of pentacene/SCG taken at (a) 72 K and (b) 170 K with electron beam energy of 18 eV.

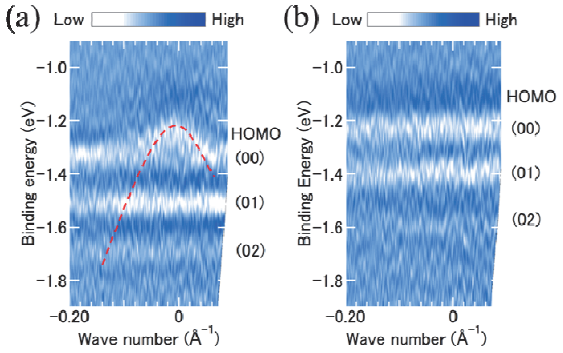


Fig. 2. Second derivative of E-k map taken from pentacene/SCG at (a) 85 K and (b) 165 K with hv = 7.4 eV.

[1] T. Yamaguchi *et al*., UVSOR Activity Report 2018 **46** (2019) 148.
[2] H. Yamane *et. al*., Phys. Rev. B **72** (2005) 153412.

Ⅲ-5

Life, Earth and Planetary Sciences

BL1U

Optical Activity Emergence in Amino-Acid Films by Vacuum-Ultraviolet Circularly-Polarized Light Irradiation (III) - Summary of Experiments -

J. Takahashi[1], T. Sakamoto[1], Y. Izumi[2], K. Matsuo[2], M. Fujimoto[3], M. Katoh[2,3], Y. Kebukawa[1] and K. Kobayashi[1]

[1]*Faculty of Engineering, Yokohama National University, Yokohama 250-8501, Japan*
[2]*Hiroshima Synchrotron Radiation Center, Higashi-Hiroshima 739-0046, Japan*
[3]*UVSOR Synchrotron Facility, Institute for Molecular Science, Okazaki 444-8585, Japan*

One of the most attractive hypotheses for the origin of homochirality in terrestrial biomolecules (L-amino acid and D-sugar dominant) in the context of astrobiology is "Cosmic Scenario" [1,2]. Several ground experiments to validate the scenario have been investigated using circularly polarized light (CPL) from high-energy particle accelerators. We have already reported optical activity emergence in solid films of racemic amino acids by CPL irradiation of 215 nm in wavelength from free electron laser (FEL) of UVSOR-II [3].

Circular dichroism (CD) spectroscopy can detect optical activity emergence with a high accuracy because CD spectra sensitively reflects the steric structures of chiral molecules. The theoretical calculation of CD spectrum of L-alanine molecule has revealed that the absorption bands of carboxyl and amino groups are derived from electronic transitions (n-π*, π-π*, n-σ*) corresponding to wavelengths below 230 nm (Fig.1) [4]. It is suggested that optical activity emergence by asymmetric photochemical reactions depends on the photon energy of CPL.

We carried out irradiation experiments by using CPL with different wavelengths to investigate the photon energy dependence of photochemical chiral reactions. We formed thin solid films of racemic mixture of alanine on quartz substrates from crystal powders of DL-alanine by using a thermal-crucible vacuum-evaporation system. Sublimation temperature was controlled in the range of 150~200°C and pressure of the vacuum chamber was approximately $5x10^{-2}$ Pa throughout the evaporation process. The CD spectra of thin solid films just after the deposition were measured from 260 to 160 nm in wavelength using a vacuum-ultraviolet CD beam line BL-12 of HiSOR and confirmed to be mostly zero CD before the irradiation, showing that the spurious CD due to the contamination of film surface were negligible.

The thin solid films of DL-alanine were irradiated with CPL in different wavelengths using the undulator beamline BL1U of UVSOR-III. In case of CPL irradiation in shorter wavelengths than 200 nm, the samples were set in a vacuum sample chamber preventing attenuation by air absorption. On the beam entrance side of the vacuum sample chamber, a gate valve with an MgF_2 vacuum sealing window was mounted. The irradiated CPL wavelengths were 180 and 155 nm corresponding to absorption bands of alanine molecule. The irradiated photon energy dose was measured with photoelectron current of a silicon photodiode (International Radiation Detectors, Inc.) settled at the sample position.

CD spectra of the CPL irradiated films were measured at BL-12 of HiSOR to clarify the optical activity emergence by CPL irradiation. In order to delete the effects of linear dichroism (LD) and/or linear birefringence (LB) components, the CD spectra were calibrated by measuring the dependence on sample rotation angle (0, 45, 90, and 135 degrees). As the results, the dependence of the CD spectra on the irradiated wavelength and also on the polarization (left- or right-handed) of CPL have been clearly observed (Fig.1) [5,6]. Detailed analysis of CD spectra is in progress to clarify full mechanism of the optical activity emergence, which potentially has relevance to the origin of terrestrial bioorganic homochirality stimulated by CPL.

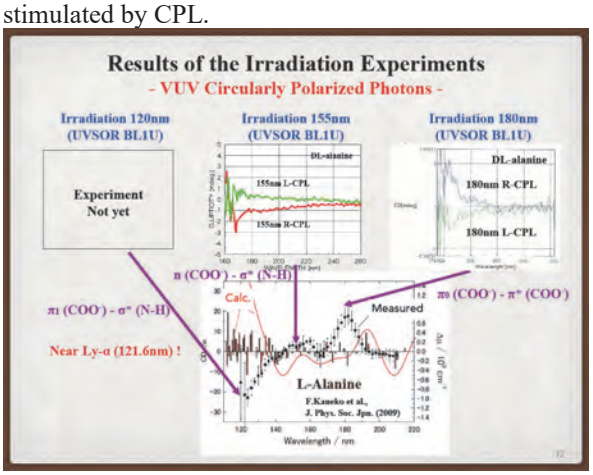


Fig. 1. CD spectra of DL-alanine film after left (L)- or right (R)-handed CPL irradiation.

[1]W. A. Bonner, Orig. Life Evol. Biosph. **21** (1991) 407.
[2] J. Takahashi *et al.*, Symmetry **11** (2019) 919.
[3] J. Takahashi *et al.*, Int. J. Mol. Sci. **10** (2009) 3044.
[4]F. Kaneko *et al.*, J. Phys. Soc. Jpn. **78** (2009) 013001.
[5] J. Takahashi *et al.*, UVSOR Activity Report 2018 **46** (2019) 156.
[6] J. Takahashi *et al.*, Proc. The 23rd Hiroshima Int. Symp. on Synchrotron Radiation (2019) 55.

BL1U

Laser Compton Scattering Gamma-ray Generation for Nonlinear Effect in QED

T. Hayakawa[1,2], K. Kawase[1], T Shizuma[1], J. K. Koga[3], H. Zen[4], T. Kii[4], H. Ohgaki[4], M. Fujimoto[5] and M. Katoh[5]

[1]*Tokai Quantum Beam Science Research Center, National Institutes for Quantum and Radiological Science and Applications, Tokai 319-1106, Japan*

[2]*National Astronomical Observatory of Japan, Mitaka 181-8588, Japan*

[3]*Kansai Photon Science Institute, National Institutes for Quantum and Radiological Science and Applications, Kizugawa 619-0215, Japan*

[4]*Institute of Advanced Energy, Kyoto University, Uji 611-0011, Japan*

[5]*Institute for Molecular Science, National Institutes of Natural Sciences, Okazaki 444-8585, Japan*

QED predicted unresolved nonlinear effects such as photon-photon interactions. However, because their cross sections are extremely small, the interactions have not been well experimentally measured [1,2]. Delbrück scattering, in which a gamma-ray interacting with a Coulomb field creates an electron-position pair, which subsequently annihilates to generate a gamma-ray whose energy is almost identical with the incident gamma-ray, is one of important phenomena to study nonlinear effects by QED and vacuum polarization. Koga and Hayakawa [3] have presented that it is possible to measure selectively the amplitude of Delbrück scattering using linearly polarized gamma-ray beams. Furthermore, if one uses a linearly polarized beam with energies lower than 1.022 MeV, which is the threshold of the pair creation, it is possible to measure only the virtual process of Delbrück Scattering, namely vacuum polarization.

For such a purpose, we have developed a laser Compton scattering (LCS) gamma-ray beam with a CO_2 laser having a wavelength of 10.6 μm at the BL1U beamline in UVSOR-III, where the energy of the electron beam stored in top-up mode is approximately 750 MeV. We have demonstrated the 1-MeV LCS gamma-ray beam generation using a randomly polarized CO_2 laser [4].

We newly installed a high power linearly polarized CO_2 laser in order to generate linearly polarized LCS gamma-ray beam. The maximum power of the laser is 130 W. We measured the energy spectra of the generated LCS gamma-ray beam using 3.5” × 4” $LaBr_3$(Ce) scintillation detector, and the energy spectra of the photon scattered from a tin or tungsten target with a diameter of 5 mm and a length of 50 mm using two high-purity Ge detectors (see Fig. 1). Figure 2 shows a typical measured energy spectrum. The Compton scattering from the target is clearly observed in the energy region of 400-600 keV. The gamma-ray from natural backgrounds are also observed.

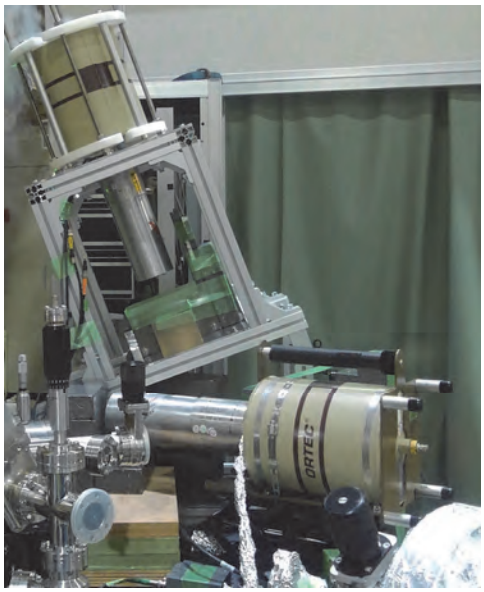


Fig. 1. Photo of the two high-purity Ge detectors at the BL1U beamline.

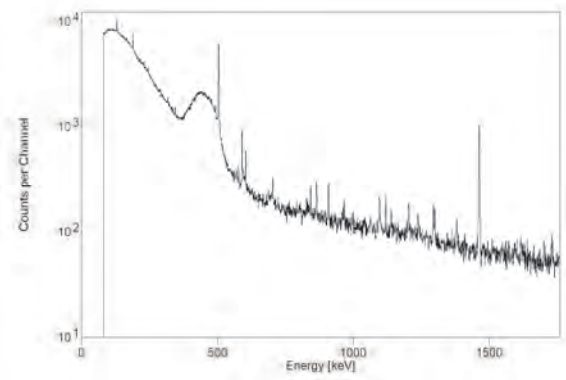


Fig. 2. Typical spectrum of scattered photons from the target, measured by the Ge detector.

[1] ATLAS Collaboration, Nat. Phys. **13** (2017) 852.
[2] T. Inada *et al*. Phys. Lett. B **732** (2014) 356 .
[3] J. K. Koga and T. Hayakawa, Phys. Rev. Lett. **118** (2017) 204801.
[4] H. Zen *et al.*, J. Phys.: Conf. Ser. **1067** (2018) 092003.

BL3U

X-ray Absorption Spectra of Lipid Molecules in Bilayer Membranes Measured in Aqueous Solution

R. Tero[1], W.-Z. Goh[1] and M. Nagasaka[2]
[1]*Toyohashi University of Technology, Toyohashi, 441-8580, Japan*
[2]*Institute for Molecular Science, Okazaki 444-8585, Japan*

The lipid bilayer is a self-assembled structure of amphiphilic lipid molecules, and is the fundamental structure of biomembranes such as cell membranes. Internal structures of lipid bilayers, e.g. two dimensional domains and hydrophobic thickness, and physical properties affect the transportation of materials, information and energy through the biomembranes. All these physiological reactions proceeds in the presence of ions. Ions in the aqueous solution significantly influence to these structures and properties of lipid bilayers. Phosphatidylcholine (PC) (Fig. 1 (a)) is the major component of eukaryotic cells. Cations bind to the phosphate and carbonyl groups of PC. However, affinity of cations to PC, and also other lipids, are still controversy especially in the fields of theoretical simulations [1]. We aim to determine the binding affinity of cations to lipids in aqueous solutions experimentally, by means of X-ray absorption spectroscopy (XAS) [2,3].

We prepared vesicle suspensions of dioleoyl-PC (DOPC) (Fig. 1 (a)), dioctadecenyl-PC (dietherPC) (Fig. 1 (b)), and digalactosyldiacylglycerol (DGDG) (Fig. 1 (c)) in a buffer solution. We introduced the suspension into the XAS flow cell consisting of Si_3N_4 membranes, to form planar lipid bilayers on the Si_3N_4 surface through the process of vesicle fusion method [3]. Fluorescence microscope imaging and fluorescence recovery after photobleaching method showed that DOPC, dietherPC, and DGDG bilayers fully covered the Si_3N_4 membrane surface.

Figure 2 shows O K-edge spectra of the planar lipid bilayers, after subtracted the spectrum of the Si_3N_4 membrane before the lipid bilayer formation. DOPC, which has phosphate and carbonyl groups (Fig. 1 (a)), showed at least two components at 531.06 and 531.94 eV. To identify these components, we measured XAS spectra of dietherPC and DGDG, which have only phosphate group and carbonyl group, respectively (Fig. 2). DietherPC bilayer showed two components at 531.34 and 532.22 eV. We attributed them to $1s \rightarrow \pi^*$ transitions of P=O and P-O-Na, respectively, on the basis of inner shell calculation. DGDG bilayer had dominant peak at 532.02 eV. Therefore, the DOPC component at 531.06 eV is attributed to P=O, and that at 531.94 eV to overlapping P-O-Na and C=O.

In conclusion, we obtained XAS spectra of lipid bilayers in an aqueous solution, and identified the components in the spectra. We expect these XAS spectrum components provide information of the effects of cation species and concentration on lipid bilayers.

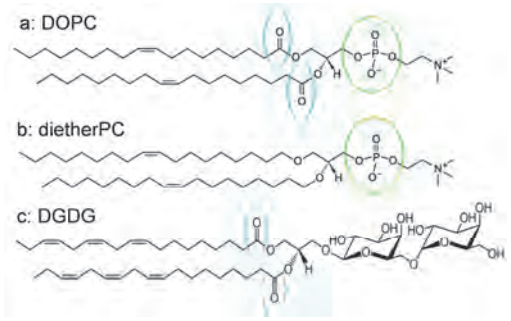


Fig. 1. (a) Dioleoylphosphatidylcholine, (b) dioctadecenylphosphatidylcholine, and (c) digalactosyldiacylglycerol.

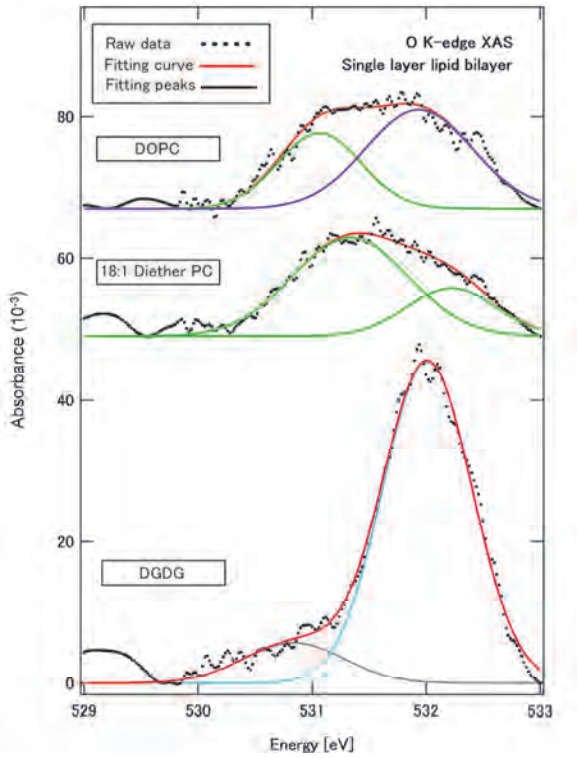


Fig. 2. O K-edge spectra of (a) DOPC, (b) dietherPC, and (c) DGDG bilayers.

[1] T. B. Woolf, Biophys. J. **104** (2013) 746.
[2] M. Nagasaka, H. Yuzawa, T. Horigome and N. Kosugi, J. Electron Spectros. Relat. Phenomena **224** (2018) 93.
[3] R. Tero, S. Nakamura, Y. Sano and M. Nagasaka, UVSOR Activity Report 2018 **46** (2019) 158.

BL4U

P-$L_{2,3}$ Absorption Spectra of Phosphates in Plasmid DNA and Adenosine Compounds

T. Ejima[1], T. Ohigashi[2] and S. Tone[3]
[1]*IMRAM, Tohoku University, Sendai 980-8577, Japan*
[2] *UVSOR Synchrotron Facility, Institute for Molecular Science, Okazaki 444-8585, Japan*
[3]*Sch. of Sci & Technol., Tokyo Denki University, Hatoyama 350-0394, Japan*

DNA is composed of simpler monomeric units called nucleotides. The nucleotides are joined to one another in a chain by covalent bonds between the sugar of one nucleotide and the phosphate of the next, resulting in an alternating sugar-phosphate backbone. The phosphate PO_4^{3-} forms ideally a tetrahedral structure in which four oxygen atoms coordinate equidistantly from a center P atom.

The NEXAFS spectrum of the P-K absorption edge in DNA is similar to those of aqueous phosphate (H_2PO_4), biological solids, and animal manures [1,2]. This similarity will be originated from the stable tetrahedral-structure of the phosphate PO_4^{3-}. On the other hand, the spectral differences among the phosphate compounds at the P-$L_{2,3}$ absorption edges are remarkable even though the energy positions of the P-L_2 and P-L_3 edges are close to each other [3]. Therefore, it seems natural to focus on P-$L_{2,3}$ absorption edges when shapes and positions of DNA are observed using an X-ray microscope, which is expected to have a high spatial resolution because of the shortness of the observation wavelength [4]. In this study, we focused on the P-$L_{2,3}$ absorption edges (~135 eV) and acquired absorption spectra for the visualization of DNA using the P absorption edges.

Two Adenosine compounds and two DNA were measured: adenosine phosphate (AMP), adenylyl- (5'-3')-adenylyl- (5'-3')-adenosine (AAA), plasmid DNA with a circular structure, and plasmid DNA with a fibrous structure.

The obtained spectra are shown in Figs. 1 and 2. Peak structures are indicated from A to G in the figures and each peak exists at almost the same photon energy positions. The difference among the spectra appears mainly at the peak E.

The density of states of AMP and AAA were calculated to understand the origin of the spectral difference, and the results showed that the P 3d states of AMP and AAA are mainly hybridized with P 3s states and located at around the energy position of peak E. Hence the similarity of the spectral structures between the figures may suggest that the difference of the peak E will be interpreted as the P 3d states difference between the DNAs. Further calculation reflecting the structural difference between the DNAs is necessary for the interpretation of the spectral difference in DNAs.

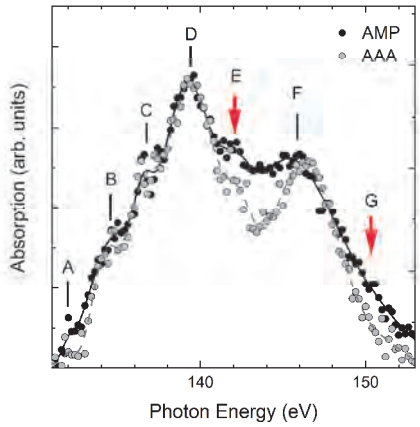


Fig. 1. P-$L_{2,3}$ XAS spectrum of AMP and AAA. Dots represent the measurement results, solid and broken curves are smoothed data.

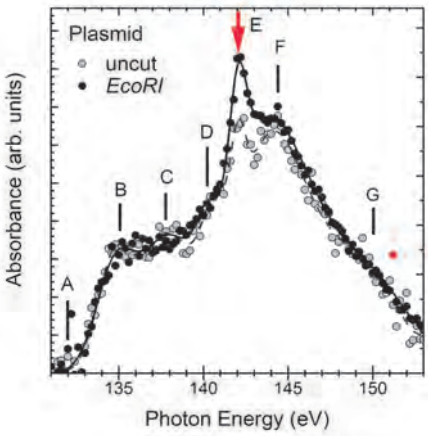


Fig. 2. P-$L_{2,3}$ XAS spectrum of plasmid DNA that air-dried as it is ("uncut"), and that cleaved with EcoRI and air-dried ("EcoRI").

[1] A. Ito, K. Shinohara, Y. Mizukami, H. Nakano, K. Yada, T. Uehara and T. Honda, J. Synchrotron Rad. **5** (1998) 1099.
[2] A. L. Shober, D. L. Hesterberg, J. T. Sims and S. Gardner, J. Environ. Qual. **35** (2006) 1983.
[3] J. Kruse, P. Leinweber, K.-U. Eckhardt, F. Godlinski, Y. Huc and L. Zuinc, J. Synchrotron Rad. **16** (2009) 247.
[4] D. Attwood and A. Sakdinawat, "X-rays and Extreme Ultraviolet Radiation" (Cambridge Univ. Press, 2016, Cambridge, UK) Chap. 11.
[5] W. R. Hunter, "Vacuum Ultraviolet Spectroscopy" (ed. by J. A. Samson and D. L. Ederer, Academic Press, 2000, San Diego, USA) Chap. 11.

BL4U

STXM/XANES Analysis of a Carbonaceous Chondrite Lithology in the Almahata Sitta Meteorite

Y. Kebukawa[1], T. Ohigashi[2] and M. E. Zolensky[3]
[1]*Faculty of Engineering, Yokohama National University, Yokohama 240-8501, Japan*
[2]*UVSOR Synchrotron Facility, Institute for Molecular Science, Okazaki 444-8585, Japan*
[3]*ARES, NASA Johnson Space Center, Houston, TX 77058, USA*

The Almahata Sitta (AhS) meteorite is a brecciated, polymict ureilite that has originated from the near-earth asteroid 2008 TC3 which is classified as an F-type asteroid (a subtype of C complex asteroids) [1]. Carbonaceous chondritic lithologies AhS 671 and AhS 91/91A are known to consist of aqueously altered mineralogy such as phyllosilicates, bruennerite, dolomite, magnetite, fayalite, ilmenite, phosphates, pyrrhotite, and pentlandite, and have similarities to CI1 chondrites, but shows evidence of heterogeneous thermal metamorphism [2]. The textures of AhS 91A and AhS 671 support formation of 2008 TC3 in a regolith environment, and could represent a volume of regolith formed when a carbonaceous chondrite-like body impacted into ureilitic body [2]. Although ureilites usually contain no or little organic matter, it is highly possible that the CI1 lithologies of AhS contain abundant organics as in the case of CI1 chondrites (e.g., Orgueil and Ivuna). To understand the nature of organic matter in CI1 lithologies, and similarity and relationships to primitive carbonaceous chondrites, we analyzed AhS 91A using the scanning transmission X-ray microscope (STXM) at BL4U.

A 100 nm-thick section from AhS 91A was prepared using a focused ion beam equipment at NASA-JSC. C, N, O, Fe-X-ray absorption near-edge structure (XANES) spectra of the sections were obtained using the STXM on BL4U at the UVSOR.

First, we obtained a C-map of the AhS 91A FIB section to locate organic matter. Carbonaceous compounds were distributed partially in the FIB section in sub-micrometer scale (Fig. 1 (a)). Then, "energy stacks" were obtained at C-rich areas. Selected C-XANES spectra generated from the energy stacks are shown in Fig. 1 (b). The C-XANES spectra of the organic-rich regions show large peaks at 284.8 eV due to aromatic carbon, smaller peaks at 286.3 eV and 288.4 eV due to C=O and C(=O)O groups, respectively.

These futures are often observed in aqueously altered carbonaceous chondrites (CI, CM, and CR chondrites), with some differences in the intensity ratios of these peaks [e.g., 3]. Some areas are rich in carbonate which is characterized by a large peak at 290.4 eV. There is no 1s-σ* exciton peak at 291.7 eV of graphene structures that is characteristic of thermally metamorphosed chondrites [4]. The molecular structures of organics as well as carbonates, support that the AhS 91A is originated from a aqueously altered carbonaceous chondrite-like parent body [2]. Although some heterogeneous thermal metamorphism are observed in the AhS 91A, the analyzed region of the AhS 91A has not experienced significant heating events.

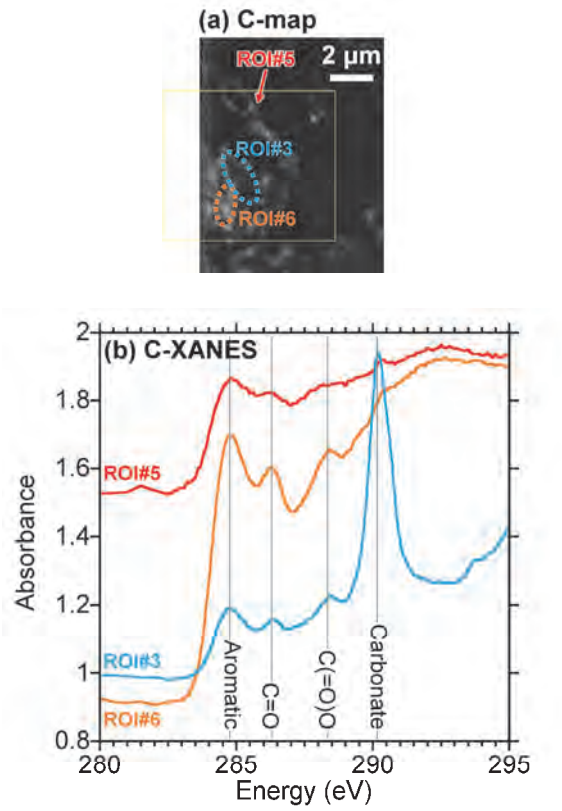


Fig. 1. (a) C-map and (b) C-XANES spectra of the selected regions in the FIB section of AhS 91A.

[1] P. Jenniskens *et al*., Nature **458** (2009) 485.
[2] C. A. Goodrich *et al*., Meteoritics & Planet. Sci. **54** (2019) 2769.
[3] C. Le Guillou *et al*., Geochim. Cosmochim. Acta **131** (2014) 368.
[4] G. D. Cody *et al*., Earth Planet. Sci. Lett. **272** (2008) 446.

BL4U

Trial of Molecular Mapping for Thin Sections of Isolated Mammalian Nuclei Embedded in Resin Using STXM

A. Ito[1], K. Shinohara[2], A. Matsuura[3], S. Toné[4], H. Yuzawa[5] and T. Ohigashi[5,6]
[1]*School of Engineering, Tokai University, Hiratsuka 259-1292, Japan*
[2]*Graduate School of Health Sciences, Fujita Health University, Toyoake 470-1192, Japan*
[3]*Research Integrity Office, Fujita Health University, Toyoake 470-1192, Japan*
[4]*School of Science and Engineering, Tokyo Denki University, Hatoyama 350-0394, Japan*
[5]*UVSOR Synchrotron Facility, Institute for Molecular Science, Okazaki 444-8585, Japan*
[6]*School of Physical Sciences, The Graduate University for Advanced Studies, SOKENDAI, Okazaki 444-8585, Japan*

Spectromicroscopy using scanning transmission X-ray microscope (STXM) has been widely accepted as a useful tool to visualize molecular distribution in specimens. Using STXM installed at BL4U of UVSOR, we have been developing an image processing procedure for the quantitative mapping of biomolecules, and successfully applied to the distribution of nucleic acids (DNA and RNA) and proteins such as histone and bovine serum albumin (BSA) in biological specimens using combined NEXAFS at the C, N and O-K absorption edges [1-3]. At present, it is difficult to obtain reliable results for thick specimens such as nucleus area in a whole mammalian cell or an isolated nucleus, due to insufficient transmitted photons through the specimens [3].

Sectioning of a specimen with a thickness as thin as the submicron level is one possible way to cope with such problem. Usually thin sections are made with a microtome for resin embedded specimens. In the present study, we tried to study the thin section of nucleus embedded in organic resin.

Isolated nuclei from human HeLa S3 cells were embedded in Quetol-812 epoxy resin with curing agents, DDSA (dodecenyl succinic anhydride) and MNA (methyl nadic anhydride), and a curing promoter DMP-30 (2,4,6-tri(dimethylaminomethyl) phenol) (Nissin EM Co., Ltd., Japan). The section of the resin was made to a thickness of 0.5 μm, and attached on an address mesh (HF-15, Nissin EM) supported with collodion film.

We applied our method to calculate the distributions of nucleic acids and proteins [3] to the observed data for the section specimens. Figure 1 shows the X-ray image of the isolated nucleus at 294 eV (panel a), and composite image of DNA, RNA and histone displayed with different colors (panel b). Contrary to our expectation to be DNA, the main component in the nucleus was found to be RNA. The cause was suspected to be on an analytical process probably due to that the major contribution to the absorbed data was resin.

To improve this situation, we made assumption that images for residual data (spect3) are mainly composed of resin. We generate energy stack file for resin from the spect3 and subtracted it from the original data at the first step of analysis. Our calculation procedure was applied to the thus-obtained stack file. The results are shown in Figure 2. Three colors, red, green and blue, are given to DNA, RNA and histone for panel a, DNA, RNA and BSA for panel b, and DNA, histone and BSA for panel c, respectively. DNA was found to the major component in a nucleus, which was in accord with our previous observations for a chromosome [1], and a whole cell [2]. Further analysis is planned to apply to isolated nuclei which undergo apoptosis.

We thank Prof. K. Tohya of Kansai University of Health Sciences for his kind help with making thin sections.

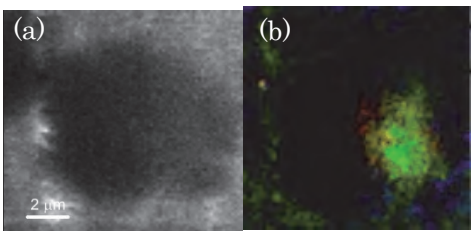


Fig. 1. Isolated nucleus of human HeLa S3 cell. (a) X-ray image at 294 eV, (b) molecular distribution in the nucleus. Red: DNA, Green: RNA, Blue: histone.

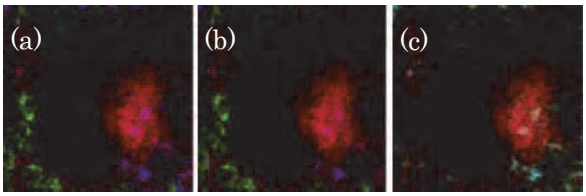


Fig. 2. Improved molecular distribution in the isolated nucleus. (a) DNA (Red), RNA (Green), histone (Blue), (b) DNA (R), RNA (G), BSA (B), (c) DNA (R), histone (G), BSA (B)

[1] K. Shinohara *et al.*, Ultramicrosc. **194** (2018) 1.
[2] K. Shinohara *et al.*, J. X-Ray Sci. Technol. **26** (2018) 877.
[3] K. Shinohara *et al.*, Cells **8** (2019) 8.

BL4U

In situ Analysis for Structure Change of Extraterrestrial Organic Materials During Heating

M. Uesugi[1], M. Ito[2], K. Tomioka[2], Y. Kodama[3], T. Ohigashi[4,5], H. Yuzawa[4], K. Uesugi[1], A. Yamaguchi[6], N. Imae[6], Y. Karouji[7], N. Shirai[8], T. Yada[9] and M. Abe[9]

[1]*Japan synchrotron radiation research institute (JASRI/SPring-8), Say-cho 679-5198, Japan*
[2]*Kochi Institute for Core Sample Research, Japan Agency for Marine-Earth Science Technology (JAMSTEC), Nankoku 783-8502, Japan*
[3]*Marine Works Japan Ltd., Yokosuka 237-0063, Japan*
[4]*UVSOR Synchrotron Facility, Institute for Molecular Science, Okazaki 444-8585, Japan*
[5]*School of Physical Sciences, The Graduate University for Advanced Studies, SOKENDAI, Okazaki 444-8585, Japan*
[6]*Antarctic Meteorite Research Center, National Institute of Polar Research, Tachikawa 190-8518, Japan*
[7]*JAXA Space Exploration Center, Japan Aerospace Exploration Agency (JAXA), Sagamihara 252-5210, Japan*
[8]*Department of Chemistry, Graduate School of Science, Tokyo Metropolitan University, Hachioji 192-0397, Japan*
[9]*Institute of Space and Astronautical Science, Japan Aerospace Exploration Agency (JAXA), Sagamihara 252-5210, Japan*

Organic compounds in extraterrestrial materials are thought to be one of the important components for the building block of the Earth, especially for the origin of life. Those organic materials would be transported to the Earth mostly by micrometeorites, because previous studies suggested that the flux of micrometeorites falling to the Earth is much larger than that of meteorites (5.38×10^4 kg/y for meteorites and 4×10^7 kg/yr for micrometeorites) [1,2]. In addition, micrometeorites show distinct features that their chemical compositions are rather similar to carbonaceous chondrites than any other meteorites [3]. It is well known that most micrometeorites are heated up to 2000 ºC during the atmospheric entry, due to atmospheric drag heating. During such intense heating under the oxidized condition, organic compounds would be modified and/or destructed. It is important to evaluate the effect of heating of organic compounds during the atmospheric entry, to investigate origin and evolution of terrestrial organics.

We found that a number of organic nano-globules survived in the Antarctic micrometeorites (AMMs) larger than 150 μm. These AMMs would have experienced intense heating during atmospheric entry due to large moments of inertia, in previous studies [4]. Numerical calculations showed that such AMMs would have heated higher than 1000 ºC, and also showed that ram pressure during the heating is almost equivalent to 1 atm.

In order to investigate the possibility of survival of organic matters during heating, we conducted heating experiments of carbonaceous meteorites at 1 atm with 600 ºC in atmosphere and 400 ºC in N_2 environment, and evaluate the effect on the organic materials using scanning transmission x-ray microscopy and near edge x-ray absorption fine structure (STXM-NEXAFS) analysis. The results of our experiments showed that organic materials were easily destructed and disappeared in oxidized condition, while organics became graphitic and did not disappear during heating in N_2 environment.

The results indicate that organic materials in meteorites would not be destructed by heating in the interplanetary space, because there are less oxygen and water vapor. The organic materials would survive from the heating by irradiation of sunlight, during the transportation from their parent body to the Earth. On the other hand, the organic materials would be easily damaged during the atmospheric entry because of highly oxidized atmosphere.

Survival of organic materials in AMMs suggests that incident velocities of the precursor meteorites are quite low, less around 1 km/s, and/or, their original size is much larger than 1 cm and they would be destructed into smaller pieces during the atmospheric entry. Then unheated materials inside the meteorites can form unheated AMMs.

[1] Yada T. *et al*., Earth Planet Space **56** (2004) 67.
[2] Zolensky M. *et al*., Flux of extraterrestrial materials, in Meteorites and the early solar system II (2006) 869.
[3] Imae N. *et al*., Geochim. Cosmochim. Acta **100** (2013) 116.
[4] Uesugi *et al*., Preparation for the analysis of Hayabusa2 returned samples JpGU meeting, abstract (2019).

BL4U

The Behavior of Sulfur in the Past Martian Surface Water Based on STXM-XANES Analysis of Nakhlite Y 000593

H. Suga[1,2], K. Suzuki[2], T. Ohigashi[3,4], H. Yuzawa[3,4], Y. Takeichi[5], A. Yamaguchi[6], T. Usui[7], Y. Takahashi[2] and M. Miyahara[8]

[1]*Japan Synchrotron Radiation Research Institute (JASRI/SPring-8), Sayo 679-5198, Japan*
[2]*The University of Tokyo, Tokyo 113-0033, Japan*
[3]*UVSOR Synchrotron Facility, Institute for Molecular Science, Okazaki 444-8585, Japan*
[4]*The Graduate University for Advanced Studies, SOKENDAI, Okazaki 444-8585, Japan*
[5]*High-Energy Accelerator Research Organization (KEK), Tsukuba 305-0801, Japan*
[6]*National Institute of Polar Research, Tachikawa 190-8518, Japan*
[7]*Japan Aerospace Exploration Agency (JAXA), Sagamihara 252-5210, Japan*
[8]*Hiroshima University, Higashi-Hiroshima 739-8526, Japan*

Nakhlites are intriguing Martian meteorites because they have various secondary minerals formed by water-rock reactions on Mars [1]. The species, assemblages, and chemical compositions of the secondary minerals record the physicochemical properties such as temperature and pH-Eh when the reactions occurred. Hence, the detailed understanding of the secondary minerals allows us to give a new constraint on the physicochemical evolution of the surface water on Mars.

The formation processes of the secondary minerals in nakhlites are enigmatic because carbonate and sulfate minerals coexist in some nakhlites [1-3]: the former precipitates under reductive alkaline condition, the latter under oxidative acidic condition. We examined the sulfide and sulfate minerals in the petrologic thin section of nakhlite Y 000593 (#58-1 stored in NIPR) by FE-SEM-EDS/FE-EPMA at the University of Tokyo, μ-XRF-XAFS at BL-15A of Photon Factory, and STXM-XANES at BL4U of UVSOR to elucidate the formation process of the sulfate minerals.

Y 000593 consisted mainly of olivine phenocryst and mesostasis (clinopyroxene, plagioclase, and FeS). Elemental mapping by EPMA showed that a trace amount of sulfur (S) distributed in the carbonate minerals occurring in the fractures of the olivine grains. μ-XRF-XAFS analysis detected the existence of SO_4 in the carbonate minerals. The abundance of S decreased from the rim to the center of the olivine grains. As for the origin of the SO_4 (or sulfate minerals), the only one S-containing mineral in Y 000593 FeS is the candidate.

FE-SEM-EPMA analysis revealed that most of the FeS minerals in the mesostasis of Y 000593 was partly altered. Hence, the oxidation state of the S in the FeS minerals of the mesostasis was measured by μ-XRF-XAFS. The altered portions of the FeS minerals were mainly composed of $FeSO_4$.

We tried to clarify the dissolution path of SO_4^{2-} from the FeS minerals to the surrounding minerals (finally, into the fractures of the olivine grains) by FIB-STXM. We made the ultrathin section including the partly altered FeS minerals by FIB for the STXM analysis. STXM Fe- and S L-edge XANES analysis revealed that the sulfates dissolved from the FeS minerals into the surrounding minerals (Fig. 1).

These results indicate that the origin of SO_4 in the carbonate minerals is the SO_4^{2-} dissolved from the FeS minerals. The chemical reaction formula could be expressed as follows (as a simplified model):

$$FeS + 5/2H_2O + 3/2O_2 + 1/3K^+ \rightarrow 1/3KFe_3(SO_4)_2(OH)_6 + H^+ + 1/3SO_4^{2-}$$

FeS is easily oxidized by liquid water and becomes sulfate mineral jarosite [$KFe_3(SO_4)_2(OH)_6$]. Also, this reaction makes sulfate-bearing acid fluid, which decreases the pH. The SO_4^{2-}(and/or jarosite) formed by this reaction should be also the origin of the SO_4 preserved in the carbonate minerals. Carbonate can be easily dissolved by acid fluid. Therefore, we expect that the sulfate minerals in Y 000593 have occurred before the formation of the carbonate minerals as a vein filling precursor.

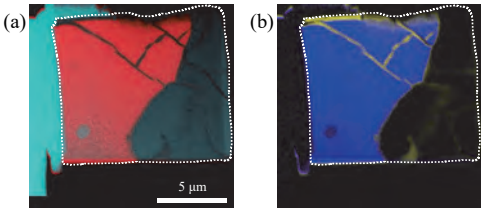


Fig. 1. FIB section scanned by STXM (white dashed line). (a) The red and dark green portions are FeS mineral and plagioclase, respectively. (b) The blue and yellow portions are FeS and $FeSO_4$, respectively. Fe^{3+} and SO_4^{2-} dissolved from FeS mineral move into the fractures of plagioclase.

[1] L. M. White *et al.*, Astrobiology **14** (2014) 170.
[2] T. Noguchi *et al.*, JGR **144** (2009) E10004.
[3] T. Tomkinson *et al.*, Nat. Commun. **4** (2013) 2662.

BL4U

Control of Drug Dermal Penetration: Quantitative Probing of Rapamycin

G. Germer[1], T. Ohigashi[2], H. Yuzawa[2], R. Flesch[1], F. Rancan[3], A. Vogt[3] and E. Rühl[1]
[1]*Physical Chemistry, Freie Universität Berlin, Arnimallee 22, 14195 Berlin, Germany*
[2]*UVSOR Synchrotron Facility, Institute for Molecular Science, Okazaki 444-8585, Japan*
[3]*Charité-Universitätsmedizin, 10117 Berlin, Germany*

Progress in quantitative probing of topical drug delivery is reported, which goes beyond our previous work performed at UVSOR III [1,2]. Briefly, hyperspectral imaging of dermal drug penetration is investigated using scanning transmission X-ray microscopy (STXM). The experiments were performed at the BL4U beamline of UVSOR III. They mostly rely on scanning of the photon energy in the O 1s regime (520 – 560 eV), allowing for the acquisition of stacks of images by concentrating on the stratum corneum, the top horny layer of skin. High spatial resolution, corresponding to pixel sizes of 50 nm, allows us to generate in this heterogeneous target reliably reference spectra of the crucial species contained in fixed human skin, especially the topically applied drug rapamycin ($C_{51}H_{79}NO_{13}$, M=914.13 g/mol), as well as identification of different skin regions, i.e. corneocytes, lipid layers between the corneocytes, and the fixation medium EPON. Data reduction is performed by using a linear combination of these site-dependently varying contributions, similar to previous work [3]. This yields the local composition of each component. The absolute absorption cross section of the drug is used to determine quantitatively its local concentration and the relation to the dermatologically relevant skin treatment conditions.

Characteristic results are summarized in Fig. 1, which are part of systematic studies. Figure 1 (a) shows the stratum corneum of untreated skin, whereas Fig. 1 (b) shows skin that has been treated for 24 h by 0.1% rapamycin in petroleum jelly. The optical density (OD) recorded at 532 eV is shown in the maps labeled A (top plots in Figs. 1 (a), (b)), clearly indicating the stratified structure of the stratum corneum. The data analysis shown in B clearly distinguishes corneocytes (Cor) (white) from lipids between the corneocytes (Lip) (black), and the viable epidermis (VE) (grey). The maps labeled C show the drug distribution with a clear enhancement, if rapamycin is topically applied (see Fig. 1 (b)). In D the drug concentration is integrated over the maps shown in C as a function of depth, yielding absolute concentrations given in fmol/μm^3, corresponding to a local maximum in drug concentration of ~270 fg/μm^3. The reference skin shown in Fig. 1 (a) indicates that no drug is found, but the error bars are sizable due to the data reduction procedure. The sample containing the topically applied drug in petroleum jelly indicates that there are distinct variations in local drug concentration due to the stratified structure of the stratum corneum, where local minima occur in the lipid matrix. This is unexpected for non-polar drugs, such as rapamycin, which are expected to occur primarily in the lipid layers [1]. Clearly, drug penetration is enhanced by occlusion due to the use of petroleum jelly for formulating the drug. Evidently, this also leads to the uptake of rapamycin into the corneocytes, so that an almost continuous drug distribution is observed in the stratum corneum. There is a characteristic drop in drug concentration near the border to the stratum granulosum, the top layer of the viable epidermis, marked by grey color (see Fig. 1 (b)). This hints that the tight junction barrier is intact so that the drug cannot penetrate efficiently into the viable epidermis.

Systematic studies involving the primary treatment of skin with serine protease for simulating the impact of inflammations have been performed and are currently in preparation for publication [4].

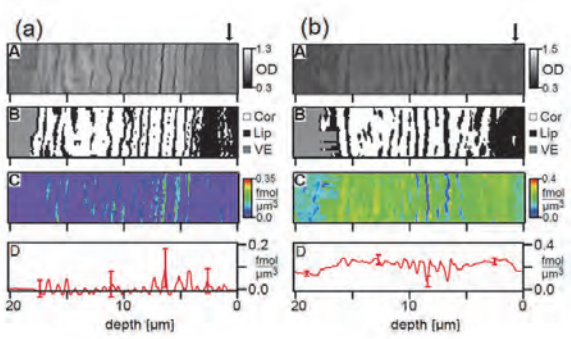


Fig. 1. Results from STXM of the top skin layers of fixed human skin: (a) untreated reference skin and (b) skin treated by rapamycin in petroleum jelly. A: optical density at 532 eV; B: assignment of skin regions due to X-ray absorption characteristics; C: local rapamycin concentration; D: integrated drug concentration as a function of depth. The skin surface is marked by an arrow. See text for further details.

[1] K. Yamamoto *et al.*, Anal. Chem. **87** (2015) 6173.
Eur. J. Pharm. Biopharm. **118** (2017) 30.
Eur. J. Pharm. Biopharm. **139** (2019) 68.
[2] G. Germer *et al.*, UVSOR Activity Report 2018 **46** (2019) 165.
[3] I. N. Koprinarov *et al.*, J. Phys. Chem B **106** (2002) 5358.
[4] G. Germer *et al.*, in preparation (2020).

BL4U

Chemical Mapping of Potassium-containing Particles from Residential Biomass Burning and in Ambient Air

X. Kong[1], M. Priestley[1], Z. Wu[2], T. Ohigashi[3], H. Yuzawa[3], J. B. C. Pettersson[1] and M. Hallquist[1]

[1]*Department of Chemistry and Molecular Biology, University of Gothenburg, 412 96 Gothenburg, Sweden*
[2]*State Key Joint Laboratory of Environmental Simulation and Pollution Control, College of Environmental Sciences and Engineering, Peking University, 100871, China*
[3]*UVSOR Synchrotron Facility, Institute for Molecular Science, Okazaki 444-8585, Japan*

Burning of wood and other biomass fuels for energy purposes is common on the global scale. Potassium, as one of the main nutrient elements in plants, is released during the burning process and it has been considered as a tracer for biomass burning activities. Here we employed the STXM technique to visualize potassium-containing particles sampled under two circumstances. One is from a campaign at the Research Institutes of Sweden (RISE), where a small-scale wood stove was evaluated regarding its environmental and climate impacts. The other is from field measurements carried out in Beijing with a focus on aerosol properties in the urban environment. The STXM results presented in this study were obtained at the BL4U beamline at UVSOR.

At RISE, aerosol samples were collected from the exhaust line of a wood log burning stove. The major components are soot, organics and inorganic particles. Figure 1 shows the optical density (OD) of a large particle aggregate comprised primarily of a large soot structure with an organic coating that has potassium particles embedded on its surface. Figure 1e shows the difference of OD between the photo energy of (c) 295 eV and (d) 297 eV. The dark spots show the locations where the OD was dramatically enhanced at 297 eV, *i.e.* the potassium L_3-edge. The potassium salt particles seem to attach on the boundaries of the aggregate. Soot is formed in the furnace at high temperatures (> 1000 °C), but under these conditions both organic and potassium compounds are mainly in the gas phase. As temperature is reduced in the exhaust line, potassium compounds first nucleate to form potassium salt particles followed by nucleation and condensation of organics at lower temperatures. The formed potassium-containing particles may agglomerate with existing soot particles, and they are all coated by organics.

Figure 2 shows an OD image of various types of aerosol sampled in Beijing, with a photo energy of 300 eV. Several particles were examined in detail with one example shown here (red square). Full stack scans were performed on this particle at carbon K-edge (potassium L-edge), nitrogen K-edge and sulfur L-edge, respectively. Figures 2 (a)-(c) show the spectra of these three edges on both the core and coating of the particle. Potassium is found in the core region but not on the coatings. The coating mainly contains organic materials. As expected from the chemical complexity of actual atmospheric particles, all of the ammonium, nitrate [1] and sulphate [2] were found in the core of this single particle, indicating this is a well-aged and -mixed particle with an organic coating.

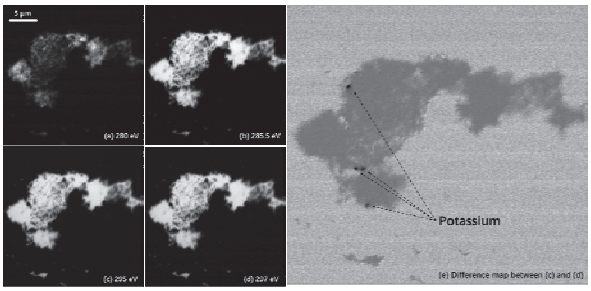


Fig. 1. Optical density of a particle aggregate. The used photo energies are: (a) 280 eV (pre-edge of carbon), (b) 285.5 eV (soot is emphasized), (c) 295 eV (total carbon is emphasized, and also as pre-edge of potassium), and (d) 297 eV (potassium is emphasized). (e) shows the difference between panel (c) and (d).

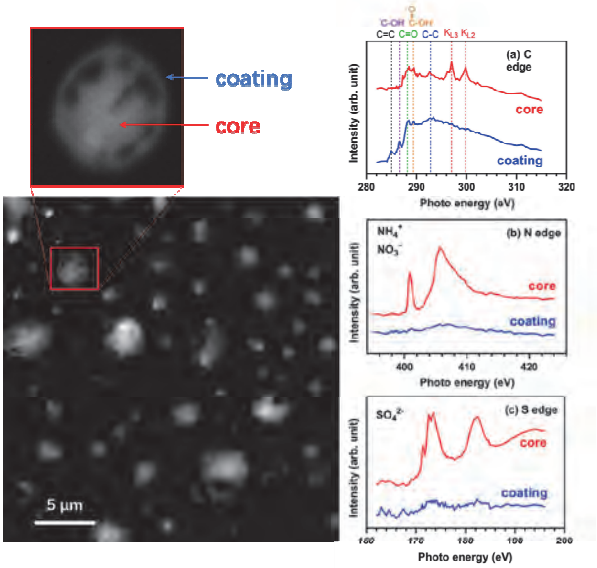


Fig. 2. OD image of urban particles sampled in Beijing. An example particle is scanned at (a) carbon K-edge, (b) nitrogen K-edge and (c) sulfur L-edge, respectively. The spectra measured at the core and on the border were differentiated in red and blue respectively.

[1] Török, S., *et al.*, Powder Diffr. **19** (2004) 81.
[2] Jalilehvand, F., Chem. Soc. Rev. **35** (2006) 1256.

BL4U

Sequestration of Boron in Sediments

Y. Hashimoto[1], K. Kobayashi[1], H. Suga[2] and Y. Takahashi[2]

[1]*Department of Bioapplications and Systems Engineering, Tokyo University of Agriculture and Technology, Koganei 184-8585, Japan*

[2]*Department of Earth and Planetary Science, The University of Tokyo, Tokyo 113-0033, Japan*

Boron (B) is ubiquitous in the environment, and major geogenic sources of B in water include desert, saline lake, and spring water. Because short-term and long-term oral exposures to B in animals lead to expressions of reproductive and developmental toxicity [1], the elevated levels of B in water supplies has long been a concern for public health. To lower the environmental risk of B contamination in water, chemical and engineering techniques for removing B from contaminated water have been developed based on physicochemical adsorption, coprecipitation, ion exchange, and reverse osmosis processes. However, the remaining issues for the current techniques in aqueous B removal reside in the inefficiency in cost for materials and reagents (e.g., resin and flocculation chemicals) and B removal capacity and kinetics. Numerous separation materials currently available for aqueous B treatments are less effective for the treatment of water with high levels of B. Therefore, there is an urgent need in the development of cost-effective methods for the treatment of (waste)water with high levels of dissolved B.

The concentrations of B are often high in discharged water from chemical industries and mining and hot spring areas. Boron in the aqueous environment was often found in minerals including calcite and Fe oxide minerals. Knowledge about how B occurs in the environment would help understand the mechanisms of B sequestration and can be used for developing technologies for wastewater with high B concentrations. We examined the distribution of B in sediment collected from a hot spring area with high B conditions using X-ray microscopy (STXM)-based

NEXAFS analyses at UVSOR BL4U. A thin section of sediment was prepared and analyzed for B on the surface.

STXM-based merged B images were obtained at the energy of 188 and 200 eV and their subtraction (Fig. 1). Framboidal pyrite (aspberry-like arrangements of pyrite grains) was found in the sediment and contained B with trigonal and tetrahedral coordination. The distribution of ^{III}B, ^{IV}B and their mixture occupied 4 %, 58 %, and 38 %, respectively. This result indicates that B in this hot spring area occurred mainly with ^{IV}B. Further investigation is needed to reveal the structure of B incorporation to framboidal pyrite.

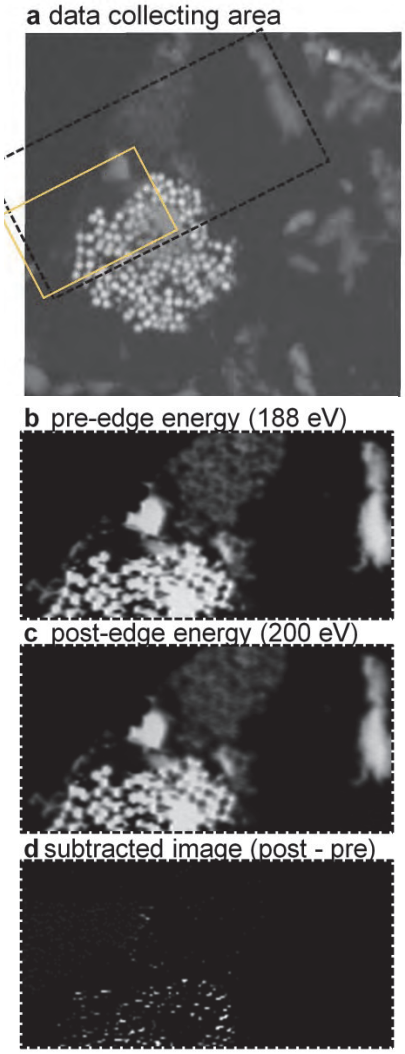


Fig. 1. The SEM image about data collecting area for STXM-based distribution map of boron (a), OD images of pre-edge energy (188 eV, b) and post-edge energy (200 eV, c), and boron distribution map subtracted counts of b from counts of c (d).

[1] WHO (World Health Organization), Guidelines for Drinking-water Quality: First Addendum to the Fourth Edition (2017).

BL4U

Preliminary Results by a STXM-XANES: Analysis of Small Carry-on Impactor Debris Operated by the Hayabusa2 Mission

M. Ito[1], Y. Takano[2], T. Ohigashi[3], H. Yuzawa[3], Y. Kebukawa[4], K. Kiryu[4], M. Uesugi[5], N. Tomioka[1], Y. Kodama[6], H. Naraoka[7], T. Yada[8] and M. Abe[8]

[1]*Kochi Institute for Core Sample Research, JAMSTEC, Nankoku 783-8502, Japan,*
[2]*Biogeochemistry Program, JAMSTEC, Yokosuka 237-0061, Japan,*
[3]*UVSOR Synchrotron Facility, Institute for Molecular Science, Okazaki 444-8585, Japan,*
[4]*Yokohama National University, Yokohama 240-8501, Japan,*
[5]*JASRI/SPring-8, Sayo-cho 679-5198, Japan,*
[6]*Marine Works Japan, Yokosuka 237-0063, Japan,*
[7]*Kyushu University, Fukuoka 819-0395, Japan,*
[8]*JAXA, Sagamihara 252-5210, Japan*

The JAXA Hayabusa2 mission is a combination of an asteroidal sample return and detailed spectroscopic observations of the C-type asteroid Ryugu for understanding of the Solar System evolution from the point of view of organics, and water as hydrous minerals [1]. The Hayabusa2 spacecraft was thought to be successfully obtained the Ryugu samples (an expected total amount of ~ 100 mg) from surface and subsurface on Feb. and Apr. 2019 and will return to the Earth on Dec. 2020.

To obtain the subsurface samples of the Ryugu, Small Carry-on Impactor (SCI) [2-4] was used to generate an artificial crater on the surface. A force of the SCI was made by HMX (High-Melting Explosive; cyclotetramethylenetetranitramine; $C_4H_8N_8O_8$, 296.15) together with HTPB (Hydroxyl Terminated Polybutadiene), IDP (Isodecyl palargonate; $C_{19}H_{38}O_2$) and IPDI (Isophorone diisocyanate; $C_{12}H_{18}N_2O_2$) [3,4]. Takano and coworkers [5] reported analytical results of SEM-EDS, TD-GC/MS, SPME-GC/MS, and isotope mass spectrometry for N and C isotopes. They found volatiles of aliphatic and aromatic carbon structures, and the several functional groups (hydroxyl, aldehyde, nitrile, and carboxyl) [5].

The explosion products generated by their chemical reactions with HMX, HTPB, IDP and IPDI should be investigated prior to analysis of the Ryugu samples because those materials might be possible contaminants in the subsurface samples in the sample container. In fact, Matsuoka and coworkers pointed out that the low albedo of the asteroid Ryugu could be explained by a combination of C-rich material, grains size, porosity and space weathering effects on the asteroid surface materials [6]. A study of the optical navigation camera on Hayabusa2 space craft reported that the asteroid Ryugu was composed of fluffy cosmic dust particles which is like the carbonaceous materials [7].

It is, therefore, necessary to analyze the SCI fragments and its products for comparison to the Ryugu samples. These results will provide relevant information to the initial analysis in advance the arrival of the Ryugu samples to the Earth.

In this study, we have conducted STXM-XANES analysis of the experimental explosion-products of the HMX mixture (Fig. 1) for sub-micrometer-scale functional groups of carbon, nitrogen and oxygen. Each fragment shows similar characteristics in O, N but some exceptions of C-XANES in sub-micrometer scale.

To acquire additional chemical properties of the products, we have carried out series of analysis utilizing an optical microscope for micrometer-scale texture, SEM-EDS for texture, microFT-IR for functional groups, micro-Raman for structures of carbonaceous materials. In the future, we will measure hydrogen, carbon and nitrogen isotopes using the JAMSTEC NanoSIMS (nano-scale Secondary Ion Mass Spectroscopy) for further characterizations of the samples.

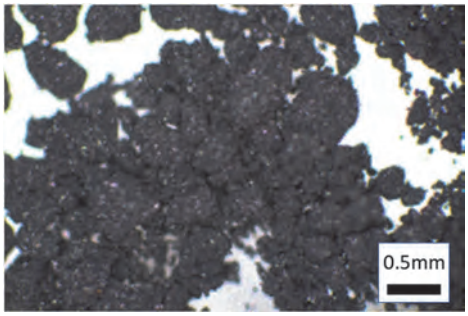


Fig. 1. Experimental products of HMX mixture.

[1] Tachibana *et al*., Geochemical Journal **48** (2014) 571.
[2] Arakawa *et al*., Science **368** (2020) 67.
[3] Saiki *et al*., Acta Astronautica **84** (2013) 227.
[4] Saiki *et al*., Space Science Reviews **208** (2016) 165.
[5] Takano *et al*., (2014) in Hayabusa 2014: 2nd Symp. Solar System Materials, P03.
[6] Matsuoka *et al.* (2019) 50th LPSC (LPI Contrib. No. 2132), abstract#1534.
[7] Okada *et al*., Nature **579** (2020) 518.

BL4U

Characterization of Lysosomal Storage Diseases Using STXM

T. Mansikkala[1,2], T. Ohigashi[3], H. Yuzawa[3], M. Patanen[1,2], I. Miinalainen[2], S. M. Kangas[4], A. E. Hiltunen[4], E.-V. Immonen[1,4], N. Kosugi[3], R. Hinttala[4], J. Uusimaa[4] and M. Huttula[1]

[1]*Nano and Molecular Systems Research Unit, PO Box 3000, 90014 University of Oulu, Finland*
[2]*Biocenter Oulu, PO Box 5000, 90014 University of Oulu, Finland*
[3]*UVSOR Synchrotron Facility, Institute for Molecular Science, Okazaki 444-8585, Japan*
[4]*PEDEGO Research Unit and Medical Research Center Oulu, and Oulu University Hospital, PO Box 5000, 90014 University of Oulu, Finland*

In this work, we have used scanning transmission X-ray microscopy (STXM) technique at BL4U beamline to study patient samples with lysosomal storage diseases and cultured patient-derived fibroblasts with a mutation in NHLRC2 gene. The NHLRC2 encodes an NHL repeat containing protein 2 ubiquitously present in various types of tissues. Mutations in NHLRC2 gene have been linked to fatal cerebropulmonary disease in children with fibrosis, neurodegeneration and cerebral angiomatosis (FINCA disease), but the functional role of the NHLRC2 is still unknown [1]. Transmission Electron Microscopy (TEM) analysis of immortalized cell cultures from FINCA patients demonstrated multilamellar and multivesicular bodies of unknown cellular origin, and it is suggested that NHLRC2 dysfunction enhances tissue fibrosis [2]. Previously, we reported an STXM study of FINCA patient tissue samples which were in line with TEM results [3].

Our aim was to investigate samples from known lysosomal storage diseases and FINCA disease. Muscle and kidney tissues samples were used, and they had clear enlarged lysosome clusters typical for lysosomal storage diseases. We also had cultured FINCA patient-derived fibroblasts to test if cell culture samples can be imaged. The tissue samples were fixed in 4 % paraformaldehyde and 2.5 % glutaraldehyde in 0.1 M phosphate-buffered saline. Prior to embedding in resin some samples were stained with 1 % OsO4 and/or uranyl acetate. The 100 nm and 150 nm thick sections of resin-embedded sample were imaged at Biocenter Oulu using a Tecnai G2 Spirit 120 kV TEM (FEI, Eindhoven, The Netherlands) equipped with a Quemesa CCD camera (Olympus Soft Imaging Solutions GmbH, Münster, Germany) to find lysosome clusters on the samples. The same area was then measured with STXM from the subsequent thin sections.

Figure 1 shows example of lysosomes in muscle tissue from patient with a lysosomal storage disease. A cluster analysis of STXM image stacks (Fig. 1 (b)) was performed using a MANTIS software [4]. The cluster analysis was able to differentiate cell components rather consistently based on their spectral information. The spectra obtained at C K-edge are very similar in each cluster as can be seen in Fig. 1 (c). This is caused by the resin that penetrates throughout the tissue and contributes mostly to the spectra. There seems to be no difference between the lysosomes and empty areas filled with resin (blue color in Fig. 1 (b)), indicating that the material inside lysosomes is lost during the preparation process.

Even though the resin fills the sample, its effect on the spectra can be reduced by removing the resin spectrum from the data. Figure 2 shows an example where the resin spectrum is subtracted with a factor of 0.9 using aXis2000. The exact multiplier is dependent on how much the embedding material penetrates the cell structures and it can vary. By removing the resin, we can detect spectral features that would otherwise be masked by the resin. In Fig. 2 we can see that there is strong peak at 288 eV differing from the typical peak for resin at 288.4 eV. This means that even though it is not ideal, we can study resin embedded samples and provide valuable data from them. However, the goal of identifying the storage material within lysosomes was not achieved.

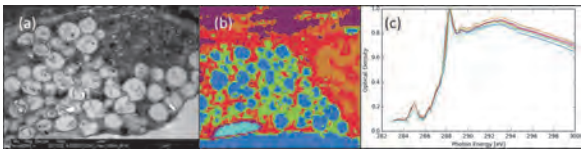


Fig. 1. (a) TEM image of the lysosome cluster from muscle tissue of a patient with lysosomal storage disease. (b) Cluster analysis of lysosomes imaged with STXM from same area as (a) but from a different thin slice. (c) Spectra of the clusters in (b).

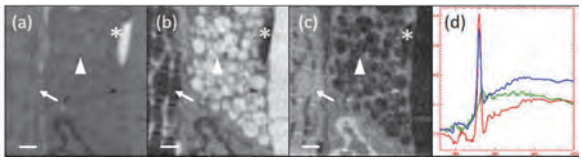
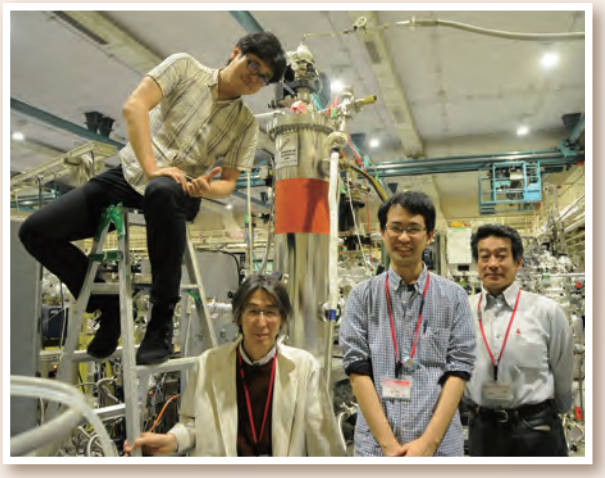


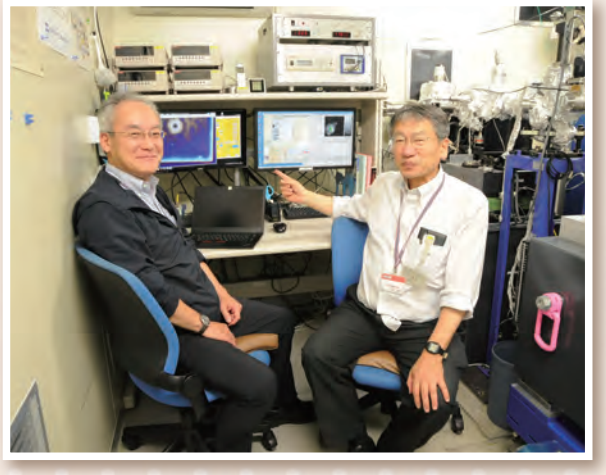
Fig. 2. Locations of fitted spectra in muscle tissue, (a) collagen, (b) lysosomes and (c) muscle fibers. (d) Spectra of the structures, red is collagen (a), green is lysosomes (b) and blue is muscle fibers (c). Collagen fiber bundle is marked with *, lysosomes are marked with Δ and muscle fiber with ↑. Scale bar is 1 μm.

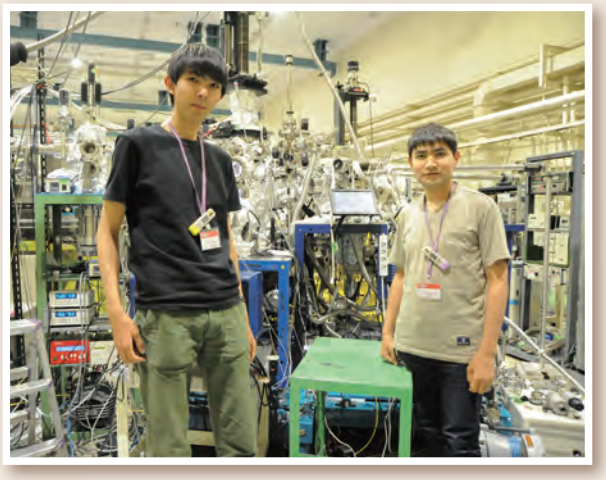
[1] J. Uusimaa *et al.*, Acta Neuropathol. **135** (2018) 727.
[2] T. Paakkola *et al.*, Hum. Mol. Gen. **27** (2018) 4288.
[3] E.-V. Immonen *et al.,* UVSOR Activity Report 2017 **45** (2018) 161.
[4] M. Lerotic *et al.*, J. Synchr. Rad. **21** (2014) 1206.

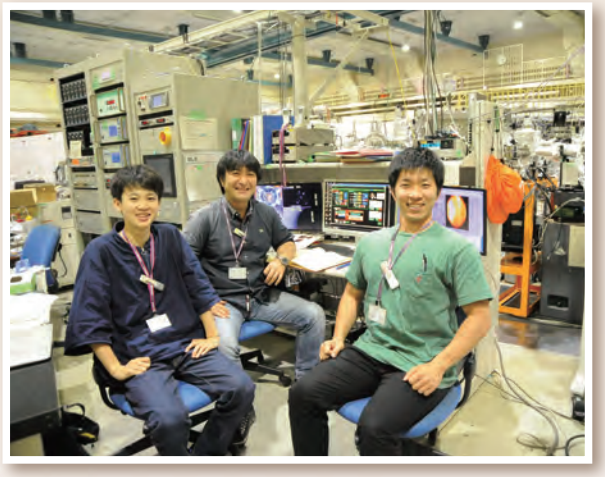
UVSOR User 1











IV

List of Publications

List of Publications

T. Adachi, S Ideta, Z- H Tin, H. Usui, K. Tanaka, S. Miyasaka and S. Tajima
"Electronic Structure of $Sr_{1-y}Ca_yFe_2(As_{1-x}P_x)_2$ (x = 0.25, y = 0.08) Revealed by Angle-Resolved Photoemission Spectroscopy", J. Phys. Soc. Jpn., **88** (2019) 084701.

Y. Hikosaka, T. Kaneyasu, M. Fujimoto, H. Iwayama and M. Katoh
"Coherent Control in the Extreme Ultraviolet and Attosecond Regime by Synchrotron Radiation", Nat. Commun., **10** (2019) 4988.

Y. Hikosaka
"A Virtual Stretch of Light Pulse Interval by Pulsed Electron Extraction Introduced into a Magnetic Bottle Electron Spectrometer", Rev. Sci. Instrum., **90** (2019) 053105.

M. Horio, K. Koshiishi, S. Nakata, K. Hagiwara, Y. Ota, K. Okazaki, S. Shin, S. Ideta, K. Tanaka, A. Takahashi, T. Ohgi, T. Adachi, Y. Koike and A. Fujimori
"*d*-Wave Superconducting Gap Observed in Protect-Annealed Electron-Doped Cuprate Superconductors $Pr_{1.3-x}La_{0.7}Ce_xCuO_4$", Phys. Rev. B, **100** (2019) 054517.

S. Ideta, N. Murai, M. Nakajima, R. Kajimoto and K. Tanaka
"Experimental Investigation of the Suppressed Superconducting Gap and Double-Resonance Mode in $Ba_{1-x}K_xFe_2As_2$", Phys. Rev. B, **100** (2019) 235135.

M. Y. Ismail, M. Patanen, J. A. Sirviö, M. Visanko, T. Ohigashi, N. Kosugi, M. Huttula and H. Liimatainen
"Hybrid Films of Cellulose Nanofibrils, Chitosan and Nanosilica—Structural, Thermal, Optical, and Mechanical Properties", Carbohydr. Polym., **218** (2019) 87.

T. Kaneyasu, Y. Hikosaka, M. Fujimoto, H. Iwayama and M. Katoh
"Controlling the Orbital Alignment in Atoms Using Cross-Circularly Polarized Extreme Ultraviolet Wave Packets", Phys. Rev. Lett., **123** (2019) 233401.

H. Kawaguchi and M. Katoh
"Orbital Angular Momentum of Liénard-Wiechert Fields", Prog. Theor. Exp. Phys., **8** (2019), 083A02.

Y. Kezuka, E. Tochigi, H. Murata, M. Yoshida, K. Eguchi, A. Nakahira, Y. Ikuhara and M. Tajika
"Synthesis of Tunable-Aspect-Ratio Calcite Nanoparticles via Mg^{2+} Doping", Cryst. Growth Des., **19** (2019) 6784.

A. Khodabandeh, R. D. Arrua, B. R. Coad, T. Rodemann, T. Ohigashi, N. Kosugi, S. C. Thickett and E. Hilder
"Morphology Control in Polymerized High Internal Phase Emulsion Templated via Macro-RAFT Agent Composition: Visualizing Surface Chemistry", Polym. Chem., **9** (2018) 213.

S. Kimura, Y. Nakajima, Z. Mita, R. Jha, R. Higashinaka, T. D. Matsuda and Yuji Aoki
"Optical Evidence of the Type-II Weyl Semimetals $MoTe_2$ and WTe_2", Phys. Rev. B, **99** (2019) 195203.

H. Kimura, T. Kato, D. Nakauchi, M. Koshimizu, N. Kawaguchi and T. Yanagida
"Vavuum-UV-Excited Photoluminescence and Scintillation Properties of CsCl Transparent Ceramics and Single Crystal", Sensors and Materials, **31** (2019) 1265.

S. Kosugi, N. Suzuki, N. Kumagai, H. Iwayama, E. Shigemasa, F. Koike and Y. Azuma
"Dominance of Angular Momentum Exchange in the PCI Recapture of Photoelectrons Revealed by High Resolution Auger Electron Measurements of Kr", J. Phys. B: Atomic, Mol. Opti. Phys., **52** (2019) 245002.

K. Kumadani, Y. Takamatsu, T. Minami, M. Togo, H. Murata and A. Nakahira
"Synthesis and Characterization of LTA-Type Zeolite by Microwaveassisted Hydrothermal Process", J.Ceramic Society of Japan, **127** (2019) 585.

Y.R. Lu, Y.F. Wang, H.W. Chang, Y.C. Huang, J.L. Chen, C.L. Chen, Y.C. Lin, Y. G. Lin, W.F. Pong, T. Ohigashi, N. Kosugi, C.H. Kuo, W.C. Chou and C.L. Dong
"Effect of Fe_2O_3 Coating on ZnO Nanowires in Photoelectrochemical Water Splitting: A Synchrotron X-ray Spectroscopic and spectromicroscopic Investigation", Sol. Energy Mater Sol. Cells, **209** (2020) 110469.

T. Makino, T. Asai, T. Takeuchi, K. Kaminaga, D. Oka and T. Fukumura
"Temperature Dependence of Dielectric Functions in Yb_2O_3 and Lu_2O_3 epitaxial thin films on sapphire (0001)", Jpn. J. Appl. Phys., **59** (2020) SCCB13.

H. Matsuda and F. Matsui
"Principle and Basic Design of Omnidirectional Photoelectron Acceptance Lens", Jpn. J. Appl. Phys. 59 (2020) 046503.

F. Matsui, S. Makita, H. Matsuda, T. Ohigashi, H. Yamane and N. Kosugi
"Identification of Twinning-induced Edges on the Cleaved Graphite Crystal Surface", J. Phys. Soc. Jpn., **88** (2019) 114704.

F. Matsui, S. Makita, H. Matsuda, T. Ueba, T. Horigome, H. Yamane, K. Tanaka, S. Kera and N. Kosugi
"Bulk and Surface Band Dispersion Mapping of the Au(111) Surface by Acceptance-cone Tunable PES System", e-J. Su rf. Sci. Nanotechnol. **18**, (2020) 18.

N. Murai, K. Suzuki, S. Idea, M. Nakajima, K. Tanaka, H. Ikeda and R. Kajimoto
"Effect of Electron Correlations on Spin Excitation Bandwidth in $Ba_{0.75}K_{0.25}Fe_2As_2$ as Seen via Time-of-Flight Inelastic Neutron Scattering", Phys. Rev. B, **97** (2018) 241112.

M. Nagasaka, H. Yuzawa, N. Takada, M. Aoyama, E. Rühl and N. Kosugi
"Laminar Flow in Microfluidics Investigated by Spatially-Resolved Soft X-ray Absorption and Infrared Spectroscopy", J. Chem. Phys., **151** (2019) 114201.

M. Nagasaka, H. Yuzawa and N. Kosugi
"Soft X-ray Absorption Spectroscopy of Liquids for Understanding Chemical Processes in Solution", Anal. Sci., **36** (2020) 95.

M. Nagasaka, H. Yuzawa and N. Kosugi
"Microheterogeneity in Aqueous Acetonitrile Solution Probed by Soft Xray Absorption Spectroscopy", J. Phys. Chem. B, **124** (2020) 1259.

Y. Nakajima, Z. Mita, H. Watanabe, Y. Ohtsubo, T. Ito, H. Kotegawa, H. Sugawara, H. Tou and S. Kimura
"Optical and Photoelectrical Studies on Anisotropic Metal-Insulator Transition of RuAs", Phys. Rev. B, **100** (2019) 125151.

T. Nakamura, Y. Ohtsubo, Y. Yamashita, S. Ideta, K. Tanaka, K. Yaji, A. Harasawa, S. Shin, F. Komori, R. Yukawa, K. Horiba, H. Kumigashira and S. Kimura
"Giant Rashba Splitting of Quasi-one-dimensional Surface States on Bi/InAs(110)-(2x1)", Phys. Rev. B, **98** (2018) 075431.

D. Nakauchi, M. Koshimizu, N. Kawaguchi and T. Yanagida
"Photo- and Radio-Luminescence Characterizations in Rare-Earth-Doped $SrAl_2O_4$ Crystals", J. Ceram. Proc. Res., **20** (2019) 307.

Y. Ohtsubo, Y. Yamashita, K. Hagiwara, S. Ideta, K.Tanaka, R. Yukawa, K. Horiba, H. Kumigashira, K. Miyamoto, T. Okuda, W. Hirano, F. Iga and S. Kimura
"Non-Trivial Surface States of Samarium Hexaboride at the (111) Surface", Nat. Commun., **10** (2019) 1.

S. Park, T. Schultz, A. Han, A. Aljarb, X. Xu, P. Beyer, A. Opitz, R. Ovsyannikov, L.-J. Li, M. Meissner, T. Yamaguchi, S. Kera, P. Amsalem and N. Koch
"Electronic Band Dispersion Determination in Azimuthally Disordered Transition-Metal Dichalcogenide Monolayers", Commun. Phys., **2** (2019) 68.

J. Ren, D. S. Achilleos, R. Golnak, H. Yuzawa, J. Xiao, M. Nagasaka, E. Reisner and T. Petit
"Uncovering the Charge Transfer between Carbon Dots and Water by In Situ Soft X-ray Absorption Spectroscopy", J. Phys. Chem. Lett., **10** (2019) 3843.

D. Shiratori, Y. Isokawa, H. Samito, M. Koshimizu, N. Kawaguchi and T. Yanagida
"Effect to Optical Properties by Changing the Al_2O_3 ratio in K_2O-Al_2O_3-P_2O_5 Glasses", J. Ceram. Proc. Res., **20** (2019) 301.

Y. Sugizaki, Y. Shimato, T. Yoshida, R. Sugimoto, N. Maejima and K. Edamoto
"Soft X-Ray Photoelectron Spectroscopy Study on the P Segregation Process And Its Effect on the Electronic Structure of Fe_2P(0001)", Jpn. J. Appl. Phys., **58** (2019) SIIC02.

J. Takahashi and K. Kobayashi
"Origin of Terrestrial Bioorganic Homochirality and Symmetry Breaking in the Universe", Symmetry, **11** (2019) 919.

D. Takane, Z. Wang, S. Souma, K. Nakayama, T. Nakamura, H. Oinuma, Y. Nakata, H. Iwasawa, C. Cacho, T. Kim, K. Horiba, H. Kumigashira, T. Takahashi, Y. Ando and T. Sato
"Observation of Chiral Fermions with a Large Topological Charge and Associated Fermi-Arc Surface States in CoSi", Phys. Rev. Lett., **122** (2019) 076402.

D. Takane, K. Nakayama, S. Souma, T. Wada, Y. Okamoto, K. Takenaka, Y. Yamakawa, A. Yamakage, T. Mitsuhashi, K. Horiba, H. Kumigashira, T. Takahashi and T. Sato
"Observation of Dirac-Like Energy Band and Ring-Torus Fermi Surface Associated with the Nodal Line in Topological Insulator CaAgAs", npj Quantum Mater., **3** (2018) 1.

N. Tatemizo, S. Imada, K. Okahara, H. Nishikawa1, K. Tsuruta, T. Ina, Y. Miura, K. Nishio and T. Isshiki
"Electronic Structure of AlFeN Films Exhibiting Crystallographic Orientation Change from c- to a-axis with Fe Concentrations and Annealing effect", Sci. Rep., **10** (2020) 1819.

S. Watanabe, T. Kawai and K. Mizoguchi
"Energy Relaxation from STE to In^+ Centers in NaI:In^+ Crystals", J. Phys. Conf. Ser., **1220** (2019) 012031.

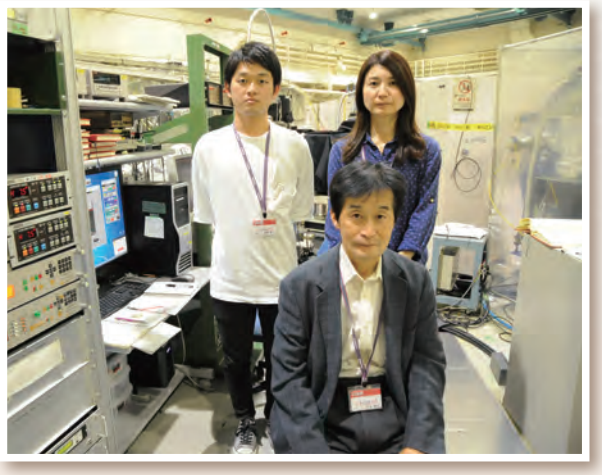
S. Yamanaka, K. Tonami, M. Iwashita, K. Yoshida, R. Takeuchi, S. Ideta, K. Tanaka, K. Mase, K. Yamada, H. Yoshida and Y. Nakayama
"High Sensitivity Detection of the Frontier Electronic States of $CH_3NH_3PbI_3$ Single Crystals by Low Energy Excitation", Appl. Phys. Express, **12** (2019) 051009.

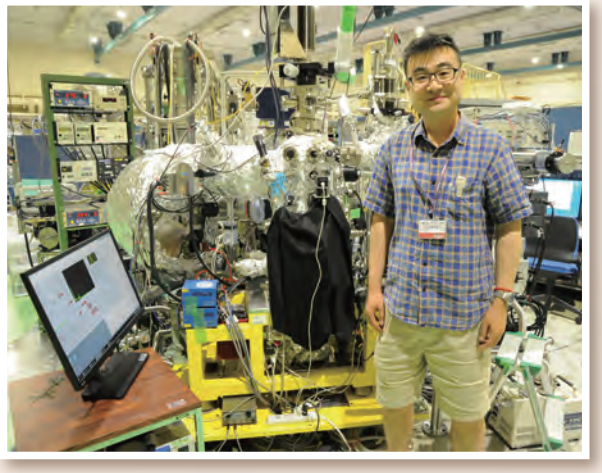
H. Yamane, F. Matsui, T. Ueba, T. Horigome, S. Makita, K. Tanaka, S. Kera and N. Kosugi
"Acceptance-Cone-Tunable Electron Spectrometer for Highly-Efficient Constant Energy Mapping", Rev. Sci. Instrum., **90** (2019) 093102.

J. Yang, S-X. Ren, T. Yamaguchi, M. Meissner, L. Cheng, L. Zhou, S. Ideta, K. Tanaka and S. Kera
"Valence Band Dispersion Measured in the Surface Normal Direction of $CH_3NH_3PbI_3$ Single Crystals", Appl. Phys. Exp., **13** (2020) 011009.

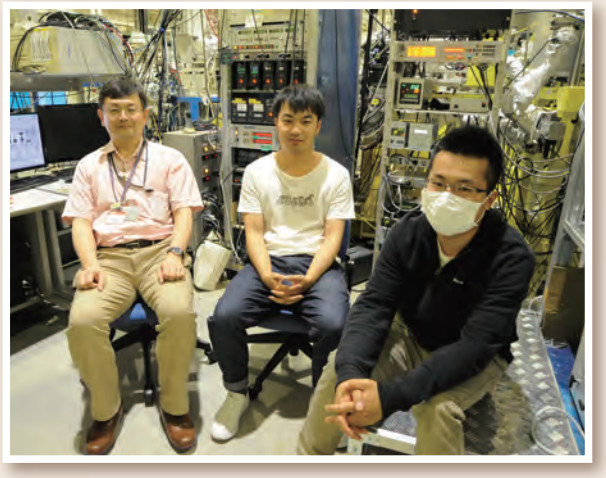
Y. Yokoyama, H. Hasegawa, Y. Mizuno, D. Asai, Y. Okamoto, H. S. Suzuki, K. Takehana, Y. Imanaka and K. Takenaka
"Effects of Y Substitution on the Electronic Structure and Charge Dynamics of SmS", Phys. Rev. B, **100** (2019) 245143.

UVSOR User 2











V

Workshops

UVSOR Symposium 2019

Date: November 16-17, 2019
Place: Okazaki Conference Center

November 16th (Sat.)

<Session 1, Chair: **T. Ohigashi** (UVSOR)>

13:05 – 13:25 Opening Remark
S. Kimura (Osaka Univ.)

13:15 – 13:50 Current Status of BL4U
T. Ohigashi (UVSOR)

13:50 – 14:15 Observation of Water Surrounding an Air Bubble by Scanning Tunneling X-ray Microscopy
Y. Harada (ISSP, Univ. of Tokyo)

14:15 – 14:30 Coffee Break

14:30 – 14:55 Phase 2 Curation "Team Kochi" for Hayabusa2 Returned Sample: In-depth Analysis of a Single Grain utilizing Linkage Microanalysis Instruments
M. Ito (JAMSTEC)

14:55 – 15:25 [Invited Talk] Development of Focusing and Imaging Systems for Soft X-ray and EUV Light Based on Axially Symmetric Mirror
H. Mimura (Univ. of Tokyo)

15:25 – 16:00 Coffee Break

<Session 2, Chair: **H. Iwayama** (UVSOR)>

16:00 – 16:20 Construction of a VIS-VUV Complex Refractive Index Measurement Instrument Dedicated to BL7B
K. Fukui (Univ. Fukui)

16:20 – 16:50 [Invited Talk] Spectroscopic Study on Alloys and Compounds -My 25-Years Research with UVSOR
K. Soda (Nagoya Univ.)

16:50 – 17:20 Short Presentation for Poster Session

17:30 – 18:30 Poster Session

18:30 – 20:00 Banquet

November 17th(Sun.)

<Session 3, Chair: **M. Fujimoto** (UVSOR)>

9:00 – 9:30 [Invited Talk] Coherent Control of Atoms using Synchrotron Radiation
T. Kaneyasu (SAGA Light Sorce)

9:30 – 9:50 Development of Gamma-ray Induced Positron Annihilation Lifetime Spectroscopy
Y. Taira (AIST)

9:50 – 10:10 Measurement of Ion Coordination to Lipid Bilayer Membranes using Artificial Biomembrane System
R. Tero (Toyohashi Univ. Tech.)

10:10 – 10:20 Coffee Break

<Session 4, Chair: **K. Tanaka** (UVSOR)>

10:20 – 10:40 Achievements and Prospects of Soft-X-ray Photoelectron Spectroscopy at BL6U
F. Matsui (UVSOR)

10:40 – 11:00 Fabrication of Novel Topological Materials and its Electronic Structure
T. Hirahara (Tokyo Inst. Tech.)

11:00 – 12:00 Discussion and Closing Remark

Poster Session

P1 Progress of Isotope-Specific CT Imaging Experiment at BL1U
H. Zen (Kyoto Univ.)

P2 Optical Activity Emergence in Bio-organic Molecules by Circularly-Polarized Undulator Light Irradiation
J. Takahashi (Yokohama National Univ.)

P3 Optical Vortex UV Light Irradiation to Zn(II) Complex-PMMA Hybrid Materials
S. Yamazaki (Tokyo Univ. of Science)

P4 Elliptical Polarized UV Light Irradiation to Zn(II) Complex-PMMA Hybrid Materials
M. Yoshida (Tokyo Univ. of Science)

P5 Development of 2π Steradian Photoelectron Spectrometer
H. Matsuda (IMS)

P6 Investigation of Charge Compensation Mechanism of SiO_2/Si by Sample Current Measurement
R. Nozaki (Waseda Univ.)

P7 Measurement of Fluorescence Lifetime under VUV-SX Excitation in Single Bunch Operation
K. Kawai (Yamagata Univ.)

P8 Study on Rear Earth Pyro-Silicate Type Scintillator with UVSOR
S. Kurosawa (Tohoku Univ.)

P9 Combined Excitation-Emission Spectroscopy on $CH_3NH_3Pb(Cl,I)_3$
T. Takeuchi (Fukui Univ.)

P10 Temperature Dependence of Dielectric Functions in Yb_2O_3 and Lu_2O_3 Thin Films
T. Asai (Fukui Univ.)

P11 Temperature Characteristics of Auger-Free Luminescence in Molecular Ionic Crystals
T. Aizawa (Yamagata Univ.)

P12 Evaluation of Fluorescence Lifetimes of Plastic Scintillators for Particle and Unclear Physics Experiments
H. Ikeda (Yamagata Univ.)

P13 Conversion Phenomena from Ag^+ to Ag^- Centers by VUV Irradiation in NaCl:I^-, Ag^+ Crystals
T. Kawai (Osaka Prefecture Univ.)

P14 Hydration Structure of *N,N*-dimethylglycine Studied by Soft-Xray Absorption Spectroscopy
N. Fukuda (Hiroshima Univ.)

P15 The Change of Hydration Structure of Glycine Betaine by Salt Addition Studied by Soft X-ray Absorption Spectroscopy

S. Ohsawa (Hiroshima Univ.)

P16 Observation of Nickel-Carbonate Electrocatalyst for Water Splitting using Operando C K-edge XAFS

T. Moriyama (Yamaguchi Univ.)

P17 X-ray Absorption Spectroscopy Measurement of Lipid Bilayer Membranes in Aqueous Solution

W. Goh (Toyohashi Univ. of Technology)

P18 Theoretical Analysis of Two-phase Network Formation and Its Visualization by STXM

Y. Sakaki (Kyoto Institute of Technology)

P19 Visualization of Orientation Distribution in Carbon Fibers by Scanning Transmission X-ray Microscopy

T. Harano (Nippon Steel)

P20 Pulsed Electron Excitation Installed into a Magnetic Bottle Electron Spectrometer

Y. Hikosaka (Toyama Univ.)

P21 Photoelectron-Auger Electron Coincidence Spectroscopy for Organic Thin Films

S. Wada (Hiroshima Univ.)

P22 Development of Soft-X-ray Detector for Removing High Order X-rays

M. Nagasaka (IMS)

P23 Characterization of Amorphous Chalcogenide Thin Films by Vacuum Ultraviolet Absorption Spectroscopy

K. Hayashi (Gifu Univ.)

P24 High-Resolution ARPES Study of Atomic Layer $NbSe_2$

Y. Nakata (Tohoku Univ.)

P25 Perpendicular Magnetic Anisotropy Induced by Rashba-type Spin-Orbit Coupling

J. Okabayashi (Tokyo Univ.)

P26 Surface Atomic and Electronic Structures of $SmB_6(001)$, a Topological Kondo Insulator, Evolving with the Cleaning Procedure

Y. Ohtsubo (Osaka Univ.)

P27 Electronic Structure of Ultrathin Bi(111) Films on InSb(111)

J. K. Modak (Osaka Univ.)

P28 Angle-resolved Photoemission Study of MAX Phase Compound Ti_2SnC

T. Ito (Nagoya Univ.)

P29 Investigation of Photon Energy Drift at BL5B

H. Zen (Kyoto Univ.)

P30 Nature of Shallow Electron Traps in $Ce:Gd_3(Ga,Al)_5O_{12}$ Crystals Studied by UV-induced Absorption Spectroscopy

T. Yagihashi (Yamagata Univ.)

P31 Distribution of the Photoelectron from MoS_2 in the Momentum Space: Comparison between the Theoretical Calculation and ARPES

S. Tanaka (Osaka Univ.)

P32 Fabrication of Bi_1Te_1 Ultrathin Films and the Surface Electronic Structure

S. Kusaka (Tokyo Inst. Tech.)

P33 Electronic State of Pentacene/Graphite upon Low-energy UV Light Excitation

Y. Hasegawa (IMS)

P34 Doping Dependence of the Electronic Structure in Triple-layer Cuprate Bi2223 Studied by ARPES

S. Ideta (UVSOR)

P35 Substrate Temperature Control in Pulsed Laser Deposition Method for VUV Sensor Development using BaF_2 Thin Film

S. Kato (Nagoya Inst. Tech.)

P36 Impurity Emission of Aluminum Nitride

Y. Maegawa (Fukui Univ.)

P37 Derivation Complex Refraction Index by Measurement Device of Complex Refractive Index for VIS-VUV

J. Omae (Fukui Univ.)

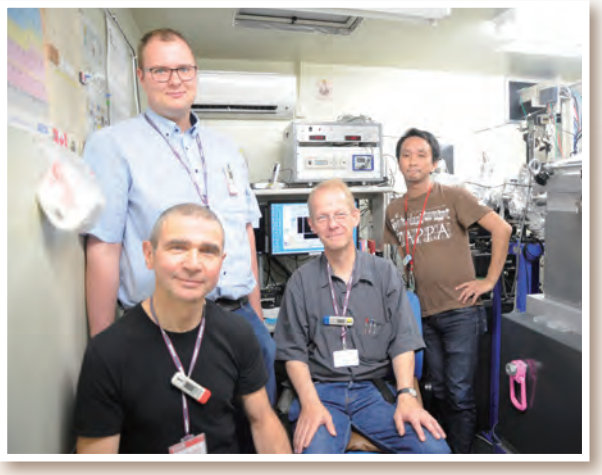
P38 Emission and Excitation Spectra of Mercury Lamp Irradiated Amorphous Carbon Nitride

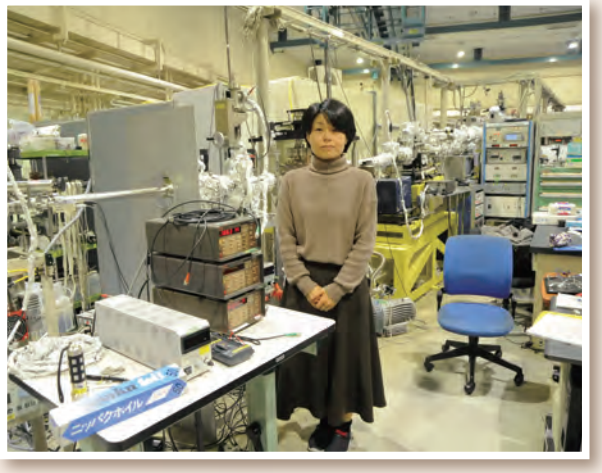
T. Jinno (Fukui Univ.)

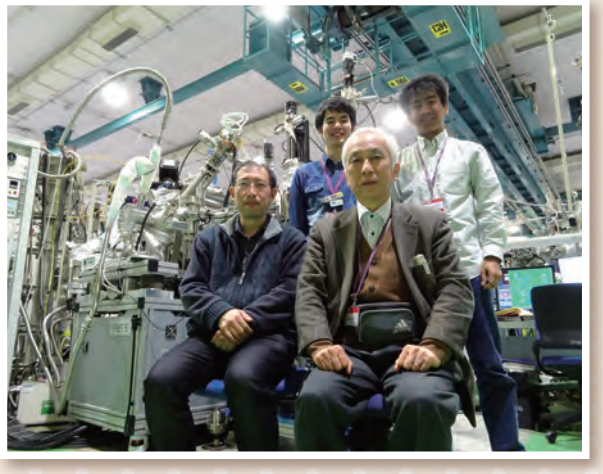
P39 The Optical Properties of High Concentration Boron-Doped Diamond Thin Film

M. Suzuki (Fukui Univ.)

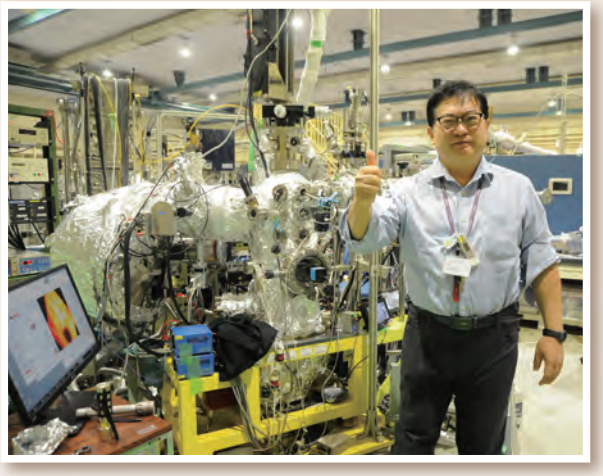
UVSOR User 3











UVSOR Symposium 2019















Editorial Board：H. Iwayama　M. Fujimoto　M. Sakai　I. Inagaki　M. Ishihara

Institute for Molecular Science
National Institutes of Natural Sciences
Okazaki 444-8585,Japan

Tel : +81-564-55-7402
Fax : +81-564-54-7079
http://www.uvsor.ims.ac.jp



ISSN 0911-5730